SAPIENZA
UNIVERSITÀ DI ROMA

Characterization of Very Low Intensity Ion Beams from the REX/HIE-ISOLDE Linear Accelerator at CERN

Department of Physics

Philosophical Doctorate in Accelerator and Beam Physics – XXXIII Ciclo

Candidate

Niels Bidault

ID number 1805240

Thesis Advisors

Mauro Migliorati, Ph.D.
University of Rome 'Sapienza', INFN

Jose Alberto Rodriguez, Ph.D.
CERN

Co-Advisors

Fredrik Wenander, Ph.D.
CERN

Antonio Villari, Ph.D.
FRIB, Michigan State University

A thesis submitted in partial fulfillment of the requirements
for the degree of Doctor of Philosophy in Physics

May 2021

Thesis defended on the 30th of June 2021
in front of a Board of Examiners composed by:

Pasquale Arpaia, Ph.D. - University of Naples 'Federico II', INFN (chairman)

James Rosenzweig, Ph.D. - UCLA

Giovanni Mettivier, Ph.D. - University of Naples 'Federico II', INFN

Characterization of Very Low Intensity Ion Beams from the REX/HIE-ISOLDE Linear Accelerator at CERN

Ph.D. thesis. Sapienza – University of Rome

This thesis has been typeset by LaTeX and the Sapthesis class.

Version: January 27, 2022

Author's email: niels0@protonmail.com

En hommage à mon frère, Brenn Bidault.

Abstract

The Isotope Separator On-Line Device (ISOLDE) at CERN is one of the world-leading research facilities in the field of nuclear physics. Radioactive Ion Beams (RIBs) are produced when 2.0 GeV protons, driven from the Proton Synchrotron Booster (PSB), impact onto a target. The RIB of interest is extracted and transported to experimental stations either directly or following an acceleration to higher energies. Before meeting the requirements for acceleration, the continuous low-energy RIB is accumulated and cooled into the REX-TRAP Penning trap and transferred toward the REXEBIS charge breeder. The ion beam extracted from the REXEBIS is pulsed and multi-ionized to reach a mass-to-charge ratio (A/q) within the acceptance of the linac. After that, the RIB is accelerated (up to 9.7 MeV/u at $A/q = 3.1$) through the Radioactive EXperiment normal-conducting linac injector and the recently completed High Intensity and Energy superconducting extension (REX/HIE-ISOLDE) and finally transported to one of the three experimental stations located at the end of High Energy Beam Transfer (HEBT) lines. The manipulation and precise knowledge of the ion beam properties are of primary importance for the experimental apparatus, as well as for the calibration and efficiency of the detection systems. The study of ion beam properties mainly concerns the dynamics over time and space distributions of density, motion and energy, correlated with beam physics, that is to say: the purity of the beam of interest by considering potential sources of contamination, the ion-pulse time-structure, the transversal and longitudinal properties (Courant-Snyder parameters and energy distribution).

The core of the thesis aims at defining instrumental methodologies that allow for the determination of RIBs properties from the REX/HIE-ISOLDE linear accelerator, at intensities often too weak to make use of conventional beam-line monitoring detectors (for instance, Faraday cups). We propose new approaches appropriate for very low-intensity ion beams, using a silicon detector as a beam collector. In general, the demonstration of a new measurement concept suitable for sub-femto-Ampere ion beams is corroborated with ordinary measurement techniques at ion

beam currents higher than several pico-Amperes. The capability to measure absolute beam intensities over three orders of magnitude is illustrated with a practical use during beam operation, tuning the Radio-Frequency Quadrupole structure. Then, we measure and study the quality of the beam produced from REXEBIS in the scope of evaluating the electron gun's performance and the general charge-breeding conditions. An effort dedicated to optimizing the ion pulse time distribution extracted from an EBIS, called Slow Extraction, led us to use measurements of axial energy distributions further. By justifying the collisional aspects of the plasma, we infer a correlation between the measured axial energy distributions and the temperature of ions. Key indicators of the extracted beam's quality can then be deduced from the ion temperature using Boltzmann distributions, such as the emittance. We illustrate the studies related to the charge-state and the energy dynamics with the case of a multi-charged xenon beam. The question of beam purity is assessed by demonstrating the possibility to map a spectrum of the contamination from residual gas ions on a wide A/q-range.

Furthermore, we characterize the beam dynamics in the HEBT lines after acceleration through REX/HIE-ISOLDE linac. The principles behind the identification of the transverse and the longitudinal beam properties are mainly based on multiple acquisitions of the respective trace-space projections. In the case of transverse beam properties, we correlate measurements using the quadrupole-scan method and the double-slit method using a $^{39}K^{10+}$ beam of less than one femto-Ampere current, at an energy of 3.8 MeV/u. We show the uncertainties associated with the evaluation of the emittance and Twiss parameters for each method. We then explain the choice made for measuring the beam energy and the analysis of results using RIB. The complete longitudinal beam properties are measured using a superconducting quarter-wave resonator as a buncher, and measuring the beam energy and time-of-flight distributions.

Acknowledgments

First and foremost, I would like to express all my gratitude towards my supervisors, Jose Alberto Rodriguez and Mauro Migliorati. Alberto introduced me to ISOLDE, taught me the intricacies of beam physics and the daily operation of the post-accelerator, with never fainting pedagogy and dedication. I gratefully acknowledge Mauro's interest in the thesis project and his support between CERN and the University of Rome 'Sapienza'. It was delicate for me to maintain the tie with academia, and I thank Mauro, who has always been there to provide me with great advice and to answer my multiple questions. It has been a sincere pleasure working with them. I would further like to thank Fredrik Wenander and Antonio Villari for accepting supervising my thesis. Fredrik has positively challenged me all through those last years, and I cannot thank him enough for being such a great source of motivation. Antonio and Fredrik have been very supportive, and I would like to thank them for their flexibility during the correction. I extend my gratitude to Daniele del Re, the Accelerator Physics PhD program coordinator at the University of Rome 'Sapienza' and Rende Steerenberg, the Operation Group leader at CERN.

I would like to acknowledge the remarkable work carried out by the Operation section at ISOLDE, namely by Erwin Siesling, Eleftherios Fadakis, Emiliano Piselli, Emanuele Matli, Miguel Lozano, Pascal Fernier and Simon Mataguez. In addition to your work, you all participated in my integration and contributed to my well-being in one way or another. Those extended hours in the control room were always more pleasant in your presence.

My initial involvement with the HIE-ISOLDE project would not have been possible without its leader, Yacine Kadi, to whom I would like to express my gratitude. A lot of this thesis would not have been likely without the help of many people doing exceptional work here at ISOLDE. These include, but non-exhaustively, the members of the Beam Instrumentation group: William Andreazza and Enrico Bravin and the members of the Vacuum group: Abel Gutierrez and Jose Antonio Somoza. The

feasibility of the thesis project relied on the improvement or the development of critical technological achievements. For this matter, I would like to express my gratitude to Sergey Sadovich and his more than precious help with silicon detectors. I want to tell all my appreciation for the excellent work done to improve the stability and performance of the REX linear accelerator from Cristiano Gagliardi and Luca Timeo. I also want to acknowledge Walter Venturini, Daniel Valuch and Akira Miyazaki for their exceptional work to commission HIE-ISOLDE superconducting structures. Finally, I would like to sincerely thank Karl Johnston and Gerda Neyens from the ISOLDE Physics Group for their constant support and for the allocation of resources and machine development time. There are many people in the ISOLDE collaboration, and it was a pleasure working with all of them.

Finally, I would like to give thanks to my friends and family who have been providing me with unwavering encouragements. Gli fratelli Badis, Elouan, Elyess, Gabriel, Gui, Hugo and Vincenzo, are the most monstrously intriguing people to hang with, and I cherish all of them for being what they are. I think about Katie, who actualized me during the scholartrip from Pearl St. to the Mayan wonders. My last and warmest thank is obviously directed to my family. I believe this thesis reflects us and the education my mother, my father and my brothers gave me. I am privileged that my mother and father allowed me to pursue long years of studies and always showed unconditional trust in me. I dedicate this thesis to the memory of my brother Brenn, who will never cease to be my unique inspiration and, in particular, motivation for doing physics.

Contents

List of Figures

List of Tables

Nomenclature

Acronyms

amu	**a**tomic **m**ass **u**nit (Dalton)	**ANL**	**A**rgonne **N**ational **L**aboratory
CERN	**C**onseil **E**uropéen pour la **R**echerche	**EBIS/T**	**E**lectron **B**eam **I**on **S**ource/**T**rap
HEBT	**H**igh **E**nergy **B**eam **T**ransfer	**HIE**	**H**igh **I**ntensity and **E**nergy
GUI	**G**raphical **U**ser **I**nterface	**ISOLDE**	**I**sotope Mass **S**eparator **O**n-**L**ine **DE**vice
REX	**R**adioactive Ion Beam **EX**periment	**RFQ**	**R**adio**F**requency **Q**uadrupole
RIB	**R**adioactive **I**on **B**eam	**rms**	**r**oot **m**ean **s**quare

Physics Constants

All numerical values will be shown using the International System Units (SI).

Symbol	Name	Value
c	Space time constant	$2.997\,924\,58 \times 10^{8}\,\mathrm{m\,s^{-1}}$
e	Elementary charge	$1.602\,176\,63 \times 10^{-19}\,\mathrm{s\,A}$
ϵ_0	Vacuum permittivity	$8.854\,187\,81 \times 10^{-12}\,\mathrm{kg^{-1}\,m^{-3}\,s^{4}\,A^{2}}$
k_B	Boltzmann constant	$1.380\,648\,52 \times 10^{-23}\,\mathrm{kg\,m^{2}\,s^{-2}\,K^{-1}}$
m_e	Electron mass	$9.109\,383\,632 \times 10^{-31}\,\mathrm{kg}$

Derived Constants

Symbol	Name	Value
m_u	Mass of 1 amu	$1.660\,539\,07 \times 10^{-27}\,\mathrm{kg}$
E_u	Rest mass of 1 amu	$9.314\,941\,02 \times 10^{8}\,\mathrm{eV/c^{2}}$

Beam Physics Parameters

Symbol	Name	Definition
ε_x, ε_x^n	Emittance and normalized emittance on x-plane	Eq. . Page .
α_x, β_x, γ_x	Twiss parameters on x-plane	Eq. . Page .
α, β, γ	Relativistic factors	Eq. . Page .
T	Transit time factor	Eq. . Page .

Plasma Physics Parameters

add specific units for beam parameters

Symbol	Name	Definition
C_P	Heat capacity	Eq. . Page .
n_L	Number of degrees of freedom	Eq. . Page .
$\ln \Lambda_{kj}$	Coulomb logarithm between species k and j	Eq. . Page .
ω_p	Plasma frequency	Eq. . Page .

CHAPTER 1

Introduction

In 1930, Ernest Lawrence was involved in the development of the first circular particle accelerator at the University of California, Berkeley. A few years later, during the course of the Manhattan Project, he participated in the creation of the Calutron, the first mass spectrometer designed for separating the isotopes of uranium. The knowledge of technological solutions for accelerators has since then not ceased to increase, bringing innumerable contributions to science and society. The maturity of the technology to produce and study Radioactive Ion Beams (RIBs) is leading us further in exploring the uncharted map of isotopes. Investigating exotic nuclei, i.e. isotopes with a proton-to-neutron ratio very different from the stable isotopes, implies several hurdles:

1. The diagnosis of the beam intensity requires coping with the extremely low production cross-sections of isotopes away from the valley of beta stability.

2. The very short half-lives of exotic nuclei imply delivering the beam to experimental stations within a constrained time frame.

3. The yield of the studied isotopes is often polluted by undesired species, which necessitate a mass-separation, sometimes to the isobaric level.

Those requirements translate into concrete indicators of the performance of RIB facilities. In this first chapter, we contextualize the study of RIB and analyze the notion of *beam quality* which is the leitmotiv underlying this thesis.

1.1 Radioactive Ion Beam Facilities

The production of RIB is obtained using a driver accelerator to bombard a target and initiate a variety of nuclear reactions, such as fission, spallation or fragmentation. The isotopes of interests are ionized and selected using either the isotope separation on-line (ISOL) technique or the in-flight separation technique. Those methods were originally complementary, but are nowadays combined to produce high quality RIB.

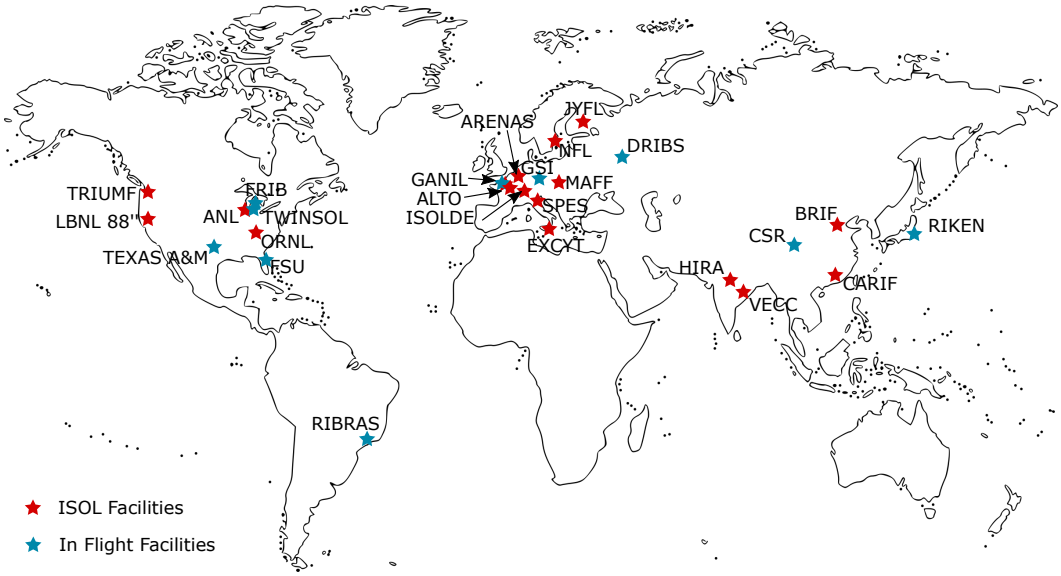

Figure 1.1. World-map of radioactive ion beam experiments or facilities.

ISOL Separation

The ISOL technique involves a primary beam of high-energy protons sent onto a thick, and generally hot, target. The RIB is produced from an ion source, then separated from isobaric contaminants.

In-Flight Separation

With the in-flight technique, the radioactive isotopes are produced by the interaction of a primary beam of heavy ions with a thin target. The fragments are then separated to select the RIB of interest.

1.2 ISOLDE

In 1951, Otto Kofoed-Hansen and Karl-Ove Nielsen reported on the first on-line produced radioisotopes of krypton, using a cyclotron at the Niels Bohr Institute in Copenhagen. Sixteen years later, the underground hall for ISOLDE at CERN is ready, and the proton beams coming from the Synchrocyclotron (SC) bombards the target for the first time. ISOLDE is the oldest and the precursor of ISOL installations worldwide. Since then, the facility and target systems have been upgraded several times, most notably in 1992, when the whole facility was moved and connected to the ProtonSynchroton Booster (PSB). The ISOLDE facility is upgraded with two isotope separators, a general-purpose separator with one magnet (GPS) and a high-resolution separator (HRS) with two magnets. REX-ISOLDE post-accelerator is put into operation in 2001 to provide beams with energies up to 3 MeV/u. The post-accelerator is finally upgraded in 2015, following the HIE-ISOLDE project, aiming at reaching 10 MeV/u and extending the reach masses over the Coulomb barrier.

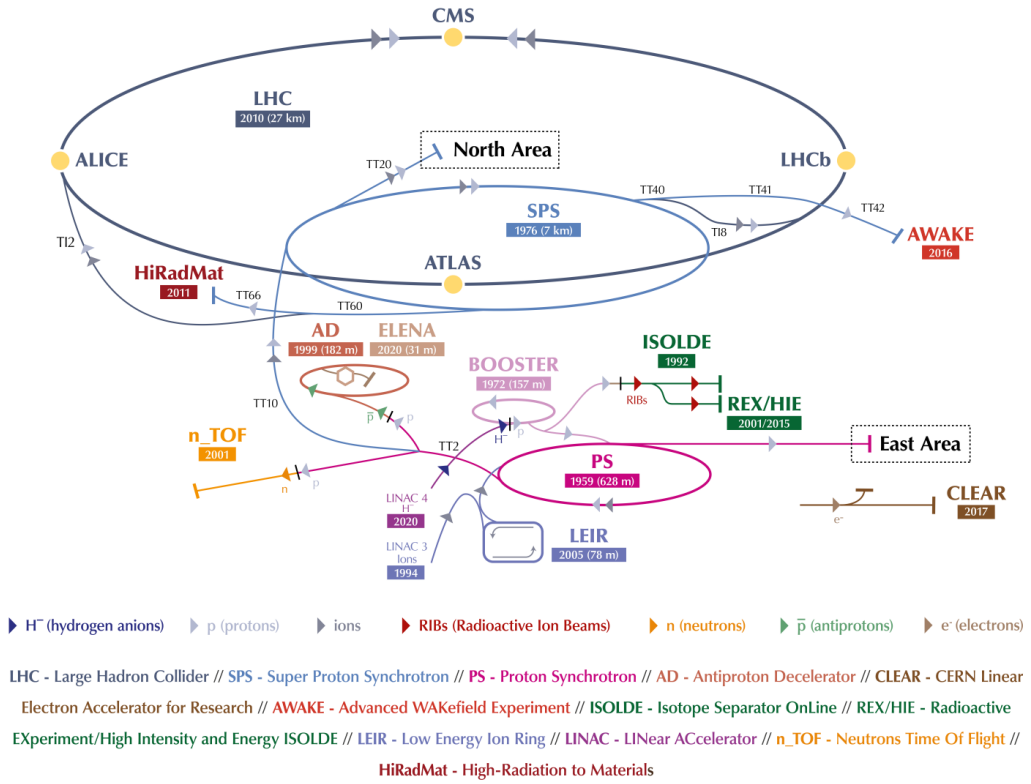

Figure 1.2. The CERN accelerator complex (2020).

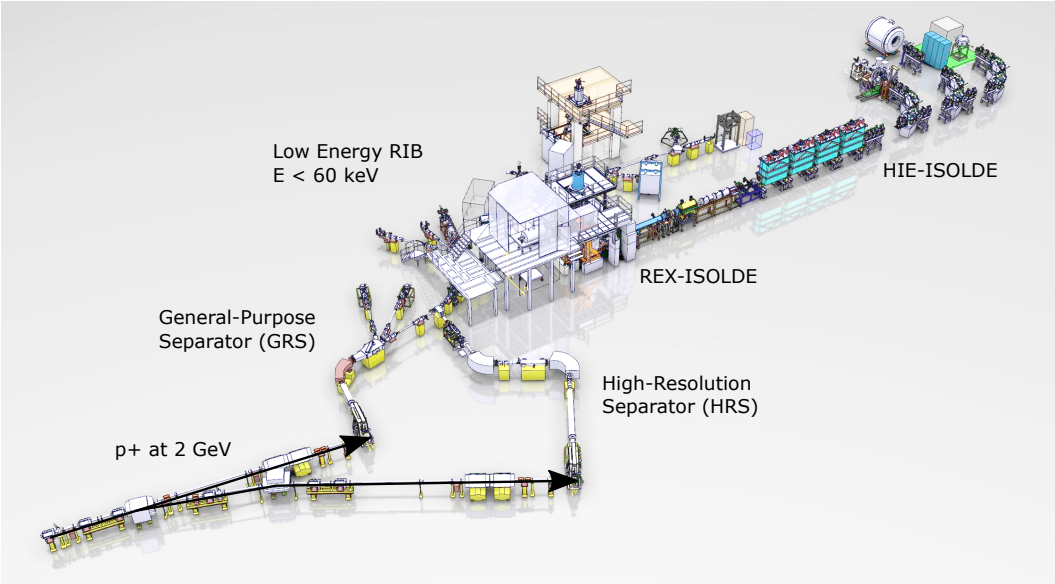

Figure 1.3

Target Yield and Ionization

High energy protons from the PSB initiate the nuclear reactions of which the products diffuse and effuse out of the heated target through a transfer line. This line is coupled to an ion source. The traditional ion sources used at ISOLDE were based on surface ionization and ionization in a plasma. In 1989, a technique of laser ionization was put into operation. The wavelengths of lasers are tuned to match the sequence of atomic transitions allowing highly efficient resonance excitation and ionization of selected atoms. The Resonance Ionization Laser Ion Source (RILIS) method is element selective, thus offers the possibility to obtain high purity beams.

Scientific Opportunities

The large variety of available isotopes allows the systematic investigation of atomic and nuclear properties of nuclei far from beta-stability. The implications concern astrophysics and weak-interaction physics. Solid-state physics and biomedical studies are also an essential part of the scientific programme. Many experiments at ISOLDE are at low energies, between 30 and 60 keV, for instance to measure ground state and decay properties of radionuclides. MINIBALL and ISS are two of the main high-energy experiments at ISOLDE.

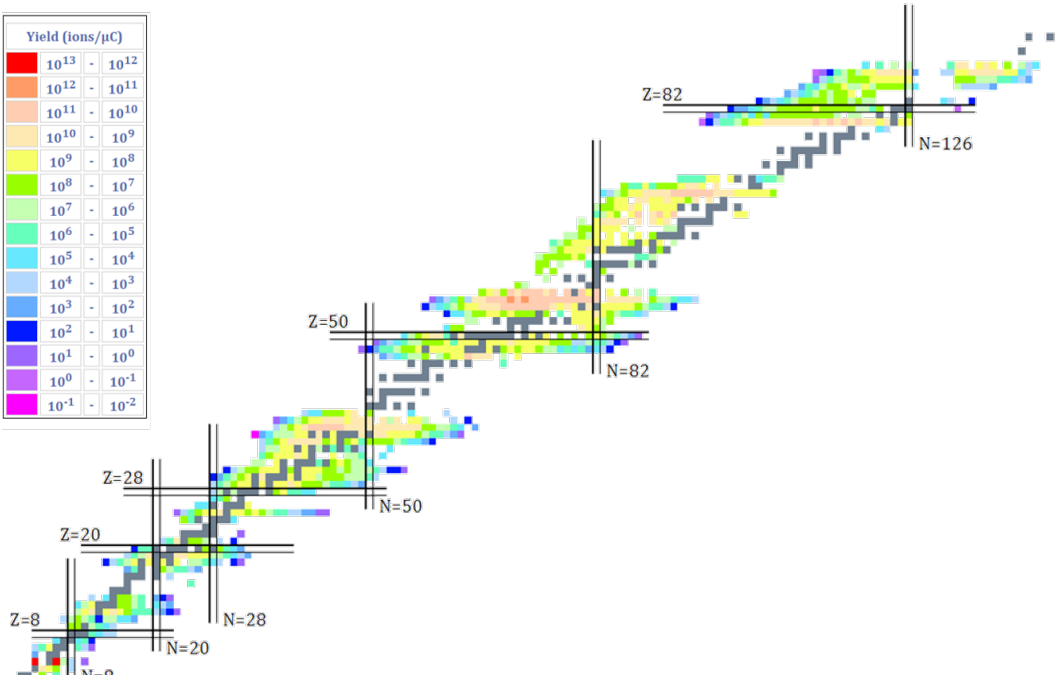

Figure 1.4. Chart of nuclides available at ISOLDE, covering more than 1200 isotopes and 73 elements (2018).

MINIBALL

MINIBALL is a high-resolution Miniball detector array that has been installed at ISOLDE for more than a decade. The germanium array consists of 24 six-fold segmented, tapered and encapsulated crystals. It is designed for low multiplicity experiments with low-intensity RIB. The Miniball array has been used in numerous Coulomb-excitation and transfer-reaction experiments with exotic RIBs produced at the ISOLDE facility.

In 2013, the MINIBALL experiment allowed to reveal that certain heavy and unstable atomic nuclei are *octupole deformed*, that is, distorted into a pear shape [Gaffney et al., 2013].

ISOLDE Solenoidal Spectrometer

The ISOLDE Solenoidal Spectrometer (ISS) concerns the studies of inelastic scattering and transfer reactions using. The solenoid was first cooled and energized in January 2017 at the ISOLDE facility. Using RIB the application notably concerns the nuclear astrophysics field. Light charged particles emitted during the nuclear

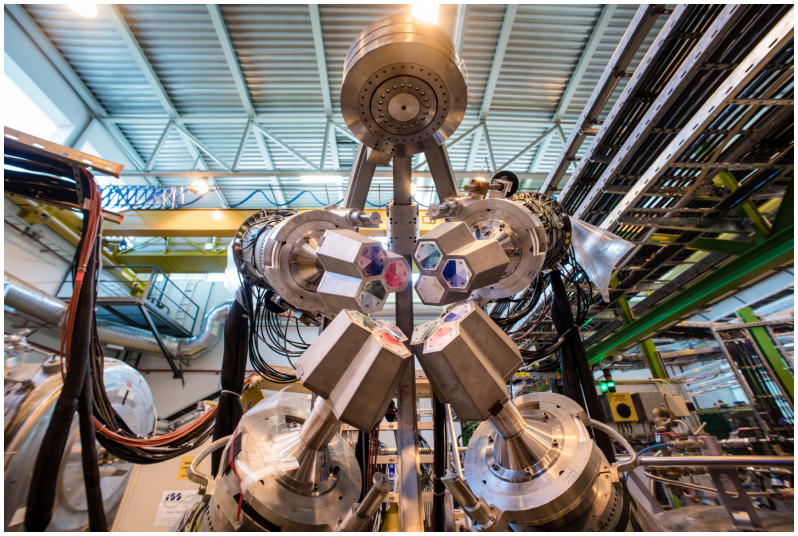

Figure 1.5. Picture of the MINIBALL Germanium array (Image: Julien Ordan (CERN)).

reactions are transported with high efficiency by the solenoidal magnetic field to an array of position-sensitive silicon detectors mounted on its axis. The energy released during the atomic reaction is then measured through the particle energies. The resolution of the atomic reaction energy is close from 20 keV.

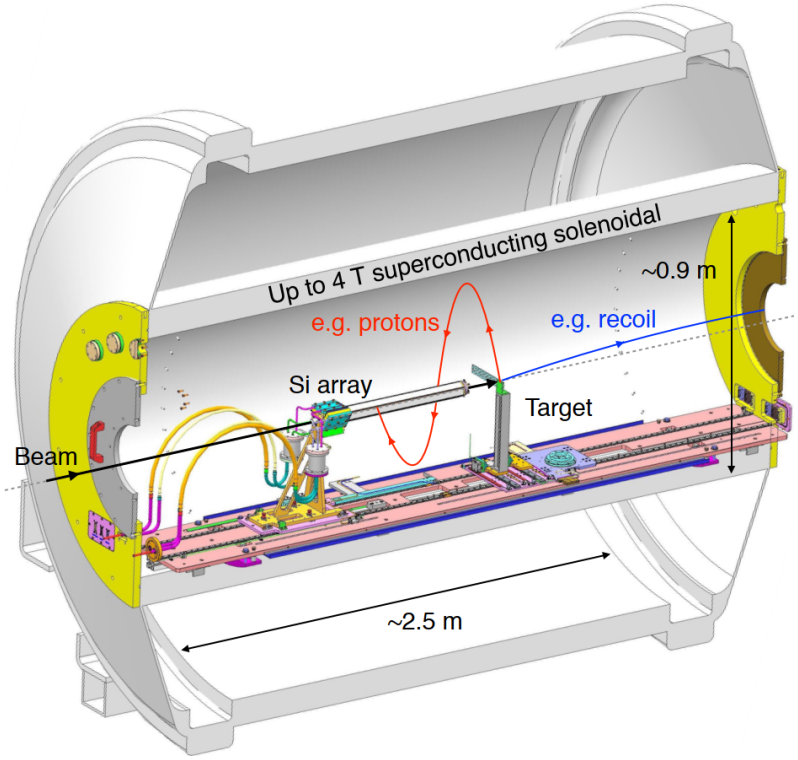

Figure 1.6. Schematic of the ISOLDE Solenoidal Spectrometer.

1.3 Beam Quality

A beam is an ensemble of particles travelling mainly in the same direction z. Transverse velocities are generally considered small compared to the longitudinal one, so $v_x, v_z \ll v_z$. The important characteristic of the particle beams, which define the contour of what is beam quality, are:

1. The beam intensity and pulse structure: Chapter 3.
2. The beam purity: Chapter 4.
3. The transverse emittance: Chapter 5.
4. The beam energy and longitudinal emittance: Chapter 6.

The very low intensity of exotic nuclei forces us to adapt the beam instrumentation techniques to current below the electrical femto Ampere (efA) range. The currents of multi-charged ion beams are expressed in *electrical Ampere*, as opposed to *particle Ampere*. The topics of beam purity and pulse structure allow increasing the detection capability of the probed mechanisms at the experimental stations by either removing a background of unwanted events or matching the detector's time resolving power. When increasing the beam intensity and lowering the divergence and spot size, the interaction zone is subject to more interactions of interest. The concept of beam brightness expresses this,

$$B = \frac{J}{\mathrm{d}\Omega} = \frac{dI}{dSd\Omega} \tag{1.1}$$

It is defined by the current density per solid angle $\mathrm{d}\Omega$ and can be written as a function of the transverse emittance $\varepsilon_x, \varepsilon_y$ to illustrate their role,

$$B = \frac{2I}{\pi^2 \epsilon_x \epsilon_y} \tag{1.2}$$

We present in the next chapters, methodologies for assessing the quality of post-accelerated very low-intensity ion beams and optimizing some of their properties.

CHAPTER 2

REX/HIE-ISOLDE Post-Accelerator

The installation of a post-accelerator at ISOLDE has opened up new fields of research with radioactive nuclei of higher energies. The REX (Radioactive Ion Beam EXperiment) section is the original ISOLDE post-accelerator. It has been operational since 2001 and has successfully provided more than 100 different post-accelerated isotopes for reaction studies and Coulomb excitation with energies up to 3.0 MeV/u. The HIE (High Energy and Intensity) project started in 2015 and allowed for the commissioning and operation of a new superconducting section of the linac [Kadi et al., 2017]. The new energies reached by the post-accelerator are over the Coulomb barrier threshold for the full range of nuclei available at ISOLDE.

Successfully delivering RIB to the experimental stations imply optimizing several aspects associated with the beam quality. The different sub-systems of the REX-HIE/ISOLDE post-accelerator are described in this chapter. Besides elaborating on the context, the objective is to introduce the theoretical elements required for the analysis of beam characterization results presented in the following chapters. The description made, reflects the operational conditions of the post-accelerator, which are flexible to the large variety of radionuclides produced at ISOLDE, from He to U.

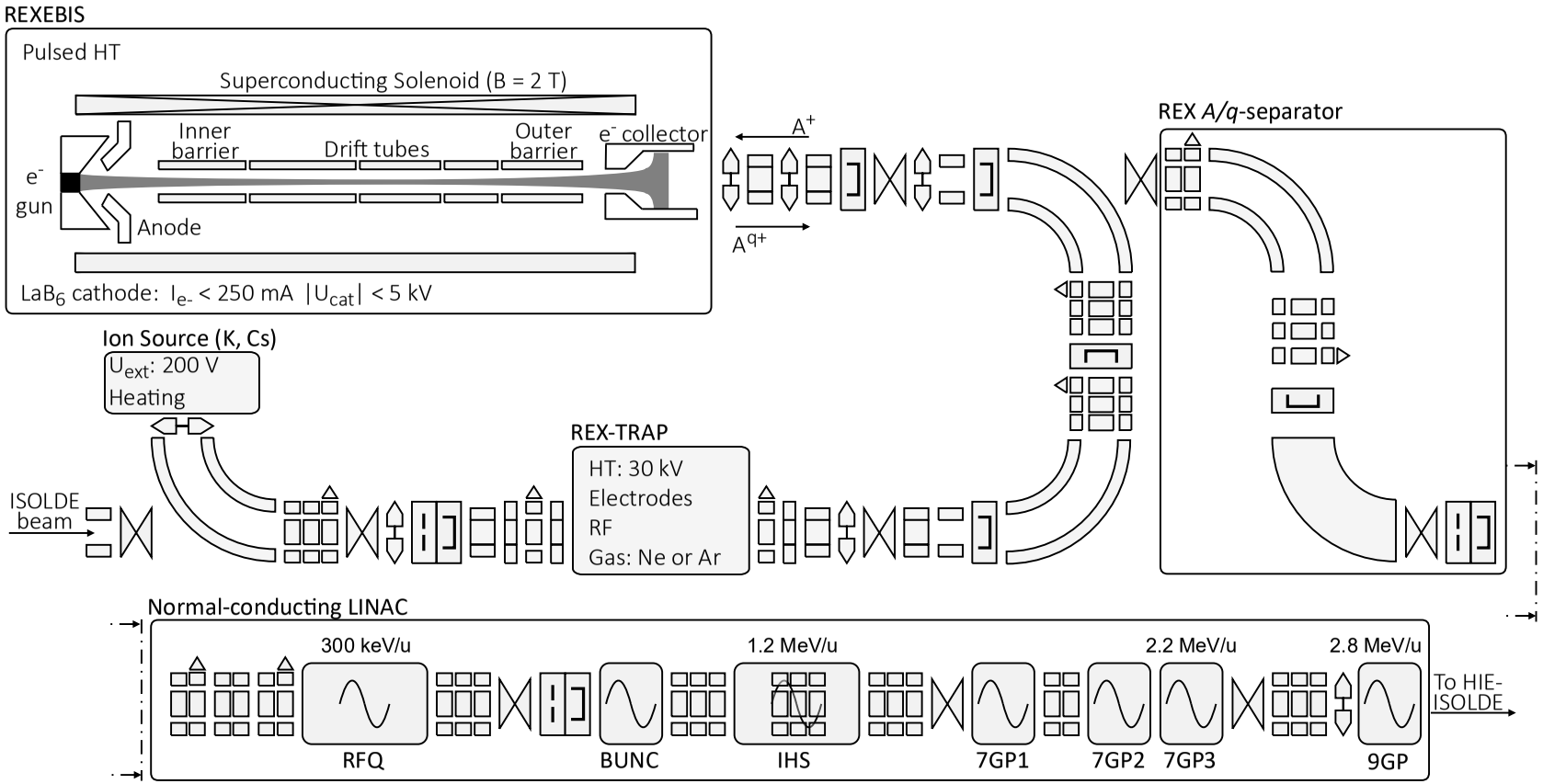

Figure 2.1. Schematic of REX low-energy section including the local ion source, REXTRAP, the beam tranfer line to REXEBIS, the A/q-Separator, and the normal-conducting linac. Details given for the REXEBIS electron gun refers to the setup prior to 2020.

2.1 REXTRAP Penning Trap

The ion beams coming from ISOLDE separators are first accumulated in the REXTRAP Penning trap. In this device, ions are cooled and bunched. The REXTRAP is filled with a buffer gas (typically Ne), and a transverse RF field can be applied for cooling ions. The charged ions are axially trapped by a strong axial magnetic field $\mathbf{B} = B_t\mathbf{e_z}$ (3 T), generated by a superconducting solenoid. They are radially trapped in a quadrupolar electrostatic potential (Figure 2.2). The ion beam extracted is pulsed to the repetition rate defined by the trapping cycle. The average hold time of ions inside the trap is half the trapping period, so the total hold time of isotopes inside the trapping machines (REXEBIS included) is 1.5 times the REXTRAP period.

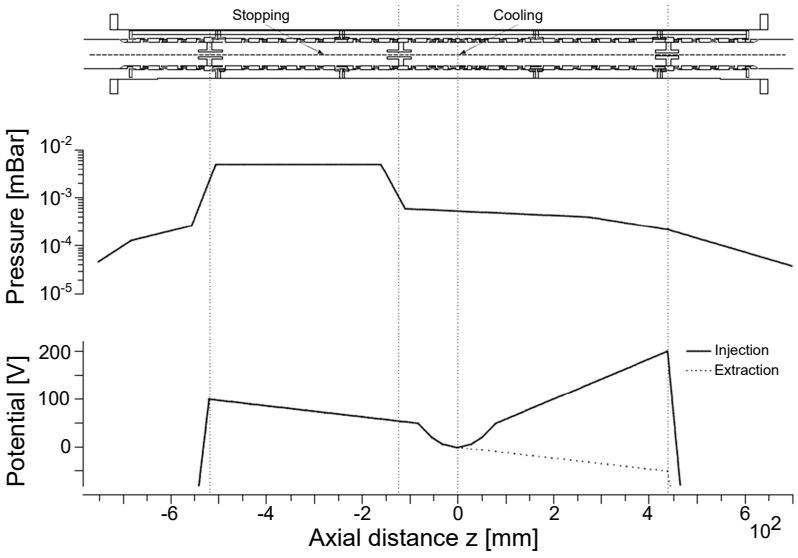

Figure 2.2. Electrode structure of REXTRAP, with a typical buffer gas pressures and the corresponding electrode potentials.

The RF cooling is mass-selective process, as expressed by the cyclotron angular frequency,

$$\omega_c = \frac{q_i e}{m_i} B_t \tag{2.1}$$

The charge state of injected ions is noted q_i and the mass m_i. In practice the effective optimal cooling frequency is also dependant on the accumulated charge

inside REXTRAP. Usually, the frequency is adjusted as a function of the trapping period which influences the space-charge in the trapping region. The Brillouin limit gives a boundary on the maximum density n_i that can be confined inside a Penning trap [Ames et al., 2001]:

$$n_i = \frac{\varepsilon_0 m_i \omega_c^2}{2q_i^2} = \frac{\varepsilon_0 B_t^2}{2m_i} \tag{2.2}$$

The rotating wall method is applied to the Penning trap such that the electric field phases are rotated to reverse the effect of a trap asymmetry. The possibility of operating REXTRAP in a mass-resolving mode is analyzed in [Gustafsson et al., 2011] using the Ion Mobility Time-of-Flight (IM-ToF) method.

2.2 REXEBIS Charge-Breeder

Before injection into the linac, the characteristics of the beam extracted from REXEBIS define the initial conditions in terms of intensity and velocities. Several experimental studies in this thesis directly relate to the REXEBIS charge-breeder, as the operational conditions of its different sub-systems are of such high impact on the beam quality. The charge-breeder must be capable of increasing the charge states of ions through successive electron impact ionization to meet the A/q-acceptance of the linac (between 2.5 and 4.5). Its working principle will be described in the following sections. The theoretical background leading to equations of charge dynamics and assumptions over the energy distributions will be explained. These introduced notions will be later applied to the experimental results of extracted beam characterization, presented in Chapters 3 and 4. The optimization of the charge-breeding performance includes minimizing the confinement time and increasing the charge-breeding efficiency. Additionally, the beam purity analysis is contingent on the residual gas contamination inside the EBIS.

2.2.1 Basic Concepts

The electron beam emitted from the cathode of the electron gun is at the heart of the working principle of an EBIS. In the schematic presented in Figure 2.1, the electron gun system is simplified, the Wehnelt cylinder, post-anode and electron suppressor are not presented. The space-charge created by the electron beam in the drift zone traps ions radially into a potential well. At the same time, the axial trapping is done by raising the potentials of the inner and outer barriers. The REXEBIS stands on a high-voltage platform allowing to extract the beam of interest at an energy of 5 keV/u. A complete description of the REXEBIS charge-breeder is given in [Wenander et al., 1999]. The performances of the charge-breeder are compared with Electron Cyclotron Resonance Ion Sources in [Delahaye, 2013] and [Vondrasek, 2016].

In Table 2.1, the REXEBIS platform voltages indicated are to be compared with the potential of the REXTRAP platform (30 kV) and the required injection energy

Table 2.1. Table of REXEBIS basic parameters associated to their corresponding variables.

REXEBIS Parameters		**Symbol**	**Value**
Geometrical	Drit tube inner radius	r_d	5.0 mm
	Drift zone length	l_d	8.0 dm
EBIS voltages	Electron gun potential	U_c	$<\mid -6.5 \mid$ kV
	Drift tube potential	U_d	0.7 kV
	Barrier potential	U_b	1.3 kV
Platform voltages	Potential during injection	U_{inj}	29.5 kV
	Potential during extraction	U_{ext}	$5 * A/q$ kV
Solenoid	Magnetic field at cathode	B_c	0.2 / 0.07 T
	Magnetic field at drift zone	B_d	2.0 T

into the REX-RFQ (5 keV/u). The determination of the precise energy of ions when injected or ejected from the REXEBIS will be assessed in the following subsections. Two values of B_c, the magnetic field at the cathode location are indicated, depending on the type of electron gun that was used.

2.2.2 Electron Beam

The electron gun in REXEBIS uses the thermal emission from a heated cathode and accelerate electrons by applying a potential gap between the cathode and the anode. The essential figures of merit for characterizing the electron beam produced are the current I_e, the current density j_e, the energy E_e, the beam radius and type of radial density distribution. The current I_e is directly measured at the collector, while several assumptions need to be made in order to estimate the current density. The information about the current density is crucial to predict the charge state evolution of ions, notably through the electron-impact ionization cross-section. The ionization is also dependent on the energy E_e which must be evaluated considering the space charge of the electron beam.

At REXEBIS, the cathode is immersed into a magnetic field (B_c) lower than the field in the drift zone (B_d) produced by a superconducting solenoid. Until 2019, a LaB_6 cathode capable of producing a current $I_e < 300$ mA was utilized. The magnetic field was slowly varying (adiabatically) along the REXEBIS axis, from the

cathode region to the inner barrier. The magnetic field is assumed constant in the drift zone. In order to increase the current density and the lifetime of the cathode, a new electron gun concept was installed and is currently operated. The Non-Adiabatic (NA) electron gun installed is composed of an IrCe cathode and conserves the main geometry of the REXEBIS. It has so far been able to produce a current $I_e < 420$ mA, before reaching electron emission limitation (inducing more current losses). An iron ring is inserted between the anode and the first drift tube, creating a sharp (non-adiabatic) modification of the magnetic field, aiming at reducing the transverse energy of electrons. By decreasing the gyromotion of electrons, the ripples of the electron beam are attenuated and it becomes in consequence more laminar, with an increased current density [Pikin et al., 2016].

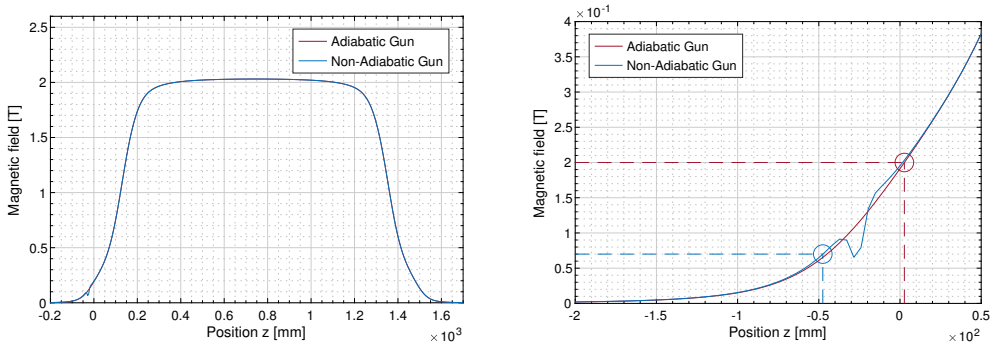

(a) Along the REXEBIS. **(b)** Close from the electron gun.

Figure 2.3. Simulation of the magnetic field along z-axis, from the cathode until the inner barrier. The vertical and horizontal dashed lines (b) show the locations of the cathode and the magnetic fields at the cathode for the two cases of electron gun.

Figure 2.3 displays the simulated magnetic field with and without the iron ring serving at reducing the gyromotion of electrons. The choice of the positioning of the iron made was made by simulating the extracted current density.

a Larmor Radius

The amplitude of the gyromotion is expressed through the Larmor radius, via the velocity $v_\perp$ perpendicular to the z-axis:

$$r_L = \frac{m_e v_\perp}{|e|B(z)} \tag{2.3}$$

The velocity $v_\perp$ is related to the thermal temperature in eV of electrons extracted from the cathode $T_e = T_c$, by $v_\perp = \sqrt{\frac{2k_B T_e}{me}}$. For a typical electron current I_e =200 mA, the LaB_6 cathode temperature is T_c = 1800 K and T_c = 1900 K for the IrCe cathode (NA gun). The Larmor radii for the two different electron guns are presented in Table 2.2. If the Larmor radius is small compared to the characteristic gradient length of density (electron beam radius), the effect of collisions can be treated by macroscopic equations of fluxes. When the Larmor radius is small compared to the average particle inter-distance, the transfer of energy from longitudinal to transverse becomes negligible [Danared, 1998].

Table 2.2. Typical Larmor radii at the cathode location for a 200 mA electron beam.

Electron guns	T_c [K]	B_c [T]	r_L [μm]
Adiabatic - Cathode LaB_6	1800	0.20	6.6
Non-Adiabatic - Cathode IrCe	1900	0.07	19.5

b Debye Length

In an electron plasma, the Debye length λ_D defines the region out of which external electric fields lose influence on the motion of the particles. It is often referred as the screening distance and logically depends on the electron density n_e according to the relation,

$$\lambda_D = \sqrt{\frac{\epsilon_0 k_B T_e}{n_e e^2}} \tag{2.4}$$

The number of electron inside a Debye sphere is simply,

$$\mathrm{N}_D = \frac{4\pi}{3} n_e \lambda_D^3 \tag{2.5}$$

If the number of particles in the Debye sphere is large $N_D >> 1$, one can use a quasi-fluid model to describe the plasma. This quasi-fluid hypothesis is also called the regime of collective behavior because a large number of particles are collectively responsible for the Debye sphere, leading to a variety of collective dynamical phenomena in the plasma. In particular, instabilities of wavelength shorter

than λ_D are Landau damped. In terms of thermodynamics, it signifies that the plasma species can be modelled with the state equation of a classical non-relativistic ideal gas. The density of electron n_e also allows to calculate the Wigner-Steiz radius a, which is an average inter-particle distance,

$$a = \left(\frac{3}{4\pi n_e}\right)^{1/3} \tag{2.6}$$

Another important characteristic distance of the electron plasma is the Landau length. This classical distance of closest approach represents the distance between two particles having an interaction energy of the same order as their kinetic energy:

$$r_0 = \frac{e^2}{4\pi\varepsilon_0 k T_e} \tag{2.7}$$

To apply the classical kinetic description of a plasma, the Landau distance must be very small compared to other scales, which means that the collisions are localized. Another criteria is that the plasma must be dilute, which translates into an average inter-particle distance small compared to the Debye length. In general, kinetic theory applies to classical plasmas that respect the inequations: $r_0 << a << \lambda_D$.

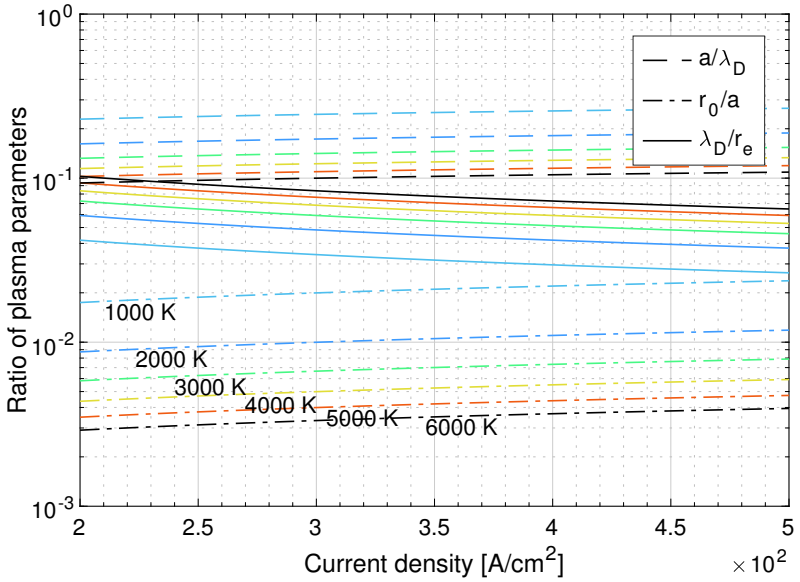

Figure 2.4. Ratios of the different characteristic lengths of the electron plasma. The plasma parameters are calculated using $E_e = 6$ keV, and an electron beam radius $r_e = 100$ μm, and are shown for different electron temperatures T_e ranging from 1000 K to 6000 K.

A comparison between the plasma parameters is shown in Figure 2.4, using relevant EBIS operational parameters such as the current density $j_e = en_e v_e$. It can be seen that the Debye length remains small compared to a low boundary of expected beam radius at REXEBIS ($r_e = 100$ μm). It signifies that the collective effects due to space charge may dominate the electron beam dynamics. An important remark is that the electron plasma has a strong shift in axial momentum, thus the temperature T_e, which relates to a squared mean of transverse velocities, is not easily accessible. One assumption is to use the cathode temperature T_c, the same way it was arbitrarily decided for the Larmor radius, and in such case the number of electrons in a Debye sphere is closer from 200. A large number of electrons inside the Debye sphere tends to indicate that the plasma reaches thermal equilibrium.

c Child-Lamgmuir law

Each of the two types of cathode presented in this section has a specific geometry optimized to counteract the space charge of the emitted electron beam. The electron guns are of Pierce-type. In order to evaluate the maximum current that can be extracted from a cathode, one may start by considering the simplified case of two parallel conducting plates separated by the distance d and powered by a voltage difference V. The electrons are considered initially at rest and are accelerated to non-relativistic speeds due to the Lorentz force. From these assumptions, the Child-Langmuir Law expresses the maximum current density limited by space charge:

$$j_e = \frac{4}{9}\varepsilon_0 \sqrt{\frac{2|e|}{m_e}} \frac{|V|^{3/2}}{d^2} \tag{2.8}$$

The constant ratio between j_e and $|V|^{3/2}$, explicitly shown in the Equation 2.8, can be directly measured or simulated for each specific electron gun. As the electron current I_e is often more accessible than the current density j_e, it is chosen to measure the perveance P:

$$P = I_e \cdot U_c^{-3/2} \tag{2.9}$$

The perveance is an indicator of the current yield from a specific electron

gun geometry. It was measured to be 0.87 μA.V$^{-3/2}$ for the adiabatic electron gun [Wenander et al., 1999]. For the non-adiabatic electron gun, simulations were performed and revealed a perveance close to 0.73 μA.V$^{-3/2}$. The resulting pervance curves are presented in the Figure 2.5.

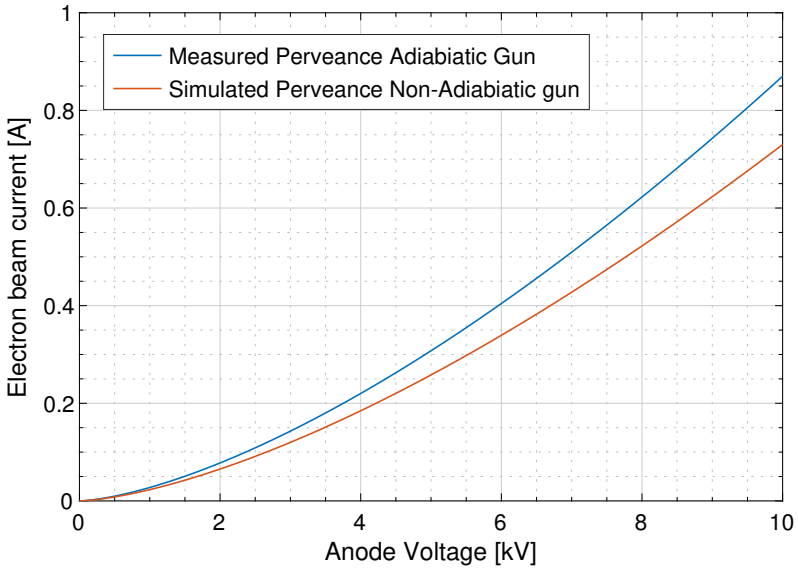

Figure 2.5. Typical perveance curves for the REXEBIS non-adiabatic and adiabatic electron guns.

d Herrmann radius

The characteristic transverse dimension of the electron beam can be estimated depending on what type of particle flow is assumed. With an ideal Brillouin flow, assuming a cathode surface temperature $T_e = 0$ eV and no magnetic field at the cathode, $B_c = 0$, the electron trajectories are parallel. The Brillouin radius depends on the electron axial velocity v_e, the magnetic field in the drift zone B_d and the electron beam current I_e:

$$r_B = \sqrt{\frac{2m_e I_e}{\pi e \varepsilon_0 v_e B_d^2}} \simeq \frac{147.6\,[\mu m]}{B_d[T]} \sqrt{\frac{I_e[A]}{\sqrt{E\,[keV]}}} \tag{2.10}$$

The axial velocity is $v_e = \sqrt{\frac{2eE_c}{m_e}}$, in the non-relativistic case. The Brillouin approach gives insights at the minimum radius of an electron beam emitted in the space charge limited regime and from a field free region into the magnetic field B_d.

When the electron gun is immersed, the beam radius becomes very sensitive to the magnetic field at the cathode surface. The theory developed by Herrmann assumes a non-laminar flow, so that the transverse motion of electrons due to the temperature T_c at emission is a taken into account [Herrmann, 1958]. The Herrmann radius starts from a cylindrical electron beam at the cathode, of dimension r_c (cathode radius).

$$r_H = r_B \sqrt{\frac{1}{2} + \frac{1}{2}\sqrt{1 + 4\left(\frac{8kT_c r_c^2 m_e}{e^2 r_B^4 B_d^2} + \frac{B_c^2 r_c^4}{B_d^2 r_B^4}\right)}} \tag{2.11}$$

In the derivation to obtain r_H, the electron axial velocity is supposed independent from the radial position, so it becomes possible to express the Herrmann radius as a function of the Brillouin radius. The Herrmann radius is often interpreted by the community as containing 80 % of the electron beam current I_e.

Table 2.3. Brillouin and Herrmann radii calculated for the two different types of electron gun, using $I_e = 200$ mA and $U_c = 6$ kV.

Electron guns	T_c [K]	B_c [T]	r_c [μm]	r_B [μm]	r_H [μm]
Adiabatic - Cathode LaB_6	1800	0.20	800	21	253
Non-Adiabatic - Cathode IrCe	1900	0.07	1000	21	188

e Transverse Density Distribution

The density of electrons is considered constant along the EBIS axis and with cylindrical symmetry, so that $n_e(r, \theta, z) = n_e(r)$. At the moment, there is no concrete experimental evidence that the electron beam produced at REXEBIS is either transversely uniform or with a Gaussian shape. These two hypotheses are the most likely considering the electron beam simulations but there is no evidence for promoting one on the other. The density n_e is either as uniform,

$$n_e(r) = \frac{I_e}{\pi e v_e r_e^2} \cdot \begin{cases} 1 & ,|r| \leq r_e \\ 0 & ,|r| > r_e \end{cases} \tag{2.12}$$

or a Gaussian distribution,

$$n_e(r) = n_e(0) \exp\left(-\frac{1}{2}\left(\frac{r}{r_e}\right)^2\right) \tag{2.13}$$

The uniform density distribution (Equation 2.12) is directly normalized meanwhile the Gaussian distribution (Equation 2.13) needs the introduction of a normalization factor $n_e(0)$. It can be calculated by integrating n_e on a closed radial surface and comparing with the expected measured linear charge I_e/v_e. Meanwhile the specific electron beam radius r_e of each distribution can be determined as a function of the Herrmann radius, when assuming that it includes 80 % of I_e,

$$\frac{I_e}{v_e} = 2\pi e \int_0^{r_d} n_e(r) r \mathrm{d}r = \frac{2\pi e}{0.8} \int_0^{r_H} n_e(r) r \mathrm{d}r \tag{2.14}$$

f Space charge potential

The potential $\phi(r)$ created by the electron beam space charge may be accessed through Poisson equation of electrostatics. By applying Gauss Law, the net electric field flux in cylindrical coordinates is:

$$\nabla \cdot \mathbf{E} = \frac{\partial}{\partial r}\left(r \frac{\partial \phi(r)}{\partial r}\right) = \frac{e n_e(r)}{\varepsilon_0} \tag{2.15}$$

This non-linear differential equation can be solved analytically for the two cases of density distributions referred before. The mixed boundary conditions are:

$$\left.\frac{\partial \phi}{\partial r}\right|_{r=0} = 0 \quad ; \quad \phi\left(r_t\right) = U_t \tag{2.16}$$

.

It is useful to introduce the potential:

$$\phi_0 = \frac{I_e}{4\pi\varepsilon_0 v_e} \tag{2.17}$$

In the case of a uniform electron beam, solving the Poisson equation gives a potential ϕ of the form,

$$\phi(r) = U_t - \phi_0 \cdot \begin{cases} \left(2\ln\frac{r_t}{r_e} - \frac{r^2}{r_e^2} + 1\right) & , |r| \leq r_e \\ 2\ln\frac{r_t}{|r|} & , |r| > r_e \end{cases} \tag{2.18}$$

The potential difference between the center of the electron beam and its edge is directly equal to the previously introduced potential $\phi_0 = \phi(r_e) - \phi(0)$. It is a key parameter for estimating the radial trapping of an ion inside the electron beam. A typical trapping potential is presented in Figure 2.6, under usual REXEBIS operation, which lead to $\phi_0 = 38.3$ V.

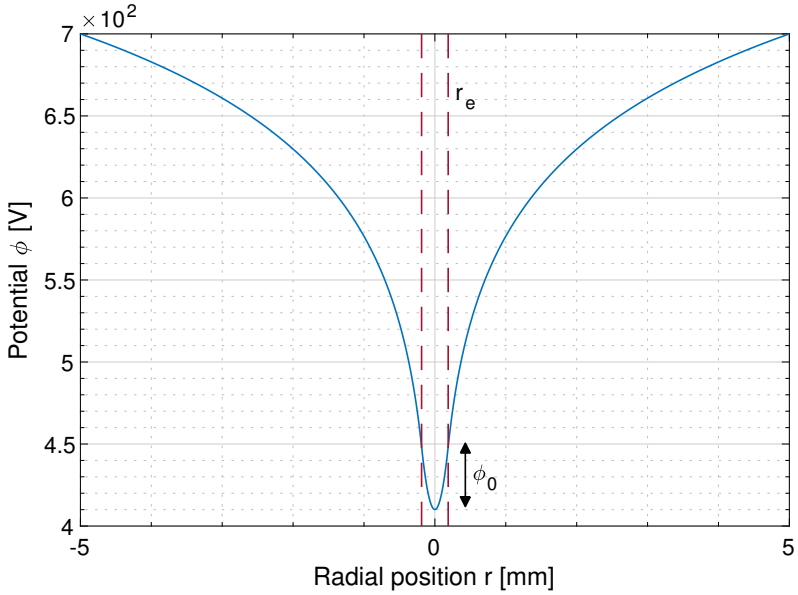

Figure 2.6. Radial representation of the potential, calculated using an electron beam with $I_e = 200$ mA and $U_c = 6$ kV.

So far, the axial velocity v_e has not been expressed as a function of the electron beam extraction potentials, but only via the potential energy E_e. As the potential inside the electron beam is now known, the energy of an electron on axis can be expressed in the form $E_e(r) = e(U_d + |U_c| - \phi(r))$.

2.2.3 Analytical Description of the EBIS Plasma

A plasma is a gas of ionized particles which shows collective behavior. An EBIS plasma gathers a variety of physical situations depending in particular, on the absolute density of electrons and on the relative density of electrons compared to ions. The temperatures of ions can also vary considerably during the charge breeding.

In the EBIS plasma studied, the particles are assumed non-relativistic.

In order to obtain a complete description of an EBIS plasma, many processes need to be treated. However, one may simplify the analytic description and proceed to a hierarchy of important processes, leading notably to neglect Maxwell interactions between ions and neutral particles and Van der Waals forces between neutral particles. Generally, the focus will be given on deriving the radial density and ion energy distributions. The main type of elastic collisions considered is the Coulomb interactions between charged particles.

a Kinetic Theory

The kinetic theory allows to model the plasma by a distribution function in the phase space. The density distribution is noted arbitrarily f_i, but applies to a definite species of ions, at a specific charge state. An infinitesimal phase space element is defined by $\mathrm{d}\mathbf{r}\mathrm{d}\mathbf{v}$, with $\mathbf{r}$ the position coordinate and $\mathbf{v}$ the velocity vector. The number of ions dN_i inside the infinitesimal element is then $dN_i = f_i(\mathbf{r}, \mathbf{v}, t)\mathrm{d}\mathbf{r}\mathrm{d}\mathbf{v}$. With this approach the individual behavior of ions is lost, to the benefit of the global evolution of function distributions in the phase space. Several important averages can be calculated via the moments of slices of distributions.

$$\begin{aligned}
\mathbf{V_i} &= \langle \mathbf{v} \rangle \equiv \int \mathbf{v} f_i(\mathbf{v}) \mathrm{d}\mathbf{v} \\
T_i &= \frac{m_i}{k_B} \left\langle (\mathbf{v} - \mathbf{V})^2 \right\rangle \equiv \frac{m_i}{k_B} \int (\mathbf{v} - \mathbf{V})^2 f_i(\mathbf{v}) \mathrm{d}\mathbf{v} \\
E_k &= \left\langle \frac{1}{2} m_i \mathbf{v}^2 \right\rangle \equiv \int \frac{1}{2} m_i \mathbf{v}^2 f_i(\mathbf{v}) \mathrm{d}\mathbf{v} \\
E_\phi &= \langle e q_i \phi(\mathbf{r}) \rangle \equiv \int e q_i \phi(\mathbf{r}) f_i(\mathbf{r}) \mathrm{d}\mathbf{r}
\end{aligned} \tag{2.19}$$

The average velocity $\mathbf{V_i}$ (different from the thermal velocity) may be high at the beginning of the trapping phase, due to the initial axial velocity of injected ions. However, the purpose of the next sections is to assess the characteristics of the EBIS plasma and notably its relaxation time through collisions. It will be shown that under usual REXEBIS operation, ions reach a thermal equilibrium within a time range shorter than the trapping time. Then $\mathbf{V_i} = 0$ and only in such case,

one is able to present the plasma with a unique temperature T_i, kinetic energy E_k and potential energy E_ϕ. This hypothesis implies that when ions are driven to a small change of temperature ∂T_i through for instance Coulomb Heating, this heat supply is converted with equipartition into potential energy and kinetic energy in each direction, by the value $k_B \partial T_i/2$. To a first order, one will assume that ions inside an EBIS have a fixed number of degrees of freedom n_f, which leads to express the total average energy of ions by,

$$\partial E_i = \frac{n_f}{2} k_B \partial T_i \tag{2.20}$$

If one only considers the degrees of freedom associated with kinetic energy ($n_f = 3$), the total average kinetic energy of ions is $\partial E_i = 3k_B \partial T_i/2$. However, because of the quadratic shape of the potential ϕ (from Equation 2.18) inside the electron beam, cold ions ions will behave like an harmonic oscillator, thus storing both kinetic and the potential energies. So, the potential energy accounts for $\partial E_\phi = k_B \partial T_i$ and the total average energy of ions becomes $\partial E_i = 5k_B \partial T_i/2$. While on the axial direction, considering that the collisions with the potential walls are brief, the only way to store energy is in kinetic energy. Due to the square shape of the longitudinal electrostatic trap, the effect of heat transfer into potential energy is for the moment neglected. We have so far considered the case of cold ions trapped deep inside the quadratic potential well created by the electron beam ($n_f = 5$). Nevertheless, hotter ions may find themselves residing at a potential $\phi(r > r_e)$ which is not quadratic outside from the electron beam (from Equation 2.18). It will be shown that in this second case, the ion system becomes unable to store heat in the form of potential energy, and progressively tend to reach only three kinetic degrees of freedom ($n_f = 3$) with increasing temperature.

The concept of degrees of freedom displays the nature of the redistribution of thermal energy, through kinetic or potential energies, however the heat capacity C_v will better help at apprehending the situation from thermodynamics perspective. The heat capacity of an ion species (at a specific charge state), is the amount of heat that can be added to ions to raise their temperature by ∂T_i, so in dimensionless

units,

$$\partial C_V = \frac{\partial E_i}{k_B \partial T_i} = \frac{3}{2} + \frac{q_i}{k_B} \int \frac{\partial \phi(\mathbf{r}) f_i(\mathbf{r})}{\partial T_i} \mathrm{d}\mathbf{r} \tag{2.21}$$

This heat capacity of an ion species at specific charge state, needs to be understood as very specific to the EBIS system where the ions are confined due to the space charge of electrons. By knowing the ion distribution f_i inside the EBIS, one can calculate the average potential seen by ions and the corresponding heat capacity which indicates as a function of temperature, the effectiveness of the radial trapping.

b Boltzmann Equation

The evolution of the density function distribution f_i is described by Boltzmann equation, and it needs to reflect the conditions of trapping inside an EBIS. The first basic model of the Boltzmann equation presented is the Poisson-Vlasov equation:

$$\frac{\partial f_i}{\partial t} + \mathbf{v} \cdot \boldsymbol{\nabla}_r f_i + \frac{Q_i}{m_i} (\boldsymbol{E}) \cdot \boldsymbol{\nabla}_v f_i = 0 \tag{2.22}$$

The Vlassov-Poisson correctly describes a classical collisionless plasma in an electric field $\boldsymbol{E}$ for ions of charge $Q_i = q_i * e$, using q_i for denoting the charge state. The inclusion of a magnetic field leads to the Maxwell-Vlasov equation. Besides, when collisions are dominant in the plasma it becomes necessary to introduce a collision operator in the right-hand side of Equation 2.22. In the case where collisions are localized, the Landau distance is small compared to the Debye length, and the Boltzmann operator for Coulomb interactions is naturally modified for using the potential at a Debye length.

The Boltzmann equation has several useful variants depending on the various assumptions, notably about the collision kernel. A summary of the different taxonomy is listed [Villani, 2002]:

- The **Poisson–Vlasov** equation concerns collisionless plasmas in electrostatic trap.
- The **Maxwell–Vlasov** equation concerns collisionless plasmas in electromagnetic fields.

- The **Fokker-Planck** equation includes the Fokker-Planck collision operator but does not include Lorentz forces. The Fokker-Planck equation is reviewed in detail in [Chandrasekhar, 1943]. This system admits a unique Maxwellian steady state distribution.

$$\frac{\partial f_i}{\partial t} + \mathbf{v} \cdot \boldsymbol{\nabla}_r f_i = \boldsymbol{\nabla}_v \cdot (\boldsymbol{\nabla}_v f_i + f_i \mathbf{v}) \tag{2.23}$$

- The **Vlasov-Fokker-Planck** equation describes collisions through the Fokker-Planck Brownian collision operator and includes the forces due to the confinement and the self-consistent interactions. This system admits a unique Maxwellian steady state distribution.

- The **Vlasov-Poisson-Fokker-Planck** equation is a particular case of the Vlasov-Fokker-Planck equation and occurs when the interactions are of Coulomb type. This system admits a unique Maxwellian steady state distribution.

Solving the collision operator has already been analytically done and collision frequencies are detailed in the following section. Without specifying the collision kernel $\left(\frac{\partial f_i}{\partial t}\right)_{\text{coll}}$, the Boltzmann equation for a species in an EBIS/T to:

$$\frac{\partial f_i}{\partial t} + \mathbf{v} \cdot \boldsymbol{\nabla}_r f_i + \frac{Q_i}{m_i}(\boldsymbol{E} + \mathbf{v} \times \boldsymbol{B}) \cdot \boldsymbol{\nabla}_v f_i = \left(\frac{\partial f_i}{\partial t}\right)_{\text{coll}} \tag{2.24}$$

2.2.4 Collision Frequencies

The collision operator is usually calculated using *test* particles travelling through a background of Maxwellian *field* particles. The derivation leads to evaluating the integral over the inverse of the impact parameter b, which is called the Coulomb Logarithm $\ln \Lambda$.

$$\ln \Lambda \equiv \ln \left(\frac{b_{\max}}{b_{\min}}\right) \tag{2.25}$$

The Coulomb logarithm defines the cut-off of the collision kernel. The smallest impact parameter $b_{\min}$ is, in the case of an EBIS, the classical distance of closest approach (Landau distance). The maximum distance $b_{\max}$ is the minimum distance

of the Debye length and the diameter of the particle beam. The Coulomb Logarithm for two ion species i and j of atomic masses A_i and A_j, densities n_i and n_j and temperatures T_i and T_j is [Huba, 2004],

$$\ln \Lambda_{ij} = \lambda_{ji} = 23 - \ln \left[\frac{q_i q_j \left(A_i + A_j\right)}{A_i T_j + A_j T_i} \left(\frac{n_i q_i^2}{T_i} + \frac{n_j q_j^2}{T_j} \right)^{1/2} \right] \tag{2.26}$$

In the case of electron-ion interactions, the Coulomb Logarithm depends on the regime of temperatures between $T_i m_e/m_i$, T_e and $10 \cdot q_i^2$ eV.

$$\ln \Lambda_{ei} = \ln \Lambda_{ie} = \begin{cases} 23 - \ln \left(n_e^{1/2} q_i T_e^{-3/2} \right) & , T_i m_e/m_i < T_e < 10 \cdot q_i^2 \text{eV} \\ 24 - \ln \left(n_e^{1/2} T_e^{-1} \right) & , T_i m_e/m_i < 10 \cdot q_i^2 \text{eV} < T_e \\ 16 - \ln \left(n_i^{1/2} T_i^{-3/2} q_i^2 A_i \right) & , T_e < T_i m_e/m_i \end{cases} \tag{2.27}$$

Finally, for collisions between electrons, the Coulomb Logarithm results in,

$$\ln \Lambda_{ee} = 23.5 - \ln \left(n_e^{1/2} T_e^{-5/4} \right) - \left[10^{-5} + \left(\ln T_e - 2 \right)^2 / 16 \right]^{1/2} \tag{2.28}$$

Collision frequencies between the different species of the plasma can be calculated using the Boltzmann operator. Those frequencies help identifying the collisional regime of the plasma and are paramount for investigating the rates of energy exchange. The collision frequency between the ion species i and j is,

$$\nu_{ij} = \frac{1}{(4\pi\epsilon_0)^2} \frac{4\sqrt{2\pi}}{3} n_j \left(\frac{q_i q_j e^2}{m_i} \right)^2 \left(\frac{m_i}{k_B T_i} \right)^{3/2} \ln \Lambda_{ij} \tag{2.29}$$

Each ion species is characterized by their mass (m_i and m_j), their temperature ($k_b T_i$ and $k_B T_j$) and their charge states (q_i and q_j). The reciprocal collision rate is related by $\nu_{ij} = \nu_{ji} n_j m_j / (n_i m_i)$. The self-collision rate is then,

$$\nu_{ii} = \frac{1}{(4\pi\epsilon_0)^2} \frac{4\sqrt{2\pi}}{3} n_i \left(\frac{q_i^2 e^2}{m_i} \right)^2 \left(\frac{m_i}{k_B T_i} \right)^{3/2} \ln \Lambda_{ii} \tag{2.30}$$

This collision rate will be utilized in the following section and measures the approach to temperature isotropy. Similarly, the self-collision frequency between

electrons (ν_{ee}) can be derived. This quantity is to be compared to the relatively short transit time of electrons through the EBIS, in the order of magnitude of 20 ns for REXEBIS electron gun. Between electrons and ions the collision frequency is simplified, assuming $m_i >> m_e$,

$$\nu_{ei} = \frac{n_i}{4\pi v_e^3} \left(\frac{q_i e^2}{\epsilon_0 m_e} \right)^2 \ln \Lambda_{ei} \tag{2.31}$$

Those collision frequencies will be used to quantify the energy balance of ion species inside the EBIS. The sum of all collision frequencies $\nu_i = \nu_{ie} + \sum_j \nu_{ij}$ an ion species is subject to, is an indicator of the tendancy to reach thermal equilibrium, which leads to the use of Maxwell-Boltzmann distributions, whereas the self-collision frequency may be used for estimating the isotropization rate.

2.2.5 Temperature Anisotropies

The assumption of isotropy of ionic temperatures is linked to the adiabatic behavior of the system. In the context of EBIS and if a specific ion species in the plasma is considered highly collisional, it is then assumed isotropy, in a sense that there is one temperature T_i defining the system. However, when the collision frequency is low, for instance due to low density, and the influence of the magnetic field becomes preponderant, the system cannot be assumed isotropic. We will examine how the relaxation to isotropy is related to the self-collision rate introduced in the previous section. It will eventually lead us to analyse the case of an ion beam of interest used during this thesis.

In a similar manner to the analytical description of the electron plasma parameters, relevant quantities need to be estimated concerning the ion species of interest in order to assume anisotropy. The ion system is said collisional when its mean free path is smaller than the characteristic spatial scale, i.e. $\zeta \ll 1$ using

$$\zeta = \frac{\lambda_{\mathrm{mfp}}}{l_d} \tag{2.32}$$

The mean free path of ions may be estimated by the division of the thermal velocity $v_{T,i}$ by the self-collision rate of Equation 2.30 [Braginskii, 1965],

$$\lambda_{\mathrm{mfp}}[\mathrm{cm}] = \frac{v_{T,i}}{\nu_{ii}} = 3 \cdot 10^{13} \frac{(T_i[\mathrm{eV}])^2}{q_i^4 n_i \,[\mathrm{cm}^{-3}] \ln \Lambda_{ii}} \tag{2.33}$$

For experiments using magnetic confinement, the ratio of the plasma pressure ($n_i k_B T_i$) to the magnetic pressure ($B_d^2/(2\mu_0)$) determines the effect of magnetization. Nevertheless in the EBIS context, one want to assess if the plasma is magnetized with respect to the collisions. This is done by comparing the time taken for an ion to orbit in the magnetic field B_d and the average time between collisions. Then, if the ratio $1 \ll 2\pi m_i \nu_{ii}/(q_i B_d)$ the ionic plasma is dominated by collisions and can be assumed isotropic. In the opposite case, the anisotropies between the longitudinal and transverse temperatures of ions will relax within a time frame close from the inverse of their self-collision frequencies. This can be demonstrated using the expressions of the double adiabatic theory. With a fluid description of the collision-less ion plasma, the pressure tensor $\boldsymbol{P}_i$ may be decoupled between parallel to field and perpendicular to field contributions while remaining diagonal,

$$\boldsymbol{P}_i = \begin{pmatrix} p_\perp & 0 & 0 \\ 0 & p_\perp & 0 \\ 0 & 0 & p_\parallel \end{pmatrix} \tag{2.34}$$

with,

$$\begin{aligned} p_\perp &= n_i m_i \left\langle v_\perp^2 \right\rangle \\ p_\parallel &= n_i m_i \left\langle v_\parallel^2 \right\rangle \end{aligned} \tag{2.35}$$

This pressure tensor is a deviation from the isotropic case in which the tensor is simply an identity matrix of the form $p\delta_{ij}$ (with δ the Kronecker symbol). Equivalently, one defines the pressure p such that,

$$p \equiv \frac{1}{3} \operatorname{tr} \boldsymbol{P}_i = \frac{2}{3} p_\perp + \frac{1}{3} p_\parallel \tag{2.36}$$

Using the adiabatic invariants (from Noether's theorem of conservation), a relation can be derived connecting the time derivative of the pressure tensor with the variations of density and magnetic field, and the isotropization due to collisions.

One then obtains [Chew et al., 1956],

$$\begin{aligned}\frac{\mathrm{d}p_\perp}{\mathrm{d}t} &= p_\perp \frac{\mathrm{d}}{\mathrm{d}t}\ln(n_i B_d) - \nu_{ii}(p_\perp - p) \\ \frac{\mathrm{d}p_\parallel}{\mathrm{d}t} &= p_\parallel \frac{\mathrm{d}}{\mathrm{d}t}\ln(\frac{n_i^3}{B_d^2}) - \nu_{ii}(p_\parallel - p)\end{aligned} \tag{2.37}$$

Which leads to the isotropization rate,

$$\frac{\mathrm{d}}{\mathrm{d}t}(p_\perp - p_\parallel) = p_\perp \frac{\mathrm{d}}{\mathrm{d}t}\ln(n_i B_d) - p_\parallel \frac{\mathrm{d}}{\mathrm{d}t}\ln(\frac{n_i^3}{B_d^2}) - \nu_{ii}(p_\perp - p_\parallel) \tag{2.38}$$

It may be simplified if one assumes that $\left|p_\perp - p_\parallel\right| \ll p$

$$\frac{\mathrm{d}}{\mathrm{d}t}(p_\perp - p_\parallel) \simeq 3p\frac{\mathrm{d}}{\mathrm{d}t}\ln(\frac{B_d}{n_i^{2/3}}) - \nu_{ii}(p_\perp - p_\parallel) \tag{2.39}$$

Using the previous simplification, the difference between the transverse and longitudinal pressures can directly be estimated. One can also rewrite the equation by using the corresponding parallel and perpendicular temperatures compared to the equivalent isotropic temperature T_i,

$$T_\perp - T_\parallel \simeq \frac{3T_i}{\nu_{ii}}\frac{\mathrm{d}}{\mathrm{d}t}\ln(\frac{B_d}{n_i^{2/3}}) \tag{2.40}$$

The temperature anisotropy in a weakly collisional and magnetized plasma stems from adiabatic invariants and collisional relaxation. The collisional isotropization of the pressure increases the hydrodynamic entropy by,

$$\frac{3}{2}p\frac{\mathrm{d}}{\mathrm{d}t}\ln\frac{p}{n_i^{5/3}} = \frac{3p}{\nu_{ii}}\left(\frac{\mathrm{d}}{\mathrm{d}t}\ln(\frac{B_d}{n_i^{2/3}})\right)^2 \geqslant 0 \tag{2.41}$$

As expected, the influence of collisions on the creation of entropy is always positive. In classical statistical mechanics, the $\mathcal{H}$-theorem predicts the tendency towards a relaxation of the anisotropy by collisions or instabilities. The trend is an exponential, or more precisely polynomial, quantifiable decay [Villani, 2002]. We assume that after the passing of few self-collission characteristic times, we are allowed to consider the ion plasma as isotropic.

Isotroprization occurs during the full trapping period, as the successive charge states are populated by the ion species. It was chosen to examine the case of Xe^{q_i+}, and to estimate the isotropization time depending on typical operational parameters during charge-breeding. As will be explained in the following chapters that are dedicated to the presentation of the actual Xe measurements, the gas can directly be injected into the REXEBIS as neutral particles. Let's assume for the sake of simplicity that the electron beam has a uniform distribution of radius $r_H = 250$ μm (value taken from Table 2.3). The volume occupied by the singly-ionized Xe^+ ions will to the first order be the same as the electron beam volume. This volume is about 160 mm^3 for the REXEBIS Adiabatic gun introduced in the previous section. By setting a value for the number of Xe ions one wish to consider, one can proceed by calculating the corresponding density and later the self-relaxation rate. For different reasons, which notably include keeping the compensation of the electron beam very low, a typical intensity of Xe^{30+} obtained during beam characterization measurements was 50 epA. This was obtained with a charge-breeding cycle of 100 ms, which translates into a an equivalent beam of 10^6 elementary charges. With those assumptions and very approximate derivations, the corresponding density of Xe^{q_i+} would be in the order of $n_i = 10^4$ mm^{-3}.

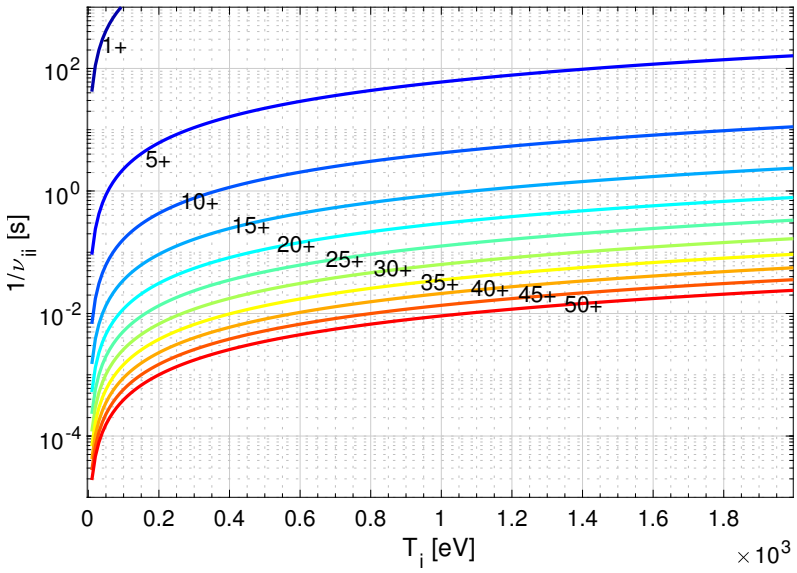

Figure 2.7. Analytical calculation of the self-relaxation time for Xe^{q_i+} ions at a constant density $n_i = 10^4$ mm^{-3}.

In the Figure 2.7 the density of ions at a specific charge state is kept constant, which does not reflect the real evolution during charge breeding but simplifies the representation. The temperatures measured in Chapter 3 for the charge breeding of Xe^{30+} are below 400 eV for usual REXEBIS operation. In this scenario, the relaxation time would be shorter than 10 ms which is lower than the required optimal breeding time, in the order of 90 ms. The inference of self-collisions leading to isotropization in a shorter time-scale than the required breeding time will be used during the following studies.

2.2.6 Boltzmann Distribution

The equilibrium spatial density distribution of ions is given by the Boltzmann distribution. A demonstration of this statement implies an analysis of the equation of classical fluxes, as long as the Larmor radii of ions stay small compared to their inter-particle distance [Currell, 2003]. It is argued that the sum of fluxes across the magnetic field cancels out and that an equilibrium is reached leading to a Boltzmann spatial density distribution of the form,

$$n_i(r, t = \infty) = n_i(0) \exp\left(-\frac{Q_i \phi(r)}{k_B T_i}\right) \tag{2.42}$$

The potential $\phi(r)$ in this equation is as seen by ions in the trap, in the sense that it will always be $\phi(r) = \phi(r) - \min \phi(r)$ depending on how ϕ was calculated (boundary conditions). In order to obtain the self-consistent solution of the potential ϕ, that was previously derived using only the space charge of the electron beam, now the Poisson equations needs to include the contribution of positive charges. The expression of the density n_i is written for one species, arbitrarily noted with the index i, at a specific charge state q_i. The ion ensemble inside and EBIS is in fact composed of a mixture of different ion species, each of them with a broad charge state distribution. If we sum over all charge states and species, the Poisson equation in an EBIS now writes,

$$\nabla \cdot \mathbf{E} = \frac{\partial}{\partial r}\left(r \frac{\partial \phi(r)}{\partial r}\right) = \frac{e}{\varepsilon_0}(n_e(r) - \sum_i \sum_q q_i n_{i,q}(r)) \tag{2.43}$$

This non-linear differential equation can be solved using a one-dimensional leapfrog symplectic solver. The electron density n_e can be assumed Gaussian (Equation 2.13) or uniform (Equation 2.12). The mixed boundary conditions are still the same as in Equation 2.16.

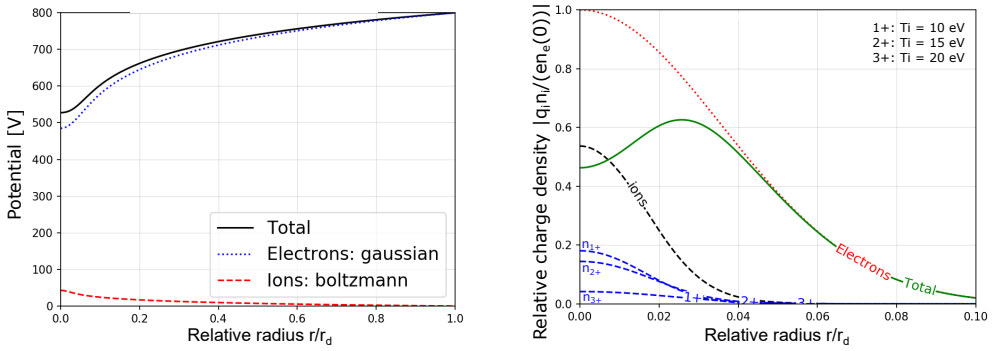

(a) Potential $\phi(r/r_t)$. **(b)** Relative charge densities.

Figure 2.8. Self-consistent solution of the Poisson equation for REXEBIS electron beam (Adiabatic gun) with $I_e = 200$ mA, $E_e = 4$ keV, and three charge states of an ion species **(a)**. The distinct contributions from ions (Boltzmann distribution) and electrons (Gaussian distribution) are shown. The spatial relative charge densities are plotted **(b)**. The blue dashed curves represent the individual density distributions $n_{i,q}/n_e(0)$ meanwhile the black dashed curve compares the charge densities $\sum_q Q_i n_{i,q}/(en_e(0))$. The characteristic radius used for the Gaussian electron beam is $r_e = 0.05 \cdot r_d$

.

A solver of the Poisson equation (2.43) was implemented using Python, with a typical example of the solutions given in Figure 2.8. In this example, only three different charge states of a single ion species where considered. The density of singly-charged ions at $r = 0$, is deliberately chosen to be $n_{i,1+}(0) = 0.2 \cdot n_e(0)$. The shape of the self-consistent potential solved from Poisson equation remains globally similar to the case where only the electron beam space charge was considered, at the exception of an initial (at $r = 0$) compensation of the electron beam. An indicator of the compensation of the electron beam by all positive ions can be written as,

$$f_c(r) = \sum_i \sum_q q_i n_{i,q}(r)/n_e(r) \tag{2.44}$$

In Figure 2.8, the compensation factor at $r = 0$ is approximately 50 %, however, due to the relatively low temperatures chosen ($T_i = 10$ to 20 eV), the ion average radii stay small compared to the electron beam radius. The compensation factor

f_c is written as a function of the charge densities at r, and would yield a different result if it was calculated as an integral of charges over the total volume. It can be intuitively seen that the solutions of the Poisson equation using the Boltzmann distribution strongly diverge when locally $\sum_i \sum_q q_i n_{i,q}(r) > n_e(r)$; an hypothesis which contradicts the trapping of ions. In such case, ions would be lost and the density n_i would need to be renormalized. More precisely, a stability condition for the trapping of ions inside the drift region can be determined depending on the temperature regime. As explained in the previous section, the radial potential felt by ions outside from the electron beam is not quadratic but of the shape $\phi(r) \propto \phi_0 \ln\left(\frac{r_t}{r}\right)$. In this latter expression the potential ϕ_0 may include positive charge compensation. Calculating the (circular) integral of the density using Boltzmann distribution leads to normalization issues depending on the ion temperature. According to our assumptions, and assuming the drift tube potential wall is infinitely far, the number of ions outside from the electron beam is proportional to:

$$\begin{aligned} N_i(r > r_e) &\propto \int_{r_e}^{+\infty} n_i(r) r \mathrm{d}r \\ &\propto \int_{r_e}^{+\infty} r^{1-2Q_i\Phi_0/(k_B T_i)} \mathrm{d}r \end{aligned} \tag{2.45}$$

This latter integral is a recognizable Riemann improper integral, with criteria of convergence $2Q_i\Phi_0/(k_B T_i) - 1 > 1$, which translates into an ion temperature $k_B T_i < Q_i\Phi_0$. The Boltzmann distribution can be tested for different ion temperatures close to this limit ($Q_i\Phi_0$) inside a closed space representative of an EBIS. Using the definition of the heat capacity shown in Equation 2.21, its evolution as a function of the dimensionless ratio $k_B T_i/(Q_i\Phi_0)$ is presented in Figure 2.9.

It can be observed that ions experience a phase transition inducing an excess of energy spread close to the critical potential $Q_i\Phi_0$. At temperatures below 20 % of $Q_i\Phi_0$, the ion beam resides completely inside the quadratic potential of the electron beam. Typically, with an electron beam current $I_e = 0.2$ mA and cathode potential $U_c = 6$ keV, the potential $\Phi_0 = 38.3$ V as shown in Figure 2.6. In order to reach 20 % of $Q_i\Phi_0$ in an uncompensated electron beam, ions at charge state $q_i = 30+$ would require a temperature of 230 eV. This temperature is an estimation of the limit until which most of the ions reside inside the electron beam. For instance, with the

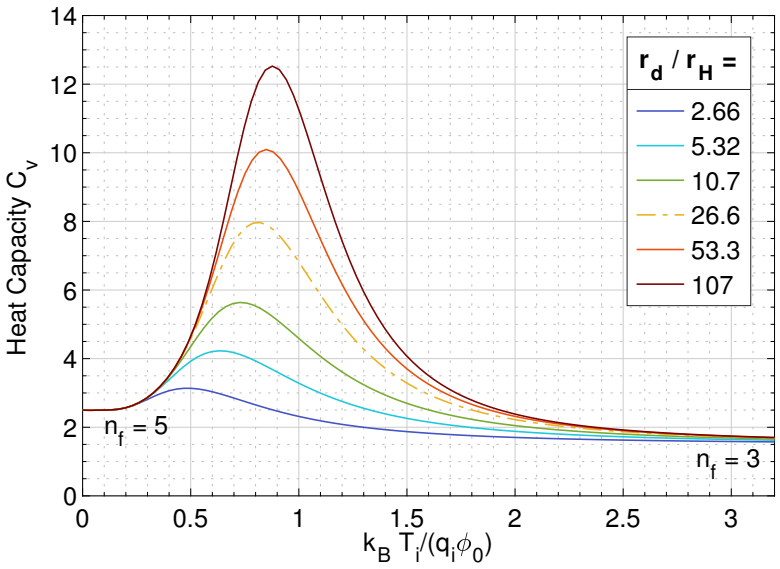

Figure 2.9. Evolution of the Heat Capacity C_v for different combinations of r_d/r_e ratios. The dash-dotted curve represent REXEBIS geometry with the Adiabatic type of electron gun.

Xe^{30+} measurements shown in Chapter 3, it will be shown that the temperature stay generally below 40 % of $Q_i\Phi_0$. At this regime the ion cloud expansion remains well confined within the electron beam but will drastically increase with temperature. It becomes necessary to introduce the average radius of the ion cloud and analyse its tendency to expand,

$$r_i = \int_{\mathbb{R}_+} r^2 n_i(r) \mathrm{d}r \tag{2.46}$$

By using the Boltzmann distribution n_i with a normalization factor $n_i(0)$ making it a probability function such that the circular integral equals one, $\int r n_i(r) \mathrm{d}r = 1$, and by integrating over the EBIS trapping region, the average radius of ions can then be estimated for different temperatures. It is useful to directly compare this radius with the characteristic electron beam radius r_e used for the analytical calculations (Figure 2.10).

In those calculations, the electron beam size is kept constant (approximately $r_e = 250$ μm) and one can observe several regime of ion cloud expansion. From temperatures approximately half the critical potential $q_i\Phi_0$, the expansion accelerates and it will result in a decreased efficiency of the charge breeding. To account for

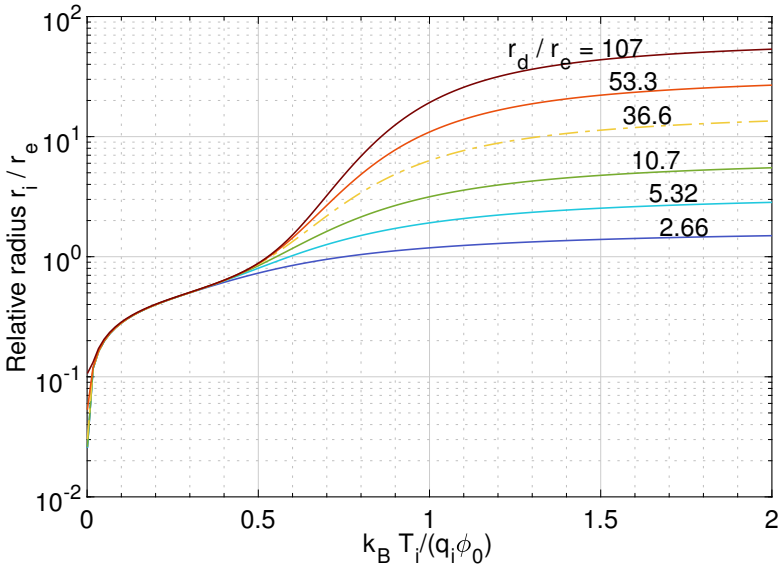

Figure 2.10. Evolution of the average ion beam radius r_i relative to the electron beam radius r_e, for different combinations of r_d/r_e ratios. The dash-dotted curve represents REXEBIS geometry with the Adiabatic type of electron gun.

the spatial overlap between the electron beam and the ion cloud, the factor $f_{i,e}$ is introduced. A good overlap between the ion and electron spatial distributions is essential, as it will affect the ionization cross-sections. On the other hand, the overlap factor between ion species scales the different charge-exchange phenomena. The overlap factor between two species affects the rate equations presented in the next section. Using the solution ϕ_k of the Poisson equation, from a set of radial positions r_k, the overlap factor can be calculated as,

$$f_{i,e} = \int f_i(\mathbf{r}) \frac{f_e(\mathbf{r})}{\max f_e} \mathrm{d}\mathbf{r} \tag{2.47}$$

A methodology to measure the temperature of ions will be shown in the following chapter, therefore leading to the knowledge of overlap factors during the typical charge-breeding conditions of the REXEBIS.

2.2.7 Maxwell-Boltzmann Distribution

The Kinetic description of the EBIS plasma tells us that the system is driven through collisions towards a Maxwellian steady state. The collisional term in Boltzmann

equation (2.24) becomes independent of time, thus $(\partial f_i\ \partial t)_{\text{coll}} = 0$. The reasoning which leads to utilize Maxwell-Boltzmann distributions depends on all collisions an ion species undergoes. An ion species is described by one temperature T_i using the isotropic assumption, although may still show a shift in axial velocity. It will be shown in the next chapter that the axial ion beam distribution can be measured and resembles a Maxwell-Boltzmann energy distribution with five degrees of freedom ($n_f = 5$), as was predicted in the previous section. This energy distribution is expressed shifted by E_0 (in axial direction for instance), as a function of the potential energy $E_\phi \equiv Q_i \cdot \phi - E_0$,

$$f_i(E_\phi)\mathrm{d}E_\phi = \frac{4}{3}N_i\sqrt{\frac{1}{\pi}}(E_\phi)^{3/2}\left(\frac{1}{k_BT_i}\right)^{5/2}\exp\left(\frac{-E_\phi}{k_BT_i}\right)\mathrm{d}E_\phi \tag{2.48}$$

The normalization to infinity of this energy density function is given here scaled by the total number of ions N_i. When ions reach a sufficient temperature to lose radial trapping, the progressive escape from the electron beam will make the equipartition tend to solely three kinetic degrees of freedom ($n_f = 3$). In such case the energy distribution asymptotically reach the form:

$$f_i(E_\phi)\mathrm{d}E_\phi = 2N_i\sqrt{\frac{E_\phi}{\pi}}\left(\frac{1}{kT_i}\right)^{3/2}\exp\left(\frac{-E_\phi}{k_BT_i}\right)\mathrm{d}E_\phi \tag{2.49}$$

Those equations will be further utilized for the fitting of axial energy scans leading to the determination of T_i.

2.2.8 Charge-State Evolution

A variety of phenomena play a part in the change of charge states of ions inside an EBIS. The most common atomic processes resulting in an increase of charge state are: electron impact ionization (EI), charge exchange (CX), photoionization, surface ionization and field ionization. Only the first two processes will be considered of relevance in the following studies. Inversely, the atomic processes resulting in a decrease of charge state include the radiative recombination (RR), the charge exchange and the dielectronic recombination (DR). When the capture of an electron by an ion results in the simple emission of a photon, the process is called radiative

recombination $A^q + e^- \rightarrow A^{q-1} + h\nu$. However, when the interaction energy is closed from a bound electron orbit energy, the capture may result in dielectronic recombination $A^q + e^- \rightarrow \left[A^{q-1}\right]^* \rightarrow A^{q-1} + h\nu$. The excitation energy allows a bound electron to be promoted to another shell. As shown in Figure 2.11 with the example of $^{39}K^{15+}$ and an electron beam energy close to 2.58 keV, it is common that the dielectronic resonant process overcomes the radiative recombination. The different models of cross sections used are described in the Appendix A.

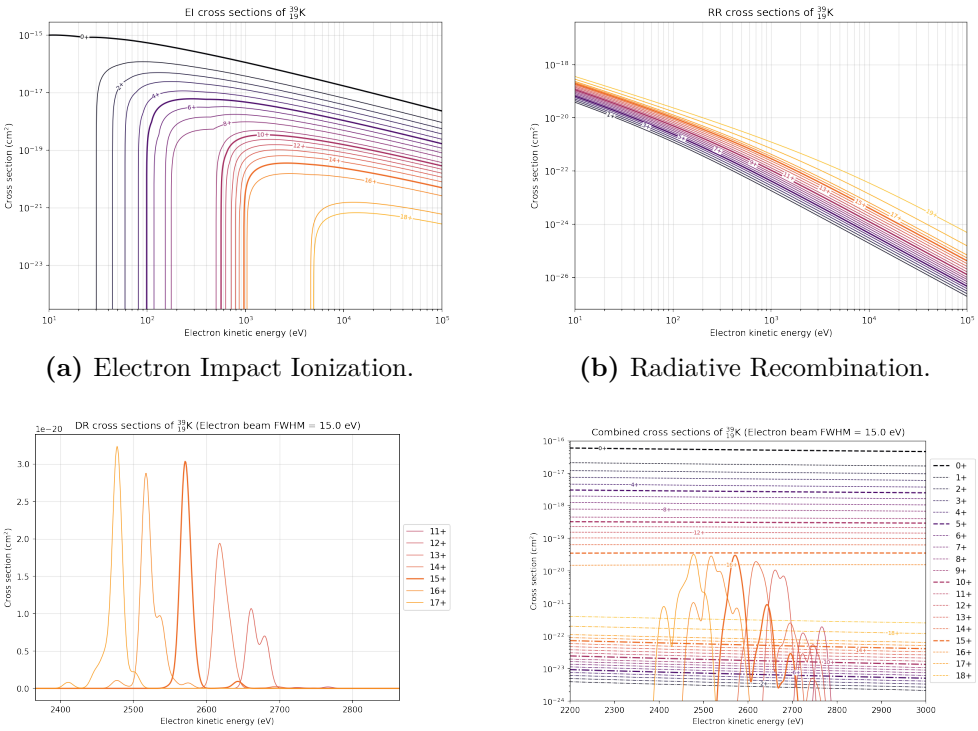

(a) Electron Impact Ionization. **(b)** Radiative Recombination.

(c) Dielectronic Recombination. **(d)** Combined cross sections.

Figure 2.11. Cross sections of the three ionization phenomena considered, plotted using EBISIM simulation package for ^{39}K. The electron beam energy spread used for processing the dielectronic recombination cross sections is 15 eV (FWHM).

The evolution of the number of ions of a species at a specific charge state N_q, is

expressed as the result from the contributions of the different cross sections,

$$\begin{aligned}\frac{\mathrm{d}N_q}{\mathrm{d}t} =& \frac{j_e}{e} f_{i,e} \left(N_{q-1}\sigma_{q-1}^{\mathrm{EI}} - N_q\sigma_q^{\mathrm{EI}} + N_{q+1}\sigma_{q+1}^{\mathrm{RR}} - N_q\sigma_q^{\mathrm{RR}} + N_{q+1}\sigma_{q+1}^{\mathrm{DR}} - N_q\sigma_q^{\mathrm{DR}} \right) \\ &+ \sum_j f_{i,j}(n_j\overline{v}_{q+1}N_{q+1}\sigma_{q+1}^{\mathrm{CX}} - n_j\overline{v}_q N_q\sigma_q^{\mathrm{CX}}) + N_q R_q^{\mathrm{esc}} + N_q^{\mathrm{source}}\end{aligned} \tag{2.50}$$

In this simplified model, the double ionization events are not considered. The first line of the Equation 2.50 shows the effect of electron impact ionization, radiative recombination and dielectronic recombination. The three of them depend on the electron beam energy and scale with the electron current density. The source term in the rate equation serves at differentiating the cases of singly-charged ion injection and neutral gas injection. An escape term (esc) is included to account for the radial and axial escapes of ions. It is expressed as,

$$R_q^{\mathrm{esc}} = \frac{3}{\sqrt{2}}\nu_i \frac{e^{-\omega_i}}{\omega_i} \tag{2.51}$$

The collision rate ν_i is the total rate including collisions with other ion species at each of their charge state, so $\nu_i = \sum_j \nu_{ij}$. The term ω_i represents the loss frequency. The axial loss frequency can be approximated by,

$$\omega_i^{ax} = \frac{Q_i(U_b - U_d)}{k_B T_i} \tag{2.52}$$

Another expression of the axial loss term can be found in [Marrs, 1999] and follows the derivations from [Khudik, 1997]. The formula is shown in Appendix B with a proposed correction on one of the different factors that were calculated in [Marrs, 1999]. The radial loss frequency is,

$$\omega_i^{rad} = \frac{q_i}{k_B T_i}\left(U_d - \phi(r_e) + B_d r_d \sqrt{2k_B T_i / (3m_i)} \right) \tag{2.53}$$

A simulation tool called EBISIM, developed in Python by H. Pahl (University of Heidelberg and CERN), notably includes as a part of a larger palette of features, the solution of the rate Equations 2.50 for ions either injected singly-charged or resulting from neutral gas ionization [Pahl, 2021]. The simulated charge state evolution of $^{39}\mathrm{K}^{q+}$ ions injected as singly-charged is presented in Figure 2.12. The main free

parameters of the simulation tool are the ions species characterized by their initial densities and temperatures, the electron current density j_e and electron beam energy E_e.

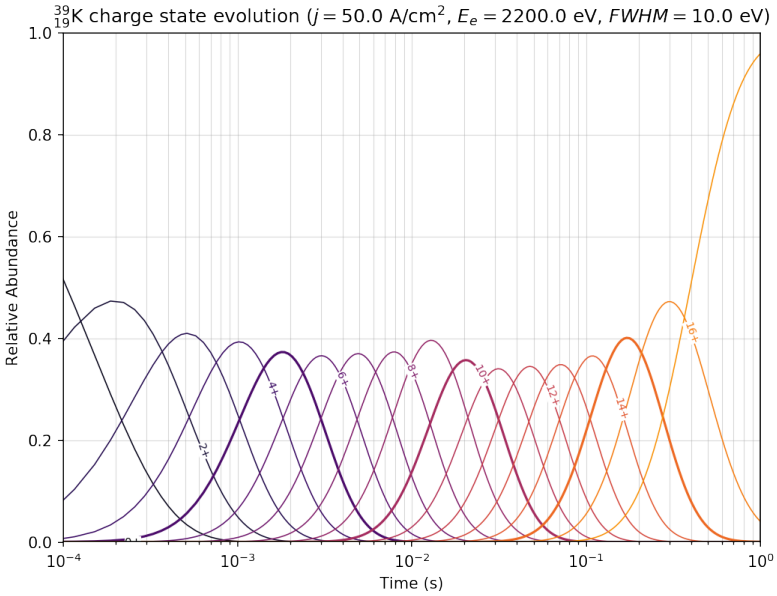

Figure 2.12. Example of EBISIM simulations for the charge state evolution of $^{39}K^{q+}$ ions with REXEBIS Adiabatic electron gun setup for j_e =50 A/cm^2 and E_e = 2.2 keV.

In Figure 2.12, one can observe that each charge state density successively reaches a maximum abundance - with respect to other charge states - that defines the maximum achievable charge breeding efficiency. EBISIM is used in the next chapter to draw comparisons with the measured charge state distributions of ions charge-bred in REXEBIS. One of the main source of uncertainty in the use of such simulation tool is the effective electron current density j_{eff} experienced by ions. This current density includes the overlap factor between ion species and the electron beam and in particular reflects the effect of the ion cloud expansion due to heating.

2.2.9 Energy Balance

The temperature of ions trapped in an EBIS is affected by several processes. Coulomb collisions with the electron beam is one process generating an increase of the ion temperature, often referred as Landau-Spitzer heating [Spitzer and Cook, 1957].

The rate equation is given by,

$$\left(\frac{\mathrm{d}k_B T_i}{\mathrm{d}t}\right)^{\text{Spitzer}} = 2 f_{ei} \nu_{ei} \frac{m_e}{m_i} E_e \tag{2.54}$$

It notably involves the collision frequency between electrons and ions ν_{ei} (Equation 2.31) and the electron beam energy E_e. Similarly, the energy transfer through Coulomb collisions between ion species is also part of the energy balance:

$$\left(\frac{\mathrm{d}k_B T_i}{\mathrm{d}t}\right)_j^{\text{Transfer}} = 2 f_{i,j} \nu_{ij} \frac{m_i}{m_j} \frac{k_\mathrm{B} T_j - k_\mathrm{B} T_i}{\left(1 + \frac{m_i k_\mathrm{B} T_j}{m_j k_\mathrm{B} T_i}\right)^{3/2}} \tag{2.55}$$

It is given by the difference of temperature (heat) between the ion species of interest and one background species, noted with index j. Technically the sum over all background species j must be operated. Heating through Coulomb collisions is not the only phenomena impacting the energy dynamics of ions. When ionisation (or recombination) occurs, the average potential seen by ions will change due to the change in charge state and it will result in an increase of temperature. The change in potential energy during an ionization event is $\Delta E_\phi = \langle \phi(\mathbf{r}) \rangle$. Using the radial function distribution $n_{i,q}$, of ions at a charge state q, the rate of ionisation heating becomes,

$$\left(\frac{\mathrm{d}N_q k_B T_i}{\mathrm{d}t}\right)^{\text{Ionisation}} = \int \Phi(r) \left[R_{i-1}^{\mathrm{EI}} n_{i-1}(r) - \left(R_{i+1}^{\mathrm{RR}} + R_{i+1}^{\mathrm{DR}} \right) n_{i+1}(r) \right] r dr \tag{2.56}$$

Lastly, the progressive escape of hot ions within the Boltzmann distribution will result in an effective decrease of the temperature. The escape term R_q^{esc} defined in the previous section is reused,

$$\left(\frac{\mathrm{d}k_B T_i}{\mathrm{d}t}\right)^{\text{Escape}} = -k_B T_i (\min(\omega_i^{rad}, \omega_i^{esc}) + 1) R_q^{esc} \tag{2.57}$$

With such formulation, the shallowest of the two (axial and radial) trapping potentials regulates the escape rate. Eventually, one arrives at a general differential equation

describing the energy balance of an ion species inside an EBIS:

$$\begin{aligned}\frac{\mathrm{d}k_BT_i}{\mathrm{dt}} = &\left(\frac{\mathrm{d}k_BT_i}{\mathrm{d}t}\right)^{\text{Spitzer}} + \left(\frac{\mathrm{d}k_BT_i}{\mathrm{d}t}\right)^{\text{Ionisation}} \\ &+ \sum_j \left(\frac{\mathrm{d}k_BT_i}{\mathrm{d}t}\right)_j^{\text{Transfer}} - \left(\frac{\mathrm{d}k_BT_i}{\mathrm{d}t}\right)^{\text{Escape}} \\ &+ \left(\frac{\mathrm{d}k_BT_i}{\mathrm{d}t}\right)^{\text{Source}}\end{aligned} \tag{2.58}$$

An external source term is included to account in particular for the possibility to inject ions with a significant initial temperature. This can for instance emulate a non-optimal injection of ions inside the electron beam, when the initial temperature from the source term may affect the overlap factor f_{ei} at low charge states.

2.2.10 Single Ion Dynamics

Analytical mechanics give us access to the motion of collisionless charged particles in electromagnetic EBIS fields after relaxation. By formulating the typical canonical variables $\mathbf{q} = (r, \theta, z)$, each index of the variable q^i is a conjugate to a coordinate in $\mathbb{R}^3(\mathbf{e_r}, \mathbf{e}_\theta, \mathbf{e_z})$.

The Langrangian $\mathcal{L} = T - U + M$ of a non-relativistic particle of mass m_i and charge $Q_i = q_i \times e$ is expressed as a function of:

- The Kinetic energy $T = \frac{m_i}{2}\left(\dot{r}^2 + r^2\dot{\theta}^2 + \dot{z}^2\right)$.
- The Electrostatic potential $U = Q_i\phi(r, z)$, for an ion confined in a self-consistent potential $\phi(r, z)$.
- The Magnetostatic potential $M = Q_i\mathbf{v}\cdot\mathbf{A} = \frac{1}{2}Q_iB_dr^2\dot{\theta}$ in the drift zone subject to a magnetic field $B_d\mathbf{e_z}$.

The Lagrangian is is then,

$$\mathcal{L} = \frac{m_i}{2}\left(\dot{r}^2 + r^2\dot{\theta}^2 + \dot{z}^2\right) - Q_i\phi(r, z) + \frac{1}{2}Q_iB_dr^2\dot{\theta} \tag{2.59}$$

From the Lagrangian, one obtains the canonical momentum (i.e. not linear),

$$\boldsymbol{P} = (P_r, P_\theta, P_z) = \left(m_i \dot{r}, m_i r^2 \dot{\theta} + \frac{1}{2} Q_i B_d r^2, m_i \dot{z} \right) \tag{2.60}$$

The Hamiltonian is derived from the Legendre transformation of the Lagrangian:

$$\begin{aligned} \mathcal{H} =& \frac{m_i}{2} \left(\dot{r}^2 + r^2 \dot{\theta}^2 + \dot{z}^2 \right) + Q_i \phi(r, z) \\ =& \frac{1}{2 m_i} \left[\left(\frac{P_\theta}{r} - \frac{Q_i B_d r}{2} \right)^2 + P_z^2 + P_r^2 \right] + Q_i \phi(r, z) \end{aligned} \tag{2.61}$$

The magnetic field contributes to the effective trapping potential felt by ions. Since the cross-field diffusion is driven by the ion-ion collisions rate on a time scale shorter than the confinement time, the trapping effect of the magnetic field is often neglected in the charge-breeding context. One can demonstrate that because of cylindrical symmetry $\dot{P}_\theta = -\frac{\partial \mathcal{H}}{\partial \theta} = 0$, the canonical momentum $P_\theta = m_i r^2 \dot{\theta} + Q_i B_d r^2/2$ is constant (Busch Theorem). From the Hamilton Equation 2.61, it becomes interesting to use the electric field $\mathbf{E} = -\nabla(\phi(r, z))$ and the canonical momentum P_θ as a constant parameter in the expressions of the differential equations describing position coordinates:

$$\begin{aligned} \ddot{z} &= \frac{Q_i}{m_i} E_z(r, z) \\ \ddot{r} &= \frac{Q_i}{m_i} E_r(r, z) - \frac{P_\theta^2}{m_i^2 r^3} + \frac{P_\theta Q_i B_d}{m_i^2 r} - \frac{Q_i^2 B_d^2 r}{4 m_i^2} \end{aligned} \tag{2.62}$$

2.2.11 Ion Beam Injection and Extraction

The optimization of the charge breeding performance is particularly dependent on the quality of injection into the electron beam. Singly-charged ions injected with a significant initial kinetic energy may orbit around the electron beam, which result in a decrease of the ionization probability.

a Injection Acceptance

There exist several modes for injecting ions inside an EBIS. The focus is only given to *pulsed* injection and neutral gas injection. With the *pulsed* injection scheme, as opposed to the *continuous* injection, the outer barrier of the EBIS is lowered

during a limited amount of time and raised at higher trapping potential during the charge breeding. The electron beam capture efficiency is then defined strictly by the geometrical acceptance. The normalized acceptance of the electron beam, seen by an ion of charge Q_i, mass m_i and injection energy E_i, is

$$\alpha_{e,i} = \frac{r_e}{2}\sqrt{\frac{Q_i^2 B_d^2 r_e^2}{16 m_i E_i} + \frac{Q_i \phi_0}{E_i}} \tag{2.63}$$

With this model, if the normalized transverse emittance of the injected ion beam is below the acceptance of the electron beam, the injection efficiency is total. With a larger transverse emittance than the acceptance, the efficiency decreases proportionally with the ratio of the two parameters. The energy of injected ions E_i, globally depends in the difference between the REXTRAP platform potential and the sum of the EBIS platform, drift tube and space charge potentials. The first term inside the square root of Equation 2.63 accounts for the focusing of ions entering the region immersed into a magnetic field B_d, and will be explained in the case of extraction.

b Extracted Beam Transverse Emittance

The transverse emittance of the extracted beam from REXEBIS will affect the resolution of the A/q-separation performed downstream and generally the quality of beam transmission through the linac. The significance of emittance will be explained in detail in Chapter 5, the definition is geometrically understable by the product of the phase space ellipse semi-axes. The non-normalized emittance used in this section is in terms of rms, and shown in units of π.mm.mrad when evaluated. In Cartesian coordinates (x, y), the rms emittance on the (x,x') trace space is,

$$\varepsilon_x = \sqrt{\langle x^2 \rangle \langle x'^2 \rangle - \langle x x' \rangle^2} \tag{2.64}$$

So far, we have worked in cylindrical coordinates because the ion cloud is known in terms of radial position and it was simpler to derive the corresponding canonical momenta. Furthermore, we have defined the average ion radius r_i with Equation 2.46, similarly the rms radius is

$$r_i^{\mathrm{rms}} = \sqrt{\int_{\mathbb{R}_+} r^3 n_i(r)\mathrm{d}r} \tag{2.65}$$

The Boltzmann radial distribution $n_i(r)$ is normalized using $n_i(0)$ such that the circular integral equals unit, $\int r n_i(r)\mathrm{d}r = 1$. For converting the different rms evaluations of Cartesian coordinates (x, x', y, y') into cylindrical coordinates $(\mathrm{r}, \theta, \mathrm{r}', \alpha')$, we use the following relations:

$$\begin{aligned} r^2 &= x^2 + y^2 \\ r'^2 + \alpha'^2 &= x'^2 + y'^2 \\ x' &= r'\cos\theta - \alpha'\sin\theta \\ y' &= r'\sin\theta + \alpha'\cos\theta \end{aligned} \tag{2.66}$$

where,

$$x' = \frac{\mathrm{d}x}{\mathrm{d}z} = \frac{v_x}{v_z}, \quad r' = \frac{\mathrm{d}r}{\mathrm{d}z} = \frac{v_r}{v_z}, \quad \alpha' = r\frac{\mathrm{d}\theta}{\mathrm{d}z} = \frac{v_\theta}{v_z} \tag{2.67}$$

Due to thermal relaxation of ions inside an EBIS, the probability density function in the cylindrical trace space can be expressed as,

$$f_i\left(r, r', \alpha'\right)\mathrm{d}r\mathrm{d}r'\mathrm{d}\alpha' = n_i(r)\frac{m_i v_z^2}{2\pi k_B T_i}\exp\left(\frac{-m_i v_z^2 r'^2}{2k_B T_i}\right)\exp\left(\frac{-m_i v_z^2 \alpha'^2}{2k_B T_i}\right)\mathrm{d}r\mathrm{d}r'\mathrm{d}\alpha' \tag{2.68}$$

The Maxwellian distribution of velocities used is directly normalized, one then verifies that $\iiint r f_i\left(r, r', \alpha'\right)\mathrm{d}r\mathrm{d}r'\mathrm{d}\alpha' = 1$. The calculations of the different terms in the emittance lead to,

$$\begin{aligned} \left\langle x^2 \right\rangle &= \frac{1}{2\pi}\iiiint f_i\left(r, r', \alpha'\right) r^3\cos^2(\theta)\mathrm{d}r\mathrm{d}\theta\mathrm{d}r'\mathrm{d}\alpha' = \frac{\left(r_i^{\mathrm{rms}}\right)^2}{2} \\ \left\langle x x' \right\rangle &= \frac{1}{2\pi}\iiiint f_i\left(r, r', \alpha'\right) r^2\cos\theta\left(r'\cos\theta - \alpha'\sin\theta\right)\mathrm{d}r\mathrm{d}\theta\mathrm{d}r'\mathrm{d}\alpha' = \frac{r_i}{2}\sqrt{\frac{2k_B T_i}{\pi m_i v_z^2}} \\ \left\langle x'^2 \right\rangle &= \frac{1}{2\pi}\iiiint f_i\left(r, r', \alpha'\right) r\left(r'\cos\theta - \alpha'\sin\theta\right)^2\mathrm{d}r\mathrm{d}\theta\mathrm{d}r'\mathrm{d}\alpha' = \frac{k_B T_i}{m_i v_z^2} \end{aligned} \tag{2.69}$$

Using the previous equations, one can derive an expression of the emittance as a function of the ion cloud characteristic radii (r_i and r_i^{rms}),

$$\varepsilon_x = \sqrt{\frac{k_B T_i}{2 m_i v_z^2}\left[(r_i^{\mathrm{rms}})^2 - \frac{r_i^2}{\pi}\right]} \tag{2.70}$$

So far ions were considered as if born immersed into a magnetic field B_d. During the transit to a field free region their emittance will increase. This can be demonstrated using the Busch Theorem. We have earlier shown that the angular component of the canonical momentum of an ion in a longitudinal magnetic field is $P_\theta = m_i r^2 \dot{\theta} + \frac{1}{2} Q_i B_d r^2$, whereas in the Cartesian coordinates the canonical momentum is,

$$P_x = m_i \dot{x} - \frac{1}{2} Q_i B(z) y \tag{2.71}$$

One can calculate the rms of this canonical momentum squared and consider that there is no correlation between P_x and y. Then in trace space coordinates and outside from the magnetic field, the rms of the phase squared becomes,

$$\left\langle x'^2 \right\rangle_{B=0} = \frac{k_B T_i}{m_i v_z^2} + \frac{Q_i^2 B_d^2}{8 m_i^2 v_z^2} (r_i^{\mathrm{rms}})^2 \tag{2.72}$$

Using the expression of the emittance in a field B_d (Equation 2.70), a new expression of the non-normalized emittance of extracted ion beams from an EBIS is:

$$\varepsilon_x^2(B=0) = \varepsilon_x^2(B=B_d) + \frac{Q_i^2 B_d^2}{16 m_i^2 v_z^2} (r_i^{\mathrm{rms}})^4 \tag{2.73}$$

By inserting the solutions of r_i and r_i^{rms} obtained from Boltzmann distribution, the emittance can then directly be shown as a function of the ion temperature, mass and charge state.

In Figure 2.13, the normalized emittance is shown, which removes the dependence in the longitudinal velocity of ions (v_z), because $\varepsilon_x^n = \beta_r \gamma_r \varepsilon_x$. It allows to draw comparisons with measurements done at other beam energies. The relativistic gamma factor is supposed close to one. It is noticeable that the emittance grows as a function of charge state, this time independently from the characteristic potential $q_i \phi_0$. In the case of REXEBIS with $B_d = 2$ T the effect of magnetic field remains

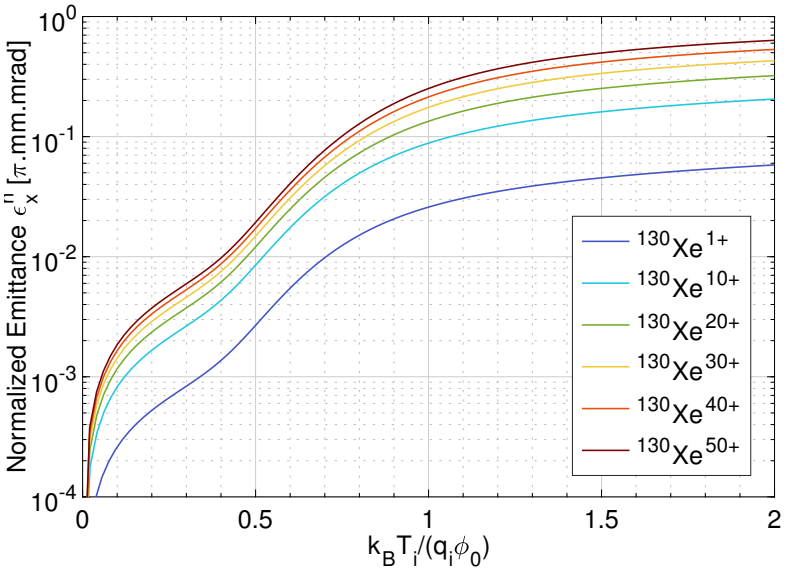

Figure 2.13. Normalized emittance in field free region calculated from ionic Boltzmann distributions for different charge states of $^{130}Xe^{q+}$ inside REXEBIS.

low for ion temperatures below the characteristic potential $Q_i\phi_0$.

c Charge Breeding Efficiencies

The characterization of the charge breeding performances is in practice performed by quantifying the ion currents entering and exiting REXEBIS. The ion beam extracted from an EBIS is a mixture of all the charge-bred residual gas components and the beam of interest. The ion beam is discriminated through an A/q-separator, which will be described in the following section. The charge breeding efficiency $\eta_{i,q}$ of a species i at a charge state q is estimated by measuring the current of the singly-charged ions entering the EBIS, noted $I_{i,1+}^{\text{in}}$, and the current of the extracted beam after the A/q-separator $I_{i,q}^{\text{out}}$. The EBIS distributes the ions over several charge states, and the relative abundance of each charge state q compared to the neighboring charge states actually defines the maximum of $\eta_{i,q}$. Meanwhile, the total charge breeding efficiency η_i accounts for the ion beam currents measured from the

all charge states of the species considered. The efficiencies are,

$$\eta_{i,q} = \frac{I^{\text{out}}_{i,q}}{qI^{\text{in}}_{i,1+}} \qquad \eta_i = \sum_q \eta_{i,q} \tag{2.74}$$

Those efficiencies include the losses at injection into the electron beam and at the extraction. However, it will be seen that the acceptance of the A/q-separator is sufficiently large compared to the beam emittance, which leads us to assume a full transmission of beam through this zone. Typically, during the measurements performed using $^{39}K^{10+}$ through this thesis, the charge breeding efficiencies were close from $\eta_{i,q} = 25$ %, to be compared with a theoretical maximum of about 35 % as presented in Figure 2.12.

d REX A/q-separator

Ion beams extracted REXEBIS are transported to the A/q-separator beam-line before injection into the linac. It a spectrometer of a Nier-type and describes a vertical "S"-shape beam line towards the RFQ. The main components are an electrostatic 90° cylinder deflector of 0.6 m radius and a 90° magnetic bender of 0.5 m radius (Figure 2.14

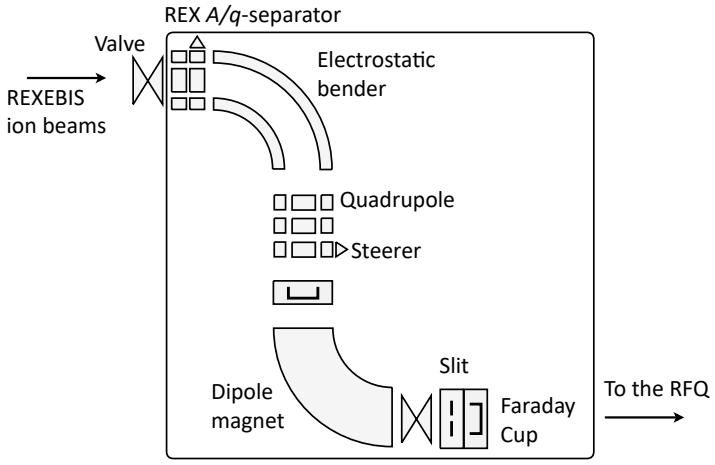

Figure 2.14. Schematic of the A/q-Separator displaying its main elements, including the Faraday cup used for the mass-scans presented.

Beam optics simulations estimate the total (100 %) transverse acceptance of

the A/q-separator to be 200 mm.mrad (0.7 mm.mrad normalized) and a factor ten lower in the dispersive plane when a 5 mm slit is introduced at the focal point [Fraser et al., 2014]. The magnetic dipole creates a constant magnetic field B_s in the transverse direction. The ion beam following the radius ρ_s of the A/q-separator has a magnetic rigidity of,

$$\rho B_s = \frac{p}{q} \simeq \sqrt{\frac{2AU_{ext}}{q}} \tag{2.75}$$

The index i that was used for the denoting the different species inside the EBIS is dropped, the charge state and mass of the beam of interest going through the separator are noted q and A.

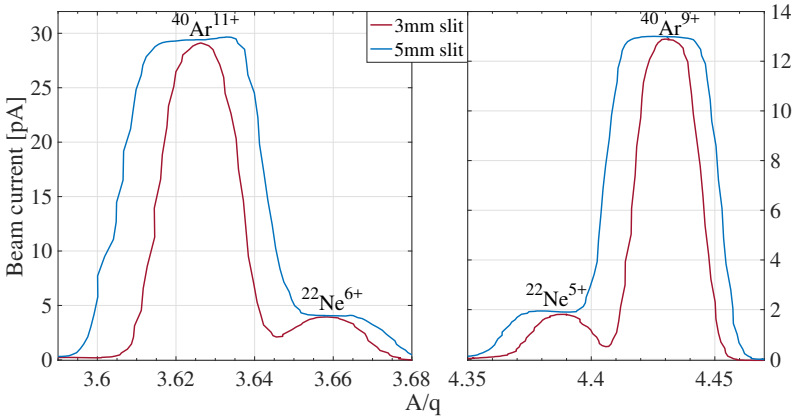

Figure 2.15. Measurements of four A/q peaks with a 3 mm slit or a 5 mm slit at the focal point of the A/q-separator

Mass spectra around four different A/q-peaks were measured using a 3 mm slit or a 5 mm slit (Figure 2.15). The mass spectra are obtained by scanning the magnetic field of the dipole while capturing the beam current passing through the slit with a Faraday cup. Two beams resulting from residual gas ionization of neon and argon inside REXEBIS were extracted. With typical charge breeding conditions and setup of the A/q-separator optics for those beams, the resolution reached is close to $\Delta(A/q)/(A/q) = 1/300$. The 3 mm-slit is typically preferred during operation. Such a resolving power does not allow isobaric separation: an increase by one to two orders of magnitude would be necessary.

2.3 REX/HIE-ISOLDE Linear Accelerator

With the completion of the HIE-ISOLDE project in 2017, the ion beam velocity has been pushed to about 10 % of the speed of light. The linac is divided into two sections, one at room temperature - the historical REX section - and a superconducting section. An overview is given of the figures of merit characterizing the accelerating structures. Finally, the different structures of REX/HIE-ISOLDE linac are detailed.

2.3.1 Quality of Acceleration

Let us consider that an ion arrives at a one-gap cavity of resonance frequency $f = \omega/2\pi$, with a phase ϕ_s. The longitudinal electric field seen is,

$$E_z(z,t) = E(z)\cos(\omega t + \varphi_s) \tag{2.76}$$

The travelling z-component of the field is decoupled and can be calculated for the different operating modes of RF-cavities. Inside the cosine, one may replace t by $z/(\beta c)$. The main objective to increase the energy of a particle of charge q through a gap of length L is given by the relation,

$$\Delta W = q\int_{-L/2}^{L/2} E_z(z,t)\mathrm{d}z \tag{2.77}$$

It is chosen to introduce the equivalent electrostatic accelerating gap voltage on axis,

$$V_0 \equiv \int_{-L/2}^{L/2} E_z(z)\mathrm{d}z \tag{2.78}$$

and the transit-time factor,

$$T \equiv \frac{1}{V_0}\left[\int_{-L/2}^{L/2} E(z)\cos(\frac{\omega z}{\beta c})\mathrm{d}z - \tan\varphi_s\int_{-L/2}^{L/2} E(z)\sin(\frac{\omega z}{\beta c})\mathrm{d}z\right] \tag{2.79}$$

In that last expression, the second term inside the brackets equals zero if the gap considered is symmetric (definition of the gap center). The transit-time factor translates the efficiency of the energy gain when a charged particle crosses the gap.

With axial symmetry the transit-time factor can be estimated using the modified Bessel functions and shows that more acceleration is provided to off-axis particles. This notably results in a change of the bunch shape. One may now rewrite the energy gain from Equation 2.77 as a function of the transit-time factor and the equivalent accelerating voltage,

$$\Delta W = qV_0T\cos\varphi_s \tag{2.80}$$

Defining an average accelerating gradient of a cavity such as $E_{\mathrm{acc}} = V_0T/L$, is an interesting figure of merit. The amplitude of the field, noted E_0 may be decoupled from the transit-time factor by using $E_{\mathrm{acc}} = E_0T$. In order to evaluate the quality factor of a cavity, one first needs to consider the dissipated power $P = P_0 + P_{\mathrm{ext}}$, which is a combination of the losses inside the cavity P_0 and outside P_{ext}. Secondly, the energy stored from the electric field and magnetic field vectors in the cavity is,

$$W_0 = \frac{1}{2}\iiint \mu\boldsymbol{B}^2\mathrm{d}\boldsymbol{V} = \frac{1}{2}\iiint \varepsilon\boldsymbol{E}^2\mathrm{d}\boldsymbol{V} \tag{2.81}$$

The quality factor Q reflects the ratio of the stored energy by the energy loss per period, so

$$Q = \frac{\omega W_0}{P} \tag{2.82}$$

It is a combination of the unloaded quality factor Q_0 and the external quality factor Q_{ext},

$$\frac{1}{Q} = \frac{1}{Q_0} + \frac{1}{Q_{\mathrm{ext}}} \tag{2.83}$$

In practice, the dissipated power inside the cavity due to losses in metal can be calculated by,

$$P_0 = \frac{R_s}{2}\iint \boldsymbol{B}^2\mathrm{d}\boldsymbol{S} \tag{2.84}$$

The surface resistance R_s may be estimated using the conductivity and the skin depth. Whereas the shunt impedance R_0 directly relates to the equivalent cavity

voltage V_0 by,

$$P_0 = \frac{V_0^2}{R_0} \tag{2.85}$$

One can also define an effective shunt impendance by including the transit-time factor: $R_{\text{eff}} = R_0 T^2$. The shunt impedance can be expressed per unit length and in that case noted Z, or Z_{eff} when including the transit-time factor.

$$\begin{aligned} Z &= \frac{E_0^2}{P/L} \\ Z_{\text{eff}} &= \frac{(E_0 T)^2}{P/L} \end{aligned} \tag{2.86}$$

Finally, another geometric parameter that is scale-invariant and often used is

$$\Gamma = Q R_s \tag{2.87}$$

2.3.2 REX Normal-conducting Structures

Historically, REX linac was constructed to accelerate beams with $A/q < 4.5$ up to 2.2 MeV/u, which allowed isotopes with a mass $A < 50$ to reach the Coulomb barrier. In 2004, with the addition of a 9-gap IH cavity the accessible beam energy was pushed further to 3.0 MeV/u for $A/q < 3.5$, which extended the reach of the Coulomb barrier to isotopes of mass $A < 85$. REX normal-conducted linac is operated at the resonance frequency of 101.28 MHz at the exception of the 9-gap based on the second harmonic. The basic parameters for all normal-conducting structures of the REX linac are summarized in Table 2.1.

a Radio-Frequency Quadrupole

The room-temperature RFQ is the first module of the REX/HIE-ISOLDE linac, it is a four-rod-$\lambda/2$ design with a total length of 3 m. The symmetrically opposite rods are connected together electrically, and a RF voltage with a DC offset voltage is applied between one pair of rods and the other. The RF quadrupole field provides transverse focusing while the longitudinal modulation of the four rods allows for the bunching and acceleration of the injected beam. The accelerating gradient of an RFQ drops with energy explaining why it is suitable for low energy beams. The

Table 2.4. Basic parameters for all normal-conducting structures of the REX linac. Parameters with an asterisk (*) are for $A/q = 4.5$.

Parameter	**RFQ**	**ReB**	**IHS**	**7GX**	**9GP**
f [MHz]	101.28	101.28	101.28	101.28	202.56
Nb. of gaps/cells	232	3	20	7	9
$\beta_{\text{in}} \rightarrow \beta_{\text{out}}$ [%]	$0.3 \rightarrow 2.5$	$2.5 \rightarrow 2.5$	$2.5 \rightarrow 5.1$	$5.1 \rightarrow 6.9$	$6.9 \rightarrow 7.8$
$\beta_{\text{in}} \rightarrow \beta_{\text{out}}$ [MeV/u]	$0.005 \rightarrow 0.3$	$0.3 \rightarrow 0.3$	$0.3 \rightarrow 1.2$	$1.2 \rightarrow 2.2$	$2.2 \rightarrow 2.8$
E_{acc} [MV/m]	0.44	0.36	2.7	~ 2.5	5.2
L [m]	3	0.2	1.5	~ 0.60	0.52
Z_{eff} [MΩ/m] (*)	-	20	225	~ 55	165
Q_0	4050	3700	13000	~ 5250	10100
P_0 [kW] (*)	36.3	1.6	50	~ 75	90
A/q acceptance	$\leqslant 5.5$	$\geqslant 2.5$	$\leqslant 4.5$	$\geqslant 2.5$	$\geqslant 2.5$

construction and testing took place at the Ludwig Maximilian University, in Munich [Bongers et al., 1999]. The design of the modulation of the rods has been optimized for $A/q = 4.5$. The resonance frequency and basic parameters are summarized the Table 2.5.

Table 2.5. Basic parameters of the REX/HIE-ISOLDE RFQ

Parameter	**Value**
Maximum duty cycle	10 %
Radial acceptance ϵ^n	0.66 π.mm.mrad
Electrode voltage ($A/q = 4.5$)	42 kV
Output phase spread $\Delta\varphi_s$	± 14 deg
Output energy spread ΔW	±1.5 %

b ReBuncher

The rebuncher is a three-gap split-ring cavity used to match longitudinally the beam from the RFQ into the acceptance of the following IH-structure. The phase spread at the RFQ exit is $\Delta\varphi = \pm 14$ deg, while the IH-Structure requires an input $\Delta\varphi = \pm 10$ deg. The acceptance of the Rebuncher concerns beams with a $A/q \geqslant 2.5$. The construction was made in Frankfurt [Kühnel, 1999]. The integrated voltage at $A/q = 4.5$ is 70 kV.

c IH-Structure

The Interdigital H-type structure is a drift-tube structure that was derived from similar structures, such as the GSI HLI-IH-structure [Nolte et al., 1979]. After a first acceleration section with a 0° synchronous phase, ions are focused in the transverse direction by an inner-tank quadrupole triplet lens (Figure 2.16). Behind the triplet, ions are rebunched by a -30° synchronous phase section (3 gaps), followed by a second acceleration section. The entire structure is composed of 20 gaps.

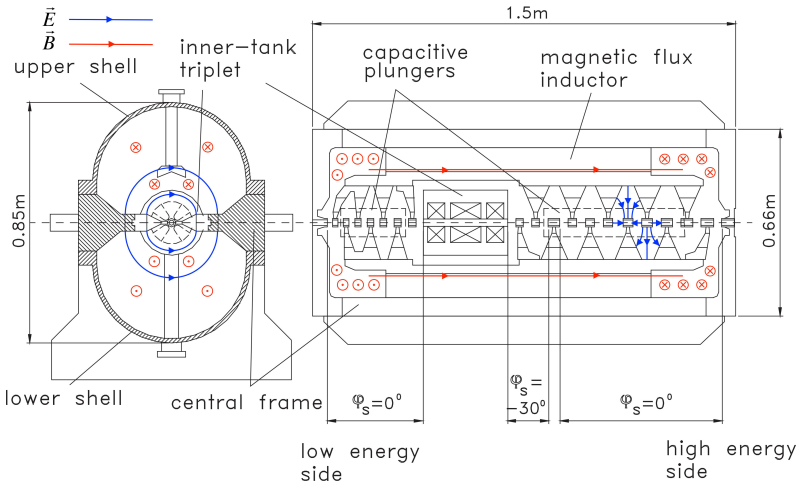

Figure 2.16. Schematic of REX IHS structure with electromagnetic field lines.

d 7GAP Resonators

The following accelerating ensemble is composed of three 7-gap resonators. A 7-gap resonator is an effective solution for balancing between the total energy gain per resonator and a high transit time factor. The split-ring resonators are designed and optimised for synchronous particle velocities of $\beta_s = 5.4$ %, 6.0 % and 6.6 % assuming a realistic total resonator voltage of about 1.75 MV at 90 kW in-coupled power [Podlech et al., 1999]. The beam matching between the output of the IH-structure to the first 7-gap resonator is done by a quadrupole triplet. An additional doublet between the first and second resonator is used for the transverse focusing. The development and construction of the three 7-gap resonators were done by the MPI für Kernphysik, in Heidelberg.

e 9GAP IH-Structure

The design of the 9-gap IH-Structure was derived from the 7-gap IH structures of the MAFF project with a modified drift-tube structure [Sieber et al., 2004]. The shunt impendance is higher than for the 7GAP split-ring resonators, thus the dynamic range of the output energy is wider, from 2.55 MeV/u to 3.0 MeV/u (at $A/q = 3.5$).

2.3.3 HIE Superconducting Structures

The HIE-ISOLDE extension of REX linac includes four cryomodules, each of them containing five superconducting Quarter-Wave Resonators (QWR) and one superconducting solenoid (Figure 2.18). The project also included the addition of three High-Energy Beam Transfer (HEBT) lines (Figure 2.17). The advantage of a superconducting linac is notably the high gradients that can be achieved, reducing the effective length require for acceleration. For normal-conducting cavities, the dissipated power depends on the surface resistance R_s which is for copper, about a factor 10^5 higher than the shunt impedance of a superconducting niobium cavity. The scaling as a function of the RF frequency is also different, for each case

$$R_s \propto \begin{cases} f^{1/2} & \text{normal-conducting} \\ f^2 & \text{superconducting} \end{cases} \tag{2.88}$$

And the dissipated power inside the cavity scales as,

$$P_0 \propto \begin{cases} f^{-1/2} & \text{normal conducting} \\ f & \text{superconducting} \end{cases} \tag{2.89}$$

The size of the cavity is proportional to the inverse of the frequency. The technical aspects of the superconducting linac are given in details in [Nilsson et al., 2006] and the scientific opportunities in [Butler et al., 2007]. The commissioning started in 2015 and continued until 2018 with the final installation of all cryomodules [Rodriguez et al., 2016]. The resonators are based on niobium sputtered on a copper substrate technology. A superconducting solenoid and normal-conducting quadrupoles are used for transverse focusing.

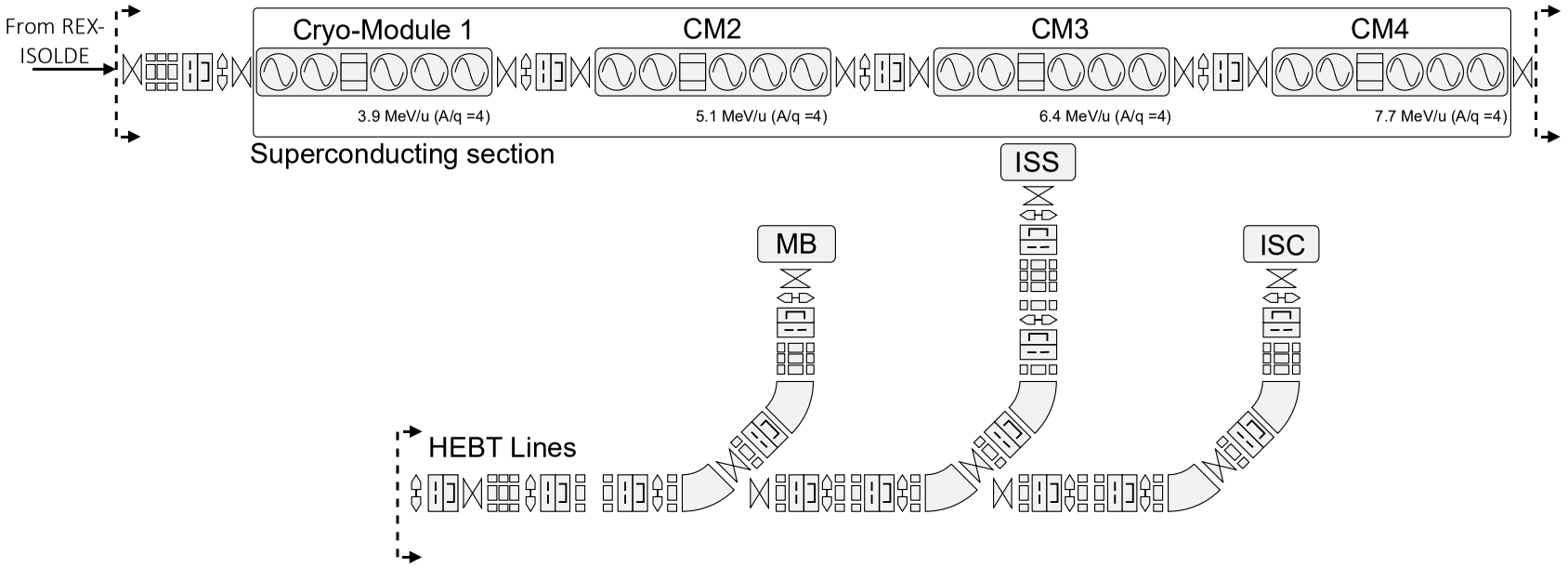

Figure 2.17. Schematic of HIE-ISOLDE linac displaying four cryo-modules, each of them hosting five quarter-wave resonators and a solenoid. The HEBT lines to the experimental stations MiniBall (MB), the ISOLDE Superconducting Solenoid (ISS) and the ISOLDE Scattering Chamber (ISC) are shown.

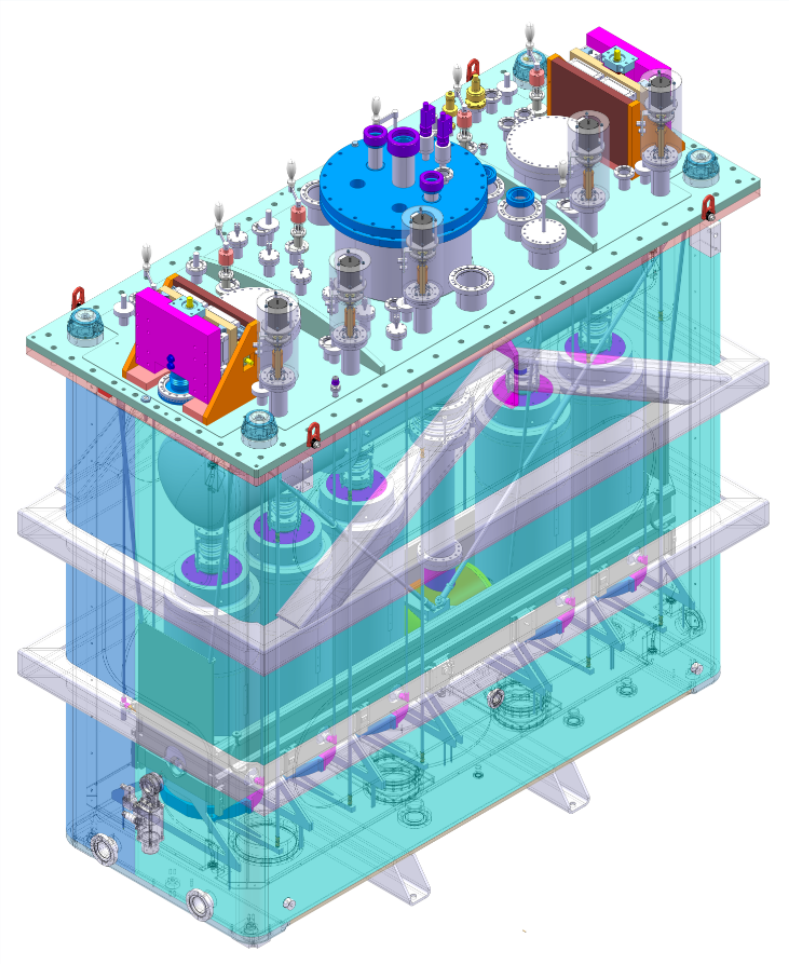

Figure 2.18. Design model of one cryomodule, shown in transparency.

a Quarter-Wave Resonators

Transverse electromagnetic resonant structures are divided into two general types depending on their electrical length ($\lambda/4$ and $\lambda/2$). The quarter-wave resonators are typically designed for $0.05 < \beta < 0.15$. The setting is independent for the phases and amplitudes. Such accelerating structure is capable of flexible operation, with energy variability and adaptability to different A/q-ratios. The synchronous particle must be replaced by a reference particle, whose velocity may differ from the design or geometric velocity [Wangler, 1998]. The transverse magnetic field and electric field components are,

$$
\begin{aligned}
E_r &= -2i\sqrt{\frac{\mu_0}{\epsilon_0}}\frac{I_0}{2\pi r}\sin(k_{z,p}z)e^{ik_{z,p}ct} \\
B_\theta &= \frac{\mu_0 I_0}{\pi r}\cos(k_{z,p}z)e^{ik_{z,p}ct}
\end{aligned}
\tag{2.90}
$$

The magnetic field is maximum at the cavity ends, while the electric field is the largest at the cavity mid-plane. The operating mode of the cavity is expressed as a function of $k_{z,p} = p\pi/L$. The quarter-wave resonator is based on the fundamental mode. The basic parameters of HIE-ISOLDE quarter-waver resonators is given in Table 2.6.

Table 2.6. Basic parameters for HIE-ISOLDE quarter-wave resonators.

Parameter	**Value**
Nb. of cavities	20
Nb. of gaps	2
f [MHz]	101.28
β_g (β_{opt}) [%]	10.3 (11.3)
$L_g = \beta_g\lambda/2$ [mm]	153
T_{max}	0.9
E_0 [MV/m]	6
L [mm]	300
Inner conductor diameter [mm]	90
Mechanical length [mm]	320
Gap length g [mm]	85
Beam aperture diameter [mm]	20
U/E_0^2 [mJ/(MV/m)^2]	207
$\Gamma = R_sQ$ [Ω]	30
P at E_0 [W]	10
Q_0 at E_0	5.0 $\times 10^8$
Helium bath temperature [K]	4.5

The standard manufacturing of the cavity implies to machine the inner and outer conductor separately before welding them together. However, micro cracks were observed near the welds of some of the cavities. A novel seamless design was then considered, and one cavity was put in place in the fourth cryomodule of HIE-ISOLDE linac. These seamless quarter-wave resonators show a higher quality factor and RF surface fields [Venturini Delsolaro and Miyazaki, 2020]. RF leakage is suppressed by changing the beam port aperture from a racetrack to a circle with a diameter reduction, as can be seen in Figure 2.19. The calculation of the energy gain in this

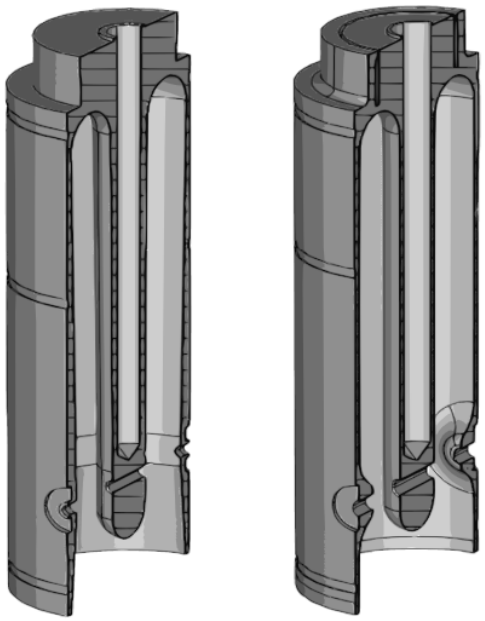

Figure 2.19. Seamless cavity (left) and welded cavity (right) 3d model designs.

last cavity is then modified by the different transit-time factor. The transit-time factor curves are shown in Figure 2.20 for the two different cavity manufacture.

The output energy as a function of the beam A/q is calculated using the Equation 2.77. If all cavities gradients are set at the maximum of 6 MV/m, with a synchronous phase of -20 deg, except for first cavity at -30 deg, the out energies are shown in Figure 2.21.

The divergence of the accelerating field leaking to the drift tube generates transverse electric field components around the beam axis that will either focus or defocus the beam depending on the RF phase. In the conditions of acceleration, the beam is focused when entering the cavity and defocused when exiting. The overall result is a net defocusing effect which needs to be compensated by focusing elements, such as quadrupoles and solenoids.

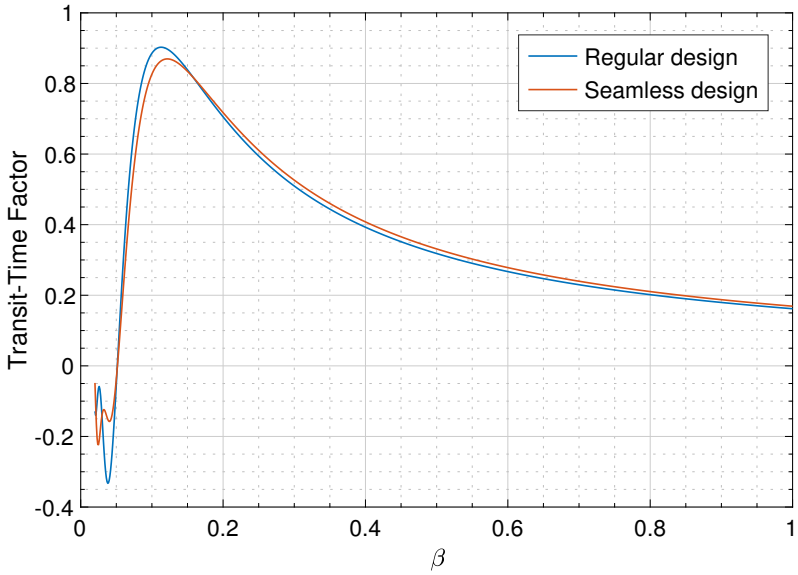

Figure 2.20. Transit-time factor curves for superconducting cavities with and without seamless design.

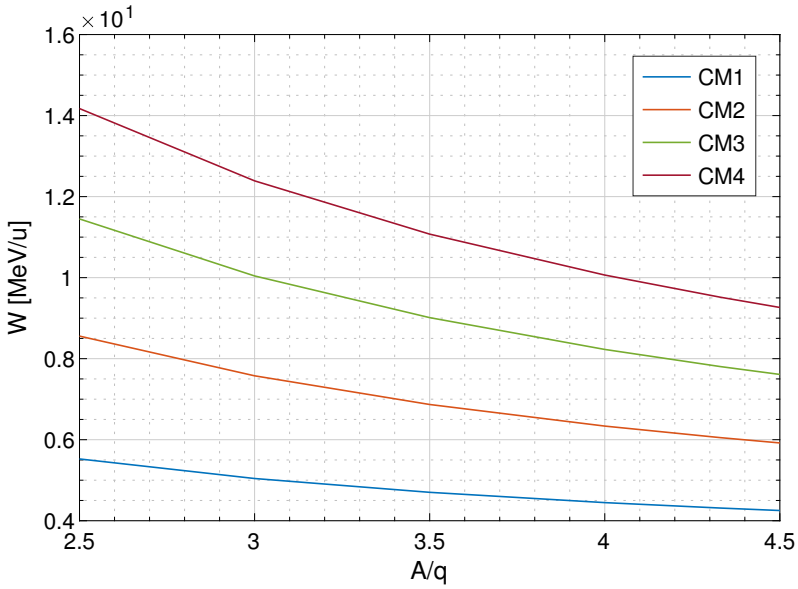

Figure 2.21. Maximum output energies accessible from the HIE-ISOLDE cryomodules (CMx), as a function of the beam A/q.

2.4 Magnetic Beam-line Optics

The main technical aspects of the magnetic focusing elements of HIE-ISOLDE linac are described in this section. The analytical description provided will be used in the following chapters concerning the transverse beam properties measurements and the characterization of the beam energy distribution. Each experimental line is composed of two 45 deg-dipoles. The transverse focusing before and after the dipoles are guaranteed by quadrupoles, and the matching into experimental stations by a triplet at the end of the HEBT lines. Several steerers allow to correct the transverse trajectory of the beam every few meters.

2.4.1 Superconducting Solenoids

Solenoids provide weak focusing to the beam, with a coupling between transverse planes. As a consequence of the coupling, the differential equations of motion are non-linear,

$$\begin{aligned} x'' - \frac{q}{p_z}\left[B_z(z)y' + \frac{y}{2}B_z'(z)\right] = 0, \\ y'' + \frac{q}{p_z}\left[B_z(z)x' + \frac{x}{2}B_z'(z)\right] = 0, \end{aligned} \tag{2.91}$$

Those equations are easier treated in the rotating Larmor frame, which allows decoupling of the transverse component. Besides, the field distribution within a solenoid may be approximated by,

$$B(z) = \frac{B_0}{1 + (\frac{z}{d})^4} \tag{2.92}$$

The maximum field in the solenoid is noted B_0, and the distance d is a field profile characteristic length. The focusing f of a solenoid of diameter D can be deduced analytically with the thin-lens assumption and assuming a step-function approximation of the magnetic field,

$$f = \frac{4}{D}\left(\frac{mc\beta\gamma}{qB_o}\right)^2 \tag{2.93}$$

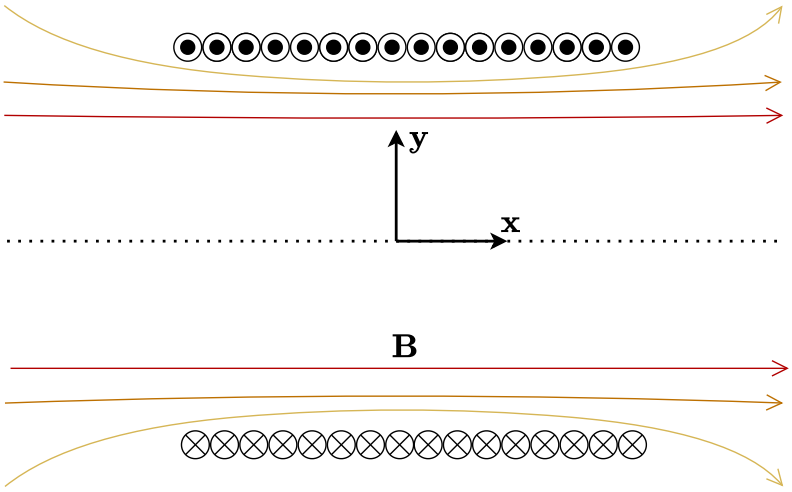

Figure 2.22. Schematic of a solenoid.

Table 2.7. Basic parameters of HIE-ISOLDE superconducting soleinoids. The parameters annoted by an asterisk (*) are at a vertical distance of 230 mm from the centre of the solenoid; representing the nearest RF cavity wall surface.

Parameter	**Value**
Inner bore diameter [mm]	$\geqslant 30$
Mechanical length [mm]	$\leqslant 400$
Magnetic integral ($\int B_z^2 \mathrm{d}r$) [T^{2}m]	16.2
Operating current [A]	$\leqslant 500$
Stray field (when powered) [G] (*)	$\leqslant 180$
Magnetic remanence (when unpowered) [G] (*)	$\leqslant 0.65$
Maximum stored energy [kJ]	$\leqslant 19$
Helium bath temperature [K]	4.5

The current direction in the solenoid is reversible to allow for degaussing when turned off. The specifications presented in Table 2.7 are currently met.

2.4.2 Magnetic Quadrupoles

Magnetic quadrupoles assure the focusing channel through HIE-ISOLDE linac and HEBT lines. The envelope of the beam is preserved below the transverse acceptance of the HEBT lines to guarantee complete transmission, and the spot size is optimized for the experimental apparatus. Quadrupoles of the HEBT lines also offer the opportunity to probe the beam's transverse properties. For this purpose, the detailed derivations leading to the deduction of transverse beam properties while varying the quadrupole focusing strength are given in Chapter 5. The Lorentz force

F experienced by an ion in the coordinates presented in Figure 2.23 is,

$$\begin{aligned} F_x(x,z) &= -qc\beta G_x(z)x \\ F_y(y,z) &= qc\beta G_y(z)y \end{aligned} \tag{2.94}$$

The gradients G_x and G_y are given by the divergence of the magnetic field,

$$\begin{aligned} G_x(z) &= \frac{\partial B_y(z)}{\partial x} \\ G_y(z) &= \frac{\partial B_x(z)}{\partial y} \end{aligned} \tag{2.95}$$

Pole contours are in theory determined by the equipotential lines, describing for a magnetic quadrupole infinite hyperbolas: $2xy = \pm a^2$. The analytical derivations of the transverse dynamics lead to the Mathieu-Hill equation and the theory behind transverse beam properties will be explained in the chapter 5.

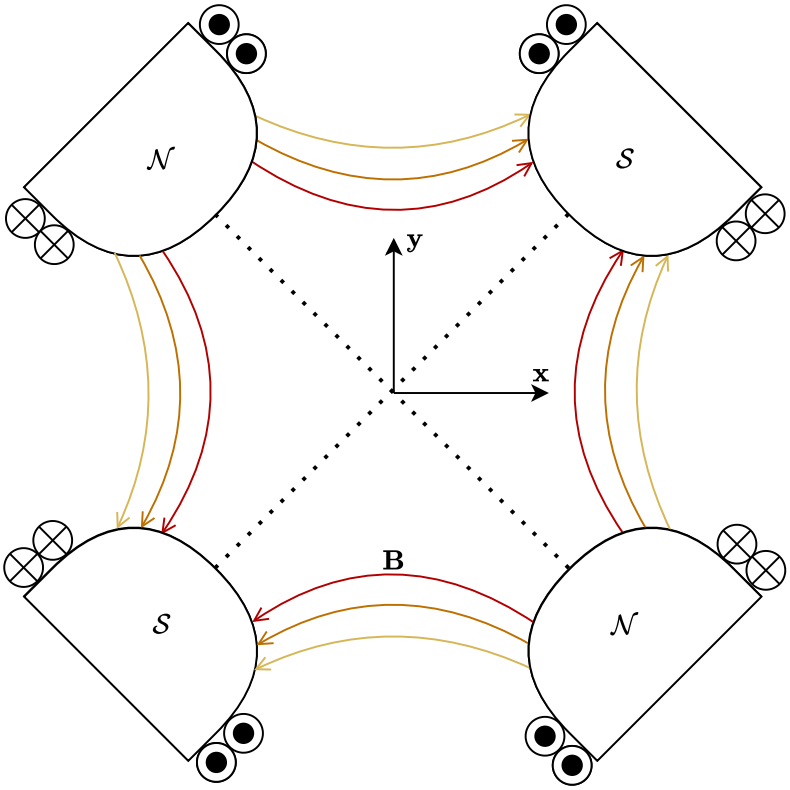

Figure 2.23. Schematic of magnetic quadrupole, focusing on the y-plane.

Magnetic measurements of the HIE-ISOLDE quadrupole series were done using two different tools: a rotating coil and a single stretch wire, both giving a similar

Table 2.8. Basic design parameters of HIE-ISOLDE magnetic quadrupoles.

Parameter	Value
Good Field Region (GFR) radius [mm]	20
Magnetic length L_m	0.2
Nominal current [A]	132
Maximum current [A]	150
Gradient at nominal current [T/m]	25
Integrated gradient [T]	5
Integrated field quality (GFR)	$\leqslant 1 \times 10^{-2}$
Inductance [mH]	30

result of the average integrated transfer function $k = 39$ mT/A ± 0.15 %. The modeling of the quadrupole magnetic field is simplified into a square field model, using k and the equivalent magnetic length $L_m = 0.2$ m which are deduced to include the effect of fringe fields (Table 2.8).

2.4.3 Dipole Magnets

Each HEBT line is equipped with a double-bend-achromat lattice of 45 deg-dipole magnets. The beam is steered from the linac axis and transported to the three experimental stations. The three HEBT dipoles have been extensively used, not only to transport the beam to experimental stations but also to measure the beam energy distribution when using them as spectrometers. The formula which is given for the A/q-Separator dipole (Equation 2.75) cannot be approximated with non-relativistic speeds anymore, so this time,

$$B = \frac{A}{q} \frac{\sqrt{E\,(2E_u + E)}}{c\rho} \tag{2.96}$$

This latter equation gives the optimal magnetic field for a beam of energy E (in MeV/u) travelling with an effective radius ρ. The rest mass of one atomic mass unit $E_u \simeq 931.494$ MeV.

The dipole magnets are of edge-focusing type, which signifies that a pole face rotation of half the bending angle provides focusing in the vertical plane. The primary technical specifications of HIE-ISOLDE dipoles magnets are summarized in Table 2.9. The dipole magnets are designed with a curved C-shape assembled from

Table 2.9. Basic design parameters of HIE-ISOLDE dipole magnets.

Parameter	**Value**
Maximum aperture between poles [mm]	50
Nominal magnetic field in center [T]	1.13
Maximum magnetic field [T]	1.2
Nominal integrated field [T.m]	1.61
Nominal current (DC) [A]	423
Maximum current (DC) [A]	500
Magnet inductance [mH]	113
Nominal dissipated power [kW]	18
Integrated relative field quality (GFR)	$\leq 5.10^{-3}$
Bending angle [deg]	45
Bending radius [m]	1.8
Effective bending radius ρ [m]	1.811

a single piece of laminated steel yoke. The homogeneity of the integrated field is requested to be within $\pm$ 5 $\times 10^4$ of the central field, over a radius of 20 mm. This is abbreviated as the Good Field Region (GFR).

2.5 Diagnostics

The HIE-ISOLDE project also assessed the question of suitable beam diagnostics for RIB. Diagnostic boxes are installed at strategic locations along the linac and HEBT lines to verify the aspects of beam quality. A diagnostic box may include a Faraday cup, a silicon detector, a pair of horizontal and vertical slits, beam collimators, attenuators and stripping foils (Figure 2.24). The stripping foils allow for separating after acceleration beams of low mass isotopes contaminated with, for instance, residual ionized gases from REXEBIS. At low masses, the possibilities to find a clean A/q are reduced, and the use of stripping foil to separate the beam components using the HEBT lines dipoles may well be the only solution. However, even if their use is relatively common during the physics campaign, the stripping foils were not utilized for the measurements presented in this thesis.

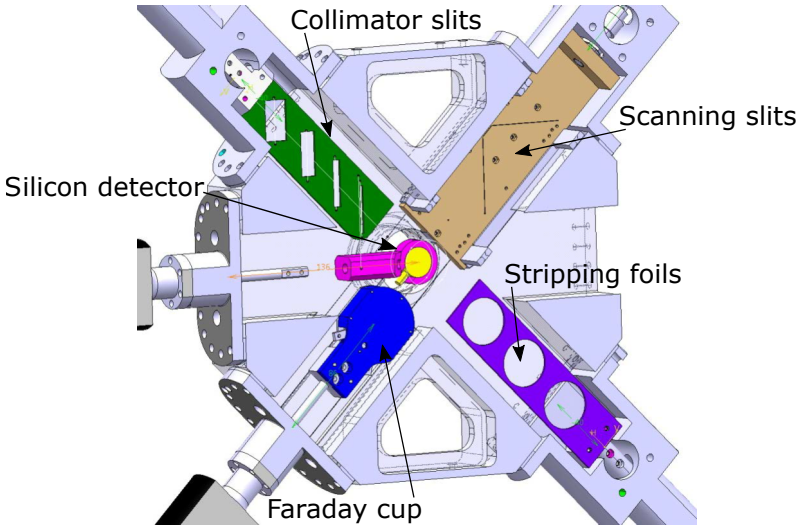

Figure 2.24. Model of a diagnostic box for HIE-ISOLDE.

The transverse beam profiles can be obtained by sampling the beam current using a Faraday cup or a silicon detector behind a scanning slit so that the value of the measured current is recorded as a function of the slit position. The opening of each slit is 1 mm. Both horizontal and vertical scanning slit is on a 45-deg blade with a V-shape. The movement generated by a stepper-motor is either continuous or with steps of minimal length 100 μm. It was noticed that the pulse of the stepper motors produce a 100 kHz noise, which may deteriorate the silicon detector signal,

so they are generally turned off after insertion and during measurements.

2.5.1 Faraday Cups

A VersaModular Eurocard (VME) board allows to control of all the required stepper motors of a diagnostic box, and the analogue-to-digital converters (ADC) are used to record the Faraday cup output signals. The VME board additionally controls the preamplifier's gain and provides the high-voltage for Faraday cups. The active diameter of the Faraday cups is 30 mm, and the resolution is about 100 efA. However, the resolution varies from one Faraday cup to another due to, for instance, the quality of cabling or the surrounding electromagnetic noise. For this reason, the location where a Faraday cup provides the best signal-to-noise ratio is naturally chosen for transverse emittance measurement.

2.5.2 Silicon Detectors

The silicon detectors used are partially-depleted PIPS detectors manufactured by Canberra, with a thickness of 300 μm. A particle impinging on the detector will deposit energy which is proportional to the pulse of charge created. If an ion is fully stopped by the silicon, the signal is directly representative of its total energy. The technical specifications and the commissioning of those silicon detectors are described in [Zocca et al., 2012]. The silicon detectors give access to several essential characteristics of the impinging particles: intensity (or count-rate), energy and time-of-flight. Three different types of silicon detectors have been utilized and are listed in Table 2.10.

Table 2.10. Silicon detectors models and primary specifications from the manufacturer's data-sheet.

Type	Canberra's model	Radius [mm]	Resolution (FWHM)	
			Energy [keV]	Time [ns]
1	PD50-11-300RM	4.0	11	5
2	TMPD50-16-300RM	4.0	15	0.2
3	PD600-20-300RM	13.8	20	5

The silicon detectors of Type 1 and 2 have a relatively small aperture which do

not guarantee to capture all the beam, they are principally used for time-of-flight or direct energy measurements, when assuming that there is no coupling between longitudinal and transverse motions. In particular, the detector of Type 2 allows for a better time-of-flight resolution and was used for the measurement of the bunch structure. The silicon detector of Type 3 has a sufficiently large aperture to assure a total capture of the beam and was used extensively for transverse beam properties characterization (Figure 2.25). The silicon detectors are biased by a voltage between 60 and 100 V.

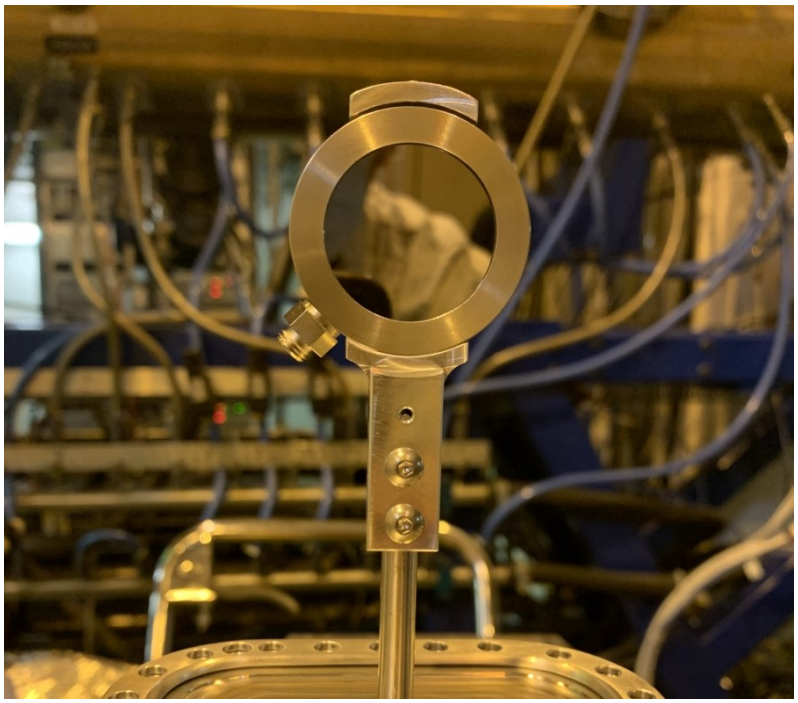

Figure 2.25. Picture of a large aperture silicon detector (Type 3) before installation inside a diagnostic box.

The choice of the preamplifier is crucial for applications in which the total beam energy may vary from from several MeV to few GeV. They will define the saturation limit until which the energy of particle cannot be resolved and electronics will encounter a dead-time. The charge-sensitive preamplifiers are usually composed of an integrator for the energy output and a pulse-shaper for the timing output. The energy signal resembles a positive pulse with a rise time in the order of 10 ns followed by an exponential decay. The preamplifiers used for HIE-ISOLDE silicon detectors have a charge capability of 1 nF. The functional schematic of the preamplifier is

shown in Figure 2.26 (a), along with the response from four consecutive ions of different masses (b).

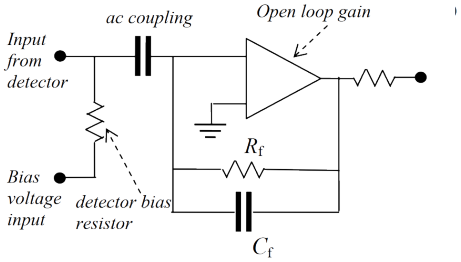

(a) Functional schematics of the integrator.

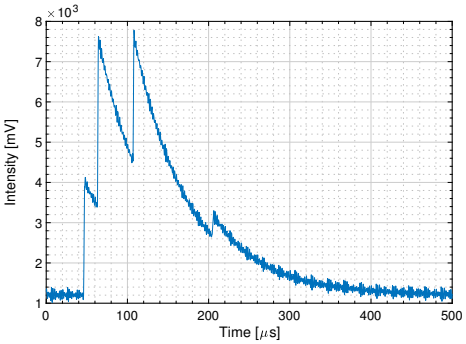

(b) Raw data from the preamplifier.

Figure 2.26. Functional schematics of the preamplifer (a) and typical response from a beam with multiple mass composition (b).

The charge provided by the detector is proportional to the total beam energy W,

$$Q_d[\mathrm{C}] = \frac{W[\mathrm{MeV}] \times e}{\varepsilon_{eh}[\mathrm{eV}]}.10^6 \tag{2.97}$$

The average energy required to produce an electron-hole pair is $\varepsilon_{eh} \simeq 3.62$ eV/e-h for Si. With a high gain A and $\tau_f = R_f C_f \ll \tau_{\mathrm{pulse}}$, the output voltage V_o directly relates to Q_d by,

$$V_o \simeq \frac{Q_d}{C_f} \tag{2.98}$$

The preamplifier sensitivity is expressed by,

$$\xi[\mathrm{mV/MeV}] = \frac{e}{C_f \times \varepsilon_{eh}[\mathrm{eV}]}.10^3 \tag{2.99}$$

The capacitor C_f can then be chosen to meet the requirements in terms of sensitivity. By dividing the maximum output voltage (10 V in our case) with the sensitivity, one deduces the maximum energy before saturation. Avoiding saturation is necessary when the silicon detector is operated to provide the count rate and energy measurement. In the case of energy acquisition, the particles impinging at saturation or during the dead-time are tagged as unresolved by the digitizer. Specific attention is given during measurements to adjust the beam intensity so that the output voltage

remains approximately below 80 % of the saturation limit.

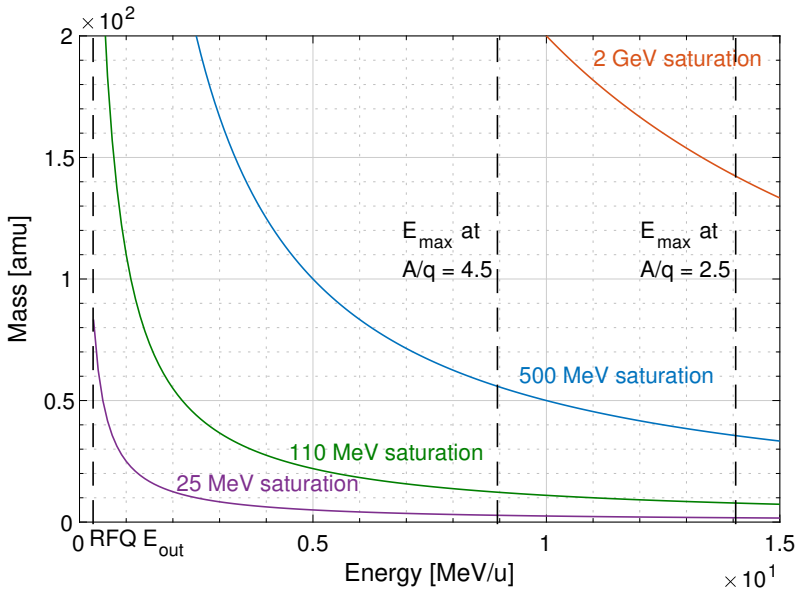

Figure 2.27. Curves of saturation depending on the preamplifier used in combination with the silicon detector.

Energy measurements are performed using a VME board digitizer V1724, manufactured by CAEN. This digitizer includes a digital pulse processing and a pulse height analysis firmware on board. There are two distinct functioning modes that require specific setups of the digitizer: the oscilloscope mode and the energy mode. The oscilloscope mode mainly serves at verifying that the detector and preamplifier are operated far from saturation.

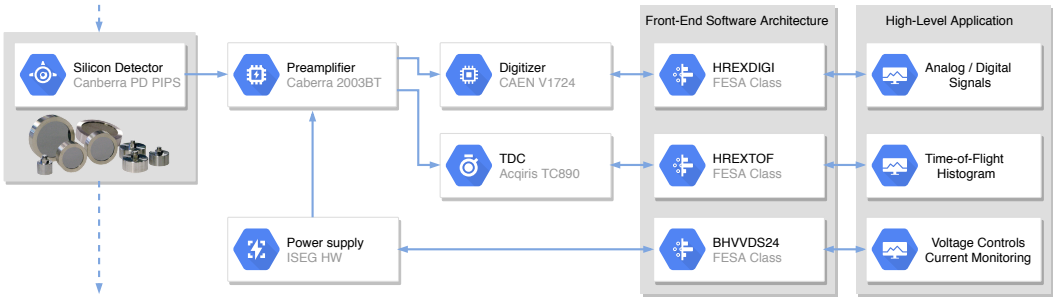

Figure 2.28. Diagram of the data acquisition system surrounding a silicon detector.

The time-of-flight measurements are performed using a Time-to-Digital Converter (TDC) which compares the time of arrival of ions at the detector with the RF master clock that determines the phase of the cavities in the linac. This functionality is

used to probe the bunch structure of the beam. The minimum sampling resolution of the TDC is 50 ps. A diagram of the acquisition system for hardware to software is shown in Figure 2.28.

The question of deterioration of the silicon detectors remains. It will be shown in Chapter 6 that the energy acquisition can be significantly impacted by deterioration, and that lead to the use of a different method for properly characterizing the real beam energy distribution. To summarize, the applications of silicon detectors contextualized in the thesis are:

- **Count rate**: derived from the TDC signal.
- **Energy**: histogram acquired from the digitizer.
- **Bunch structure**: acquired from the TDC.
- **Pulse structure**: derived from the digitizer.

2.6 Control System

Nowadays most of the accelerator technology is manipulated from the control rooms. At ISOLDE, each console has access to high-level graphical applications, Graphical User Interfaces (GUIs), that interact with the control system. A dichotomy is made between the high-level variable of the GUI and the corresponding low-level parameter of the hardware. Three software applications were developed during the course of thesis to carry out the necessary measurements with reliability and flexibility.

2.6.1 Data Flow Layers

The timing system continuously delivers events that are used to trigger the acquisitions of the various accelerator elements. A timestamp is associated with each read event. Then, the real-time applications access the hardware and read the low-level values. After some conversions and association with the event timestamp, the real-time applications publish the updated acquisitions over the network. The server receives the data from the different sources and uses the timestamps to group the data belonging to the same acquisition cycle. Post-processing of the data is often done before being sent to the GUI. To summarize, the primary purpose of the front-end computers is to perform the low-level control and acquisition of the accelerator hardware. Most of the server processes are written in Java and communicate with the GUIs using Java-specific protocols.

The device-property model defines the structure and the manipulations and the behaviour required to exchange data between the low-level software and the high-level software. The two fundamental concepts are the device and the property. Each piece of equipment is a device, for instance, a power converter or a digitizer. A device has properties, and one can read (get operation), write (set operation) or monitor (subscribe operation) a property. As in object-oriented languages, objects are instances of classes, and therefore, devices are instances of classes as well.

a Silicon detector Application

An application was developed to provide a live treatment of silicon detectors' digitizer and TDC signals into relevant information about the beam. The application is used to set up the digitizer for its different operating modes: oscilloscope and energy. By selecting the energy mode, the user has access to an energy histogram of the impinging beam and the pulse structure. The application operates a roll-over treatment of each particle's time-tag and conversion into a physical time, then provides a histogram that is coloured depending on the energy information. The pulse structure is reconstructed as shown in Figure 2.29. The oscilloscope mode requires different settings of the digitizer to acquire a time window extensible to more than 5 ms.

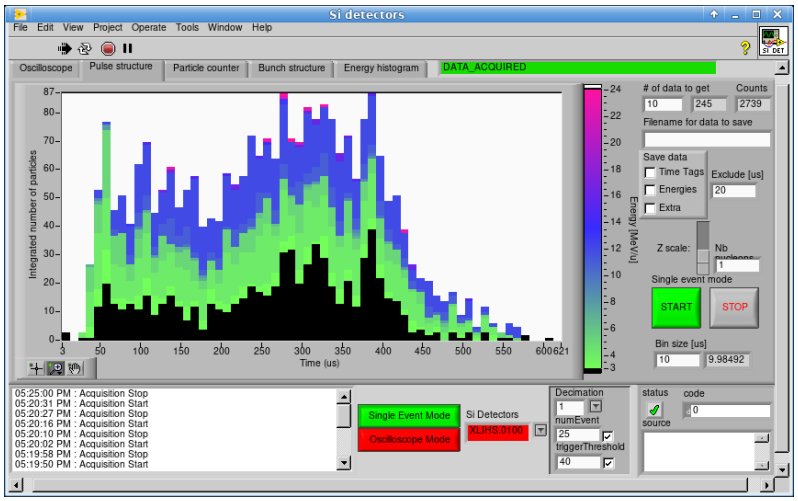

Figure 2.29. Display of the pulse time structure acquisition of the Silicon detector application.

The application also acquires the TDC data and allows to accumulate and display the particle time distribution inside bunches. In parallel, a treatment is provided to extract the count rate of the beam. The application was developed with National Instruments LabView and regularly used during operation.

b Automation Application

The experimental methodologies to characterize the beam properties can be re-formulated by a sequence of instructions in the control system. The instructions

consist of setting properties to a device and of saving the relevant data. In the lexical field of programming, a measurement is a module that includes a list of instructions. The objective of the automation application is to provide a flexible tool for assembling modules and scripting a variety of measurements. More than thirty different modules were coded in Python to complete essential tasks such as longitudinal beam characterization, transverse beam characterization or dipole scans. The scripting of the modules is done by writing in a text file the list of tasks to accomplish with the possibility to adopt conventional tools («loop», «if», «load»,...) if necessary. An elementary example of a scripting file is given:

```
Loop(x = 10:10:100)
    EBIS_breeding_time(x)
    Mass_scan(Collector = SD, Dipole_range = [500, 1000])
```

Loading this text file into the application will automatize the measurement of mass scans for different breeding times of REXEBIS (10 to 100 ms), using a silicon detector as a beam collector. The values for the dipole are given as an indication (from 500 to 1000 mT). Each module is configurable with relevant arguments: the type of collector, the range of values to sweep, the time step, etc. The GUI of the application serves at loading the scripting file and starting the application. Several acquisition windows are available to display the live result (Figure 2.30)

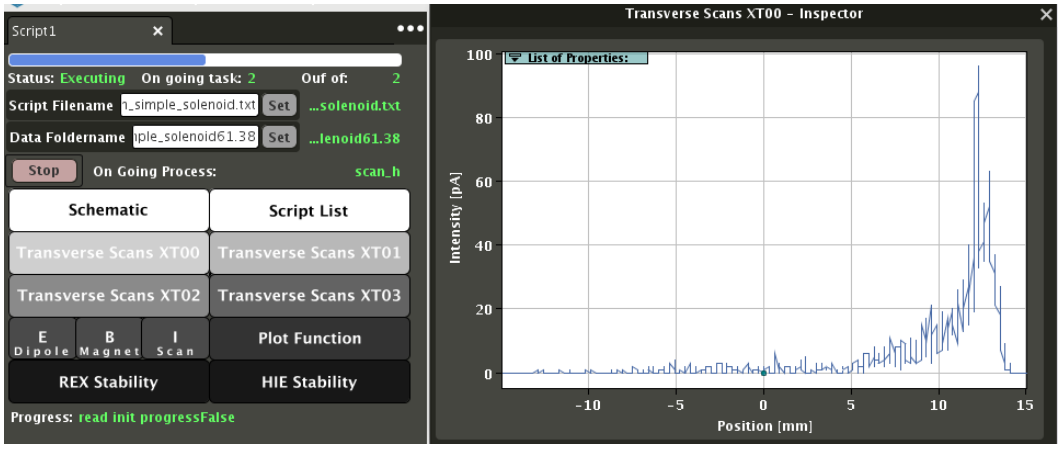

Figure 2.30. Front panel displaying an automated scripting to complete transverse beam profile scans. The right window shows the live result of each scan.

c Slow Extraction Application

The slow extraction application was developed with the purpose of providing an automated tool for setting a distribution voltage to the outer barrier of REXEBIS that allows a modulation of the pulse structure. The application was developed using National Instruments LabView software. The aim is to stretch the pulse length and reduce the instantaneous rate. This reduction benefits the mitigation of pile-up effects and logically increases the effective exploitable data provided by the experimental stations' detectors. The methodology and the results obtained are presented in the following chapter.

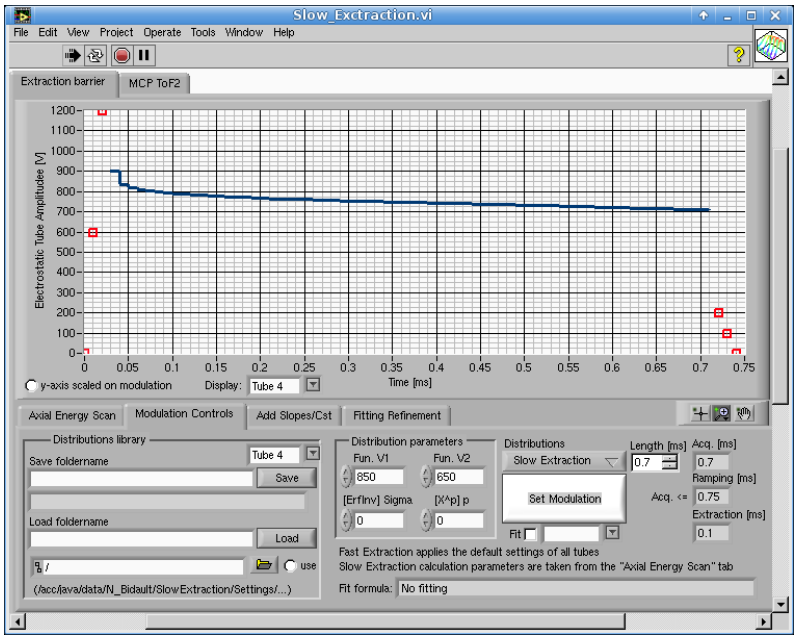

Figure 2.31. Front panel of the Slow Extraction application and example of a voltage distribution sent to the outer barrier function generator.

The architecture of the application is divided into three main parts. The first part allows to complete an axial energy scan of the beam extracted from REXEBIS; this can be accomplished by using either a Faraday cup or a silicon detector as a beam collector, both located after REX-ISOLDE A/q-seperator. The second part concerns the axial energy scan interpretation to deduce the voltage distribution to send to the function generator controlling the EBIS outer barrier hardware. The length of the pulse required is user input. It is possible to use a fitting with custom

functions to smooth the distribution and manually adjust the fitting parameters. A typical example of outer barrier voltage distribution is shown in Figure 2.31. Finally, the last part of the application controls a Micro-Channel Plate (MCP) and acquires the pulse structure. This solution for verifying the quality of the pulse structure was exploited during the first years of the commissioning of the Slow Extraction method. However, it was deemed more robust to use silicon detectors for measuring the pulse structure - for reasons explained in the following chapter.

CHAPTER 3

Intensity Scales and Modulation

Studies of radioactive ion beams lead us to be confronted with a wide range of intensities. In the scope of REX/HIE-ISOLDE post accelerator, the optimization of the beam intensity starts from REXTRAP and ends at the experimental station. The efficiency of all sub-systems and the transmission through the transport lines define the contour of the question of maximizing the luminosity of the beam. The methods for characterizing the performances of each sub-system need to be in adequation with the dynamical range of beam currents. The tune of an accelerating structure or the operating conditions of an EBIS is generally decided based on a vast set of performance indicators: output transverse and longitudinal emittance, output energy, purity of the beam and intensity. The questions of transverse and longitudinal beam emittances and beam purity are treated in the following chapters. In this chapter, we focus on the capability of measuring with reliability absolute beam intensities in the sub-femto Ampere range. A typical case study is presented concerning the measurement of the RFQ transmission using very low-intensity ion beams. The optimization and modulation of the pulse structure are then studied with the concept of Slow Extraction from REXEBIS. Finally, a new methodology is implemented to evaluate the temperature of ions inside the charge-breeder and evaluate critical figures of merit about the extracted beam.

3.1 Orders of Magnitude in Ion Beam Intensity

The range of sub-femto-Ampere intensity, typically less than 10^5 particles per second (pps), corresponds to very low yields of exotic isotopes produced in radioactive ion beam facilities. At ISOLDE, such production rate would represent about 50 % of the beam accelerated for high-energy experiments during the physics campaign. The maximum intensity at which the post-accelerator can be operated is a few nano-Ampere, which is limited by the REXTRAP Brillouin limit (Equation 2.2) and the charge capacity of the REXEBIS electron gun. In practice, the pilot beams used for the commissioning of the linac are in the pico-Ampere range. Those beams produced by residual gas ionization inside the charge-breeder are convenient for commissioning the accelerating structures and preparing reference setups of the linac depending on the mass-to-charge ratio (A/q). With beam currents above the pico-Ampere range, the signal-to-noise ratio output from Faraday cups is usually sufficient for accurately quantifying the intensity. However, the resolution of the Faraday cups (about 0.1 pA) does not allow us to measure the beam intensities of rare isotopes practically. When delivering RIB to the experimental stations, the performance of the linac is assessed blindly by relying on the reference setups. The shift in A/q between the RIB of interest and the reference setup of the linac imply to scale the power delivered by accelerating structures. This scaling often underlies discrepancies stemming from non-linearities in the behaviour of cavities as a function of the accelerating gradient. The reference setup never absolutely mirror the actual conditions of the accelerated RIB.

3.1.1 Intensity Attenuation

The first step to validate a method for measuring sub-fA currents is to attenuate the beam intensity in a controlled manner. By doing so, one may compare the current measured to the expectation. Controlling the beam attenuation must be done in a way that does not significantly affect the emittance of the beam; otherwise, the transmission through the transport lines is not comparable. We identified three

main ways.

Attenuation Grids

Several attenuation grids are available in a diagnostic box located between the A/q-separator and the first accelerating structure. Within the diagnostic box, a barrel hold eight pepperpot foils with different geometry that filters the beam with the following transmission factors: 0.001 %, 0.01 %, 0.1 %, 0.3 %, 1 %, 8 %, and 50 %. The advantage of using an attenuation grid before the RFQ is that the transverse phase space is mixed during acceleration. Nevertheless, because the beam spot is in the order of magnitude of 1 mm, the sampling of the transverse space using the 0.001 % and 0.01 % attenuation grids, do not ensure the preservation of the original emittance of the beam passing through it. We did not use those attenuation foils when the engaged studies required to preserve the transverse emittance of the beam. The six other attenuator grids offer a convenient way to cover the range between pico-Ampere and femto-Ampere.

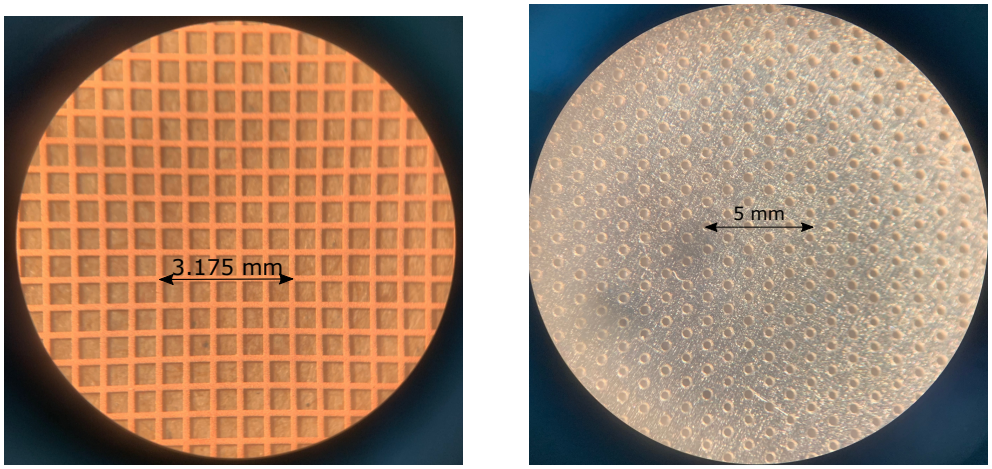

(a) Transparency 50 % **(b)** Transparency 8 %

Figure 3.1. Pictures of two attenuation foils manufactured by electrodeposition of pure copper (a) and by laser drilling on a stainless steel sheet (b). Note that the apparent non-parallelism is due to achromatic effect of the camera lens.

It is more accessible from a manufacturing point of view to produce a foil with low transmission than the contrary. Pepperpot-type of foils with holes are usually made using micro (mechanical) drilling or laser drilling, and the cost of fabrication is

proportional to the number of holes needed. By using electrodeposition metal forming processes, the high transmission foils can be manufactured at cost-effectiveness. Foils manufactured from electrodeposition (a) and laser drilling (b) are shown in Figure 3.1. The thickness of both foils is 100 μm.

Charge-Breeding Modulation

As was discussed in the previous chapter, the breeding time, i.e. the confinement time of ions inside REXEBIS, is one of the main parameters together with the with the electron beam current density to influence the charge state distribution. The breeding time is set to maximize the abundance of the desired charge state. Logically one may want to use the breeding time as a parameter for reducing the beam intensity. However, this solution is not recommended in the scope of the studies engaged hereafter, as the the time spent by ions inside the electron beam also defines the transverse emittance of the extracted beam. In fact, we observe in Chapter 5 that the emittance effectively varies with the breeding time. We preserve the conditions of charge breeding to ensure that no other effect is induced, such as emittance variations.

Ion Source Heating

An ion source is installed before REXTRAP to produce (stable) beams of 39-potassium or 133-caesium. The intensity of the beam extracted from the source is modulated at ease by controlling the heating power delivered to the oven. The power supply allows adjusting the intensity of singly charged ions with accuracy from 0.1 to 100 pA. The beam is then transported to REXTRAP for transverse cooling, and, to a certain extent, the influence of the ion source heating on the resulting beam emittance is minimized. Nevertheless, one needs to take into account the difference in the charge breeding conditions of REXEBIS when varying the intensity of the injected ion beam, more particularly the compensation of the electron beam. We consider that if the compensation of the electron beam remains low (below 1 %) the relative change in the emittance of the extracted beams is negligible. For this reason, we limit the beam extracted from the ion source to 50 pA.

Two setups of the post-accelerator are required for demonstrating the possibility to measure general beam properties of very low-intensity ion beams. Using the ion source located before REXTRAP is convenient for modulating the intensity from 50 pA to 1 pA without impacting the beam transport and charge breeding conditions. The beam intensity is then reduced to the sub-efA range by using attenuator foils at the entrance of the linac.

3.1.2 Sub-efA Intensity Monitoring

Two principal technologies were considered for monitoring beam currents in the sub-efA range. Micro-channel plates (MCPs) are installed after REXTRAP and REXEBIS and offer one possibility for such a measurement. The MCPs are of Chevron-type and accompanied with a P46 phosphor screen. Such device may allow for single-ion detection however careful calibration is required. The accelerating voltage between the MCP's front and back chevron is a source of uncertainty on the absolute value of the intensity signal. The response of the MCPs available at REX/HIE-ISOLDE also showed non-linear behavior as a function of the mass of the beam. It was deemed that the solution did not provide enough reliability for measuring absolute beam currents. The MCP installed after REXTRAP particularly

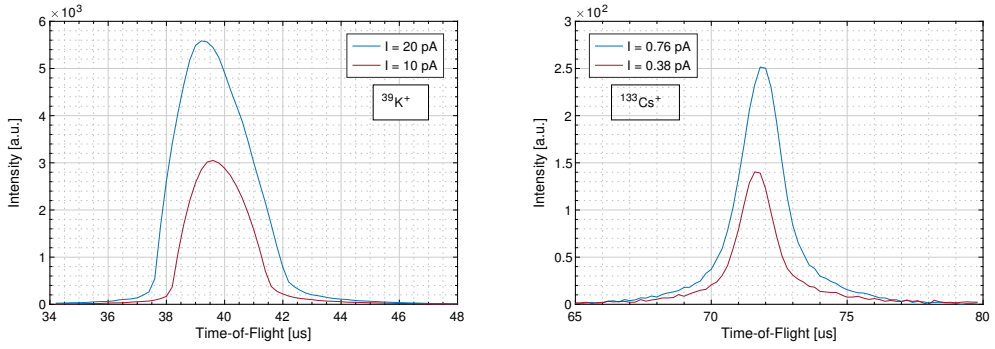

(a) $^{39}K^{+}$ **(b)** $^{133}Cs^{+}$

Figure 3.2. Time-of-Flight of a beam composed of $^{39}K^{+}$ and $^{133}Cs^{+}$ acquired using a MCP located after REXTRAP.

remains helpful for characterizing the relative purity of the beam. The beam produced by the ion source is a mixture of $^{133}Cs^{+}$ and $^{39}K^{+}$, and using the MCP in

time-of-flight mode allows measuring the proportion of each component. The time-of-flight acquisition from the MCP is shown in Figure 3.2 for two beam intensities. By integrating under the curves presented, one determines that the beam of 133-caesium, which is used for the studies of the REXEBIS performance in the next chapter, represents 3.8 % of the total yield from the ion source. We also verify that this production rate does not vary significantly with the power of the source.

The MCPs installed historically for characterizing low energy beams at REX-ISOLDE did not offer enough reliability, and silicon detectors were preferred to measure very low ion beam currents.

3.2 Case Study: REX-RFQ Transmission Efficiency Measurements

REX-RFQ is the first accelerating structure of the linac. An interesting case of study for proving the capability of measuring very low-intensity currents is to attempt at reproducing the transmission efficiency curves of this accelerating structure by using silicon detectors and regular beamline instrumentation (Faraday cups).

The RFQ gradient is an essential tune parameter, directly impacting the transmission efficiency throughout the whole linac. An electrode voltage pick-up serves for the acquisition and control of the gradient. The correlation between the pick-up and the gradient is linear. At the design electrode voltage for $A/q = 3.9$, i.e. 36.4 kV, the corresponding pick-up value is 2300 mV.

3.2.1 Transmission Measurements at Very Low-Intensity

For the purpose of solely characterizing the RFQ, all downstream accelerating structures are turned off. The energy of the beam entering the RFQ is 20 keV/u, and it is transported through the linac at 0.3 MeV/u. The beamline's electrostatic and magnetic optical elements (quadrupoles, steerers and solenoids) are kept at constant values deemed optimal for transport efficiency at the nominal RFQ gradient. The repetition rate (pulse per second) was 20 Hz during the measurements, with a charge-breeding time of 30 ms. A beam of $^{39}K^{10+}$ is used, with the possibility to modulate the intensity according to the techniques presented in the previous section.

We first present different transmission efficiency curves obtained using Faraday cups at the locations shown in Figure 3.3. During each measurement, the accelerating gradient of the structure is varied while acquiring the output beam current. The resulting transmission curves are normalized with the input beam current measured prior to injection into the RFQ ($I_{FC} = 50$ pA, at location XRFQ). Particles accelerated at a voltage below the design value of the RFQ are lost in the region between XIHS and XLN2 (Figure 3.4). When the RFQ is operated at an electrode voltage above its design value, the energy spread of the beam becomes non-optimum, and parts of the beam may be lost.

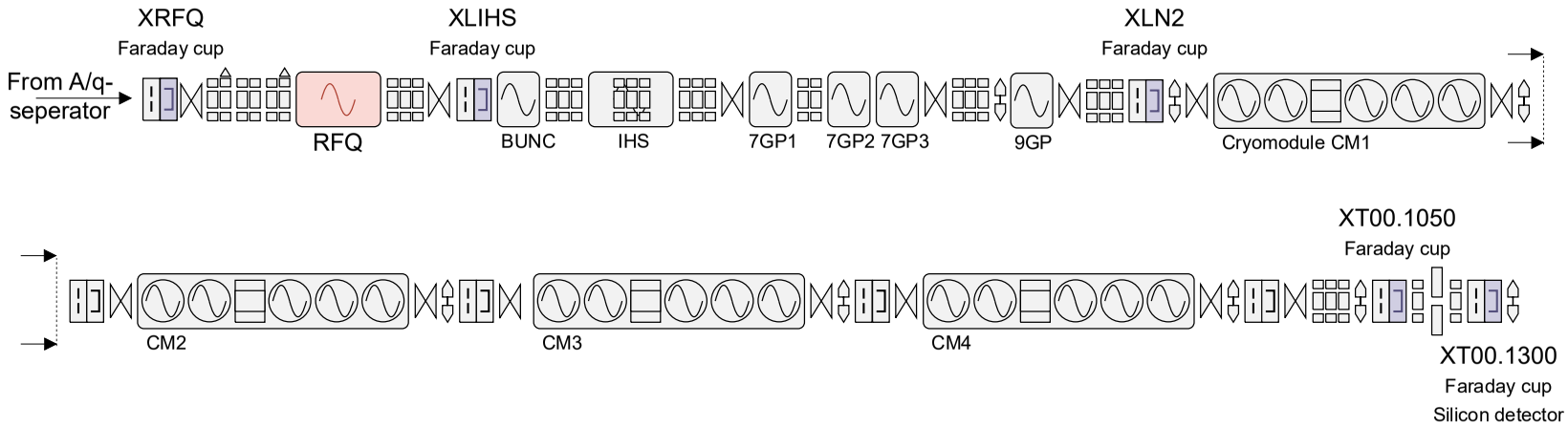

Figure 3.3. Schematic of REX/HIE-ISOLDE linac displaying the RFQ in color and the diagnostic boxes used for the RFQ transmission measurements.

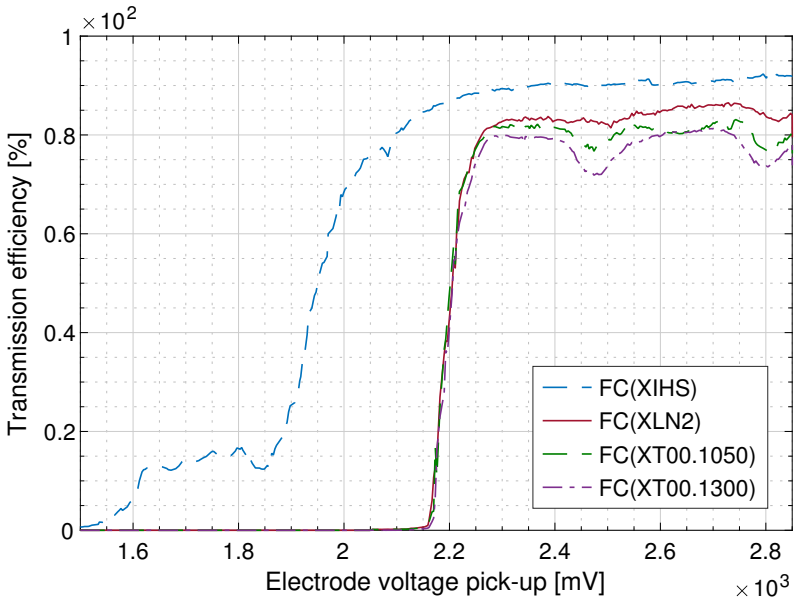

Figure 3.4. Transmission through the RFQ for $^{39}K^{10+}$ beam, measured in different locations with Faraday cups.

Measuring the transmission efficiency in the location XT00.1300 allows for comparison at an entirely different beam intensity scale with the large-aperture silicon detector located in this same diagnostic box. A silicon detector, operated in particle-counter mode, monitors the transmission through the RFQ, probed similarly as a function of its accelerating gradient. This time the input intensity of the $^{39}K^{10+}$ beam is limited to 800 ions/s, which corresponds to 1.2 fA, approximately 6.10^4 less than I_{FC}, the beam intensity when using Faraday cups. Several series of measurements corroborate the method's effectiveness, which consists of using the large-aperture silicon detector in XT00.1300 (Figure 3.5). Comparisons in between the two ways were reproduced for different transport tunes and beam-A/q. When the beam-A/q is changed to different charge states of $^{39}K^{q+}$ ($A/q = 3.55$ for q = 11 and $A/q = 4.33$ for q = 9), each method for probing the beam transmission yields consistent results.

Scaling linearly, the RFQ electrode voltage pick-up from one beam-A/q to another often yields a few per cent shift from the design gradient. When scaling the RFQ to a very low-intensity beam-A/q, one generally uses a more intense pilot beam close to the reference A/q. Traditionally, the RFQ optimal accelerating gradient was tuned for the pilot beam and blindly scaled to the very low-intensity beam-A/q. One is

now able to tune the RFQ accelerating gradient directly in the sub-fA range of beam intensity. The operational use of this method was later improved by installing a large-aperture silicon detector in the normal-conducting linac section. The new silicon detector, its preamplifier and digitizer are specifically calibrated for low-energy beams.

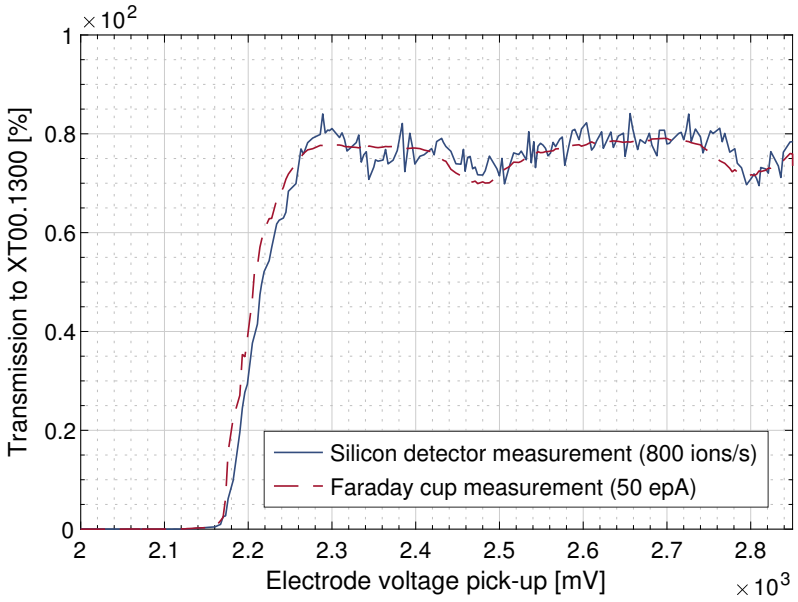

Figure 3.5. Transmission efficiency to XT00.1300 measurements for $^{39}K^{10+}$, using a Faraday cup and a silicon detector.

3.2.2 Longitudinal Acceptance

During the charge-breeding of ions inside the REXEBIS, various heating phenomena contribute to the increase of spread in ion energy density distribution. Highly-charged ions are more subject to heating and will show a larger energy spread than low-charged ions. Similarly the transverse emittance of the beam extracted from REXEBIS will grow as the temperature of the ions increases. It becomes necessary to characterize the RFQ in terms of longitudinal acceptance, for anticipating potential losses due to the large energy spread or transverse emittance of highly-charged ions.

The REXEBIS resides on a high-voltage platform that defines the input beam-energy into the RFQ. The optimal platform voltage for injection of $^{39}K^{10+}$ beam into the RFQ is $W_0 = 19300$ V. For the measurement of the longitudinal acceptance, the breeding-time is reduced to 20 ms to minimize the energy spread of the beam

while maintaining a detectable current using a Faraday cup. The relative input beam energy is then varied via the platform voltage. For each different input energy, the A/q-Separator was scaled to the new energy in order to maximize the transmission efficiency to the XIHS location. The main components from the A/q-Separator that were tuned are an electrostatic 90° cylinder deflector of 0.6 m radius and a 90° magnetic bender of 0.5 m radius. The current measured prior to the RFQ injection, at the location XRFQ, remained constant during the whole scan. An estimate of the uncertainty relative to the measurement of the longitudinal acceptance is given within 5% accuracy (Figure 3.6). The contributions to the error-bars were not evident to disentangle and essentially are: beam instabilities, instrumentation uncertainties and the A/q-Separator tune.

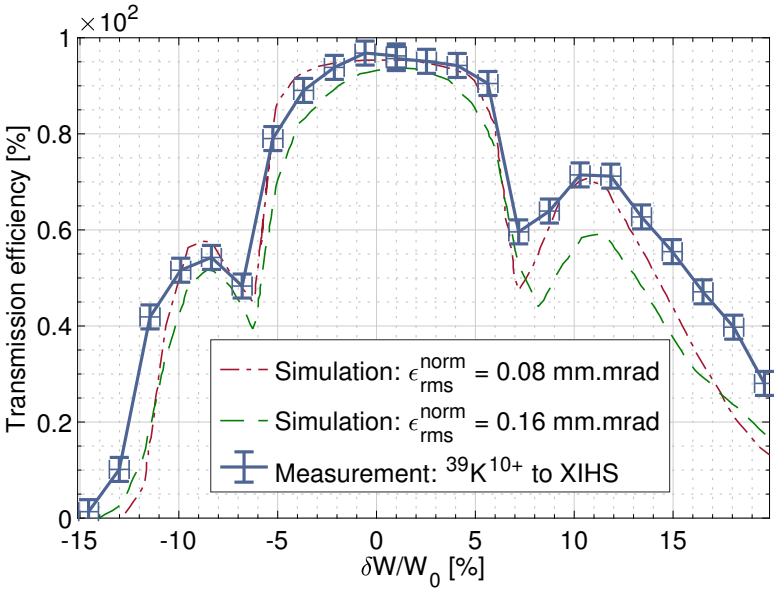

Figure 3.6. Measurement of the RFQ longitudinal acceptance and simulations for different transverse emittances [5].

Finally, the longitudinal acceptance result may be compared to beam dynamics simulations in order to estimate the input transverse emittance of the beam. Beam dynamics studies of the RFQ, using PARMTEQM, have shown the effect of the input transverse emittance on the resulting longitudinal acceptance [Fraser and Wenander, 2012]. In Figure 3.6, two of the beam dynamics simulation results are exploited. Both right and left lobe are present in the simulations and the measurement. The central region between the lobes is very similar for the measure-

ment and the simulation with an input normalized rms transverse emittance of 0.08 mm.mrad. A more adapted use of the PARMTEQM simulations will be described in a future contribution. The comparison between the displayed simulations and the experimental result here only serves as a demonstration of feasibility rather than a precise statement about the input transverse emittance.

3.3 Pulse Structure Optimization using Slow Extraction

The beam intensity measured by, for instance, a Faraday cup translates the accumulation of charge over a specific time delimited by the pulse length and multiplied by the pulse frequency. At constant beam current, stretching the pulse length implies lowering the instantaneous rate of charges. This action is beneficial to the detection capability of the experimental stations. Depending on the time-resolution of the detector, pile-up effects may be reduced, and the amount of time-resolved data increased. The concept of lengthening the pulse width of an EBIS beam is called Slow Extraction and has already been used extensively [Beebe et al., 1993] and theorized [Lapierre, 2017].

There was no existing formal procedure for applying a Slow Extraction of ions from REXEBIS. The typical extraction method, which consisted of quickly reducing the potential on the barrier trapping the ions, does not assure sufficient temporal event discrimination due to the high linear current density of ions within the brief extracted ion pulse. The ion pulse width deriving from an abrupt opening of the extraction barrier is less than 200 µs long and is essentially dependent on the trap length, on the ion mass, on the energy spread and on the slew rate of the extraction electrode (55 V/µs). Consequently, we decided to commission a method for Slow Extraction at REXEBIS and obtain an ion pulse length in the millisecond range. The pulse length of the radio-frequency systems of the REX-ISOLDE normal-conducting linear accelerator is constrained by a maximum duty cycle of 10% and by the average power limitation of the 9-gap IH resonator (2.5 kW). Typically, when operated at 50 Hz repetition rate, the RF pulse could be up to 2 ms long, and, ideally, the pulse width of the REXEBIS extracted ion beam should match this length.

3.3.1 Methodology

The principle of the Slow Extraction is to apply a voltage distribution to the outer barrier of REXEBIS that spread the extracted spill of ions. The power supply of the outer barrier is logically equipped with a function generator. The first step to

determine the extraction barrier voltage temporal function is to measure the axial energy distribution of the ion beam extracted from the REXEBIS and transported to the REX/HIE-ISOLDE linear accelerator. For this measurement, the extraction barrier is reduced and held for 2 ms at successively lower voltage thresholds during consecutive EBIS extraction cycles. After the 2 ms retarded extraction, the barrier is lowered to completely empty the EBIS ion trap in preparation for the next ion breeding cycle. During the first 2 ms, only the ions having an axial energy above the threshold barrier voltage are able to escape and to consecutively be captured by beam current monitor. The population of ions with an axial energy under the threshold voltage is discriminated by the detector. The splitting of the ion beam extracted from REXEBIS when commissioning the Slow Extraction is illustrated in Figure 3.7 with a threshold voltage at 720 V. By progressively lowering the threshold voltage from 1.2 kV to 0 kV, while acquiring with a Faraday cup the intensity of the first extracted pulse, one is able to reconstruct the axial energy distribution of the ions de facto transported through the accelerator. For very low intensity beam not measurable with a Faraday cup, the intensity is monitored using a Silicon detector as a particle counter.

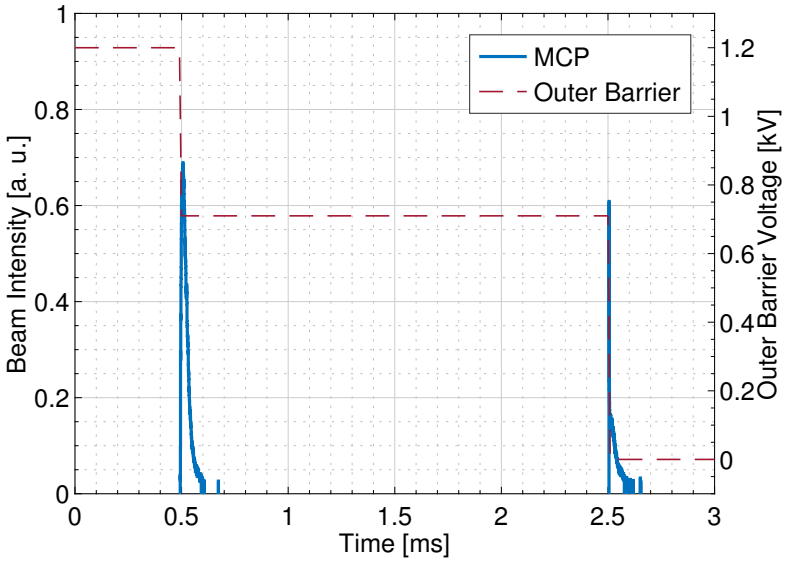

Figure 3.7. Measurement of the macro time structure of $^{39}K^{10+}$ using a MCP, when gating the extraction from the REXEBIS.

The use of the outer barrier for modulating the extracction from REXEBIS is

justified by the large energy acceptance of the A/q-seperator. Progressively raising the drift region over the barrier during the extraction lead to similar results, however was less convenient for REXEBIS because two distinct power supplies control the drift tubes. The EBIS outer barrier voltage is controlled by a function generator driving an amplifier, with a minimum time interval of $\Delta t = 10$ µs, therefore the discrete integral of the axial energy distribution $f(U)$ is set equal to a fraction of the total amount of ions per pulse. Considering the required length of the ion pulse T_p and the initial barrier voltage $V_{t_0} = 1.2$ kV, all successive V_{t_i} values of the step-function can be numerically deduced from:

$$\int_{V_{t_i}}^{V_{t_{i+1}}} f(U)\,\mathrm{d}U \quad = \quad \frac{\Delta t}{T_p}\int_{0}^{V_{t_0}} f(U)\,\mathrm{d}U \tag{3.1}$$

An example of the resulting pulse shape elongated to the maximum possible length of the RF pulses of 0.7 ms available in 2017, for ions with $^{140}Sm^{34+}$ is presented in Figiure 3.8. The time structure displayed, acquired with a Silicon detector and the MINIBALL spectrometer, is directly obtained from the application of Equation 3.1, without refinement nor smoothing of the barrier voltage function. The ripples at the beginning of the ion pulse distribution are a consequence of the voltage difference between the drift tubes and can be corrected for.

The MINIBALL spectrometer at the end of the first out of three HEBT lines can record the time-of-flight distribution of the incoming ions [Warr et al., 2013]. In addition, two other types of diagnostic along the REX/HIE-ISOLDE accelerating line are used to develop the Slow Extraction method at REXEBIS. A MCP installed following the A/q-separator offers a good approximation of the envelope of the time structure for ion pulses with intensities above 10 pA. In the case of a very low-intensity ion beam, five solid-state Silicon detectors provide digital counting of every ion event signal within a time resolution of 1 µs, allowing one to reconstruct a histogram of the extracted ion pulse.

3.3.2 Results

A preliminary requirement for making operational use of the Slow Extraction method is to assess the reliability of the time structure measurement. As explained in the previous section, the use of a silicon detector is the chosen solution over an MCP for very low-intensity beams. After applying the Slow Extraction procedure to a radioactive beam of $^{140}Sm^{34+}$ ($t_{1/2}$ = 14.82 min), the resulting beam pulse distribution is measured at the MINIBALL experiment, and using a large aperture silicon detector located in the HEBT line. Both results are consistent (Figure 3.8) and display similarly the features of the distribution, notably the ripples at the beginning. Those substantial variations could be suppressed by fine adjusting the drift tube electrode voltages; however, they help verify the detection capability. The beam intensity was reduced by approximately a factor thousand, using a lower ion source temperature and attenuation grids, in order to remain below the saturation limit of the silicon detector and its preamplifier.

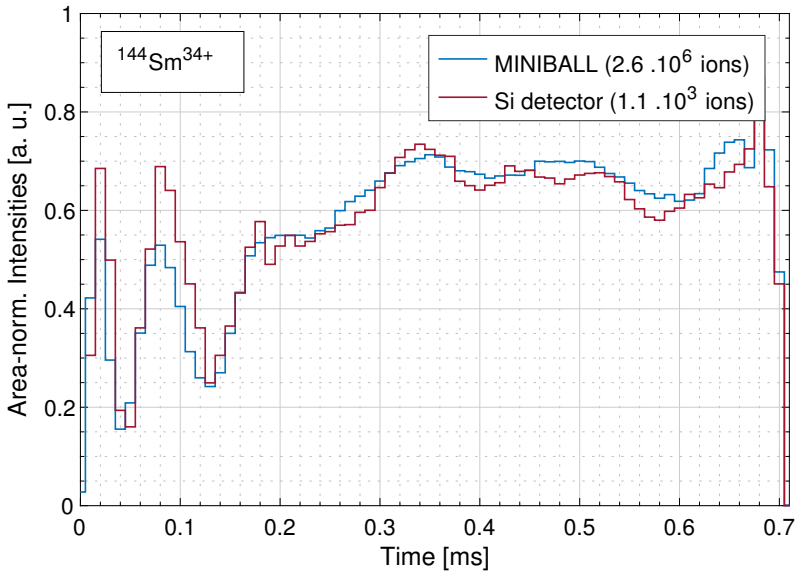

Figure 3.8. Time structure of $^{140}Sm^{34+}$ accelerated at 4.65 MeV/u, measured by a silicon detector and the MINIBALL detector. The integrated number of number of ions is shown in between parenthesis.

Since the commissioning of the new Slow Extraction method in 2016, time structure shaping from 0.7 ms to 5 ms has been achieved for more than a hundred different radioactive or stable ion beams, satisfying the A/q range requirement. The

possibility to adapt the ion pulse to any desired length has also been demonstrated and will be useful when longer RF pulse lengths are available. Figure 3.9 illustrates the scaling of the applied outer barrier distribution with time and the resulting stretching the pulse. This measurement was done with $^{132}Xe^{32+}$ with a beam intensity of 50 epA.

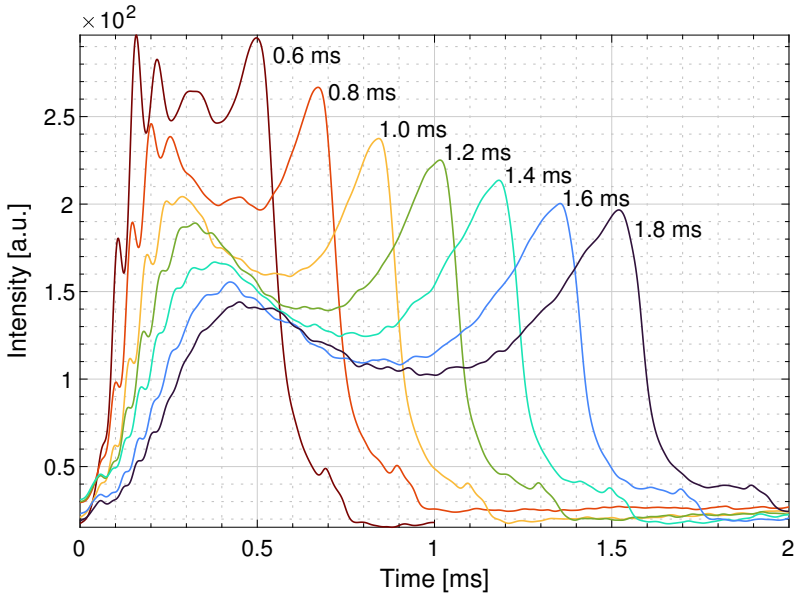

Figure 3.9. $^{132}Xe^{32+}$ time structures acquired with the MCP when extending the extraction voltage step-function from 0.6 ms to 1.8 ms (0.2 ms steps).

3.3.3 Observations

The time structure distribution extracted from REXEBIS when directly applying the inversion formula (Equation 3.1) from an initial axial energy scan is satisfactory in terms of uniformity. However, if the conditions of charge breeding somehow change, the axial energy distribution that initially serves as a base of the Slow Extraction is no longer representative, and the uniformity of the pulse may degrade. The first observation of such an impact on the pulse structure was made when the electron gun from REXEBIS was unstable during few months of operation. Rather abrupt variations of about 5 to 10 % of the electron beam current would appear approximately every hour due to a poor clamping of the cathode head. This created fluctuations of the extracted pulse structure during the physics campaign, implying to readjust the outer barrier voltage. In order to anticipate and preserve an optimal

Slow Extraction, the situation was reproduced by probing axial energy distributions as a function of a broader range of electron beam current. The reconstructed axial energy distributions of $^{39}K^{10+}$ shown in Figure 3.10 are obtained at a fixed breeding time but varying the electron beam current.

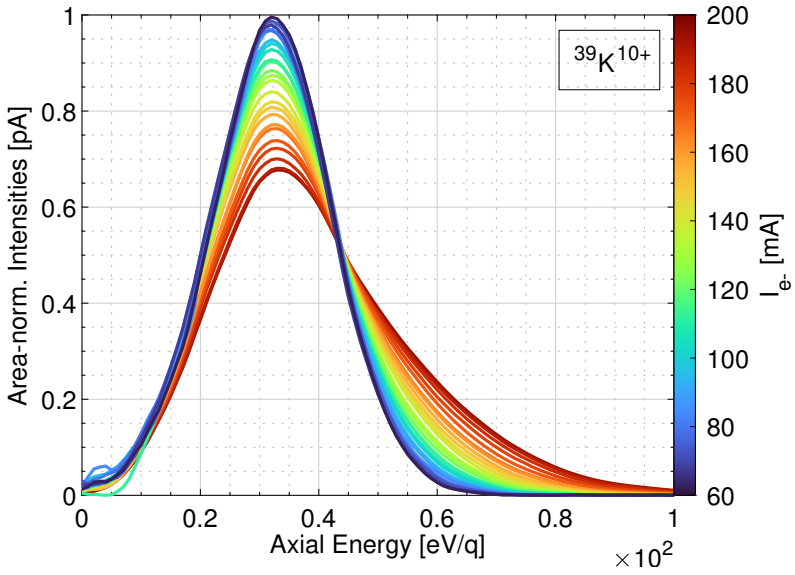

Figure 3.10. First observation of the effect of electron beam heating when varying the electron gun intensity and measuring the axial energy distribution of $^{39}K^{10+}$ beam.

The reconstructed axial energy distributions display a clear dependence on the electron beam current fairly resolved by the scans. This measurement opened us doors for exploring more in depth axial energy distributions and gaining insights at the ion temperature and remaining questions concerning the charge-breeding efficiency, such as the overlap factor with the electron beam.

3.4 Access to the Ion Temperature inside an EBIS

With the capability of scanning the axial energy of ions escaping from REXEBIS, one may infer their temperature and crucial indicators of the charge-breeding performance. By assuming that the probed ions are thermalized, and an important consequence is that they relaxed to a Boltzmann radial distribution, one direct application is to assess the overlap between the electron beam and the ion distribution. This frame of assumption allows to deduce the ions' radial distribution from a measurement of their temperature, and underlying properties such as the emittance. It is justified in Chapter 2 that the equivalent density of a 50 epA-xenon beam for the charge state $q_i = 30$, would typically be within the time frame of thermalization.

3.4.1 Methodology

We choose to evaluate the typical variations of the ion temperature for an average mass isotope as a function of the breeding time. This study aims at investigating the efficiency of the electron beam trapping of ions inside REXEBIS under typical operating conditions. A beam of $^{129}\mathrm{Xe}^{q_i+}$ is obtained from gas injection inside the EBIS and transported to a Faraday cup after the A/q-separator in order to perform the typical axial energy scan procedure that is described in the previous section.
At low ion temperature compared to the trapping potential well felt inside the electron beam ($q_i\Phi_0$), the axial energy distribution reassembles a Maxwell-Boltzmann (M-B) distribution with five degrees of freedom (Equation 2.48). The raw experimental result from a scan of the axial energy is actually a transformation of the M-B distribution. The acquired current as a function of the outer barrier potential U is given by the escape rate over this barrier. The measured distribution is fitted by the function f,

$$f(U) = I_0(1 - \gamma\left(\frac{q_iU - E_0}{k_BT_i}, \frac{5}{2}\right)) \tag{3.2}$$

with the lower Gamma incomplete function γ defined as,

$$\gamma(x, a) = \int_0^x t^{a-1}e^{-t}\mathrm{d}t \Big/ \int_0^\infty t^{a-1}e^{-t}\mathrm{d}t \tag{3.3}$$

The fitting parameters are the temperature of ions T_i, the shift in axial energy E_0 and the intensity I_0.

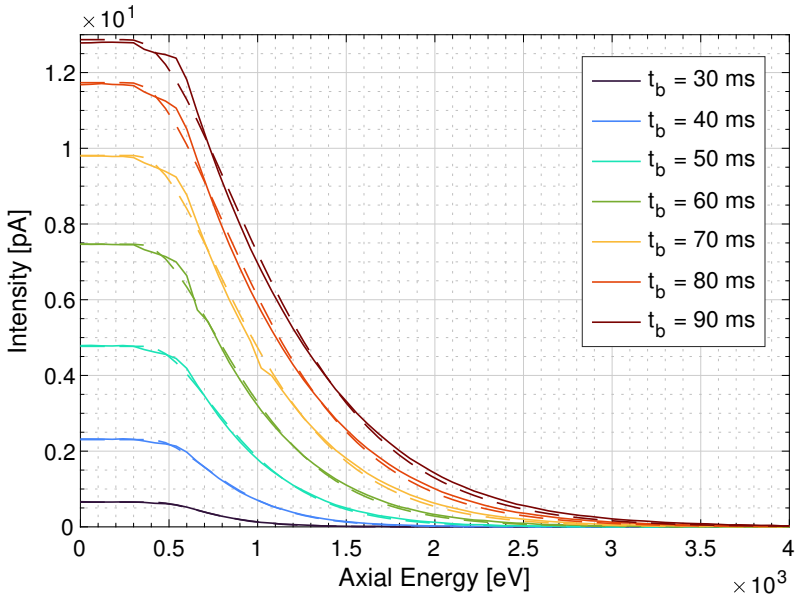

Figure 3.11. Axial energy scan results for $^{129}Xe^{30+}$ for different charge breeding time t_b, with REXEBIS Non-Adiabatic electron gun setup, with I_e =200 mA and E_e = 6.3 keV. The dashed lines are the corresponding fitting with a Maxwell-Boltzmann distribution (5 degrees of freedom)

The scans of the axial energy distribution for different values of the charge-breeding time t_b are shown in Figure 3.11. The optimal breeding time for $^{129}Xe^{30+}$ is measured to be 90 ms, so we probe fast-bred ions and inspect how the extended time spent in the electron beam results in an increase of the temperature.

3.4.2 Results

From the fitting results, of the function defined in Equation 3.2, the evolution of the temperature and axial energy shift can be plotted as a function the breeding time. This information can be compared with the heating rate derived by Landau and Spitzer (Equation 2.54). The temperature appears to be linearly increasing as a function of the time, by a coefficient of about 3.5 keV/s. By applying Landau-Spitzer formalism to the EBIS context (Equation 2.54), the calculated heating rate is 2.9 keV/s at $q_i = 30$ and using $j_e = 400$ A/cm^2. Knowing the temperature of ions is not enough to characterize the expansion of the cloud. One needs to add the

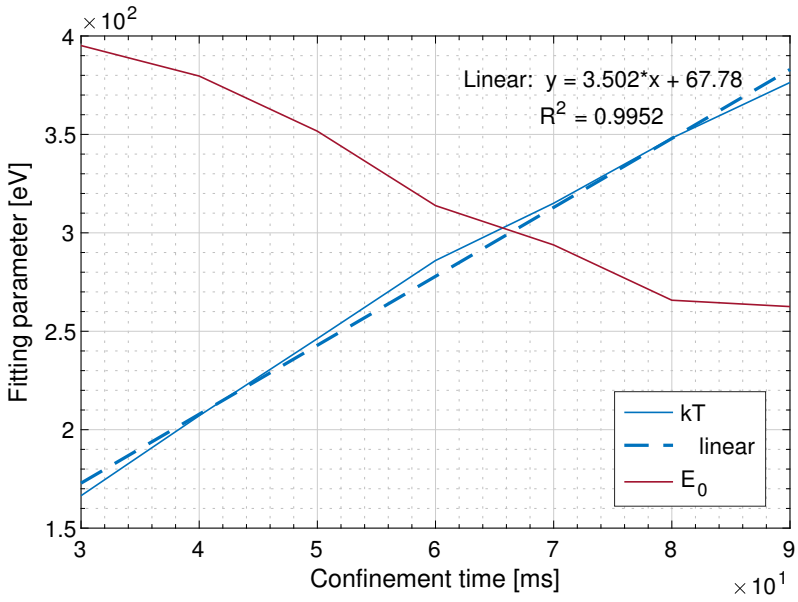

Figure 3.12. Fitting parameters E_0 [eV] and $k_B T_i$ [eV] plotted as a function of the breeding time from the axial energy scans of $^{129}Xe^{30+}$. The evolution of temperature is fitted with a linear function (blue dashed line).

contribution of the growing number of ion charges inside the electron beam and the space charge compensation it implies. The total current I_t extracted from REXEBIS (all ion charges) is integrated over a period T by a Faraday cup that is located before the dipole of the A/q-separator. The period T is the repetition period of the trapping cycles and is fixed, whereas the charge-breeding time varies to a maximum value delimited with this period. The degree of compensation of the electron beam is calculated using,

$$f_c = \frac{T I_t}{l_d I_e} \sqrt{\frac{2E_e}{m_e}} \tag{3.4}$$

The drift length l_d is given in Table 2.1 and the electron beam energy, with space charge correction, is estimated to be 6.4 keV when the cathode voltage is set at 6 kV. With an increasing breeding time, the compensation of the electron beam raises linearly, from 0.9 % at $t_b = 10$ ms, and up to 7.5 % for $t_b = 90$ ms. The Hermann radius, or the width of the Gaussian model for the electron beam radial distribution, does not vary significantly with the compensation factor (less than 0.1 % change). So, in Figure 3.13, we display only one fixed electron beam radial distribution (black dashed curve). Additionally, the change of the Boltzmann radial

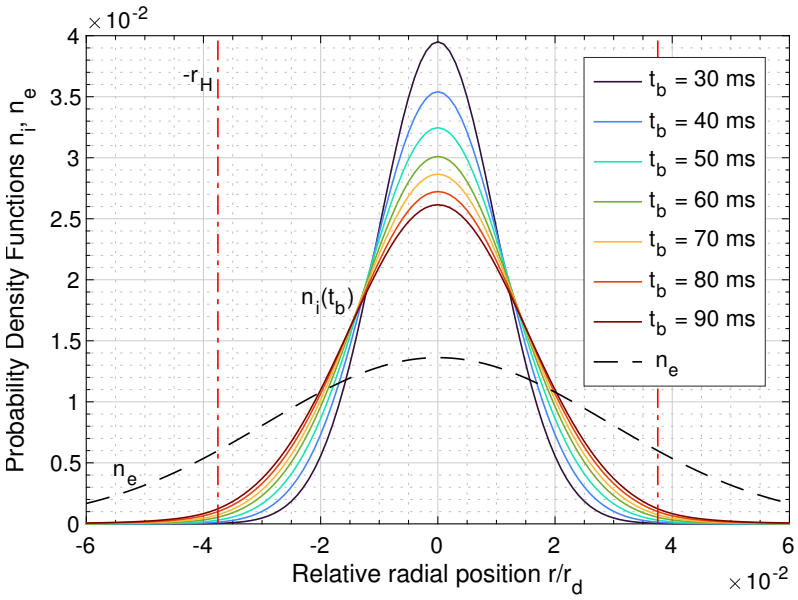

Figure 3.13. The Herrmann radius (red dashdotted vertical lines), the electron beam Gaussian density profile (black dashed line), and the evolution of the Boltzmann radial distributions of ions are shown when varying the breeding time t_b for $^{129}Xe^{30+}$.

distributions for a compensation of the electron beam between about 1 and 8 % is not significant. The sole effect of compensation, thus reshape of the electron and ion distributions, impacts the overlap factor between the electron beam and $^{129}Xe^{30+}$ by less than a 1%. Indeed, the characteristic radial trapping potential is $q_i\phi_0 \simeq 1150$ V in the uncompensated case, and 1080 V with $f_c = 7.5$ %. When we refer to Figure 2.10, which exhibits the influence of the ratio $k_BT_i/(q_i\phi_0)$ on the ion beam radius, one notices that with $^{129}Xe^{30+}$ at $T_i = 400$ eV, the ion distribution resides mainly within the electron beam and the effect of compensation logically remains low. The two ratios $k_BT_i/(q_i\phi_0)$ for the uncompensated case and 7.5 %-compensated case are respectively 0.35 and 0.38. Figure 3.14 shows that the overlap factor between the electron beam and $^{129}Xe^{30+}$ degrades from 95 % to about 88 %. This study illustrates a regime where the ions are still mainly confined in the electron beam.

3.4.3 Perspectives

The determination of the ion temperature from axial energy scans is a powerful tool to estimate the overlap factor but also the emittance of the beam. We foresee measuring the beam emittance extracted from REXEBIS for different regimes, notably different

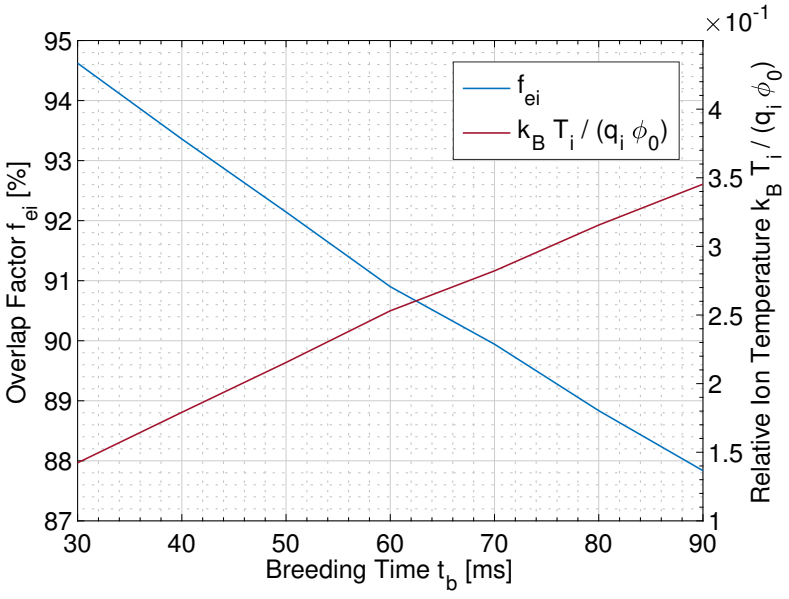

Figure 3.14. Evolution of the overlap factor and the ratio $k_B T_i/(q_i\phi_0)$ as a function of the breeding time t_b for $^{129}Xe^{30+}$.

ratios of $k_B T_i/(q_i\phi_0)$ and observe if the expectations from Boltzmann distributions are met. The studies of $^{129}Xe^{30+}$ reveal that the overlap factor is reduced by about 7 % when charge-breeding from 10 to 90 ms. One consequence is that the effective electron beam current for ionization is reduced. Estimating the electron beam current is a crucial task for characterizing the performance of the electron gun. In the following chapter, we make use of measured charge state distributions, and by drawing comparisons with simulations, we extrapolate the electron current density. We then expect that the effective current density decreases with time, following the reduction of the overlap with the ion distribution.

CHAPTER 4

Beam Purity Measurement and Optimization

The beam purity is an essential figure of merit for a RIB facility and its users, it will define in particular the feasibility for the detection of specific nuclear physics events. The selection of the charge state of an isotope to study is a compromise between meeting the linac specifications, minimizing the trapping time while preserving a sufficient charge breeding efficiency and providing the purest beam after A/q discrimination. Beam contamination comes from various origins (gas desorption, sputtering, discharges, etc.) and is, in a non-negligible range of A/q, barely detectable from the use of a Faraday cup. Additionally, the REXTRAP is operated with neon as a buffer gas to thermalize the accumulating ions and its presence is inevitable before the A/q-separator. We first determine the spectra of abundant residual ionized residual gas from REXEBIS. By analyzing the charge state distributions of charge-bred ions as a function of breeding time, we then extrapolate the effective current density of the electron gun. Another scale of contamination is then investigated, concerning residual gas of less than a pico-Ampere of intensity. A new methodology is developed for obtaining a large A/q mapping of rare contaminants. We additionally elaborate on an indirect technique that could potentially serve at estimating the purity of a beam from its α-decay reactions. Finally, the observation of dielectronic recombination is put in perspective with the idea of optimizing the purity of the beam.

4.1 Neutral Gas Ionisation

The A/q-separator serves at performing scans of the residual species ionized in the EBIS. This information is crucial because it will indicate which are the A/q regions free from contamination. During the commissioning of the EBIS, A/q-scans of abundant contaminant allow deducing the equivalent partial pressures and evaluate the quality of vacuum. Neutral gas ionization presents another advantage: it is simpler to model than the injection of singly-charged ions. By removing the uncertainty on the quality of injection of ions into the electron beam, one can deduce the current density of the electron beam from the analysis of the charge state distributions.

4.1.1 Methodology

Depending on the intensity, we use two different ways for performing A/q-scans of the beams extracted from REXEBIS. When investigating abundant contaminants, with currents above 100 efA, the dipole of the A/q-separator is used as a mass spectrometer. While scanning the magnetic field of the dipole field, the beam intensity is recorded by a Faraday cup after selection through a 3 mm-opening slit. One then applies the scaling rule shown in Equation 2.75, to retrieve the value of the A/q as a function of the measured magnetic field. The second method concerns very low-intensity beams. Because we choose to use a silicon detector, the beam is accelerated to RFQ energy before detection. The A/q-scan is then performed by varying the EBIS platform voltage to match the input energy of the RFQ. A scaling is simultaneously applied to the RFQ electric gradient and to all the beam optics elements.

Figure 4.1, shows the main elements used during the two types of A/q-scans. The Faraday cup in DB.0 serves to measure the total ion current extracted from REXEBIS and indicate the compensation of the electron beam. Abundant contaminants are recorded using a Faraday cup placed in DB.2, the same diagnostic box in which the separation slit is inserted. For the measurement of very low-intensity contaminants, the silicon detector used belongs to DB.3 and attenuation foils can be inserted in

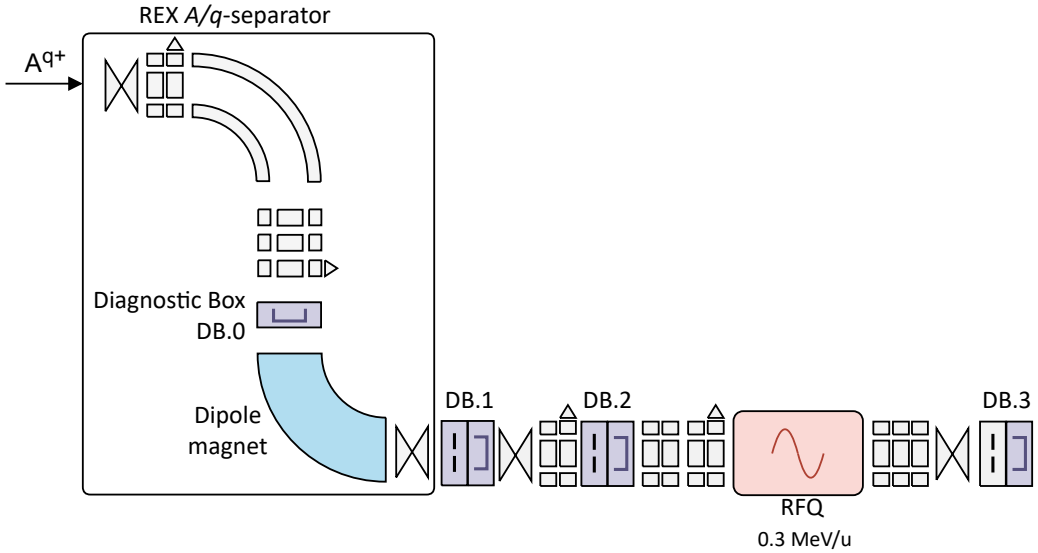

Figure 4.1. Schematic of the A/q-spectra measurement from REXEBIS. Four diagnostic boxes are utilized, three of them containing Faraday cups and DB.3 containing a silicon detector. Horizontal slits are inserted either in DB.1 or in DB.2.

DB.2 to avoid saturation. In order to fully characterize the continuum of residual gas ions, one needs to measure its variations in the range of trapping times that are used during the experimental runs. The knowledge of A/q-spectra on a wide range of trapping times allows anticipating completely the attainable beam purity of a similarly wide variety of isotope masses of interest. The repetition period was fixed at 50 ms during the scans and not optimized to each breeding time. It is possible to retrieve the maximum intensity achievable at each breeding time, using a form of normalization by the ratio between the breeding time and the repetition period. The spectrum are presented as they were acquired, i.e. without normalization, so the intensity of residual gas ions is monotonously increasing with the breeding time.

4.1.2 Spectra of Abundant Contaminants

The partial pressures of contaminants may vary during long-term operation depending on progressive desorption and outgassing from materials. They are investigated carefully during the commissioning an EBIS after venting in order to evaluate the quality of vacuum reached. The first series of spectra shown in Figure 4.2 are obtained by varying the breeding time from 10 to 40 ms. The main species coming from the outgassing of metal surfaces are identified. When injecting beam into

the EBIS and measuring the produced charge state distribution, we remove the background contribution from residual gas ionization by using those scans.

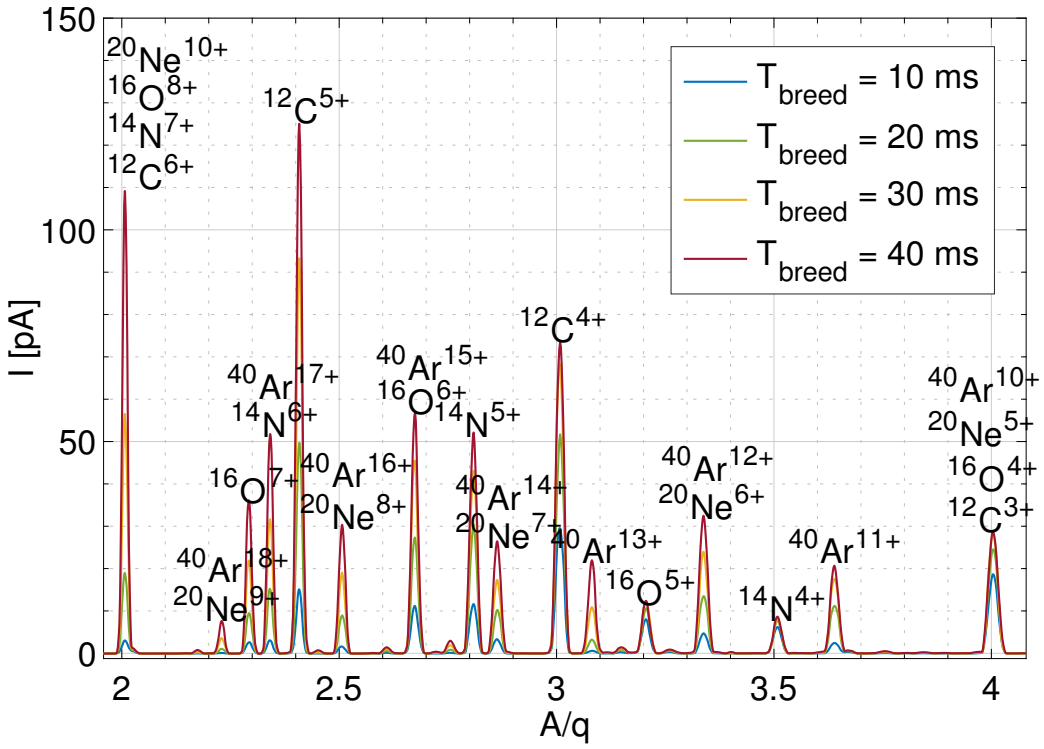

Figure 4.2. A/q-spectra for different trapping times. The electron beam current is I_e = 200 mA and the cathode potential at U_c = 6 kV. The following isotopes are not labelled: ^{13}C (abundance 1.07 %), ^{15}N (0.36 %), ^{17}O (0.04 %), ^{18}O (0.21 %), ^{21}Ne (0.27 %), ^{22}Ne (9.25 %), ^{36}Ar (0.33 %), ^{38}Ar (0.06 %) and $^{40}Ar^{19+}$ (< epA)

The partial pressure of the most abundant species can be deduced from A/q-scans and the help of simulations. We use the code EBISIM, which is introduced in Chapter 2, to disentangle the overlap between species and estimate each independent charge state distribution. One can then calculate the total number of ions extracted for each species. For instance, all measured intensities of the $^{20}Ne^{Q+}$ charge states are superimposed with $^{40}Ar^{2Q+}$, so the EBISIM code the deduction of the full charge state distribution using a fitting on the available clean (non-superimposed) data points. At least three relevant clean charge states are available for each residual gas species. The simulations are performed using the analytical rate equations presented in Chapter 2 (Equation 2.50) without charge exchange and ion escape at low charge states and considering that the electron beam energy is far from the dielectronic recombination resonance of the residual gas ions.

During the charge-breeding, the electron beam is constantly fed by H_2. N_2, O_2, Ar, CO, CO_2 and Ne; to quote only species with more than 10^{-3} % abundance in the gas desorption. The presence of He is measured negligible mainly because the vacuum vessel for the REXEBIS superconducting solenoid is separated. Additionally, ionized H_2 was not observed as the molecule must break within a time frame shorter than millisecond range. As a result of the feeding rate depending on the partial pressures of residual gases, the total number of ions, $\sum_Q N_Q$, linearly increases during the charge-breeding. For simplification, the quoted partial pressures are given artificially in terms of atomic partial pressures and not molecular pressures. By using the measured A/q-spectra for different breeding time, coupled with the EBISIM code to deduce the entire charge state distributions, we estimate the rate R_0 which is equal to the derivative of $\sum_Q N_Q$ as a function of time. The linear fittings used for deducing the rates R_0 are generally very satisfactory for species with a fully clean charge state distribution or semi-empirical measurements, providing a coefficient of determination of one close to 10^{-3}. The atomic partial pressures are then derived assuming the law of perfect gas, as shown with Equation 4.1.

$$R_0 = \frac{d}{dt}\left(\sum_Q N_Q\right) = p_0 \frac{I_e}{e} \frac{l_d}{k_B T_0} \sigma_0^{\mathrm{EI}}. \tag{4.1}$$

The atomic partial pressure of each species, noted p_0 are calculated from the measured rates R_0, the drift length l_d of the EBIS (0.8 m), the electron beam current I_e and the ion temperature T_0 assumed to be 300 K. Finally, the number of particles inside the electron beam $N_0(r \leq r_H)$ are calculated using the Herrmann radius presented in Table 2.3 (IrCe cathode) for an electron beam current $I_e = 200$ mA. It appears that for the set of charge state distributions fitted with the EBISIM code, the suited electron current density input for matching the simulations with the experimental results is found to be $j_{\mathrm{eff}} = 180\,\mathrm{A/cm^2}$, which is in perfect accordance with the Herrmann prediction.

Figure 4.3 is a zoom with log-scale of the A/q-spectrum shown for 20 ms breeding time in Figure 4.2. We identify the less abundant isotopes also naturally present. The resolution of the Faraday cup limits us to peaks with currents above 0.1 epA,

Table 4.1. The atomic partial pressures and number of particles inside the volume enclosed by the Hermrmann radius and drift lenth, for each of the main residual gas species ionized in REXEBIS.

Element	$N_0(r \leq r_H)$	p_0 [mbar]
Hydrogen	8.4×10^4	3.9×10^{-11}
Carbon	6.2×10^3	2.9×10^{-12}
Nitrogen	1.1×10^4	5.2×10^{-12}
Oxygen	1.9×10^3	8.7×10^{-13}
Neon	4.1×10^4	1.9×10^{-11}
Argon	2.5×10^3	1.2×10^{-12}
Total	1.5×10^5	6.8×10^{-11}

and clearly, already at this level, the identification is difficult. This is one of the motivations for developing a dedicated technique for probing very low-intensity contaminants.

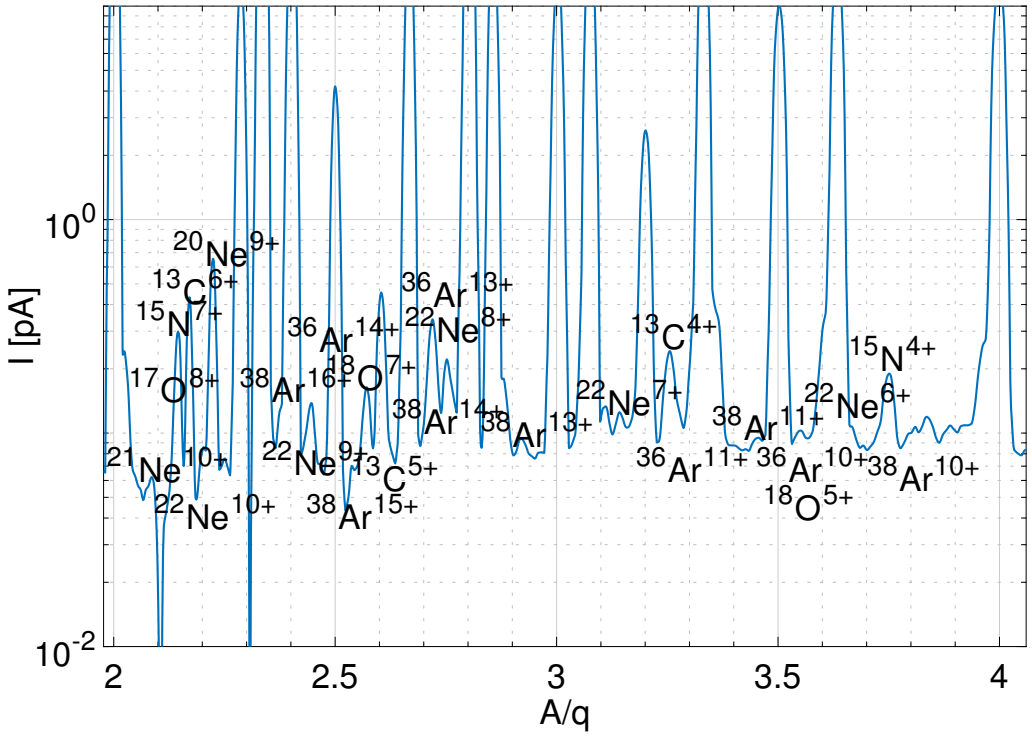

Figure 4.3. Zoom on low intensities of the A/q-spectrum shown in Figure4.2 for a breeding time of 20 ms. Species with intensity below 1 epA are identified.

4.1.3 Electron Beam Current Density Estimation

The measured charge state distributions of an ionized gas inside the EBIS are compared with the theoretical rates (Equation 2.50) using the EBISIM code. The specific module of EBISIM used in this section is called "basic simulation" [Pahl, 2021]. We assume that the electron beam energy is fixed (about 6.3 keV) and known by estimating the space-charge potential inside the electron beam at each specific investigated breeding time. The electron beam current density is used as a variable to fit the simulation to the measurement. We use a least-squares type of minimization algorithm between the relative abundances of measured and simulated charge state distributions. The *effective* current density estimation, noted j_{eff}, is then derived to help evaluating the performance of the electron gun.

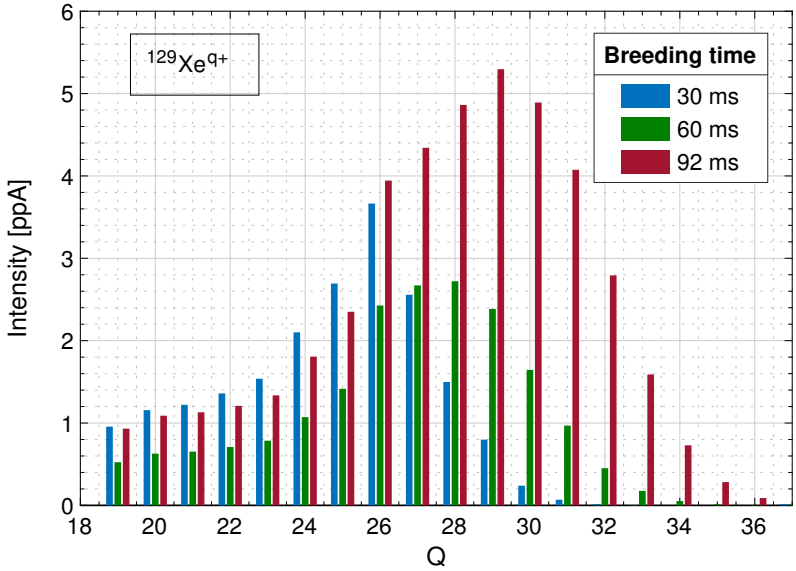

Figure 4.4. Charge state distributions of $^{129}Xe^{q+}$ from neutral gas injection, for three different breeding times, measured using a Faraday cup after the A/q-Separator.

We choose to inject neutral xenon gas into REXEBIS as a tool for evaluating the performance of the electron gun. The charge state distributions of $^{129}Xe^{q+}$ were recorded for seven different breeding times using the A/q-scan method previously presented for the abundant contaminant. Three of the resulting charge state distributions are presented in Figure 4.4. The measured intensities are divided by the corresponding charge state to be homogeneous to particle-pA. If a charge state of Xe^{q+} is contaminated with another ionized residual gas, we suppress this

contribution using the A/q-scans measured without xenon injection.

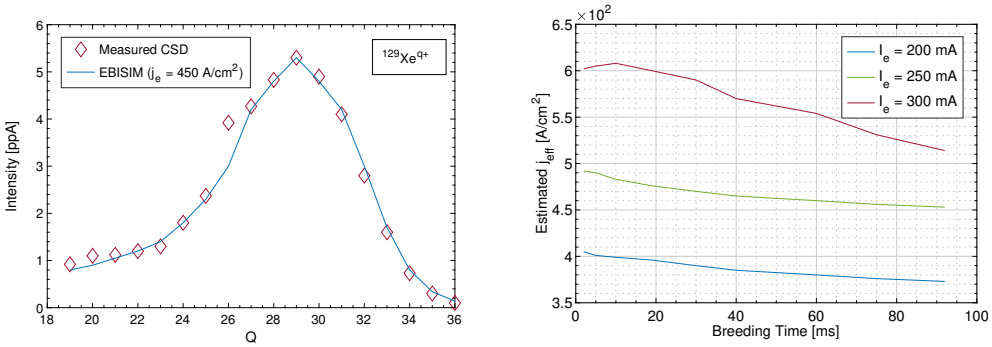

(a) Fitting at fixed breeding time. **(b)** Estimation of j_{eff}.

Figure 4.5. Fitting of a measured charge state distribution for $^{129}\text{Xe}^{q+}$ with EBISIM at a fixed breeding time (a). Results of the estimated current densities j_{eff} for the charge state distributions obtained with different electron beam currents.

The use of a fitting between the measured charge state distributions and the simulated model is subject to several biases. We decide to give the most abundant charge states more weight in the least-squares method at each breeding time. A typical fitting result is presented in Figure 4.5 (a), in which the charge states around 29+ are more weighted. The resulting effective electron beam current density estimates are displayed in 4.5 (b). The measurements were repeated for three different electron beam currents: 200, 250 and 300 mA. The uncertainties related to such estimations are broad (above 10 %) and certainly dominated by those of the ionization cross-sections. Between the case $I_e = 200$ mA and $I_e = 250$ mA, the current densities are in average increased by 21 %. Between $I_e = 250$ mA and $I_e = 300$ mA, they are increased in average by 22 %. It means that the effective radius of the electron beam slightly increases by about 1 % for each step of 50 mA, between 200 to 300 mA, which is coherent with the expected raise in the Herrmann radius. The three curves presented (Figure 4.5 (b)) are not constant as a function of breeding time, and all show a decrease of the effective current density estimate. This trend may be explained by the progressive heating of Xe ions inside the electron beam. The axial energy measurements detailed in the previous chapter reveal that when using a 200 mA electron beam, the overlap factor between the Xe^{30+} ions and the electron beam is reduced by 7 %, over a trapping time from 10 to 90 ms. From

the estimation of the effective current density in this similar case ($I_e = 200$ mA), it appears to decrease by 8 % between 10 and 90 ms. Of course the overlap factors of the neighboring charge state around 30+ are not exactly similar, but trends followed by this overlap factor and the effective current density correlate well, despite using two completely different experimental methodologies.

4.1.4 Spectra of weak contaminants

The absence of visible peaks in the A/q-spectra measured with a Faraday cup provides the first hint at a reasonable beam purity but does not necessarily guarantee a pure injected beam. An identification technique is detailed in this section which benefits from the particle detection efficiency of one of the silicon detector located after the RFQ (DB.3 in Figure 4.1). Moreover, one needs to demonstrate that the transmission from the A/q-separator to the silicon detector is conserved. For the proof of concept, mass scans were first measured with Faraday cups directly after the RFQ, at the position of the silicon detector. We chose two reference points for scaling the low energy part of REX/HIE-ISOLDE and the RFQ at $A/q = 4$ and $A/q = 4.4$. This implies that the REXEBIS high tension, the RFQ electric gradient and optics were optimized at those two A/q's to maximize the transport efficiency from the exit of the A/q-separator to the silicon detector position. Then, all the necessary scaling factors are interpolated from those two reference points. In particular, the scaling of the REXEBIS platform potential had to be adjusted to include the drift zone potential minus the electron beam space charge (assumed constant in the whole A/q range). The transmission efficiency at $A/q = 4$ and $A/q = 4.4$ from the A/q-separator (DB.2) to the exit of the RFQ (DB.3) is 96 %. Once the A/q-spectrum collected after acceleration and transport to DB.3 were deemed to be enough in accordance with the spectra obtained before the RFQ (in DB.2), a mass-scan over a range of A/q from 4.05 to 4.36 - indistinctly resolved by a Faraday cup - is acquired using a silicon detector (Figure 4.6). The beam intensity is deliberately reduced by inserting a 5 %-transmission foil so that the detector is operated below its saturation limit. As the size of the silicon detector used for this measurement was larger than the beam size, we have access to representative beam intensities. Another attractive

aspect of using a silicon detector is to record in the meantime the total energy of the incoming ions. This information allows identifying the species. For instance, we identify the presence of Kr isotopes that a Faraday cup measurement did not reveal. The Slow Extraction is applied to REXEBIS over a 1 ms long pulse to decrease the instantaneous rate and to avoid pile-up effects on the detector.

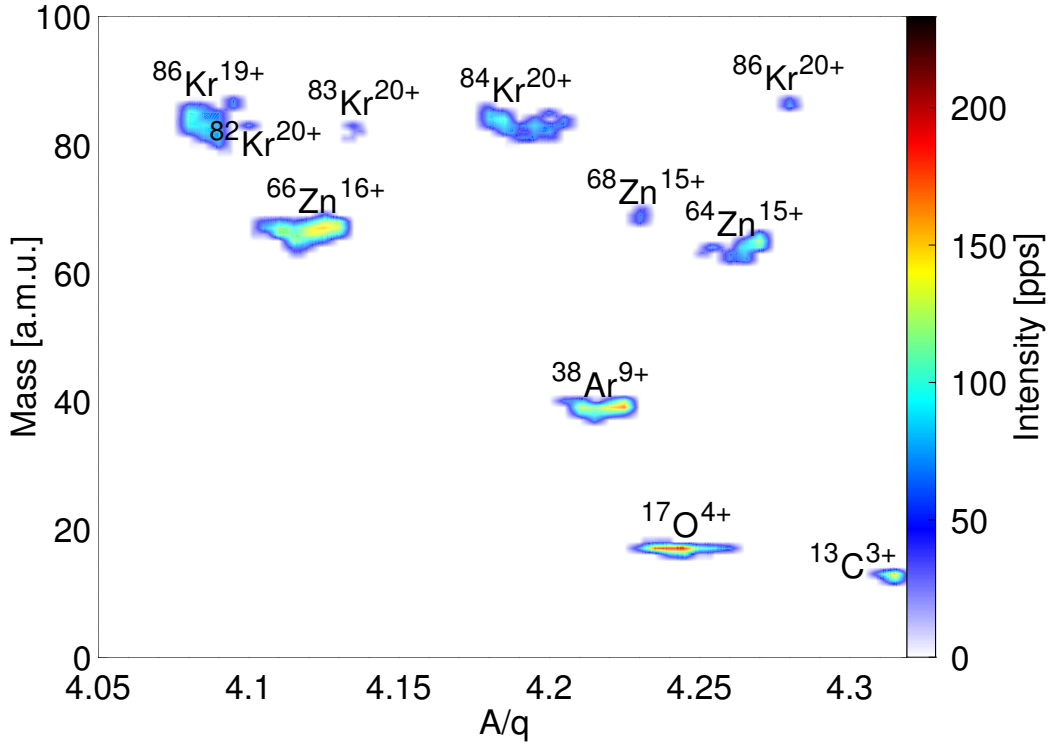

Figure 4.6. A/q-spectrum of the residual gas ionized in REXEBIS measured using a silicon detector. The relative intensities are shown as before attenuation through the foil, so as extracted from the EBIS.

4.1.5 Investigation on the Contamination from the Cathode Material

The characterization of the very low-intensity ionized residual gas from REXEBIS is useful for evaluating the purity of the future beams but also investigating the possible degradation of the cathode material. The heating power delivered to the cathode is high, varying between 24 and 27 W, for emission of 200 to 300 mA current. Residuals of iridium or cerium could be found in the EBIS and polluting

a large array of A/q's considering their high masses. We apply the methodology explained in the previous section to quantify the amount of iridium and cerium in the extracted beam. There are four stable isotopes of cerium and two of iridium. The most abundant isotope of cerium is ^{144}Ce (88.5 %), meanwhile both ^{191}Ir (37.3 %) and ^{193}Ir (62.7 %) could be expected. In order to meet the A/q-acceptance of the linac, the accessible charge states of those species start from 43+ for iridium and 32+ for cerium. We choose to investigate three neighboring charge states for each of the most abundant isotopes in order to confirm the identification of those two species. For reflecting the operational conditions of such beam, we use a relatively high electron beam current of 300 mA and a breeding time of 200 ms. The energy resolving power of the detector is poor for high masses; for instance, the peak at A = 193 a.m.u spreads over 10 units of mass. However, the confirmation of the presence of the same peak for neighboring charge states allowed the identification. Three examples of energy histograms obtained from the silicon detector are shown with Figures 4.7. One notices that the relative intensities of iridium and cerium are weak compared to other residual gas ions. Hence, the cathode surface degradation does not affect the purity of the beam extracted from REXEBIS more than any other contamination source.

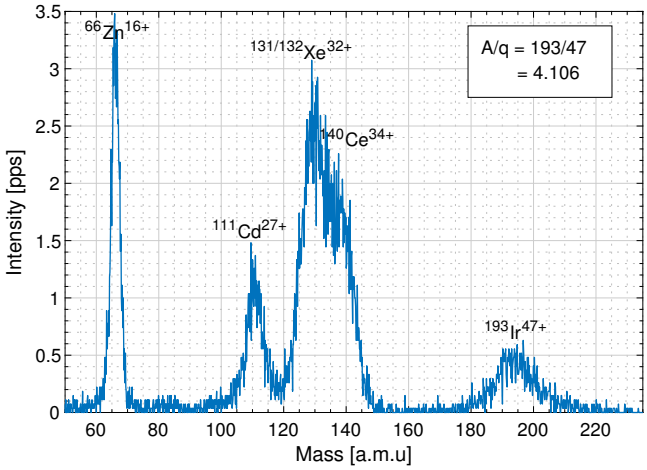

(a) Presence of $^{193}Ir^{47+}$ and $^{140}Ce^{34+}$.

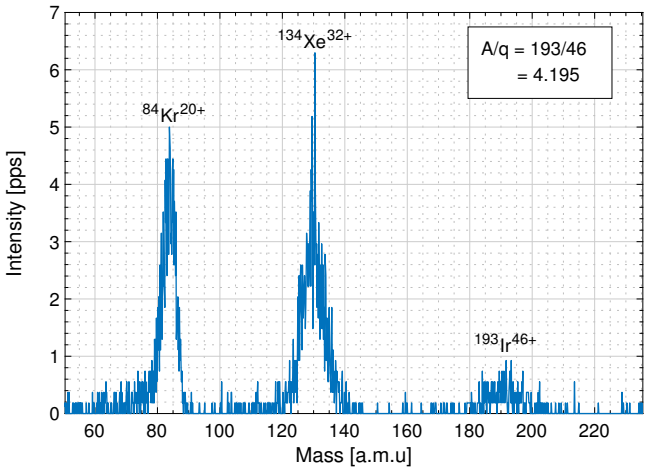

(b) Presence of $^{193}Ir^{46+}$.

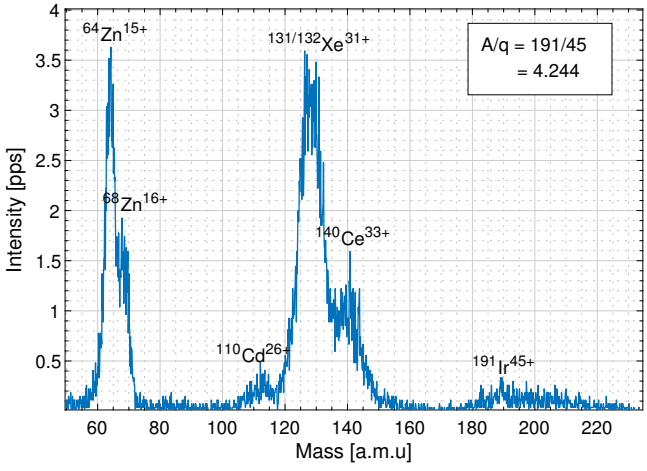

(c) Presence of $^{191}Ir^{45+}$ and $^{140}Ce^{33+}$

Figure 4.7. Investigation on the presence of cerium or iridium in the extracted beam coming from REXEBIS. The electron beam current used was $I_e = 300$ mA, for a breeding time of 200 ms.

4.2 Indirect Methods for Selectivity

In this last section, we evaluate the remaining, less direct, methods that were considered during the course of this thesis for either measuring the purity of very low-intensity beams or optimizing it. Those methods are only potentially useful in particular situations. We demonstrate the efficiency reached by those methods using typical REXEBIS conditions of operations.

4.2.1 Use of Dielectronic Recombination

The cross-sections of dielectronic recombination are generally lower than ones of electron-impact ionization; however, it can exceed the radiative recombination process. Dielectronic recombination is a resonant process, so one charge state is promoted on another by tuning the electron beam energy to the cross-section maxima. We investigate the case of 39K for which the most effective process, the KLL recombination, can be observed at an electron beam energy of about 2.5 keV. The dielectronic recombination cross-section for $^{39}K^{17+}$ peaks at 10^{-20} mm^2, whereas the radiative recombination cross-section is 10^{-22} mm^2. We indeed observe the variations of the relative abundances of the charge states 13 to 17+ of potassium when varying the electron beam energy around the energies of resonance. In Figure 4.8 the measurements of the relative abundances are compared with simulations provided by the EBISIM code. The fitting parameters are the electron beam effective energy (including the space charge potential) and the energy spread. Reciprocally, the measurement of the resonant energies can also serve as a tool for deducing the space charge potential of the electron beam. The electron beam current was decreased to 50 mA so that the energy spread is minimized. The reduction of the energy spread raises the amplitude of the resonance. Consequently, the breeding time is increased to 1 s in order to reach the charge state up to $^{39}K^{17+}$. In practice, this method is difficult to apply because the electron beam energies needed for the KLL resonances are not easily accessible by the electron gun for arbitrary isotopes. With potassium, we show that at the electron beam energy of 2570 eV the charge, for instance, 15+ is enhanced.

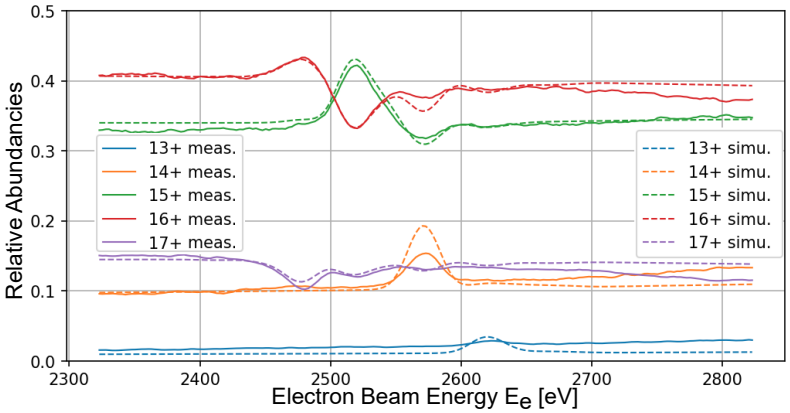

Figure 4.8. Dielectronic recombination measurement and comparison with EBISIM code. The measurements were done using $^{39}K^{q+}$ beam confined during $t_b = 1$ s, with an electron beam of $I_e = 50$ mA and while varying the electron beam energy E_e.

4.2.2 Selective Extraction from REXEBIS

During the investigation surrounding the topic of Slow Extraction, several observations led to the investigation of the potential use of this extraction scheme to separate the different components of a beam. At a specific A/q, if a beam is composed of species with significantly different charge states, their temperatures may differ, and one might consider separating those species at extraction. The concept was tested with a mixed beam of $^{133}Cs^{30+}$ produced from an ion source located before REXTRAP, and $^{40}Ar^{9+}$ naturally present as a residual gas inside REXEBIS. The electron gun is operated at $I_e = 200$ mA with a breeding time of 40 ms, optimal for $^{133}Cs^{30+}$. This test aimed at reproducing the case of a mid-mass beam of interest polluted by residual gas from the EBIS. After applying the Slow Extraction method, one observes that the species are extracted, on average, at different times. However, the method is not conclusive in terms of fully separating the beam of interest from contamination.

A silicon detector is used after the RFQ to probe the pulse structure of the resulting beam. Using the capability to record the energy of impinging particles, one can discriminate the contributions from caesium or argon. Even though there is a clear indication that argon resides at a lower trapping potential than caesium, this difference does not allow the separation of those two species with reasonable purity. Further investigations are planned with an injected beam of higher mass than

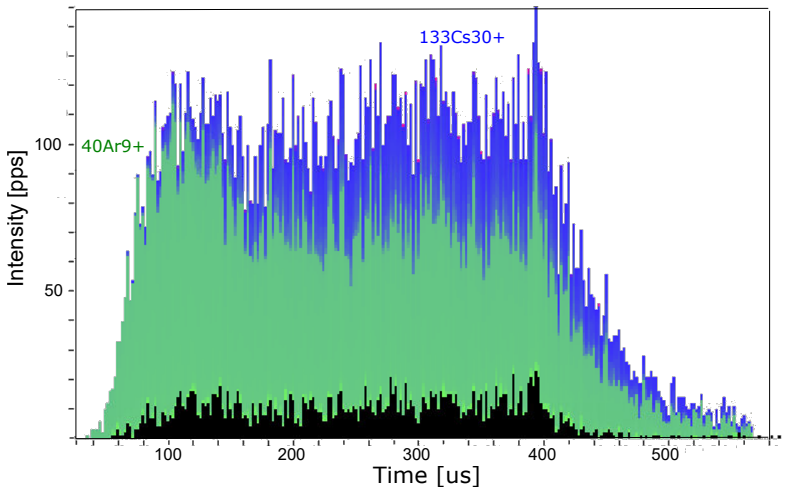

Figure 4.9. Pulse structure of a beam mixed beam of $^{133}Cs^{30+}$ and $^{40}Ar^{9+}$ measured using a silicon detector. Slow Extraction is applied to the EBIS outer barrier.

caesium and charge breeding conditions that would result in a larger temperature difference between the beam of interest and the ionized residual gas.

4.2.3 Use of α-decays for Purity Estimations

The course of the physics campaign sometimes confronts us with radioactive ion beams of relatively short α-decay. The emitted $^{4}He^{2+}$ particles can be detected using conventional silicon detectors. This information provides an indirect way of estimating the intensity of the beam; however, it relies on the irradiation of material and the evident constraints involved. With a beam in the sub-efA current range, the irradiation of a plate close to the silicon detector for few seconds is acceptable. An illustration of such a process is shown in Figure 4.10. A slit of a diagnostic box in the linac was irradiated with a beam of $^{222}Fr^{51+}$ and $^{222}Ra^{51+}$. One can fit the energy histogram with a series of Gaussian and extract the centroid of each peak to calibrate the energy scale of the detector. At such low energy, the calibration of the silicon energy is linear to an excellent approximation. The decay chain of ^{222}Fr and ^{222}Ra are shown in Table 4.2. The measured ratio of $^{218}Rn(J^{\pi} = 2^{+})$ over $^{218}Rn(J^{\pi} = 0^{+})$ is 97.1 % and compares well with the expected abundances. In this case, the amount β-decay from ^{222}Ra is not detected by the silicon detector, so one cannot assess the relative intensity of each component. This indirect method only

proved to be useful for particular cases of a superimposed RIB with α-decay modes.

Table 4.2. Table of the main decay chains from ^{222}Fr to ^{214}Po with probabilities higher than 10^{-3}

Isotope	Decay mode	Probability	Half-life
^{222}Fr	^{222}Ra $+\beta^{-}$(2.028 MeV)	100	14 m
^{222}Ra	^{218}Rn($J^{\pi}=0^{+}$) $+\alpha$(6.558 MeV)	96.9	38 s
	^{218}Rn($J^{\pi}=2^{+}$) $+\alpha$(6.239 MeV)	3.05	
^{218}Rn	^{214}Po $+\alpha$(7.129 MeV)	99.87	34 ms
^{214}Po	^{210}Pb $+\alpha$(7.687 MeV)	100	160 μs

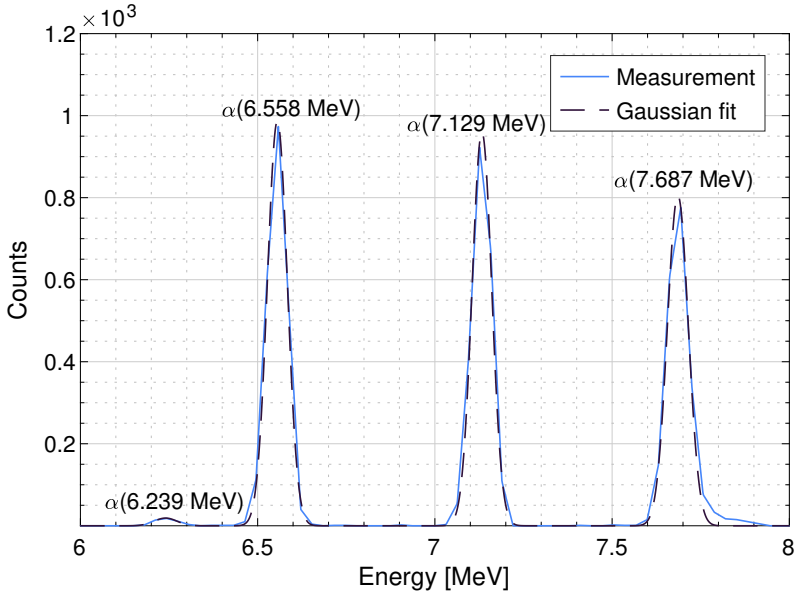

Figure 4.10. Energy spectra measurement of the emitted α particles from an implementation of the mixed beam ^{222}Fr^{51+} and ^{222}Ra^{51+}.

CHAPTER 5

Transverse Beam Properties Characterization

Generic approaches to characterize the transverse phase space of ion beams using charge-interceptive diagnostics have been widely presented and analytically studied in the literature [Wiedemann, 2015] [Sander, 1990]. Ion beams with intensities in the pico-Ampere range can be probed using conventional diagnostics such as Faraday cups. In practice, difficulties emerge at regimes of weak beam intensities, motivating for experimental studies that aim at bridging the gap between the use of pico-Ampere beams and single-ion detection. The range of sub-femto-Ampere intensity, typically less than 10^4 particles per second (pps), corresponds to very low yields of exotic isotopes produced in Radioactive Ion Beam facilities. An underlying motivation for the accurate characterization of low yields isotopes transverse beam properties is to better estimate the initial beam dynamic conditions for experimental apparatus without relying on the performance of the linac when scaling from a more intense pilot beam. By gaining direct access to the transverse properties of ion beams at very low intensity, one would not require the use of pilot beams, nor to assume machine-scalability from different A/q's, in order to estimate the transverse phase space distribution of weak RIB. Removing this layer of uncertainties underlying the indirect type of measurement naturally gives more confidence in the characterization of the beam's actual transverse phase space distribution. A new technique was therefore developed to overcome the impracticability of characterizing the transverse properties of very low-intensity ion beams.

The analytical framework and the definition of transverse beam properties are described in the first section, along with the underlying assumptions that will be followed. The experimental setup is then described, followed by the demonstration of the capability to measure transverse beam profiles of ion beams at very low intensity. In the next section, two distinct techniques of phase space characterization are utilized and validated using sub-femto Ampere ion beams. A comparison is thoroughly drawn with existing methods using conventional beam-line diagnostics. The main distinctions in terms of data treatment and analysis are discussed. Finally, the measurements of transverse beam properties for different beams or beam energies are presented.

5.1 Transverse Beam Properties

The transverse dynamics of a charged particle through a focusing channel is expressed by using the theory of beam physics. The derivations lead to a description of the transverse motion in the *phase space*. Usually, the term *phase space* relates to the variables of space and kinetic momentum. In contrast, the term *trace space* is associated with the variables of space and canonical momentum.

5.1.1 Analytic Description

The description of beam transverse properties resides in the application of a norm metric onto the dynamical components of each (transverse) direction. We will discuss the differential equations governing the motion of a charged particle during transport in a focusing channel, leading to the equations of phase space density conservation.

a Mathieu-Hill Equations

The dynamics of a charged particle in a quadrupole focusing channel along z-axis tells us that the motion in transverse directions (x, y) follows Mathieu-Hill equation [Wiedemann, 2015] [Wangler, 1998]. The simplified version resulting from paraxial approximation is:

$$\frac{d^2x}{dz^2} + k(z)x = 0 \tag{5.1}$$

$$\frac{d^2y}{dz^2} - k(z)y = 0 \tag{5.2}$$

where the focusing function k is defined using G, the magnetic field gradient:

$$k(z) = \frac{qG(z)}{mc\beta\gamma} \tag{5.3}$$

The equivalent with a gradient of electrostatic lens is: $G_e = \beta cG$.

b Courant-Snyder Invariant

The distinction is sometimes made between the phase space (x, p_x) and the trace space (x, x'), and because our studies only concerns the latter coordinate system, the phase space will be associated with trace space. One will use the arbitrary variable **u** to describe the phase space coordinates in the transverse directions $u = x$ or y. The phase similarly corresponds to $u' = \frac{du}{dz}$.

$$\mathbf{u} = \begin{pmatrix} u \\ \\ u' \end{pmatrix} \tag{5.4}$$

The Mathieu-Hill equations are solved for an arbitrary focusing function $k(z)$, by using a set of periodic solutions, that are represented by the ansatz:

$$u(z) = \sqrt{2\varepsilon_u} a_u(z) \cos\left(\Phi_u(z) + \Phi_0\right) \tag{5.5}$$

A constant to be determined from initial conditions ε_u, appears in this solution. The transverse amplitude of oscillations noted $a_u(z)$ is a function of z, as well as the phase advance function $\Phi_u(z)$ between the points 0 (Φ_0) and z. By inserting the solution into Equation 5.1, one derives two equations in order to independently cancel the cosine and sine parts. Firstly, the non-linear differential equation describing the evolution of the amplitude function appears,

$$a_u'' - \frac{1}{a_u^3} + k(z) a_u = 0 \tag{5.6}$$

Secondly, an equation describing the slope of the advance function is valid,

$$\Phi_u' = \frac{1}{a_u^2} \tag{5.7}$$

The latter relation is in particular useful to simplify the expression of the phase:

$$u' = \sqrt{2\varepsilon_u} \left(a_u' \cos(\Phi_u + \Phi_0) - \frac{\sin(\Phi_u + \Phi_0)}{a_u} \right) \tag{5.8}$$

Finally, by rearranging the last three equations, one obtains the expression of

the Courant-Snyder invariant as a function of ε:

$$\left(u' a_u - a'_u u\right)^2 + \frac{u^2}{a_u^2} = \varepsilon_u \tag{5.9}$$

Equation 5.9 is implicit in terms of (u, u') and corresponds to a recognizable quadratic curve, an ellipse with a constant area $\mathcal{A} = \pi\varepsilon_u$. The area occupied by particles within the phase space ellipse, divided by pi, defines what is considered to be the beam emittance ε_u. The metric chosen hereafter for defining the transverse spread is the RMS, in consequence the emittance boundary is delimited to one standard deviation.

c Liouville's Theorem

When the motion of a statistical set of particles obeys to Hamilton's equations, Liouville's Theorem states that the distribution function is conserved along any phase space trajectories and the phase space volume occupied is invariant.

Liouville's Theorem can be demonstrated by first defining an infinitesimal phase space element $d\mathbf{p}d\mathbf{q}$, with $\mathbf{p}$ the canonical coordinate and $\mathbf{q}$ the conjugate momenta. So, the number of particles dN inside the element is logically $dN = f(\mathbf{q}, \mathbf{p}, t)d\mathbf{q}d\mathbf{p}$, with f the density distribution not necessarily at equilibrium. Because the change of particle density is assumed equal to the divergence of the flux density (conservation), the Equation of Continuity becomes:

$$\frac{\partial f}{\partial t} = -\frac{\partial}{\partial \mathbf{q}}(f\dot{\mathbf{q}}) - \frac{\partial}{\partial \mathbf{p}}(f\dot{\mathbf{p}}) = -\frac{\partial f}{\partial \mathbf{q}}\dot{\mathbf{q}} - \frac{\partial f}{\partial \mathbf{p}}\dot{\mathbf{p}} - f\left[\frac{\partial \dot{\mathbf{q}}}{\partial \mathbf{q}} + \frac{\partial \dot{\mathbf{p}}}{\partial \mathbf{p}}\right] \tag{5.10}$$

By adding Hamiltonian equations $\dot{\mathbf{q}} = \frac{\partial H}{\partial \mathbf{p}}$ and $\dot{\mathbf{p}} = -\frac{\partial H}{\partial \mathbf{q}}$ to Equation 5.10, one obtains that the total time derivative of the distribution function is null (Liouville's Theorem):

$$\frac{\partial f}{\partial t} + \dot{\mathbf{q}}\frac{\partial f}{\partial \mathbf{q}} + \dot{\mathbf{p}}\frac{\partial f}{\partial \mathbf{p}} = \frac{df}{dt} = 0 \tag{5.11}$$

The validity of Liouville's Theorem is violated under several circumstances that despite not being considered as true in the following studies, are still worth mentioning:

- Creation or annihilation of particles.
- Presence of collisional or dissipative forces (foil, residual gas,...).
- Presence of synchrotron radiation.
- Trapping of particles that lead to discontinuity in the function distribution.
- Spatial inhomogeneites that lead, for instance to $\mathbf{E} \wedge \mathbf{B}$-drifts.

Liouville's theorem provides a powerful tool to describe a beam in phase space. The knowledge of the phase space distribution f at a location of the beam transport line allows to transport it conveniently at any other point of the focusing lattice, without having to calculate the trajectory of each individual particle.

5.1.2 Transverse Beam Parameters

The analytical framework gathering the Courant-Snyder invariant and Liouville's theorem allows to describe the beam transverse motion with practical geometry tools. Starting from the Courant-Snyder invariant, transverse beam parameters are hereafter derived in a two-dimensional phase space.

a Ellipse Geometry

The Courant-Snyder invariant (Equation 5.9) shows that the phase space can be described using the general equation of an ellipse $\mathscr{E}$, which is:

$$\mathscr{E} : \gamma u^2 + 2\alpha u u' + \beta u'^2 = \varepsilon_u \tag{5.12}$$

The parameters α, β and γ are called Twiss parameters and determine the family of possible ellipses, as a function of the emittance ε. Twiss parameters are particularly meaningful for beams with phase space distribution that preserve the $\pi/4$-periodicity of ellipses, so typically phase space distributions without filaments or strong asymmetries.

As shown in Figure 5.1, an ellipse is often represented with its semi-axes M and N. The area of the ellipse is simply $\mathcal{A} = \pi M N = \pi\varepsilon$, which is also the reason

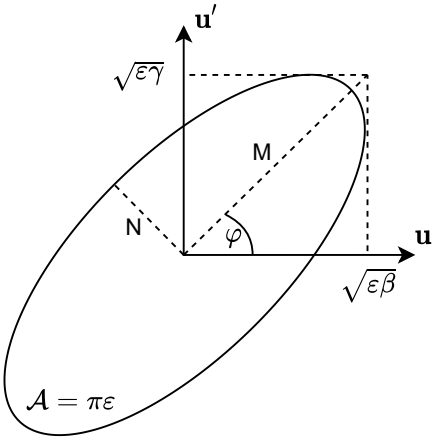

Figure 5.1. Phase space ellipse and useful notations introduced.

why emittance values are expressed in units of π.mm.mrad throughout the chapter. Another useful parameter is the rotation angle of the ellipse φ which is calculated as a function of Twiss parameters as such,

$$\tan 2\varphi = \frac{2\alpha}{\gamma - \beta} \tag{5.13}$$

The rotation angle φ and the semi-axes M and N, can also be used to prove the following relation connecting Twiss parameters:

$$\beta\gamma - \alpha^2 = 1 \tag{5.14}$$

b Beta Function

By going back to the Courant-Snyder invariant (Equation 5.9), one can directly associate Twiss parameters with the amplitude function, noted a:

$$\alpha = -aa' \quad \beta = a^2 \quad \gamma = \frac{1}{a^2} + a'^2 \tag{5.15}$$

Now, one rewrites Equation 5.6 using $a_u = \sqrt{\beta_u}$ to derive the expression of the Beta function in a quadrupole lattice:

$$\frac{1}{2}\beta_u''\beta_u - \frac{(\beta_u')^2}{4} + k(z)\beta_u^2 = 1 \tag{5.16}$$

Finally, combining Equation 5.14 and Equation 5.16, an additional relation between Twiss parameters α and β' is expressed:

$$\alpha(z) = -\frac{\beta'(z)}{2} \tag{5.17}$$

The beam is converging when the slope of the Beta function is decreasing, so $\alpha > 0$, and is diverging when $\alpha < 0$. Searching for the waist of the beam in a transverse direction translates into finding z for $\alpha(z) = 0$.

c Beam Envelope

The beam envelope in a transverse direction R_u is a crucial parameter to assess when, for instance a physical aperture is obstructing the path. It can be accessed by setting $R_u(z) = \max u(z)$ in Equation 5.5, resulting in $R_u(z) = \sqrt{\varepsilon_u} a_u(z)$. By rewriting the latter equation in terms of Twiss parameters, the beam envelope becomes:

$$R = \sqrt{\varepsilon\beta} \tag{5.18}$$

And the slope of the beam envelope is:

$$\frac{dR}{dz} = -\alpha\sqrt{\frac{\varepsilon}{\beta}} \tag{5.19}$$

d Normalized Emittance

When the beam is accelerated, the axial velocity component increases, in consequence the transverse angles decrease and the beam size shrinks. A gain in beam energy will effectively imply lower transverse emittance. In order to factor out the influence of the longitudinal velocity and preserve an invariant emittance, the normalized emittance ε^n is introduced and defined as the product of emittance and relativistic parameters,

$$\varepsilon^n = \beta_r \gamma_r \varepsilon \tag{5.20}$$

The normalized emittance before and after acceleration is the same. The practical

use made in this chapter is when comparing emittance values measured for different beam energies. In any other cases, the emittance values reported are unnormalized.

5.1.3 Beam Matrix Theory

The beam matrix theory stems from Liouville's theorem only applied to particle systems subject to conservative forces. The beam parameters are gathered in matrices facilitating the mathematical treatment of transport through the beam-line. In our case, each plane of transverse motion is represented by a 2×2 matrix.

a $\boldsymbol{\sigma}$-Matrix

The phase space enclosed by the beam can be described by an ellipse (Equation 5.12). This ellipse equation can be written using the $\boldsymbol{\sigma}$-matrix and the vector of phase space coordinates $\boldsymbol{u}$,

$$\boldsymbol{u}^T \boldsymbol{\sigma}^{-1} \boldsymbol{u} = 1 \tag{5.21}$$

By developping the Equation 5.21 and identifying the elements σ_{ij} with the Twiss parameters in Equation 5.12, one obtains the following definition,

$$\boldsymbol{\sigma} = \varepsilon \begin{pmatrix} \beta & -\alpha \\ -\alpha & \gamma \end{pmatrix} \tag{5.22}$$

The area of the ellipse can be calculated using the determinant of the $\boldsymbol{\sigma}$-matrix and, after simplifying using the relation presented in Equation 5.14, one verifies that $\mathcal{A} = \pi\sqrt{\det \boldsymbol{\sigma}} = \pi\varepsilon$.

b Statistical Description

As evoked earlier, Twiss parameters and the emittance are adjusted according to a specific statistical metric, or geometrical norm, which is chosen to be the average distance from the center of the particle distribution f in the (u, u') phase space. The center of the distribution is noted $(\bar{u}, \bar{u}')$. It is implicitly defined that the emittance values calculated in this chapter are RMS-emittances. With a discrete distribution f_k

of N number of samples k, the second moments $\langle u_i u_j \rangle = \langle u_{i,k} u_{j,k} \rangle_k$ (with $i, j = 1, 2$) are written,

$$\begin{aligned} \left\langle u^2 \right\rangle &= \sum_{k=1}^{N} f_k (u_k - \bar{u})^2 \\ \left\langle u'^2 \right\rangle &= \sum_{k=1}^{N} f_k (u'_k - \bar{u}')^2 \\ \langle u u' \rangle &= \sum_{k=1}^{N} f_k (u_k - \bar{u})(u'_k - \bar{u}') \end{aligned} \tag{5.23}$$

One can calculate the second moments of the distribution, by using Equations 5.5 and 5.8 describing $\boldsymbol{u}$ as a function of the amplitude and the phase advance. Then, by substituting with the previously derived relations linking with Twiss parameters, therefore the beam matrix elements σ_{ij}:

$$\begin{aligned} \left\langle u^2 \right\rangle &= 2\varepsilon a^2 \left\langle \cos^2 (\Phi + \Phi_0) \right\rangle = \varepsilon\beta = \sigma_{11} \\ \left\langle u'^2 \right\rangle &= 2\varepsilon \frac{\alpha^2}{\beta} \frac{1}{2} + 2\varepsilon \frac{1}{\beta} \frac{1}{2} = \varepsilon\gamma = \sigma_{22} \\ \langle u u' \rangle &= -2\varepsilon\alpha \frac{1}{2} = -\epsilon\alpha = \sigma_{12} \end{aligned} \tag{5.24}$$

If a sampling of the phase space distribution f_k is available, one can easily access to all the $\boldsymbol{\sigma}$-matrix elements by using Equations 5.23 and 5.24. The choice of the RMS as a statistical remains somewhat arbitrary and deriving Twiss parameters and beam emittance following such convention assumes that the type of phase space distribution is known. Let's consider the fraction of the beam inside of the RMS-ellipse $\mathscr{E}$, noted,

$$F = \int_{\mathscr{E}} f(\boldsymbol{u}) \mathrm{d}\boldsymbol{u} \Big/ \int_{\infty} f(\boldsymbol{u}) \mathrm{d}\boldsymbol{u} \tag{5.25}$$

One can calculate the percentage of the beam included in one or several RMS-ellipse and it differs drastically depending on the type of distribution (Table 5.1). The fraction of the beam F is an essential parameter to evaluate in order to correlate the meaning of RMS-emittance with the distribution.

Table 5.1. Fraction of the beam included in an ellipse of Area $n\pi\varepsilon$ RMS-emittance, for different types of phase space distributions.

Area $\mathcal{A}$	F [%] for f_{Gaussian}	F [%] for f_{Uniform}	F [%] for $f_{\text{Maxwellian}}$
$\pi\varepsilon$	39	25	35
$2\pi\varepsilon$	63	50	64
$4\pi\varepsilon$	86	100	93
$6\pi\varepsilon$	95	100	99
$n\pi\varepsilon$	$1-\exp(-n/2)$	$n/4$	$\text{erf}(\pi n\sqrt{96})$

c $\mathcal{R}$-Matrix

Several of the presented measurements will require to transfer the Twiss parameters or directly the phase space coordinates, from a location of the beam-line to another. We therefore adopt conventional transport theories by defining beam optics segments by their respective transfer matrices, noted $\boldsymbol{\mathcal{R}}$. Indeed, the phase space coordinates at any location can be written as a linear combination of initial conditions (u_0, u_0'),

$$\begin{aligned} u &= \frac{\partial u}{\partial u_0}u_0 + \frac{\partial u}{\partial u_0'}u_0' \\ u' &= \frac{\partial u'}{\partial u_0}u_0 + \frac{\partial u'}{\partial u_0'}u_0' \end{aligned} \tag{5.26}$$

So, the transfer matrix can be written as,

$$\boldsymbol{\mathcal{R}} = \begin{pmatrix} \dfrac{\partial u}{\partial u_o} & \dfrac{\partial u}{\partial u_o'} \\ \dfrac{\partial u'}{\partial u_o} & \dfrac{\partial u'}{\partial u_o'} \end{pmatrix} \tag{5.27}$$

The determinant of the $\boldsymbol{\mathcal{R}}$-matrix is recognized as being the Jacobian, which due to Liouville's theorem, equals one. The transfer of phase space coordinates from the location z_i to z_j, is more generally expressed as,

$$\mathbf{u}\left(z_j\right) = \boldsymbol{\mathcal{R}}\left(z_j|z_i\right)\mathbf{u}\left(z_i\right) \tag{5.28}$$

Twiss parameters are transferred from one location to another by using the

transformation of the $\boldsymbol{\sigma}$-matrix,

$$\boldsymbol{\sigma}(z_j) = \boldsymbol{\mathcal{R}}\,(z_j|z_i)\,\boldsymbol{\sigma}(z_i)\boldsymbol{\mathcal{R}}^T\,(z_j|z_i) \tag{5.29}$$

The $\boldsymbol{\mathcal{R}}$-matrix for a series of beam transport elements $\boldsymbol{\mathcal{R}}_0, ..., \boldsymbol{\mathcal{R}}_n$ is the product of each individual matrix:

$$\boldsymbol{\mathcal{R}} = \prod_{i=0}^{n} \boldsymbol{\mathcal{R}}_{n-i} \tag{5.30}$$

d Transfer Matrices

Each beam matrix element is derived from the Hamiltonian of a charged particle to the first order (paraxial approximation). As described in the Chapter 2, the beam transport lines after the linac are composed of magnetic focusing quadrupoles. In a field-free drift space ($k = 0$) extending from the location z_i to z_j, the transfer matrix is simply,

$$\boldsymbol{\mathcal{R}}_{\mathrm{D}}(z_j|z_i) = \begin{pmatrix} 1 & z_j - z_i \\ 0 & 1 \end{pmatrix} \tag{5.31}$$

Quadrupoles are focusing (QF) on one plane and defocusing (QD) on the other. The magnetic field inside a quadrupole is assumed to be constant through the magnetic length L_m. The term $\phi = \sqrt{|k|}L_m$ is introduced, with k the focusing strength of a quadrupole. The focusing quadrupole ($k > 0$) transfer matrix is,

$$\boldsymbol{\mathcal{R}}_{\mathrm{QF}} = \begin{pmatrix} \cos\phi & \frac{1}{\sqrt{k}}\sin\phi \\ -\sqrt{k}\sin\phi & \cos\phi \end{pmatrix} \tag{5.32}$$

and the defocusing quadrupole ($k < 0$) transfer matrix,

$$\boldsymbol{\mathcal{R}}_{\mathrm{QD}} = \begin{pmatrix} \cosh\phi & \frac{1}{\sqrt{|k|}}\sinh\phi \\ \sqrt{|k|}\sinh\phi & \cosh\phi \end{pmatrix} \tag{5.33}$$

The simplified version of the quadruple transfer matrix, usually called thin lens approximation, occurring when $\phi \sim 0$, are not considered in this chapter considering this approximation is not always valid in the frame of the studies.

5.1.4 Summary of Assumptions

The analytical framework involving the use of Liouville's theorem and beam theory gather many assumptions that were mentioned in the previous sections. Other assumptions more specific to this studies were also evoked. A summary is listed hereunder, as well as the necessary controls during measurements of transverse beam properties,

- The emittance is an invariant. In particular, the beam losses must be considered negligible along the experimental setup, which implies to verify that the full beam transmission is conserved through the measurement zone.

- Space-charge and beam-impedance effects are not considered, which is natural in the context of studies using below 100 epA.

- Beam transport hypotheses through the measurement zone assume no correlation between transverse and longitudinal plane.

- Correction factors due to dispersion are not included in the Courant-Synder Invariant (Equation 5.9). The relative energy spread of the beams probed in this chapter is typically below 0.5 %.

- The transverse motion of particles inside a focusing lattice are treated independently between the two planes, using separately two-dimensional matrices.

- The emittance and Twiss parameters are calculated using the RMS metric. In the exception of specification, the RMS-emittance values are unnormalized.

- The measured phase space distributions are assumed with $pi/4$-periodicity. Results of Twiss parameters and beam emittance are presented along with the percentage of the fraction of the beam inside of the RMS-ellipse.

- The formulae for calculating the second moments (Equation 5.23) are weighted and only valid if the sum of phase space density distribution samples f_k is equal to one (probability distribution). The samples of measured beam count-rate or current $c_k = f_k$ are normalized to the sum over all the set, so that the weighted standard deviation formulae stay valid in the presented form.

5.2 Experimental Overview

The objective is to demonstrate the capability to measure the transverse properties of ion beams at very low intensity (sub-efA currents). The measurement zone after the linac where the ion beam properties were probed is firstly described. Secondly, the two main experimental setups used to conduct the measurements are presented, requiring to provide ion beams in a large dynamical range of currents. Finally, the data acquisition systems such as diagnostics and software applications are detailed.

5.2.1 Measurement Zone

An ion source located at the entrance of the post-accelerator section (Figure 5.3) serves at producing stable ion beams, with enough flexibility to vary the intensity of the singly-charged ion beam resulting from thermal ionization, which is a mixture of predominantly 39-potassium with traces of 133-cesium. After accumulation and transverse cooling in the REXTRAP Penning trap, the beam is transferred to REXEBIS, to increase its charge state by successive electron-impact ionization. A beam with a mass-to-charge ratio A/q of interest is selected through a spectrometer of Nier-type and sent towards the linac, as described in the Chapter 2.

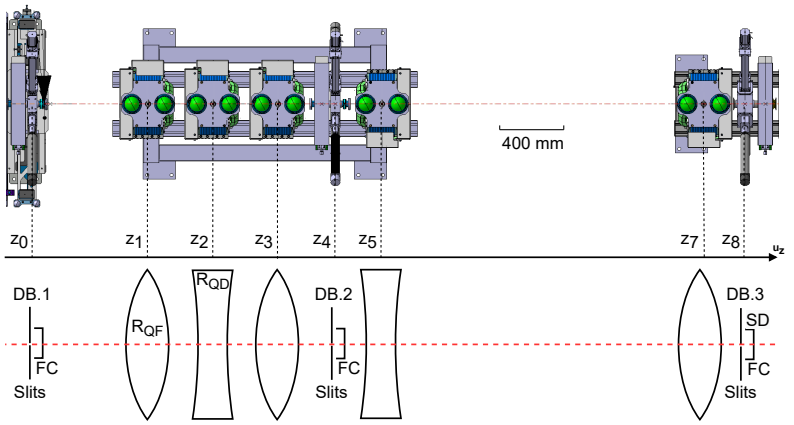

Figure 5.2. Detailed schematic of the measurement section presented in Figure 5.3. Diagnostic boxes (DB) gather slits, a Faraday cup (FC) and for one of them a large aperture silicon detector (SD).

The zone of interest for transverse beam properties measurements follows the linac and is located in the straight section before the three high-energy beam transfer

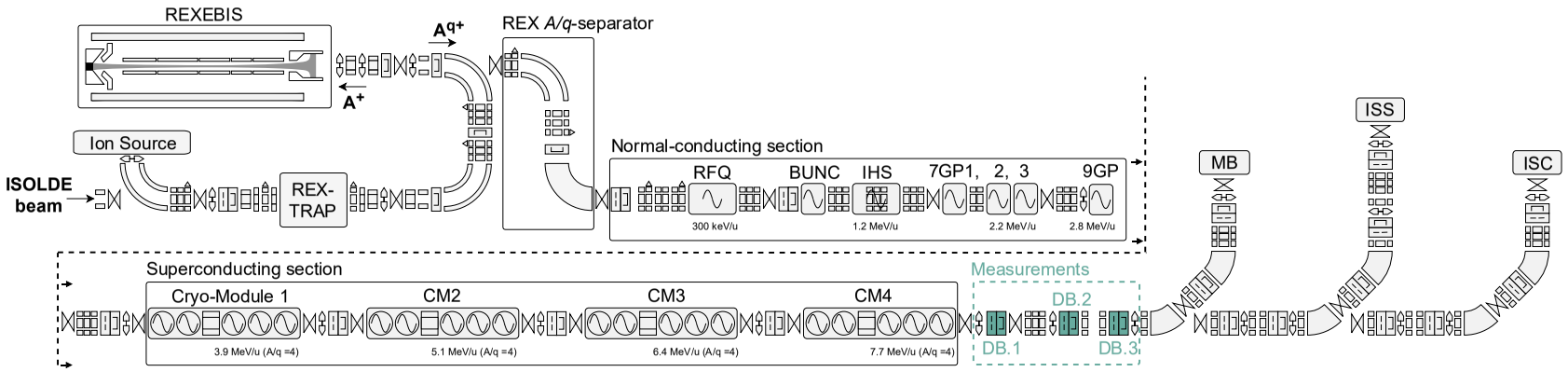

Figure 5.3. Schematic of REX/HIE-ISOLDE post-accelerator at the time of the measurements, from the low-energy trapping and charge-breeding sections to experimental stations. All measurements of transverse beam properties were achieved within the zone delimited with a colored dash line.

lines to the experimental stations. In the Figure 5.3, the three consecutive diagnostic boxes, DB.1 located at z_0, DB.2 in z_4 and DB.3 in z_8 along the measurement zone, offer the necessary tools for measuring transverse beam properties. The defocusing and focusing quadrupoles are represented using the analogy of optical lenses, the center of their magnetic lengths are noted z_1, z_2, z_3, z_5 and z_7.

5.2.2 Main Beam Setups

The validity of results obtained with the newly developed technique was tested with measurements using beam currents three orders of magnitude higher. Two setups were used for either obtaining 50 epA of $^{39}K^{10+}$ or 1 efA of the same beam at the measurement zone (Figure 5.3). Several steps were verified so that the change of intensity would not influence the transverse beam properties measured after acceleration. The maximum injected current into REXTRAP was kept two orders of magnitude below the trap charge capacity, so that the emittances of the singly-charged ion beams injected into REXEBIS for the two mentioned setups are comparable. The charge-breeding conditions are also kept constant in between the two setups and the difference in the compensation of the electron beam is negligible compared to its total capacity. In the conditions of the measurements, the extracted charge from REXEBIS is dominated by the ionization of various residual gases, the most abundant being neon, used as a buffer gas for the trap.

The cleanest A/q for 39-potassium within the linac acceptance is at the charge state 10+, however not all contamination is suppressed, a background of around 100 pps of $^{35}Cl^{9+}$ is still present in the measurement zone. Because even at very-low intensity, producing enough 39-potassium beam to make the 35-chlorine contamination from REXEBIS negligible is necessary, we chose to attenuate the current before the RFQ by a factor 20 using a pepperpot filter. The diameter of the holes on the attenuation filter is about a factor 100 smaller than the beam size. The use of an attenuation filter is subject to caution since it is not excluded that it may influence the beam properties measured downstream. Generally, the RFQ mixes the beam transverse components enough to make the beam properties transparent from the use of the filter. This question is discussed further in the chapter. Five

Table 5.2. Main REX/HIE-ISOLDE beam setups used for proving the capability of measuring the transverse beam properties of very low intensity ions beams.

	Parameter	**Setup 1**	**Setup 2**
Ion source	Ion	$^{39}K^{+}$	$^{39}K^{+}$
	Filament heating	30 W	40 W
	Intensity	15 fA	45 pA
Low energy	Trapping rate	20 Hz	20 Hz
	Breeding time	20 ms	20 ms
	Efficiency	12 %	12 %
	Attenuation	95 %	none
High energy	Ion	$^{39}K^{10+}$	$^{39}K^{10+}$
	Energy	3.8 MeV/u	3.8 MeV/u
	Efficiency	75 %	75 %
	Typical intensity	1 efA	50 epA

superconducting cavities were operated at 90 % of their maximum gradient field, accelerating the beam to a final energy of 3.8 MeV/u. As explained in the Chapter 2, the count-rate is limited by the total beam energy deposited on the silicon detector per pulse, which is kept below the saturation limit of the preamplifier.

5.2.3 Beam Diagnostics

Two types of beam diagnostics were employed for the measurement of transverse properties, depending on the ion beam intensity. Ion beams with current in the epA range are probed using Faraday cups of 30 mm-diameter, present in all three diagnostic boxes (DB.1, DB.2 and DB.3) of the measurement zone in Figure 5.2. Measurements of the transverse properties are hereafter based on multiple phase space projections or beam slices from a pair of slits, vertical and horizontal with 1 mm-opening, available in all DB. On the other scale of beam intensity, for currents below the efA range, a solid-state 300 µm-thick partially-depleted Passivated Implanted Planar Silicon (PIPS) detector is utilized. The silicon detector installed in DB.3

has a diameter of 28 mm, which is an aperture large enough to capture all the beam or beamlets. The technical specifications of the detector are presented in Table 2.10 (Type 3). The use of silicon detectors is not only beneficial for single-ion detection but also for drastically reducing the impact of noise and background current. The acquisition of the count-rate is analogous to a digital signal. Typically a silicon detector rejects all counts below a threshold energy, to eliminate for instance secondary electrons or the E-M radiation emitted by accelerating structures. As the natural time structure of the beam is relatively short when extracted from REXEBIS (about 100 µs), a slow extraction mode was applied to avoid pile-up effect on silicon detectors by stretching the time distribution to 1 ms.

5.2.4 Data Acquisition Tools

The different techniques involved for the measurement of beam properties are fitted for the use of Automation application, presented in the Chapter 2, which has been specifically designed for such type of extensively scripted measurements. The procedure consists in defining the technique(s) that will be used and the diagnostic tools associated: slits, beam collectors, focusing elements, etc. The application takes care of assigning the chosen devices to the technique used with flexibility. Each technique used for the characterization of transverse beam properties requires slit-scans, which can be easily adjusted for different length of step during the slit movement, current collection time-lengths and total transverse widths swept. In general, the collection of beam current is synchronized with the slit movement, so that only beam pulses passing when the slit is stopped are acquired, reducing the uncertainty on the slit position. Checkpoints are added to the script for verifying that the transmission does not fluctuate during the measurement, by typically recording the total current at the entrance of the linac and in the measurement zone. When using silicon detectors, the data acquired include the count-rate but also the raw analog and digital signals provided by the digitizer and time-to-digital converter, so that the quality of the acquisition is controlled. Indeed, it is necessary to verify that the silicon detector does not saturate or that impinging ions are enough separated in time to be discriminated by their energies.

The Automation application offers flexible programming of the individual tasks of full transverse characterization measurements, which may take in average between 5 to 30 minutes. The application also facilitates the looping of the full transverse characterization measurement, in order to obtain a more complete statistical description of the accuracy the method or the evaluation of the beam stability. Such scripting may require several hours-long automated measurements.

5.3 Transverse Beam Profiles at Very Low Intensity

The quadrupole-scan and the double-slit methods rely on the measurement of intensity profiles using vertical and horizontal slits at a front position, although with different rear apparatus. Position-density distributions give access to the first element of the $\boldsymbol{\sigma}$-matrix σ_{11}, so in Equation 5.24 when u_i and u_j are both equal x or y. The process for measuring beam slices is made similar for the two ranges of intensity, except in one case, the current is measured in epA, and in the other case, the count-rate (along with energy information) is acquired in terms of particles per second (pps). It is first chosen to verify the capability of measuring similar transverse beam profiles with both types of beam collector.

5.3.1 Data Treatment

The main advantage of using silicon detectors in a count rate mode is to resolve each count digitally. Intrinsically, the influence of electrical noise is drastically reduced compared to Faraday cups. A measurement of the bias when using Faraday cups is necessary, substracting it to the data. In order to allow for the deduction of the background bias, it was decided to extend each beam profile scan beyond the beam distribution and to conduct series of slit-scans without beam. An average value of the noise is calculated from slit-scans without beam and, importantly, must avoid showing any pattern of mechanical resonance in the drive of the slit.

During the acquisition of a transverse profile, the slit moves with constant stepping, equalling a fifth of its opening width. When the slit movement stops at a position, the measured intensity is averaged over a certain number of beam pulses. The convergence of an RMS measure on a beam slice was evaluated for each technique by measuring the number of pulses integrated at each slit-position step, required to reach the 1 %-confidence zone. Considering the beam current enunciated in Table 5.2 and a typical case of beam profile with a window size of five times the beam size, the integration time needed when using the silicon detector was twice higher (8 beam pulses per slit step) than for measurements with the Faraday cup in DB.2.

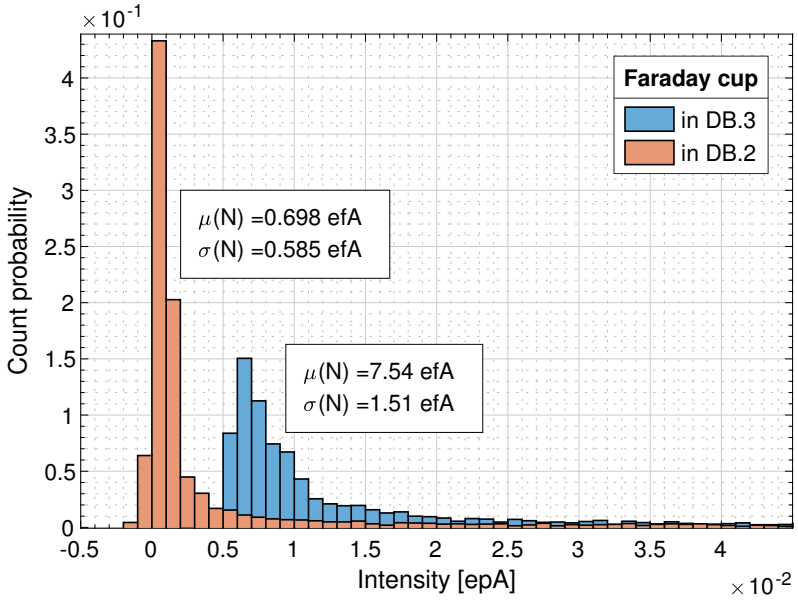

Figure 5.4. Histograms of the noise acquired by Faraday cups located in DB.2 and DB.3.

The statistical chain of periodic and random deviations of the post-accelerator structures influencing the transverse beam dynamics defines the lower boundary of uncertainties for the set of c_k. The silicon detector and its electronics are carefully operated far from pile-up, saturation and dead-time effects, with ad hoc post-treatment discarding unresolved events. It is then possible to consider that such collector system does not introduce additional uncertainties. The statistical uncertainties related to the use of Faraday cups include amplified electronics noise superimposed with background picked-up currents. The Faraday cups present in DB.2 and DB.3 are of different depth and display disparate behavior when analysing histograms of background projections. Histograms of the background allow to estimate the mean noise value $\mu(N)$, called bias, and its RMS $\sigma(N)$. On another hand, deriving the frequency-weighted mean value of the beamlet intensity $\mu(S)$ serves at approximating a signal-to-noise ratio SNR $= \mu(S)/\sigma(N)$. The bias is the subtracted at beam profiles acquired with Faraday cups. In DB.2 the Faraday cup typically shows $\sigma(N) =$ 1.5 efA meanwhile in DB.3 the RMS of the noise is twice higher (5.4). A SNR in the range of 1e3 with both DB is largely sufficient for probing the projections of single beam slices, as shown in Figure 5.6 and later with quadrupole-scans. Nevertheless when making use of two pairs of slits, so achieving a double slicing of the phase

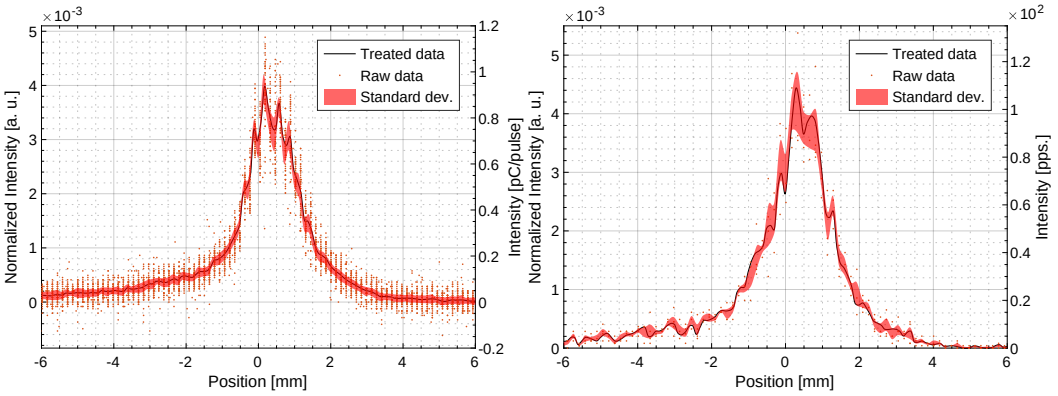

(a) Faraday cup measurement. **(b)** Silicon detector measurement.

Figure 5.5. Comparison between the raw and treated data obtained from transverse beam profiles using either a Faraday cup or a silicon detector as collector. The beam used was $^{39}K^{10+}$ at 3.8 MeV/u, with absolute intensities indicated on the right y-axis.

space, we decided not to use the Faraday cup in DB.3 and to prefer DB.2 therefore guaranteeing a SNR always above 100.

The measures of RMS on beam or beanlet-sizes above 1 mm are considered not affected by the slit opening-size and it was purposefully chosen to stay in those conditions so that an additional uncertainty is not introduced. Nevertheless when necessary a scaling factor on the projection scale is applied. The uncertainty related to the the slit opening-width is in that case dependent on the beam density profile as it will increase when digressing from the Gaussian model used to deconvolute the real beam-size from the measured one.

5.3.2 Results

A direct comparison of the transverse beam profile was made using the Setup 1 and 2 presented in Table 5.2. It is demonstrated that the silicon detector can be used as a beam collector for this type of measurement. In order to evaluate the consistency between results obtained using a silicon detector and a Faraday cup one can evaluate the shape of the relative residuals. This shape resembles a uniform distribution and allows to rule out the hypothesis of the count rate acquired is not linear across all the dynamical range of beam intensity. The Chi^2 is comparable to one meaning that the comparison is satisfactory, it is within the confidence interval.

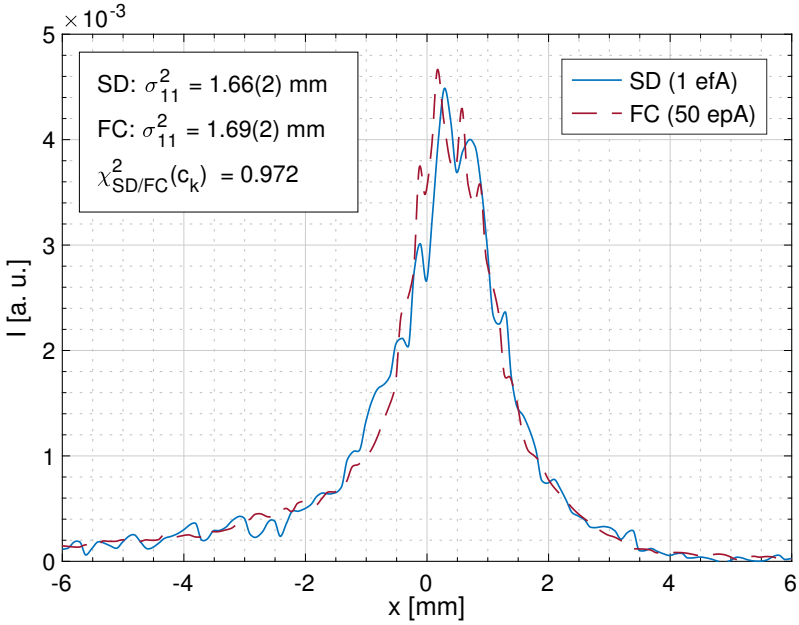

Figure 5.6. Area-normalized transverse beam profile, on the x-plane and at two different intensity scales, with the use of a silicon detector (SD) or a Faraday cup (FC) as beam collector.

5.4 Comparison of Measurement Techniques

Transverse beam properties of ion beams in the linac may be deduced from diverse methods, some of which require the design of a specific device, for instance an Allison-scanner, or a system with a peppertpot filter and a Micro-Channel Plate (MCP) [Pitters et al., 2019]. Two different methods were used in this section: the *quadrupole-scan* and the *double-slit* method, each of them is applied to both the Setup 1 or to the Setup 2 presented in Table 5.2. These two methods are relatively convenient to employ, as they make use of typical beam-line instrumentation: beam monitors, scanning-slits, and the focusing elements.

The simple fact of using two different types of beam collectors already leads to tackle uncertainties separately, adding another method decouples further such treatment. When measuring transverse beam properties, few uncertainties are purely systematic, in fact only drift lengths and the optical modeling of quadrupoles will be considered as such. Uncertainties dependent on the sample number N are called statistical, as opposed to systematic, and it is fundamentally the case for any measured current, as well as uncertainties related to the nature of the method employed. In order to estimate the influence of the beam intensity and background uncertainties, on the measure of $\boldsymbol{\sigma}$-matrix elements, it is chosen to first analyze the simplified case of transverse density characterization, operating with the Setup 1 and the Setup 2. The inherent spread introduced by the measurement apparatus depends on the input phase distribution, so the number of samples, and cannot be treated as a systematic uncertainty.

5.4.1 Data Treatment

The bias measured from scans without beam is subtracted to the beam profiles. It is then useful to define a threshold, especially for measurements involving a Faraday cup. The threshold ζ defines the cut-off of what is considered as noise. The threshold is used as the boundary of an exclusion ellipse when the measurement allow for a full reconstruction of the phase space (double-slit scan). However, with the quadrupole-scan the threshold is calculated as a percentage of the peak intensity.

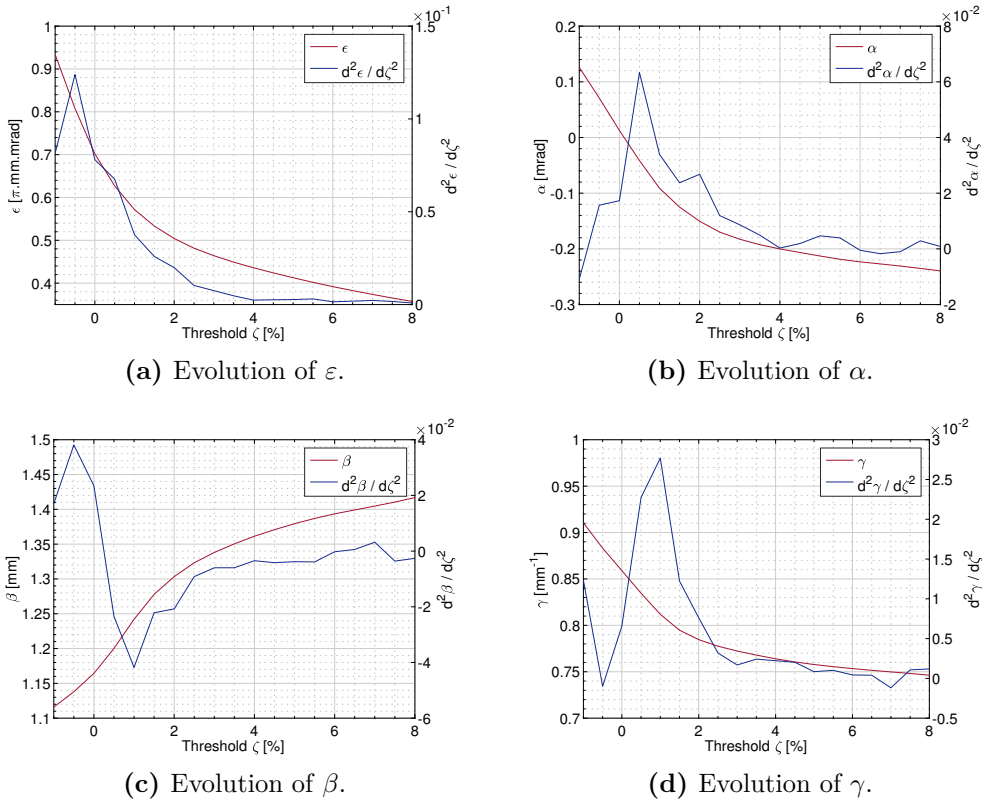

(a) Evolution of ε. **(b)** Evolution of α.

(c) Evolution of β. **(d)** Evolution of γ.

Figure 5.7. Evolution of Twiss parameters and their second derivative as a function of the threshold ξ chosen for each the beamlet profiles measured with the double slit method. The measurements were performed with the Faraday cup in DB.2, and the threshold is chosen at approximately 4%.

By analyzing when the second derivative of the Twiss parameters, as a function of the threshold, becomes close from zero, the ideal threshold can be chosen. A typical example is shown in Figure 5.7 where the threshold was selected to be 4 %. This is the limit after which the threshold reduces linearly the Twiss parameters.

5.4.2 Phase Space Reconstruction from the Double-Slit Method

The method presented is the most evident to comprehend in terms of geometrical reconstruction of the phase space. A first slit filter the beam at a position u_k, while a second slit is used to filter the resulting beamlet position v_k at a distance L downstream. The current c_k acquired directly after the front pair of slits is a result of a first slicing of the phase space around the position u_k and a second slicing centered in $u'_k = \arctan(v_k - u_k)/L$. In other words, the position of the front slit scanning

the beamlet, is translated into an angular variable of the beam impinging the rear slit.

It was considered practical and coherent to increase the total beam intensity of the Setup 1 to 5 efA, prior to the double-slicing, so that the convergence towards a measure of the RMS within 1 % stays at about 8 pulses per slit-step with a silicon detector. As explained earlier, any measurement using the Faraday cup is subtracted from its bias, that is selected after analysis of the frequency-weighted histogram of background currents. To preserve the phase space reconstruction from improper grid spacing, the steps are ideally chosen with similar ratios of $|u_{k+1} - u_k|$ and $|u'_{k+1} - u'_k|$ divided by their respective second moment, $\sqrt{\sigma_{11}}$ and $\sqrt{\sigma_{22}}$. The phase space grid resolution is adjusted during post-treatment by processing a Delaunay triangulation on the measured phase space and by applying an interpolation on the new meshing. The next step in the treatment consists in determining the exclusion ellipse $\mathscr{E}_O$, as described in [Stockli, 2006], by iterating on its area and setting all values $c((u, u') \not\subset \mathscr{E}_O) = 0$. At each iteration, the exclusion-ellipse is calculated from the Twiss-ellipse parameters of the previous iteration except for a larger emittance. A threshold to stop the iterations was arbitrarily defined when the emittance reaches a confidence zone within 3 % of the mean value in the convergence plateau. The contribution of the finite slit width is analyzed following the formulas derived in [D'Arcy and Shemyakin, 2015] to disentangle the real $\boldsymbol{\sigma}$-matrix elements from the measured ones. In the typical case of Twiss parameters shown in Figure 5.8 (a), the relative uncertainties due to the apparatus is 1.1 % on average. In order to simulate the effect of nonparallel slits, one can artificially increase the slit sizes using the previous model. Once the Twiss parameters are derived, two other indicators are calculated: $\langle c_k \rangle_{\mathscr{E}}$, the mean intensity in the Twiss-ellipse $\mathscr{E}$, and $F(\mathscr{E})$, the fraction of beam within the same boundaries.

Series of multiple measurements were conducted to directly evaluate the standard deviation of the double-slit method for the two types of current collectors. The relative uncertainties gathered from series of the same measurement span over a longer time-scale and the stability of the beam in itself must be checked repeatedly

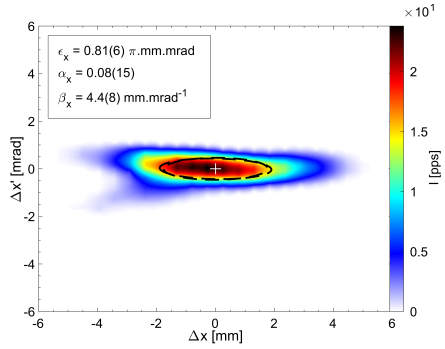

(a) Silicon detector measurement of (x, x').

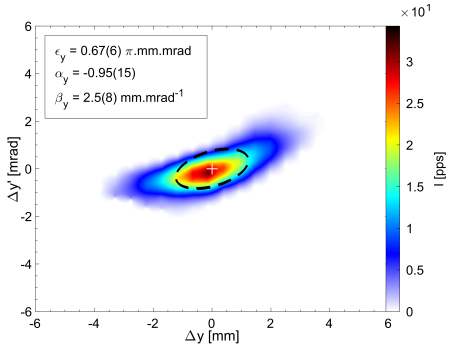

(b) Silicon detector measurement of (y, y').

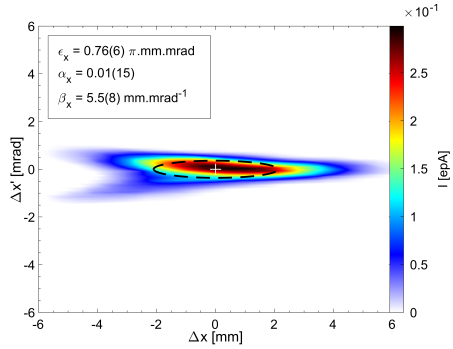

(c) Faraday cup measurement of (x, x').

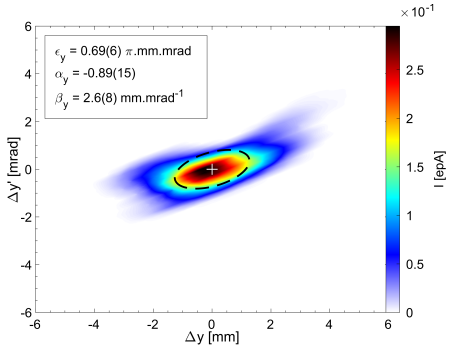

(d) Faraday cup measurement of (y, y').

Figure 5.8. Comparison of phase space reconstruction obtained from the double-slit method using a beam of $^{39}K^{10+}$, at 3.8 MeV/u, either at very low intensity (5 efA) or higher current (50 epA). The measurement using a silicon detector is reconstructed in location z_4 and presented for x-plane (a) and y-plane (b). Higher intensity measurements using a Faraday cup are reconstructed in z_0 and transfered to z_5 for x-plane (c) and y-plane (d).

along the linac in order to observe if possible long-term trends appear. After a series of ten batches of measurements the evaluated standard deviation for each technique is already comparable with their total statistical uncertainties. The averaged results are shown on Figure 5.8, for x and y planes at two distinct ranges of beam intensity. The phase space reconstruction obtained using the Faraday cup with the least noise (in DB.2) had to be transferred from z_0 to z_4, which is the location of the reconstructed measurement using the silicon detector. Such transfer from Equation 5.29 implies an increase on the uncertainties of the Twiss parameters derived at the new location, by including systematic uncertainties on the lengths and quadrupole strengths within the $\mathcal{R}$-matrix. A table gathering all results for x-plane measurements, along with additional information is presented in the next section (Table 5.3). The consistency

of the measurements between the two ranges of beam intensity is satisfactory as they fall in each other's standard deviation. The silicon detector appears to be a perfectly viable solution as a beam collector in the double-slit method, allowing to probe very low intensity ion beams with in our case a total intensity before slicing of 3.10^3 pps.

5.4.3 Response to Quadrupole-Scan Method

The quadrupole-scan method consist in measuring the variance σ_{11} for at least three independent beta functions. In practice, the focusing strength of a quadrupole at locations z_3 or z_5 (Figure 5.2) was varied while probing the σ_{11} element on x-plane or y-plane after the beam had drifted to the diagnostic box DB.3 in z_8. The transfer matrix noted $\mathcal{R}$ in Equation 5.34 depends on the focusing strength.

$$\mathcal{R} = \mathcal{R}_L(z_5 + L_m/2|z_8).\mathcal{R}_{QF} \tag{5.34}$$

In the thin lens approximation σ_{11} is quadratic as a function of the focusing strength. It was instead decided to derive the Twiss parameters using a thick model as defined with Equations 5.32 or 5.33 and to solve the system of nonlinear equations built from Equation 5.35 and for several values of the matrix $\mathcal{R}$.

$$\sigma_{11}(z_8) = \varepsilon \begin{pmatrix} \mathcal{R}_{11}^2 & 2\mathcal{R}_{11}\mathcal{R}_{12} & \mathcal{R}_{12}^2 \end{pmatrix} \begin{pmatrix} \beta \\ \alpha \\ \gamma \end{pmatrix}_{z_5} \tag{5.35}$$

The mean relative standard deviation between the solution of the system and the measured values of σ_{11} is typically 1 % for the data presented hereafter.

The data treatment of each individual profile is similar to the description made in the previous section, with notably the subtraction of a bias on the data acquired with Faraday cups. Unlike with the double-slit method, there no direct access when combining all profiles together to a self-consistent threshold from exclusion-ellipses (Figure 5.9). It was decided to use a threshold based on the percentage of the peak

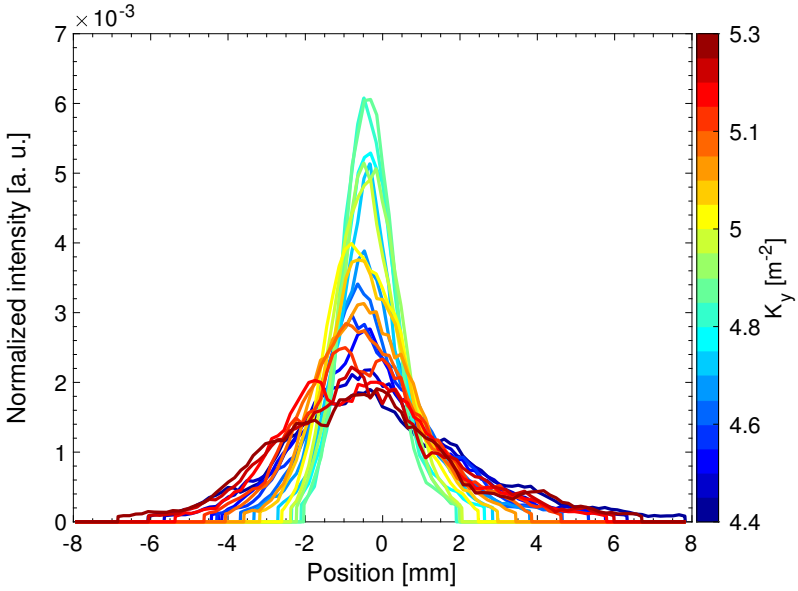

Figure 5.9. Typical transverse beam profiles obtained using a silicon detector as beam collector, during a quadrupole-scan. The color scale is the focusing strength k on the y-axis in that case.

intensity and to examine the evolution of Twiss parameters. The threshold is chosen similarly as a function of a variation of the second derivative of the Twiss parameters. The uncertainties related to the quadrupole model and drift length are in that case statistical because dependent on the measure of the Twiss parameters.

Series of quadrupole-scans were performed to estimate the uncertainties related to the method and statistical uncertainties. The number of scans per batch of measurement was chosen to be twenty and after eight repeated measurement, the standard deviation between the obtained Twiss parameters already converge into the zone of estimated total statistical uncertainties. Results for series of five quadrupole-scans are presented in the Figure 5.10 with associated uncertainties represented by the trace thickness. The Twiss parameters derived for the x-plane and the y-plane are finally transferred to the location z_4, and displayed in Table 5.3 along with the correlation factor between the two technique of beam capture. The comparison of results is satisfactory however limited compared to a full phase space reconstruction, which logically leads to investigate beam tomography techniques.

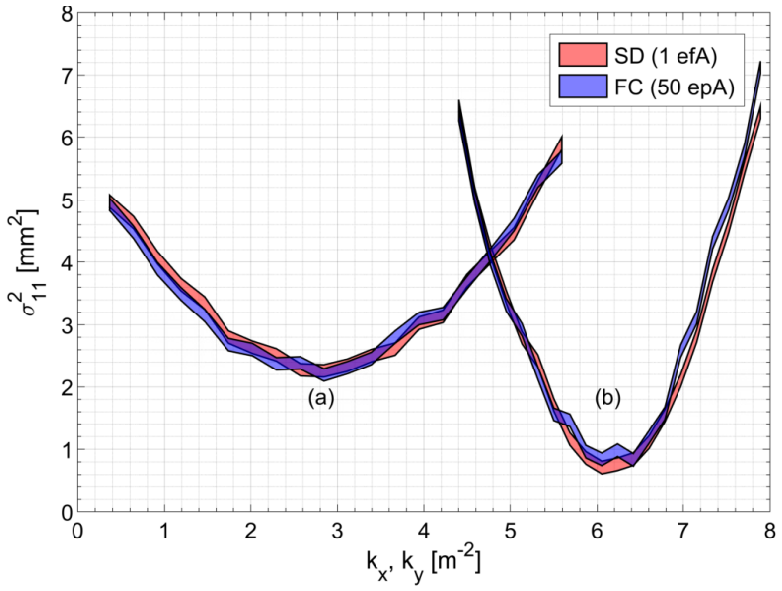

Figure 5.10. Comparison of quadrupole-scans on the x-plane (a) and the y-plane (b), at two ranges of intensity using a Faraday cup (FC) or a silicon detector (SD).

Table 5.3. Comparison of Twiss parameters transfered to z_4 and of the correlation parameter between quadrupole-scans acquired with a silicon detector (SD) and a Faraday cup (FC).

Plane	**Parameter**	**Value SD**	**Value FC**
x-plane (a)	ε_x [π.mm.mrad]	0.80(5)	0.82(5)
	α_x	$-0.10(15)$	0.05(15)
	β_x [mm.mrad^{-1}]	4.8(5)	5.1(5)
	γ_x [mrad.mm^{-1}]	0.21(3)	0.20(3)
	$\chi^2_{SD/FC}(\sigma^2_{11})$	0.988	
y-plane (b)	ε_y [π.mm.mrad]	0.71(5)	0.75(0.5)
	α_y	$-0.64(15)$	$-0.60(15)$
	β_y [mm.mrad^{-1}]	2.4(3)	2.8(3)
	γ_y [mrad.mm^{-1}]	0.25(11)	0.23(9)
	$\chi^2_{SD/FC}(\sigma^2_{11})$	0.984	

5.4.4 Beam Tomography from Quadrupole-Scans

The objective underlying to beam tomography is the reconstruction of the phase space distribution from multiple transformed projections. The beam profiles acquired

during quadrupole-scan measurements are rotated and compressed back-projections of the phase space at the quadrupole location. The coordinates of the phase space sliced at the scanning slit location are transfered back to the entrance of the apparatus. The transfer matrix R from Equation 5.34 is characterized by a rotation angle θ and a homothety factor s, following the same formalism as developed in [Hock et al., 2014].

$$\tan(\theta) = \frac{\mathcal{R}_{12}}{\mathcal{R}_{11}} \quad s = 1/\sqrt{\mathcal{R}_{12}^2 + \mathcal{R}_{11}^2} \tag{5.36}$$

Let's call the searched beam phase space distribution $f(u, u')$, entering the quadrupole-scan apparatus. The count-rate or current measured at the collector $c_k(\theta)$ is a projection along the coordinate t at the slit-position k,

$$c_k = \int_{\mathbb{R}} f(k, t)dt \tag{5.37}$$

The transformation from the coordinates (u, u') before the quadrupole and the coordinates (k, t) at the location of the collector is given by,

$$\begin{pmatrix} u \\ u' \end{pmatrix} = s \begin{pmatrix} \cos\theta & -\sin\theta \\ \sin\theta & \cos\theta \end{pmatrix} \begin{pmatrix} k \\ t \end{pmatrix} \tag{5.38}$$

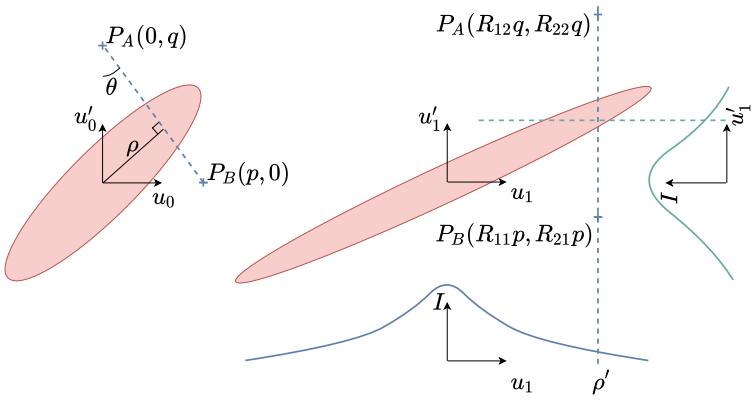

Figure 5.11. Drawing showing the transformation of the phase space ellipse and the tomography variables.

An algorithm was developed to reconstruct the phase space distribution $f(u, u')$ from rotated back-projections, by making use principally of the inverse Radon

transform and a re-scaling of the axis. The total angular amplitude swept during the quadrupole-scan measurements presented in the previous section are $\Delta\theta_x = 50\,\text{deg}$ and $\Delta\theta_y = 20\,\text{deg}$. It was chosen not to perform any tomography on the y-plane as the angular amplitude does not allow for enough coverage of the beam features, drastically weakening the coherency of reconstruction through the algorithm. The result of tomographic reconstruction of the quadrupole-scan measurement on the x-plane at very low intensity, is displayed in the Figure 5.12. Already with $\Delta\theta_x = 50\,\text{deg}$, the reconstruction shows patterns of irregular noise distribution (the beam appears slightly pinched) due to the impartial sweeping of the phase space. In fact the angular amplitude of the sweeping defect is particularly visible on the raw data obtained after processing the inverse Radon transform. An additional threshold of 4 % of the maximum intensity was eventually introduced in order to arbitrarily match the resulting measure of the emittance with the value derived prior reconstruction.

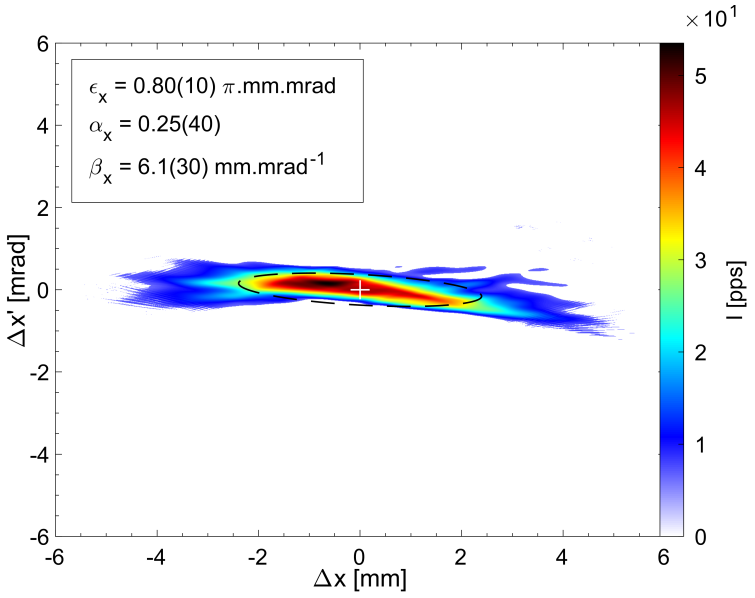

Figure 5.12. Tomography from quadrupole-scans measurement using a beam of $^{39}K^{10+}$ at a sub-efA intensity.

The additional uncertainties introduced by tomographic reconstruction and inherent to the algorithm or the measurement apparatus and especially the angular amplitude $\Delta\theta_x$, considerably increased the error-bars on the derived Twiss parameters. However the tomographic reconstruction does not directly suffer from the use of a silicon detector as a beam collector, or from the simple fact of probing very low

intensity ion beams. The uncertainties could be reduced by improving the algorithm and for instance by including maximum-entropy optimization [Minerbo, 1979]. The dependence of the tomographic reconstruction quality, strictly on the apparatus and angular amplitude $\Delta\theta$, may also indicate a level of confidence to derived Twiss parameters from the regular quadrupole-scan method.

5.4.5 Consistency and Convergence

The Twiss parameters that were calculated for the x-plane using two ranges of ion beam intensity and different methods of reconstruction are summarized in Table 5.4. The only values directly reconstructed at the location z_4 are from the double-slit measurements, otherwise the Twiss parameters or phase space coordinates were transferred to match the same beam optics. The global consistency between the methods reinforce the trust in the viability of using a silicon detector to collect the beam current and the feasibility to probe the transverse ion beam intensity in sub-efA range. The statistical and systemic uncertainties measured from series of the same type of measurement are coherent with what is to be expected from the analytical models used and from the apparatus finite resolution. So far we have considered the deviations introduced by the different apparatus of quadrupole-scans or double-slit method as purely statistical because dependent on the set of data points, nevertheless when strictly comparing one method, for instance quadrupole-scans proceeded the same way and only changing the type of beam collector, the agreement between results is generally below one standard-deviation. In such case the uncertainties due to the model of the apparatus can be considered as systematic and influencing the Twiss parameters derivation the same way independently from the technique engaged in the beam collection.

The value I in Table 5.4 corresponds to the intensity of $^{39}K^{10+}$ beam entering the measurement zone (in Figure 5.2). As the average beam intensity in the Twiss-ellipse $\langle c_k \rangle_{\mathscr{E}}$ is naturally more reduced with the double-slit method than with the quadrupole-scan, the input intensity was adjusted for measurements using a silicon detector so that $\langle c_k \rangle_{\mathscr{E}}$ are comparable, and with the aim of comparing the respective

duration to reach the quoted precision. Between the two methods only the number of scans would differ, meaning that quadrupole-scans were done for twenty different values of focusing strengths, the double-slit method achieved with forty different position of the rear slit. Fundamentally the double-slit method requires more time because of the full phase space reconstruction and in our case twice more time than the quadrupole-scan method to reach similar uncertainties. In terms of absolute uncertainties however, the latter statement is limited to beam with phase space distributions close to an ellipse. As observed with tomographic reconstruction, the quadrupole-scan method convergence depends notably on the angular width swept on the phase space, in that context similarly to the double-slit method, so the derivation of Twiss parameters would quickly diverge from reality with a non-elliptic beam and limited angular coverage. All convergence times quoted depend on $\sqrt{\langle c_k \rangle_{\mathscr{E}}}$ and the repetition rate of the post-accelerator (20 Hz), but the duration of quadrupole-scans is also a consequence of the type of beam phase space distribution.

Table 5.4. Summary of results obtained with different methods of transverse characterization and using two main ranges of current for $^{39}K^{10+}$ beam, at 3.8 MeV/u.

Method	I [epA]	$\langle c_k \rangle_{\mathscr{E}}$ [pps]	ε_x [π.mm.mrad]	α_x	β_x [mm.mrad^{-1}]	γ_x [mrad.mm^{-1}]	$F_x(\mathscr{E})$ [%]	Time [mn]
Double-slit	50	1.4×10^5	0.76(6)	0.01(15)	5.5(8)	0.18(3)	39	20
Double-slit	1×10^{-3}	20	0.81(6)	0.08(15)	4.4(8)	0.23(5)	41	40
Quad-scan	50	7.2×10^5	0.82(5)	0.05(15)	5.1(5)	0.20(3)	-	10
Quad-scan	3×10^{-4}	30	0.80(5)	−0.10(15)	4.8(5)	0.21(3)	-	20
Tomography	3×10^{-4}	30	0.80(10)	0.25(40)	6.1(30)	0.15(15)	35	20

5.5 Variations of Transverse Beam Properties

Several tests were done for consolidating the new methodologies of transverse beam properties characterization. The first test consists in emulating an emittance growth by varying the breeding time of REXEBIS. Finally, the transverse emittances of very low intensity ion beams are measured for different energies accessible by HIE-ISOLDE linac.

5.5.1 Changes of Initial Ion Temperatures

It was chosen to put into application the newly developed methodologies with a practical case that can highlight variations of the transverse beam properties. An emittance growth occurs when the temperature of ions inside the REXEBIS charge breeder is increased due to Spitzer heating, as was demonstrated in Chapter 2. A way to emulate an emittance growth is to increase the trapping time of REXEBIS. Furthermore, the composition of the beam changes when the trapping time deviates from the optimal value for the stable beam that was used, $^{39}K^{10+}$. In particular, with trapping times above 30 ms another beam of $^{133}Cs^{34+}$ coming from the same ion source is now accelerated and mixed with the $^{39}K^{10+}$ beam.

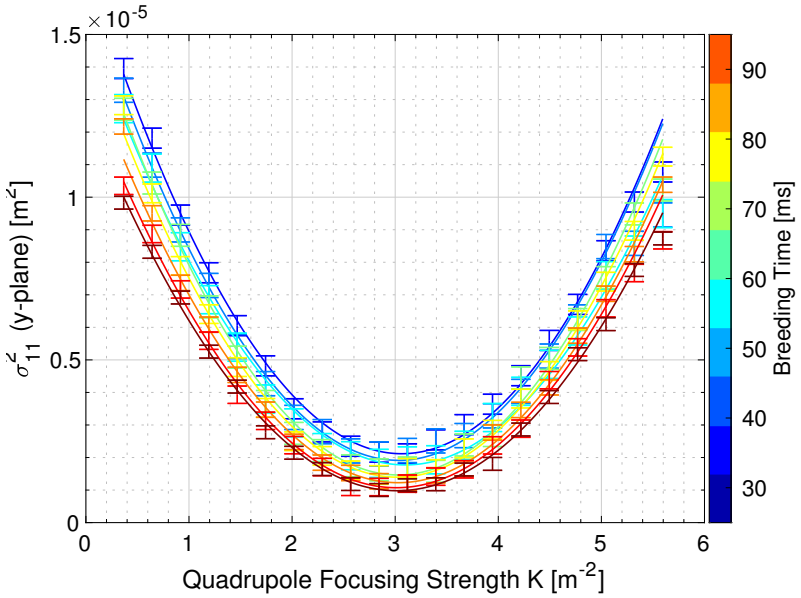

Figure 5.13. Raw results of the quadrupole scans operated using a 1 efA beam of $^{39}K^{10+}$ and $^{133}Cs^{34+}$ at 3.8 MeV/u for different REXEBIS trapping periods.

The electron beam current of REXEBIS was at 160 mA during those measurements. Several batches of quadrupole-scans were acquired when varying the breeding time from 25 to 95 ms. It is to be noted that the conditions of the charge breeding and heating of the ion source were different from the previous section - strictly dedicated to comparison with regular techniques - resulting in different Twiss parameters although the beam energy is similar. The quadrupole-scans in Figure 5.13 are presented without treatment of the threshold but already display a clear tendency. After selecting the adequate threshold, the Twiss parameters are derived. Silicon detectors also offer the potential to record the energy information of incoming ions. It is then possible to determine the composition of the beam during the transverse emittance scans. The fraction F of $^{39}K^{10+}$ inside the beam varies from 95 % to less than 50 % when increasing the breeding time of REXEBIS.

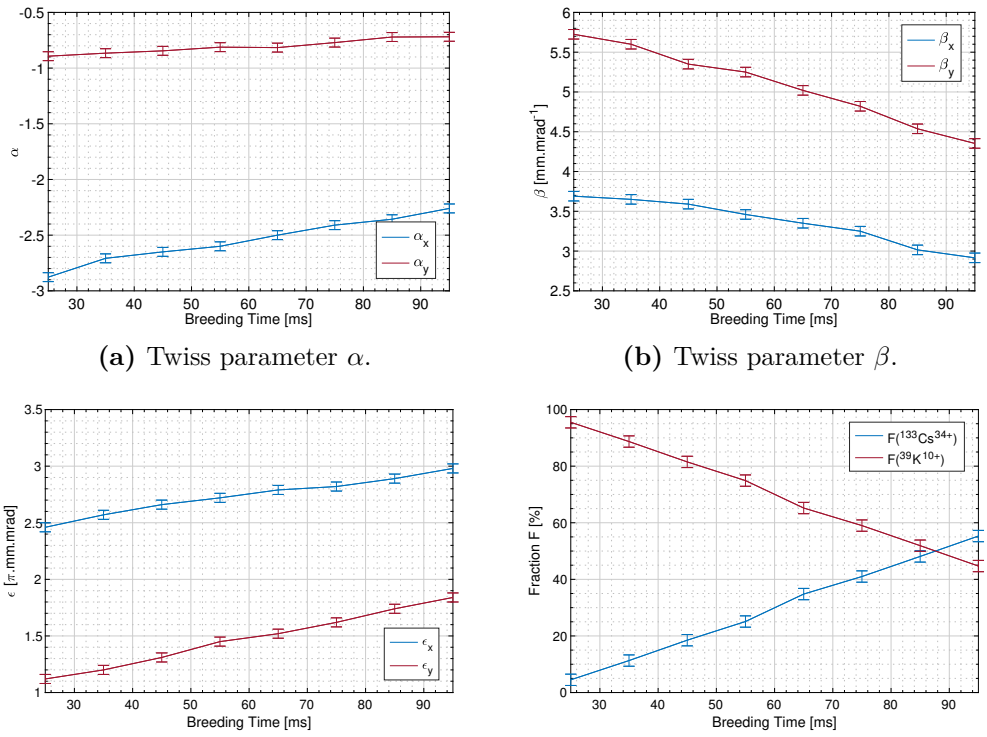

(a) Twiss parameter α.

(b) Twiss parameter β.

(c) Emittance ε.

(d) Purity Fraction F.

Figure 5.14. Evolution of Twiss parameters and emittance when varying the REXEBIS charge breeding time, resulting in change of the fraction of $^{133}Cs^{34+}$ and $^{39}K^{10+}$.

The emittance on the x-axis increases by 20 % while the emittance on the y-axis increases by 60 %. Those discrepancies may be explained by the different apertures

along the linac, starting from the vertical slit of the A/q-Separator. A proper investigation of the effect of the charge breeding conditions on the beam emittance would require performing the quadrupole scans as close as possible from the EBIS. However, those measurements indicate that the resolution of the quadrupole-scan using a beam collector measurement allows identifying the trend of the emittance growth during the typical conditions of operation.

5.5.2 Normalized Emittance and Beam Energy

The beam energy used for the previous measurements was 3.8 MeV/u, which was an arbitrary choice representative of a typical energy reachable by HIE-ISOLDE linac. The capabilities of silicon detectors for transverse beam property characterization were then demonstrated for higher energies. The total energy deposited on the silicon detectors must remain bellow the saturation of the detector and its preamplifier. When the measurements were conducted, the preamplifier was with a saturation limit at 500 MeV and was later changed for a more optimized limit of 2 GeV.

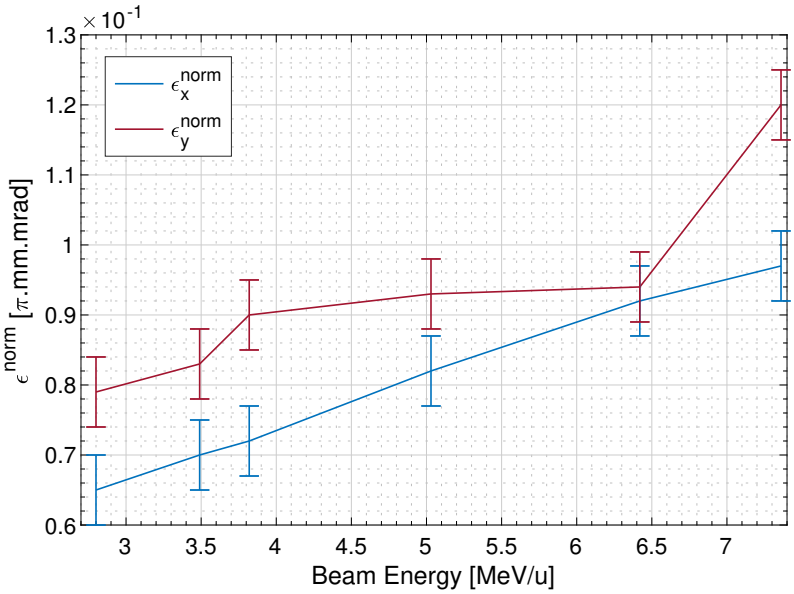

Figure 5.15. Measurement of the normalized emittance of $^{39}K^{10+}$ beam using the quadrupole-scan method for different beam energies. The average intensity of the beam was approximately 1 efA.

The corresponding curves of the accessible masses per beam energy are shown in Chaper 2 (figure 2.27). The interest is this time driven by the analysis of the

emittance rather the Twiss parameters, and more particularly the variations, if any, of the normalized emittance. The beam used was similar as the Setup 1 presented in Table 5.2: $^{39}K^{10+}$ with an intensity of 0.6 efA but this time different beam energies. The number of superconducting cavities used for acceleration is varied, between zero (2.8 MeV/u) and thirteen (7.3 MeV/u). Six different setup of the linac were used, and quadrupole-scans performed using the silicon detector in DB.3 (Figure 5.3). The normalized emittance tends to increase when utilizing more superconducing RF cavities but remains below 0.12 π.mm.mrad (Figure 5.15). The relative energy spread varied between 0.8 % and 1.1 % for the different setups. The beam energy distributions were measured using the technique presented in the next chapter.

CHAPTER 6

Longitudinal Beam Properties Characterization

Beam energy measurements are essential to demonstrate the performance of particle accelerators. Another aspect justifying on its own to examine the energy of the beam delivered to experimental stations is the paramount influence on the underlying data analysis. Knowing the average beam energy is necessary, however often not sufficient and must be accompanied with a statistical description of uncertainties or relative deviations. Due to the relatively low yields in the context of exotic RIBs, the precise characterization of the energy distribution reveals to be challenging. The first section of this chapter will review the three available techniques at REX/HIE-ISOLDE for measuring the beam energy. The limits and uncertainties associated with the chosen methodology are discussed. We present results of the measured RIBs energy distributions during a typical year of Physics campaign.

Minimizing the beam energy spread or trying to optimize it is a great leap from the simple characterization of the energy profile; nevertheless, an initial velocity spread is undesirable for probing nuclear mechanisms. A current example is the ISOLDE Superconducting Solenoid apparatus resolution (ISS experimental station), which notably relies on a low beam energy spread. The first step to reducing the beam energy spread at experimental stations is to apprehend the evolution of the longitudinal beam properties through the linac. Based on the possibilities offered by HIE-ISOLDE superconducting cavities, we will describe two experimental methods allowing the characterization of longitudinal beam properties for very low-intensity

ion beams. The consecutive sections will concern the measurement results, analysis of uncertainties and comparison between methods.

6.1 Energy Measurement of Radioactive Ion Beams

Beam energy measurements are of fundamental interest for the validation of linac performance and, later, to analyse the Physics campaign data. Similarly to previous chapters concerning beam intensity and transverse beam properties measurements, the capability of measuring weak beams will be at the centre of the demonstration. The silicon detectors installed along the linac allow for direct and indirect measurement of the beam energy. Indirect measurement with a silicon detector implies using other instruments to achieve a measure of the beam energy distribution. Three different techniques to probe the energy distribution were identified, although only one method is preferred during operation. This introductory section aims at giving an overview of the available techniques and at explaining the reasons which lead to consider the energy spectrometer method as the most efficient.

6.1.1 Direct Silicon Detector Measurement

The deposition of a charged particle impinging on a silicon detector creates an analogue signal that translates into a measure of the particle energy after calibration. During the preliminary studies for the HIE-ISOLDE project, an agreement was reached on a specific silicon detector model and judging that it would be out of the scope of those studies, the solid-state physics phenomena governing the detector will not be reported hereafter. Canberra, the silicon detector manufacturer, provides data-sheets with information related to the energy resolution (FWHM) given for ^{241}Am 5.486 MeV alpha particles (Table 2.10).

Several tests were initiated to evaluate the possibility of using the direct energy measure provided by silicon detectors. By using a beam composed of different masses at $A/q = 4$, one reads the dispersion in the resolved energy per mass from the raw energy histogram obtained from the digitizer. The dispersion is not regular as a function of the mass and not easily readable (Figure 6.1 (b)). In fact, each silicon detector of the post-accelerator shows different behaviour in terms of absolute energy response and would require individual calibration. The reliability is additionally put at strain by the radiation damage on the silicon. A uniform deterioration of the

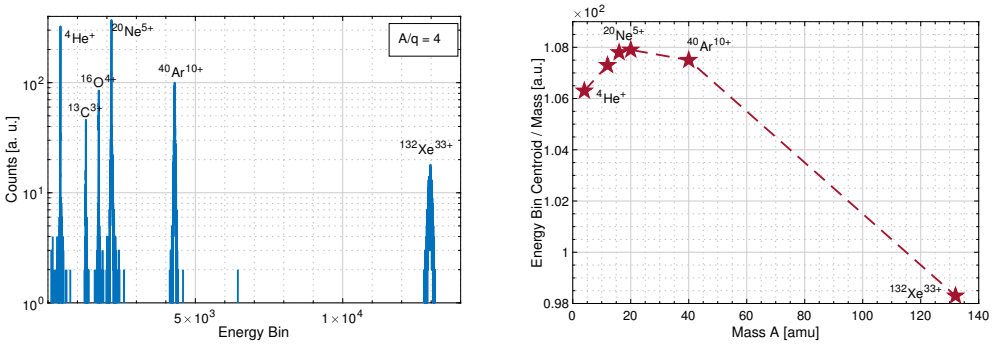

(a) Raw energy spectrum. **(b)** Deviation from total energy.

Figure 6.1. Analysis of the raw energy histogram measured for a beam at $A/q = 4$ with an energy $W = 2.8 MeV/u$. An energy bin corresponds to 7.6 keV.

silicon results in a larger energy resolution and shift in absolute energy output. A silicon detector installed in the HEBT lines showed an irregular deterioration of the silicon on its surface, probably due to a damaging exposure to a focused beam. By using a 1 mm-diameter collimator, we scanned the detector surface with a beam at an energy of 2 MeV/u.

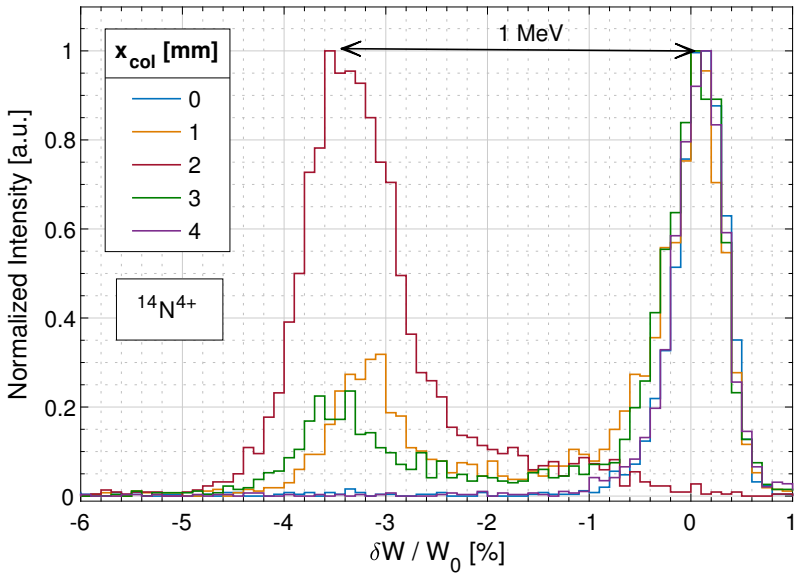

Figure 6.2. Energy spectra acquired from $^{14}N^{4+}$ beam at $W_0 = 2\,\mathrm{MeV/u}$ through a 1 mm-diameter collimator with a displacement off-axis noted x_{col}.

The resulting energy spectra show an apparent discrepancy when exposing the damaged spot of the silicon detector. The relative energy deviation is approximately

3.5 % which is several times above the expected energy spread of the beam (Figure 6.2). The absolute value of the beam energy is not measured with enough certainty from the silicon detectors installed at REX/HIE-ISOLDE to use this method. The resolution of the detector (measured energy spread) is also not linear as a function of the mass, which complicates further the use of such a method.

6.1.2 Relative Time-of-Flight measurement

Silicon detectors also allow measuring the Time-of-Flight (ToF) of impinging ions with precision down to RF-bucket structure. By using two silicon detector spaced by a distance L along the HEBT line, the average velocity is determined from the difference in ToF. Typically with a relativistic beta factor $\beta = 10$ %, the difference between the arrival times is $\Delta t[\beta = 0.1] \simeq 33.4$ ns/m. In order to proceed to this type of measurement, the effective cable lengths between the detectors and the front-end were measured to assure similar transmissions of the signals. The resolution of the measurement is limited by the minimum sampling precision of 50 ps achievable by the Time-to-Digital Converter. One may calculate the minimal underlying energy resolving power. The first relativistic derivative of time relate to the velocity by,

$$\mathrm{d}t = \mathrm{d}\left(\frac{L}{\beta c}\right) = -\frac{L}{c}\frac{\mathrm{d}\beta}{\beta^2} \tag{6.1}$$

Then we can change variables from relativistic velocity to kinetic energy W by expressing the (logarithmic) first derivative of β in such a way,

$$\frac{\mathrm{d}\beta}{\beta} = \frac{1}{\gamma(\gamma+1)}\frac{\mathrm{d}W}{W} \tag{6.2}$$

For $\beta = 0.1$, and $\mathrm{d}t = 50$ ps, the minimum resolution achievable of relative energy distribution per meter between the detectors is $\mathrm{d}W/(WL) \simeq 3.10^{-3}$ m^{-1}. This resolution is a lower boundary of the uncertainty associated with the measured beam energy. Globally, the method has revealed to be reliable for absolute energy measurement but with uncertainties limiting the energy spread resolution.

6.1.3 Energy Spectrometer Measurement

The methodology that is deemed the most reliable for measuring the beam energy distribution at REX/HIE-ISOLDE is a type of spectrometry using a dipole magnet. After presenting several results of energy measurements, we will outline the associated uncertainties with the help of simulations.

a Experimental Setup

At this stage, the beam energy and intensity are sufficiently low to use slits without risking damaging the material. By inserting two vertical slits (VS1 and VS2) in the linear part of the HEBT line, before one of the three bending dipoles, we slice the beam into a thin beamlet. Then we make use of the first dipole of the bending lattices similarly to an energy spectrometer. A third vertical slit (VS3) is inserted after the dipole and right before a silicon detector to assure that the acquired resulting beamlet is centred horizontally relative to the detector (Figure 6.3). The triplet before the first slit is turned off, as well as the focusing and steering elements to the detector, to reduce the induced spread by measurement apparatus. The silicon detector is operated far from saturation, in count rate mode, and provides the intensity of beamlet passing through the three slits.

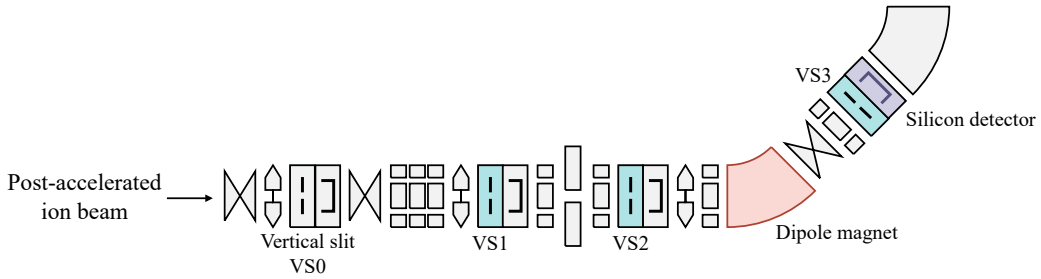

Figure 6.3. Experimental setup for beam energy measurement representing one branch of REX/HIE-ISOLDE HEBT lines. The three vertical slits, the dipole magnet and the silicon detector are grayed.

The number of ions detected on the silicon detector is measured as a function of the dipole magnetic field. As the product of relativistic factors $\beta\gamma$ is directly related to the momentum and the rest energy of the particle E_0, one can rewrite the dipole

equation (Equation 2.96). The relation obtained involves an implicit quantifiable of the beam energy, as a function of the magnetic field of the dipole B, its effective radius ρ, the mass-to-charge ratio A/q, the equivalent rest energy of an atomic mass unit E_0^u and the speed of light in vacuum (Equation 6.3). From the product of relativistic terms $\beta\gamma$, one can extract the total energy W.

$$\beta\gamma = \frac{cp}{E_0} = \frac{cB\rho}{E_0^u}\frac{q}{A} \tag{6.3}$$

The procedure for performing a beam energy scan is implemented in a stand-alone application ([E. Matli, 2019]) and is available as a programmable script for the Automation application described in Chapter 2. The dipole magnet is field regulated, and one generally sweep around the optimal field value by steps between of 0.5 to 2 mT. The acquisition of the particle count rate is synchronized with the read magnetic field value during the post-treatment.

b Identified Uncertainties

The energy spectrometer method using the dipole and three vertical slits and silicon detector acquisition does not give a direct measurement of the beam energy distribution. The measured energy distribution is a convolution of the real distribution and the spread introduced by the measurement apparatus. Ideally, one would want the measurement apparatus - the probing tool - to be similar to a Dirac function, precisely measuring the actual energy distribution. However, due to the finite opening of the slit width (1 mm) combined with the horizontal emittance of the beam, the measurement channel introduces an inevitable spread that needs to be determined. This inherent spread of the energy spectrometer is dependent on the initial beam energy distribution. A Monte Carlo method was developed using Matlab to estimate the product of convolution introduced by the measurement channel. The dipole characteristics and its effective dipole radius are taken from Table 2.9. An example of the tracking is given in Figure 6.4 for arbitrary dimensions.

The magnetic field model implemented in the simulations is with hard-edges delimited by the pole-face rotations, which are visually represented by black dashed lines in Figure 6.4. Considering the length between the two first slits and the typical

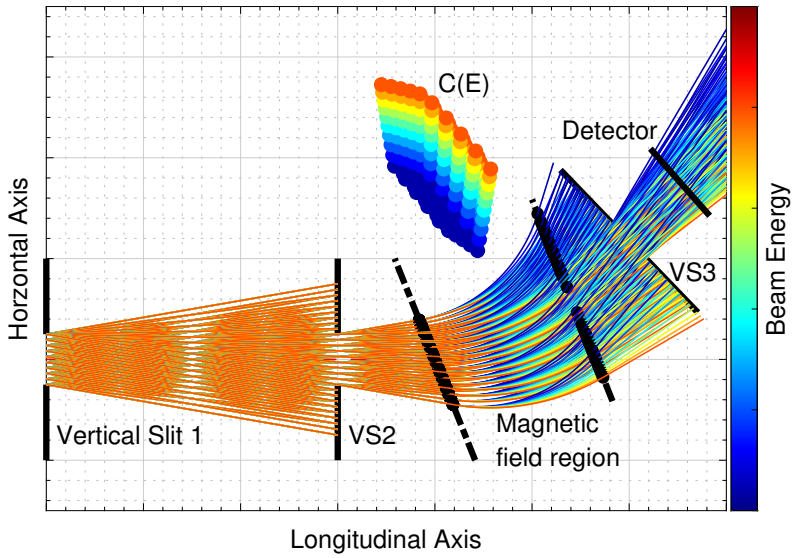

Figure 6.4. Monte Carlo trajectory tracking simulations of the energy distribution measurement apparatus, using arbitrary dimensions and beam properties for visual representativeness.

transverse beam emittance at REX/HIE-ISOLDE, it is considered that the beam fills the horizontal phase space acceptance of each slit. We choose to examine the energy distribution at the collector from an initial beam with uniform energy distribution. The output energy distribution, measured at the collector, resembles a Gaussian with a characteristic standard deviation noted σ. To a certain extent, this response is analogous to a Point Spread Function for the spectrometer system. The determined σ is the maximum spread introduced by the slit width and the global geometry of the system coupled with the transverse beam characteristics. When varying the distance between the first two slits, from a configuration using VS.1 and VS.2 to an arrangement with VS.0 and VS.2, the spread introduced by the system reduces as expected. The benefit of using a long distance between the first two slits is shown in Figure 6.5a (a).

The Monte Carlo methods allow to easily test the impact of a misalignment of the slits or the uncertainty related to the magnetic field probe. This latter uncertainty is simulated to be negligible in our context. The uncertainty on the slit position, which is estimated to be 0.1 mm from alignment studies, necessarily

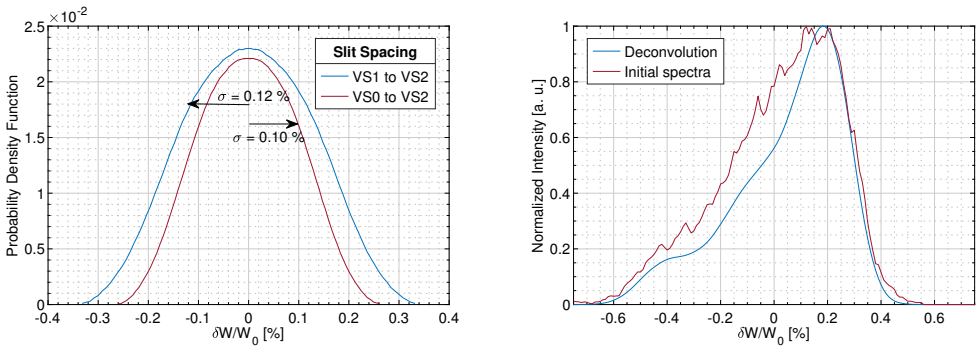

(a) Induced spread from spacing between the first two slits.

(b) Example of deconvoluted energy distribution.

Figure 6.5. Results from simulations on the influence of slit geometry (a) and deconvolution of a measurement of a $^{224}Rn^{52+}$ beam at 5.98 MeV/u (b).

affects the spread introduced by the energy spectrometer. Rigorously, one defines an effective slit opening in the simulation model that emulates the influence of misalignment. Finally, the measured beam energy distribution may be deconvoluted by using an iterative process aiming at minimizing the residuals between the initial spectra and the reconvolution of the results. A typical result of deconvolution from measured data using a beam of $^{224}Rn^{52+}$ ($W = 5.98$ MeV/u) is presented in Figure 6.5 (b). The variations of the initial distribution strongly impact the efficiency of the deconvolution, so it is common to use noise reduction in the frequency domain, which visibly results in smoothing.

c Commissioning of the Methodology

The energy spectrometer method was commissioned using pilot beams in order to evaluate the statistical requirements for reaching a satisfactory standard deviation on the measured distribution. The beam intensity is modulated using attenuation foils inserted before the RFQ, so that the intensity at the silicon detector remains below the saturation limit. The method was commissioned using a well optimized post-accelerator setup for a beam of $^{20}Ne^{8+}$, accelerated by ten superconducting cavities. The typical peak intensity at the collector was kept below 40 pps, It is usually prefered to repeat several scans of, for instance, few minutes and accumulate the data, rather than perform slow scans. After a series of five scans of two minutes

each, the standard deviation is within 1 % confidence interval.

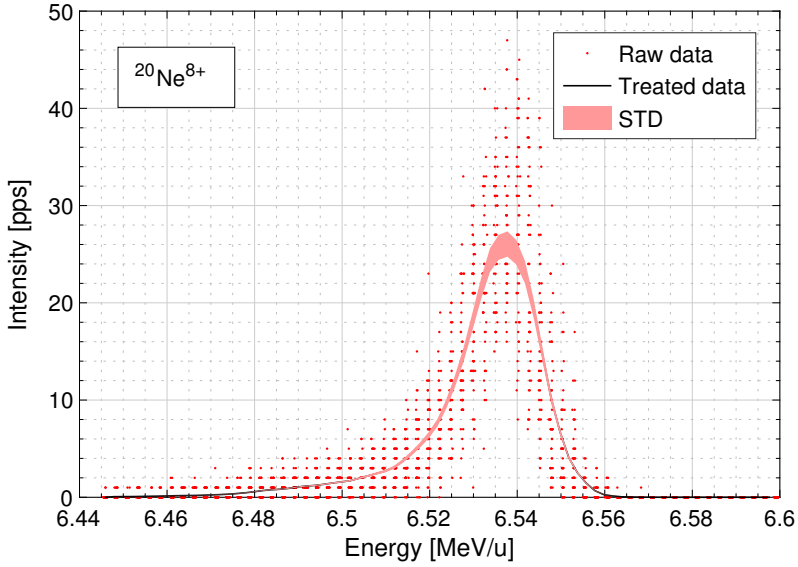

Figure 6.6. Measurement of the beam energy distribution of 20Ne^{8+} using a dipole as a spectrometer and acquiring the intensity with a silicon detector.

The raw data of such accumulated scans is displayed in Figure 6.6 with the standard deviation associated with each data point.

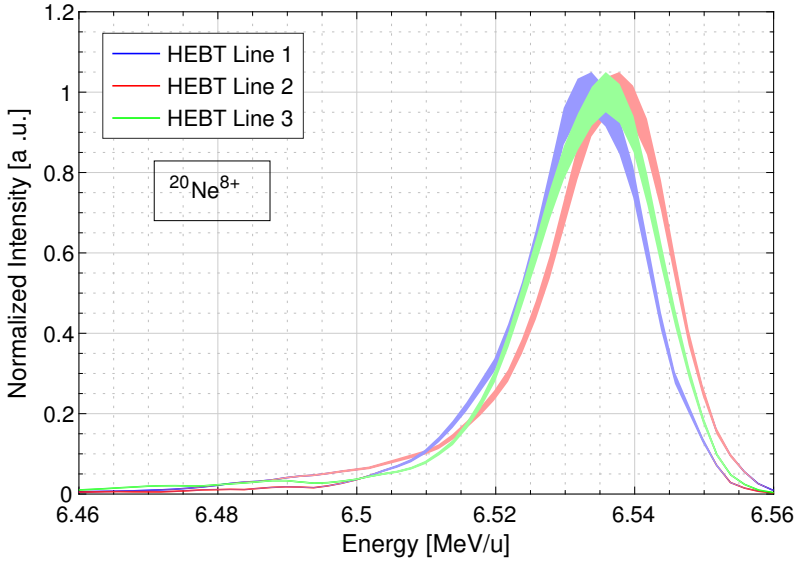

Figure 6.7. Comparisons of the energy distribution of 20Ne^{8+}, measured using each of three HEBT lines dipoles.

As three dipole magnets in combination with silicon detectors are available, it is

practical to observe the matching between the energy distributions measured from each spectrometer of the HEBT lines. The agreement between the measurements, as presented in Figure 6.7, demonstrate the reliability of such a method. Despite the difference in the slit positioning of each energy spectrometer apparatus, the measured distributions fall within each other statistical confidence interval.

d Energy Distributions of Radioactive Ion Beams

Beam energy characterizations were done routinely during the physics campaign, with at least one energy distribution measurement per high-energy physics run. They are representative cases of the difficulty to probe exotic ion beams. Two energy distributions are illustrated in Figure 6.8 for $^{106}Sn^{26+}$ (a) and $^{28}Mg^{9+}$ (b) with average energies of, respectively, 4.41 MeV/u and 9.49 MeV/u. Before slicing those RIBs with three vertical slits, the intensities were between 10^5 and 10^6 pps. Therefore, it was necessary to modulate this intensity to avoid saturation of the detection system. The preamplifier used at the time of the measurement was limited to 500 MeV/pulse, which in the case of masses higher than 100 atomic mass unit basically limits the count rate to a single ion per pulse. The duration of the measurement is consequently extended to meet the statistical requirements in terms of accuracy, which are generally a 0.1 % precision on the average energy and 10 % on the standard deviation.

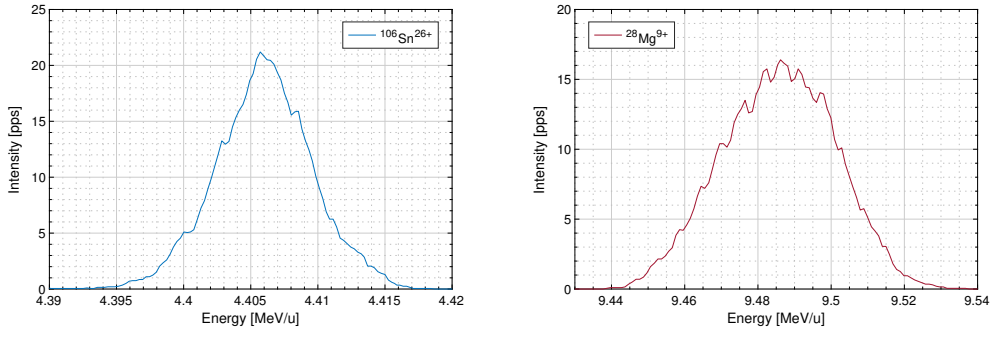

(a) $^{106}Sn^{26+}$ **(b)** $^{28}Mg^{9+}$

Figure 6.8. Energy distribution measurements of two RIBs acquired using a dipole as a spectrometer and a silicon detector as beam collector.

The results of energy measurement for eight of the ten RIBs were compared

with the pilot beams used for setting up the post-accelerator (Table 6.1). In several cases, the discrepancies between the average energies measured for pilot beam and RIBs exceed the confidence interval of 0.1 %. The complexity of the post-accelerator sub-systems makes the task of identifying the source of discrepancies difficult within the frame of this thesis. Nevertheless, it justifies the motivation for directly probing RIB in situ rather than relying on measurements using pilot beams of higher intensities. We did not identify a direct correlation between the $\Delta(A/q)$ required by the scaling of the post-accelerator from the pilot beam to RIB and the deviations measured in terms of average energy or standard deviation. In fact, during a year of physics campaign, the energy spread of the RIB was not necessarily optimized each time. For instance, the measured standard deviations of $^{222}Ra^{51+}$ and $^{222}Rn^{51+}$ are different by a factor of three despite the similarity of the beam in terms of A/q-ratio. This is because a specific work was made to reduce the energy spread for the beam of $^{222}Rn^{51+}$. With the growing maturity of REX/HIE-ISOLDE linac, the stability of the accelerating cavities will improve. At the time of the measurement, various issues were being assessed concerning the operation of the 9GAP IH-Structure and the stability of a few of the newly installed superconducting cavities. Those questions were progressively solved during the year but necessarily resulted in discrepancies between the longitudinal characteristics of the RIBs delivered to experimental stations. The methodology for measuring the energy distribution of RIBs met all requirements in terms of reliability and accuracy and revealed to be essential during the conduct of the physics campaign.

Table 6.1. Non-exhaustive list of average energies and spread, for RIB and the associated pilot beam measured during a year of physics campaign. The pilot beams noted with an asterisk (*) are superimposed with $^{12}C^{3+}$.

RIB energy profiles				**Pilot beam energy profiles**		
Isotope	μ [MeV/u]	σ [keV/u]	I [pps]	Isotope	μ [MeV/u]	σ [keV/u]
$^{28}Mg^{9+}$	9.486(9)	14(2)	1.10^6	$^{22}Ne^{7+}$	9.438(9)	6(1)
$^{206}Hg^{46+}$	7.374(8)	17(2)	1.10^6	$^{40}Ar^{9+}$	7.388(8)	10(2)
$^{224}Rn^{52+}$	5.082(5)	19(2)	1.10^5	$^{129}Xe^{30+}$	5.060(5)	19(2)
$^{96}Kr^{23+}$	4.723(5)	13(2)	3.10^3	$^{129}Xe^{31+}$	4.705(5)	14(2)
$^{106}Sn^{26+}$	4.406(5)	4(1)	1.10^5	$^{16}O^{4+}$*	4.408(5)	21(2)
$^{212}Rn^{50+}$	4.354(5)	24(3)	1.10^7	$^{16}O^{4+}$	4.361(5)	18(2)
$^{228}Ra^{53+}$	4.314(5)	15(2)	3.10^5	$^{40}Ar^{9+}$	4.310(5)	13(2)
$^{222}Ra^{51+}$	4.308(5)	21(3)	6.10^5	$^{40}Ar^{9+}$	4.310(5)	13(2)
$^{222}Rn^{51+}$	4.230(5)	5(1)	6.10^5	-	-	-.
$^{142}Ba^{33+}$	4.192(5)	17(2)	1.10^6	-	-	-

6.2 Longitudinal Beam Properties Measurements

The objective of reducing the beam energy spread at the end of the HEBT lines starts by characterizing the longitudinal properties of the beam. Two methods are validated, relying on repeated measurements of the energy or of the ToF, for different configurations of the phase space ellipse. The assumptions stemming from the theory of beam physics are equivalent to the ones expressed in Chapter 5. Two methods are presented that allow for the longitudinal characterization of very low-intensity ion beams.

6.2.1 Longitudinal Phase Space

The description of the longitudinal motion of charged particles accelerated through REX/HIE-ISOLDE linac provides the analytical tools to quantify the evolution of the beam energy and ToF. Equivalently to what is presented in Chapter 5, the beam properties are derived from multiple known transformations of the phase space ellipse and the measurements of projections.

a σ-Matrix

The longitudinal phase space is treated independently from the transverse motion. In the same way that the coupling from longitudinal motion to the transverse motion was considered negligible in Chapter 5, the reciprocal is also true within this chapter. The longitudinal σ-matrix, is treated in dimension two using the following parameters:

$$\sigma_z = \epsilon_z \begin{pmatrix} \beta_z & -\alpha_z \\ -\alpha_z & \gamma_z \end{pmatrix} \tag{6.4}$$

The variables chosen to describe the *phase space* or *trace space* are all equivalent possibilities of couples of independent physics variables that fully generate the vector space. For instance and non-exhaustively, one can describe the longitudinal trace space using the spatial bunch length (Δs) and the longitudinal momentum spread

(Δp) or the bunch phase spread ($\Delta\Phi$) and the relative longitudinal momentum spread ($\Delta p/p$). The transformation between the previously enunciated bases is simply homothetic. It is generally practical to represent the second momentum using a relative (normalized) variable due to the variety of beam energies used for RIB experiments. For longitudinal beam properties description, we choose as a couple of variables: the temporal bunch length noted Δt, in ns units, and $\Delta W/A$, and the energy spread per atomic mass expressed in keV/u. Using such convention seems common within the linac community dedicated to RIB. It is also justified here by the linac design orders of magnitude (π ns keV/u) derived in a comprehensive dimension for the longitudinal emittance. All longitudinal trace space transfer matrices will be consistently presented in a basis ($\Delta t_z, \Delta W_z/A$) at a position z along the ideal beam path.

b $\mathcal{R}$-Matrix

Before developing the reduction, which allows determining the longitudinal properties, the same procedure as the transverse phase space analysis is applied by defining useful beam transfer matrices. The linearized transport through n beam matrix elements is defined as follows,

$$\begin{pmatrix} \Delta t_n \\ \\ \Delta W_n/A \end{pmatrix} = (\prod_i \boldsymbol{\mathcal{R}}_{n-i}) \cdot \begin{pmatrix} \Delta t_0 \\ \\ \Delta W_0/A \end{pmatrix} \tag{6.5}$$

Drift Transfer Matrix

To the first-order and as long as the beam does not cross an accelerating structure, the optical transverse focusing elements will be seen by the longitudinal phase-space distribution as a drift section. We briefly derive here the longitudinal transfer matrix for a drift section of length L, by using equations 6.1 and 6.2 and applying those variations to the longitudinal phase space parameters during beam transport,

$$\Delta t = -\frac{L}{c}\frac{\Delta\beta}{\beta^2} = \frac{-L}{\beta\gamma(\gamma+1)c}\frac{\Delta W}{W} \tag{6.6}$$

Finally leads to the longitudinal phase space drift matrix,

$$\boldsymbol{\mathcal{R}}_{\mathrm{D}}(L) = \begin{pmatrix} 1 & \frac{-AL}{\beta\gamma(\gamma+1)cW} \\ 0 & 1 \end{pmatrix} \tag{6.7}$$

RF Gap Transfer Matrix

The gain of work of a charged particle in an electromagnetic field classically expressed by the path integral of Lorentz force and applied to an RF gap of length g and periodicity L (0.3 m). The Figure 6.9 shows the typical magnetic field longitudinal distribution inside the quarter-wave resonators (non-seamless design), which is simplified by a uniform model.

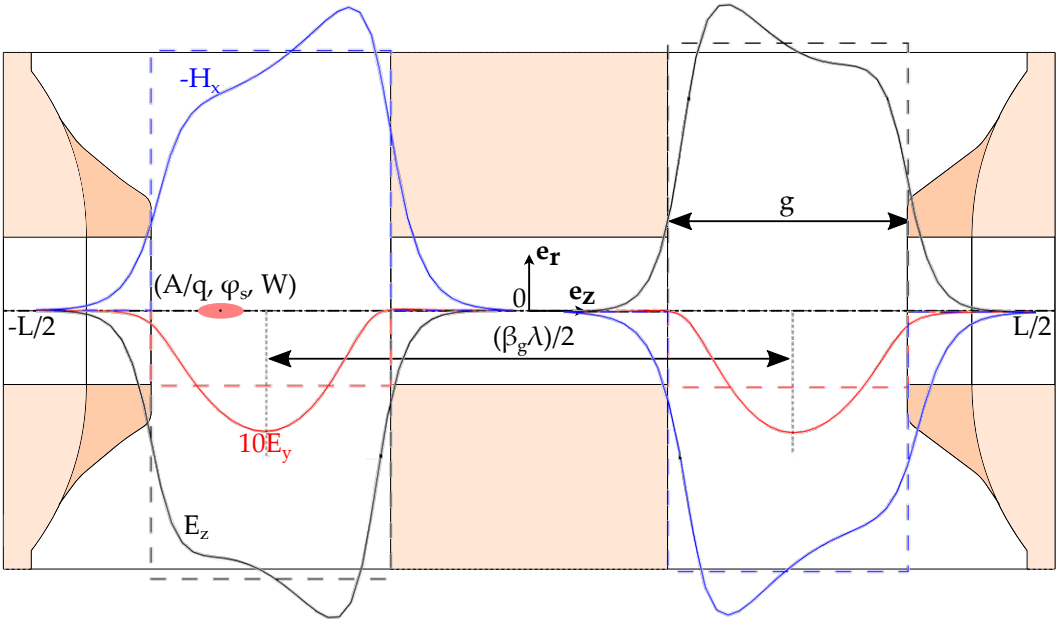

Figure 6.9. Schematic of a quarter-wave resonator with fields (adapted from [Fraser, 2012])

.

The cross-field contribution $|v_y B_x| << |E_z|$ is considered negligible and we consider an uniform radial energy distribution with a mean on $r = 0$. The time of arrival of the synchronous particle is noted t_s and one may decouple its differential into two parts: φ_s the phase at the origin ($z = 0$) and the longitudinal phase number $k_z = 2\pi/(\lambda\beta)$. Then, the differential of the phase of the field oscillations dψ appears

in the equation,

$$\omega \mathrm{d}t_s = \varphi_s + \frac{\omega}{\beta(z)c}\mathrm{d}z = \varphi_s + k_z(z)\mathrm{d}z = \varphi_s + \mathrm{d}\psi \tag{6.8}$$

The field felt by the charged particle is expressed as a function of the RF-gap field E_g,

$$E_z(z,t) = E_g(z)\cos(\omega t_s(z)) = E_g(z)[\cos(\varphi_s)\cos(\psi) - \sin(\varphi_s)\sin(\psi)] \tag{6.9}$$

Only under the assumption that the mean path integral of $E_z(z)$ has an average at the center of each gap, we may call φ_s the synchronous phase. We introduce the TTF term (T) from Equation 2.79, and the equivalent accelerating field $E_0 = V_0/L_a$, using V_0 from Equation 2.78 and the active length of acceleration L_a. The average energy gain through an accelerating gap is given by Equation 6.10. The variation of the energy spread, from ΔW_0 (entering the gap) to ΔW_1 (exiting the gap) is expressed by the change in energy relative to the synchronous particle,

$$\Delta W_1 - \Delta W_0 \equiv \Delta(W - W_s) = qE_0L_aT(\cos(\varphi_s + \Delta\varphi_0) - \cos\varphi_s) \tag{6.10}$$

With the thin lens cavity approximation, i.e. for low rate of acceleration and small oscillation, the term $\mathrm{d}\psi \ll 1$. The expression of the change in energy spread is then simplified,

$$\Delta W_1 - \Delta W_0 \equiv \Delta(W - W_s) = -qE_0L_aT\Delta\varphi_0\sin(\varphi_s) \tag{6.11}$$

One can finally deduce the transfer matrix of an equivalent quarter-wave resonator in the longitudinal trace space $(\Delta t, \Delta W/A)$,

$$\boldsymbol{\mathcal{R}}_{\mathrm{RF}}(E_0) = \begin{pmatrix} 1 & 0 \\ 1 & -2\pi f\frac{q}{A}E_0TL_a\sin(\varphi_s) \end{pmatrix} \tag{6.12}$$

Total Transfer Matrix

In order to simplify the expression of the total transfer matrix, consisting on the

drift and the RF-gap matrices, we introduce the terms,

$$\begin{aligned} K_D &= \frac{-AL}{\beta\gamma(\gamma+1)cW} \\ K_G &= -2\pi f \frac{q}{A} E_0 T L_a \sin(\varphi_s) \end{aligned} \tag{6.13}$$

The total transfer matrix from the center of a quarter-wave resonator to downstream location is,

$$\boldsymbol{\mathcal{R}} = \boldsymbol{\mathcal{R}}_{\mathrm{RF}} \cdot \boldsymbol{\mathcal{R}}_{\mathrm{D}} = \begin{pmatrix} 1 + K_D K_G & K_D \\ K_G & 1 \end{pmatrix} \tag{6.14}$$

It is also convenient for the derivations using the three-gradient method to introduce the variable $\tilde{K}_G$, such that $K_D = \tilde{K}_G E_0$.

6.2.2 Three-gradient Method

As its name indicates, the three-gradient method consists of measuring multiple (at least three) energy or ToF distribution for different gradients of a cavity. The procedure first consists of determining the zero-crossing phase of the cavity that is operated as a buncher. When operating a quarter-wave resonator at the zero-crossing ($\varphi_s = \pi/2$) and if the bunch length is small compared to the RF-period, the assumption of using the thin gap transfer matrix is justified. The transport of the longitudinal coordinates from the buncher cavity (z_0) to the experimental setup used to measure the energy or the ToF distribution (z_1) is,

$$\boldsymbol{\sigma}(z_1) = \boldsymbol{\mathcal{R}} \cdot \boldsymbol{\sigma}(z_0) \cdot^t \boldsymbol{\mathcal{R}} \tag{6.15}$$

The derivation of the ellipse equation from the Courant-Snyder invariant is shown in Chapter 5. In the longitudinal trace space and at the location z_0, the ellipse equation is,

$$\mathscr{E}(z_0) : \gamma_z(\Delta t)^2 + 2\alpha_z \Delta t \Delta W/A + \beta_z(\Delta W/A)^2 = \varepsilon_z \tag{6.16}$$

The Twiss parameters in the longitudinal direction are noted $(\alpha_z, \beta_z, \gamma_z)$ and the emittance ε_z.

Three-Gradient from Δt

By calculating the element $\boldsymbol{\sigma}_{11}(z_1)$, one obtains a quadratic relation as a function of the equivalent cavity gradient E_0,

$$\Delta t^2(z_1) = E_0^2[\underbrace{\tilde{K}_G^2 K_D^2 \varepsilon_z \beta_z}_{a}] + E_0 \underbrace{\left[2\widetilde{K}_G K_D \varepsilon_z \beta_z - 2\widetilde{K}_G K_D^2 \varepsilon_z \alpha_z\right]}_{-2ab} + \underbrace{\varepsilon_z \beta_z - 2K_D \varepsilon_z \alpha_z + \varepsilon_z \gamma_z K_D^2}_{c+ab^2} \quad (6.17)$$

The ToF spread at the detector location z_1, $\Delta t^2(z_1)$, is measured when varying the equivalent gradient E_0 and the result is fitted with a quadratic curve using the variables (a, b, c) as shown in Equation 6.17. The Twiss parameters and emittance are then accessible from the follow equations,

$$\begin{aligned}
\varepsilon_z &= \frac{\sqrt{ac}}{K_D^2 |\tilde{K}_G|} \\
\alpha_z &= \frac{a}{\varepsilon K_D^2 \tilde{K}_G} \left(b + \frac{1}{K_D \tilde{K}_G}\right) \\
\beta_z &= \frac{a}{\varepsilon_z \tilde{K}_G^2 K_D^2} \\
\gamma_z &= \frac{1}{\varepsilon_z K_D^2} \left(c + a\left(b + \frac{1}{\tilde{K}_G K_D}\right)^2\right)
\end{aligned} \quad (6.18)$$

Three-Gradient from ΔW

In this case, the element $\boldsymbol{\sigma}_{22}(z_1)$ is derived as a function of the equivalent cavity gradient E_0,

$$\Delta W_1^2 = E_0^2[\underbrace{K_G^2 \varepsilon \beta}_{a}] + E_0 \underbrace{\left[-2\widetilde{K}_G \varepsilon \alpha\right]}_{b} + \underbrace{\varepsilon\gamma}_{c} \quad (6.19)$$

The Twiss parameters and the emittance are trivially derived from the fitting

parameters (a, b, c),

$$\begin{aligned} \varepsilon_z &= \frac{1}{\tilde{K}_G}\sqrt{ac - \frac{b^2}{4}} \\ \alpha_z &= -\frac{b}{2\varepsilon_z \tilde{K}_G} \\ \beta_z &= \frac{a}{\varepsilon_z \tilde{K}_G^2} \\ \gamma_z &= \frac{c}{\varepsilon_z} \end{aligned} \tag{6.20}$$

6.2.3 Experimental Setup

The energy distribution is measured using the procedure described in the previous section. The bunch structure is measured at a location in the straight section of the HEBT line (Figure 6.12). We have two distinct ways to quantify the same information, and naturally, one wants to use the same beam in both cases to compare the results. A beam of $^{20}Ne^{8+}$ was accelerated using ten superconducting cavities at an average energy of 6.56 MeV/u. The first quarter-wave resonator (QWR) of the fourth cryomodule is used as a buncher (Figure 6.10). The buncher cavity must offer the possibility to observe the waist of the energy or ToF spread at the detector. It is crucial for the quality of the fitting. The energy distribution measurements imply using three vertical slits, so the intensity required is different than when measuring the ToF. We used an attenuation foil of 0.1 % transparency inserted before the RFQ for the ToF measurement and no attenuation in the case of the energy characterization. The beam intensity was then limited to about 50 pps on the detector for both cases. The gradient of the buncher cavity is varied to a maximum value of $E_0 = 5\,\mathrm{MV/m}$.

The measurements of the average energy or the average ToF while varying the buncher gradient are within a narrow relative interval of 0.5 % confidence zone. Additionaly, the measured variations of those average values appear random as a function of the buncher gradient, so it can be considered that there is effectively no acceleration (or deceleration) and the zero-crossing was accurately determined.

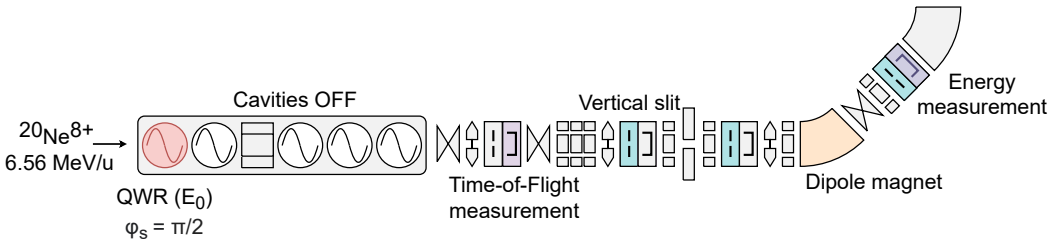

Figure 6.10. Experimental setup for the longitudinal phase space characterization measurements.

6.2.4 Results and Comparison

The uncertainties associated with both measurement type (energy and ToF) are presented in the previous section. Durations of each measurement are chosen so that the values Δt and ΔW are within a confidence interval of 1 %. Several series of entire longitudinal characterization measurements were performed to evaluate the standard deviations on the Twiss parameters and emittance results. We first present typical results from the three-gradient scans; the ToF and energy distributions obtained from different values of the buncher gradient are shown in Figure 6.11. The average value and standard deviation are calculated from each scan, which implies that the emittance and Twiss parameters extrapolated relate to 1-rms.

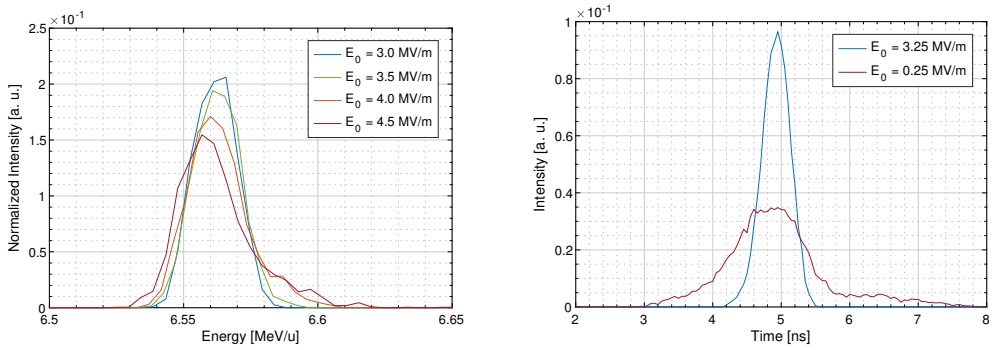

(a) Energy distribution measurement. **(b)** Bunch structure measurement.

Figure 6.11. Measured variations of the energy spread and time-of-flight spread when varying the gradient of the buncher cavity for a beam $^{20}Ne^{8+}$ at an average energy of 6.56 MeV/u

.

Three-Gradient from ΔW

The energy spread is measured for nine different values of the cavity gradient. Each energy scan lasts about 6 min 40 s to ensure the prerequisites in terms of accuracy. The results are shown in Figure 6.12. The minimal value of the energy spread reached is 8 keV/u, which translates into an energy spread of 0.12 %. The r^2 of the fitting is deemed satisfactory for modelling the measurement with the Equation 6.17, and the Twiss parameters and emittance can be derived. The absolute uncertainties on those parameters are estimated by repeating the entire procedure ten times.

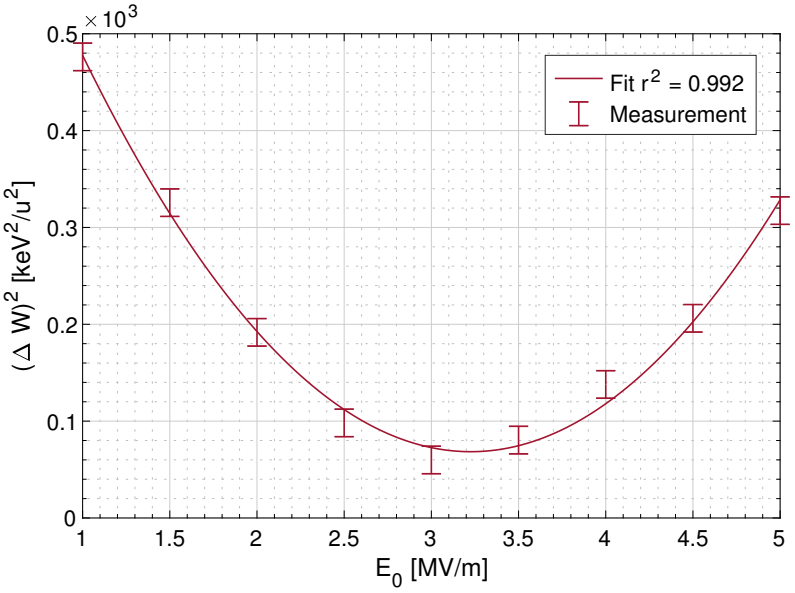

Figure 6.12. Square of the energy distribution's standard deviation, when varying the buncher cavity gradient, for a beam $^{20}Ne^{8+}$ at an average energy of 6.56 MeV/u.

Three-Gradient from Δt

When using the silicon detector for measuring the bunch length of the beam, the integration time needed to reach a measure of Δt within 1 % is, in theory, lower than with the energy spectrometry technique. We chose to record for 3 min the ToF of the beam for twenty different gradient values around the waist. Statistically both methods yield a R^2 very close from one and we cannot claim that one technique is better than the other (Figure 6.13). However it is observable that the bunch

structure measurement suffers from a discrepancy with the parabolic model at high gradient field. Although the measure of Δt stabilizes within a 1 % confidence interval, an unknown systematic seems to remain. The residuals of the fitting inexplicably deviate from the measurement for $E_0 > 4MV/m$. Using the fitting parameters from Equation 6.19, one may determine the Twiss parameters and emittance. The uncertainties on those parameters were estimated by repeating the entire three-gradient method measurement ten times and calculating the standard deviation from all the batches of measurements.

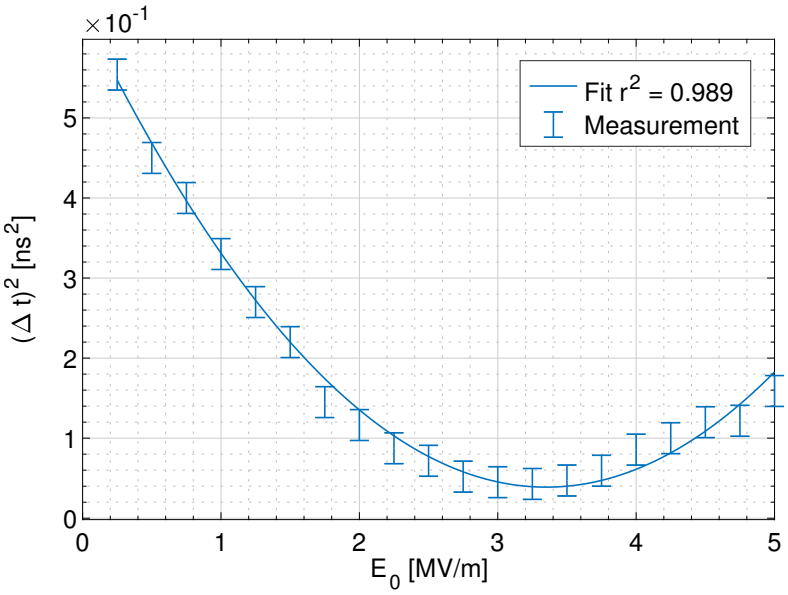

Figure 6.13. Spread of the bunch structure when varying the buncher cavity gradient for a beam $^{20}Ne^{8+}$ at an average energy of 6.56 MeV/u.

Comparison

The results of the derived Twiss parameters and emittance from each type of measurement are shown in Table 6.2. The Twiss parameters in differ for each method, however the emittance values fall within each other confidence interval. The derivation of Twiss parameters using the measurement of the bunch length is sensitive to the drift length between the buncher cavity and the detector. We calculate that a change of 20 cm from the theoretical (design model) distance yields to Twiss parameters within the confidence zone of the energy spread method. The value of

20 cm is less than the cavity length, and it is likely that the deduction of the Twiss parameters from the bunch length measurement needs to be consolidated by more precise estimations of distances. Apart from the determination of the longitudinal trace space ellipse parameters, it was also indirectly confirmed that one might use a quarter-wave resonator as a buncher for decreasing the energy spread. The typical duration of a longitudinal characterization of the beam, from the measurements of ΔW or Δt, was 60 min. The results obtained using the energy spectrometer technique shows more minor uncertainties from repeated series of measurements. The comparison between the Twiss parameters measured show discrepancies that remain to be fully understood. One perspective is to precisely measure the distance between the superconducting cavities and the detectors. Another option is to use the simulation model developed during the REX/HIE-ISOLDE linac design ([Fraser, 2012]), and first adjust this model to the current situation of the linac, in order draw a comparison with the measurements. The comparison with simulation can help in better understanding which measurement method is the closest from expectations and lead the investigation to improve the quality of the other.

Table 6.2. Comparison of the longitudinal 1-rms beam properties of a $^{20}Ne^{8+}$ beam at an average energy of 6.56 MeV/u measured using the three-gradient method.

Beam Property	**From ΔW**	**From Δt**
ε_z [π.ns.keV/u]	1.25(8)	1.18(10)
α_z	-3.54(30)	-4.68(50)
β_z [ns.(keV/u)$^{-1}$]	0.0183(20)	0.0194(30)
γ_z [keV/u.ns^{-1}]	970(40)	1110(50)
Fitting r^2	0.992	0.989

CHAPTER 7

Conclusion

The studies presented in this thesis encompass several themes related to beam quality at REX/HIE-ISOLDE post-accelerator. As the beam intensities encountered from exotic isotope production are often below the detection capability of traditional beamline instruments, we have developed new methodologies to characterize radioactive ion beams in situ. The novelty of the work presented in this thesis resides in the demonstration of the capability to probe beam properties for any range of intensity. The measurement of the following properties are now possible at REX/HIE-ISOLDE linac:

1. The beam intensity can be measured absolutely, which notably allows to fine tune accelerating cavities using RIB.

2. The beam purity can be estimated down to single-ion detection for a large range of A/q.

3. The transverse beam properties can be determined directly using RIB.

4. The longitudinal beam properties can be deduced from energy spread or bunch structure measurements.

In parallel, we show direct applications of those methods, contextualized with the operational use of the post-accelerator. Accelerating structures, such as the RFQ, can be tuned with very low-intensity beams. Moreover, we are capable of assessing

that the emitted material from the cathode does not significantly impact the beam purity. The longitudinal and transverse beam properties are measured using very low-intensity beams of less than 0.1 efA. We correlate the results obtained using multiple techniques: the double-slit and quadrupole-scans for transverse properties and energy spread or bunch length measurements for the longitudinal plane. One perspective would be to compare the measured emittance with the simulation model, which was initially developed during the design of REX/HIE linac. This would help in fully validating the optics model and to better apprehend the validity of the measurements.

We furthermore detail an analytical frame that serves at evaluating the performance of the REXEBIS charge-breeder. A method for scanning the axial energy of the extracted beam is presented. One direct application is the Slow Extraction of ions from the EBIS to reduce the instantaneous rate. We show that the overlap factor between ions and the electron beam can also be deduced from axial energy scans. This information is put in perspective with measured charge state distributions and the extrapolation of the effective electron current density.

APPENDIX A

EBIS Cross Sections

A.1 Electron Impact Ionization

The collision between an electron and ion may result in ionization if the electron energy E_e is higher than the energy E_b of a bound electron. The sum of the energies of the two emitted electrons corresponds to the difference between the impacting electron energy and the (negative) binding energy.

$$\begin{aligned} &A^{q+} + e^- (E_e) \rightarrow A^{(q+1)+} + e^- (E_1) + e^- (E_2) \\ &E_e - E_b = E_1 + E_2 \end{aligned} \tag{A.1}$$

The electron-impact ionization cross section is then a function of the electron beam energy. Lotz formula approximates cross section [Lotz, 1967],

$$\sigma^{\mathrm{EI}} (E_e) \, [\mathrm{cm}^2] \simeq 4.5 \cdot 10^{-14} \sum_{\forall k : E_e > E_{b,k}} \frac{N_k \log (E_e / E_{b,k})}{E_e E_{b,k} [\mathrm{eV}^2]} \tag{A.2}$$

with N_k the number of electrons in shell $k = (n, l)$. The required electron beam energy for the ionization of neutral atoms is a few eV, meanwhile for H-like uranium it is up to about 115 keV. The maximum of electron impact ionization cross sections occur at 2 to 3 times the binding energy E_b. The cross sections for Xe^{q+} are shown in Figure A.1.

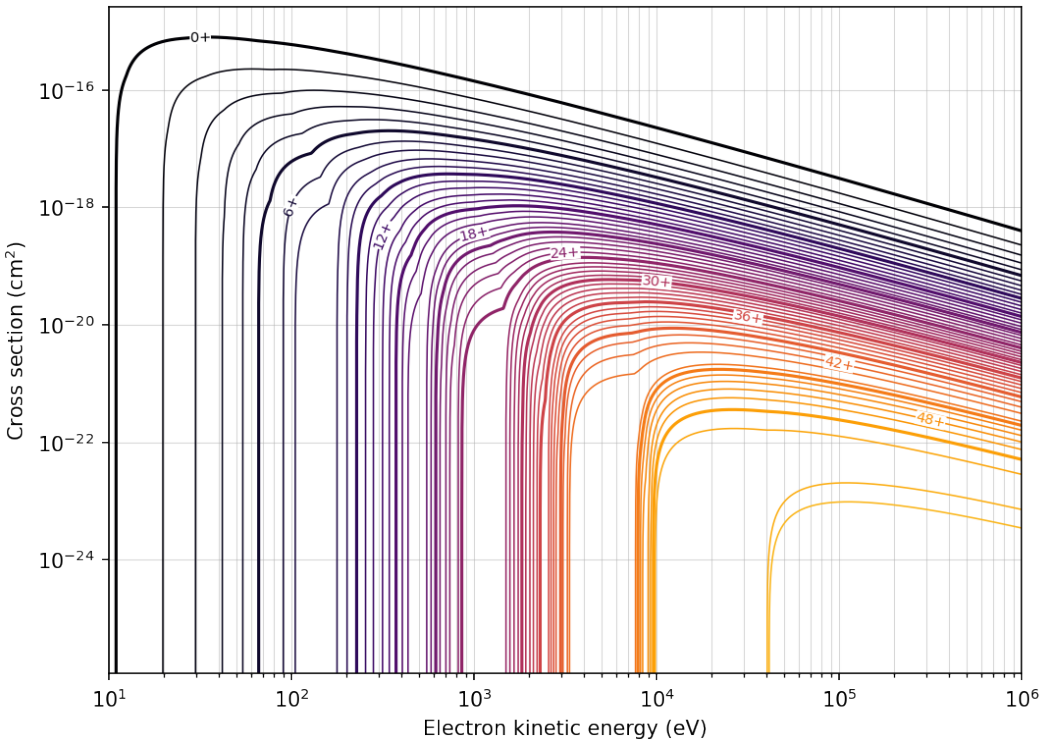

Figure A.1. Electron impact ionization cross sections for 54-xenon. Calculated from Lotz formula and plotted using EBISIM.

A.2 Radiative Recombination

The radiative recombination process implies the capture of an electron from the beam and simultaneous emission of a photon. This process is the reverse of photoionization and may happen at any electron beam energy. The energy of the emitted photon is the sum of the electron energy and the binding energy.

$$\begin{aligned} A^{q+} + e^{-}\left(E_e\right) &\rightarrow A^{(q-1)+} + \hbar\omega \\ \hbar\omega &= E_e + E_b \end{aligned} \tag{A.3}$$

The cross sections are computed using Kim and Pratt estimations of direct radiative recombination [Kim and Pratt, 1983],

$$\sigma^{\mathrm{RR}}\left(E_e\right) = \frac{8\pi\alpha}{3\sqrt{3}}\left(\frac{\hbar}{m_e c}\right)^2 \chi \log\left(1 + \frac{\chi}{2n_{0,\,\mathrm{eff}}^2}\right) \tag{A.4}$$

where α is the fine-structure constant, and

$$\begin{aligned} \chi &= 2Z_{\mathrm{eff}}^2 \frac{\mathrm{R_y}}{E_e}, \quad Z_{\mathrm{eff}} = \frac{Z+q}{2} \\ n_{0,\,\mathrm{eff}} &= n_0 + (1 - w_{n_0}) - 0.3 \end{aligned} \tag{A.5}$$

with $\mathrm{R_y}$ the Rydberg constant and w_{n_0}, the fraction of occupied states in valence shell n_0. The cross sections for Xe^{q+} are shown in Figure A.2.

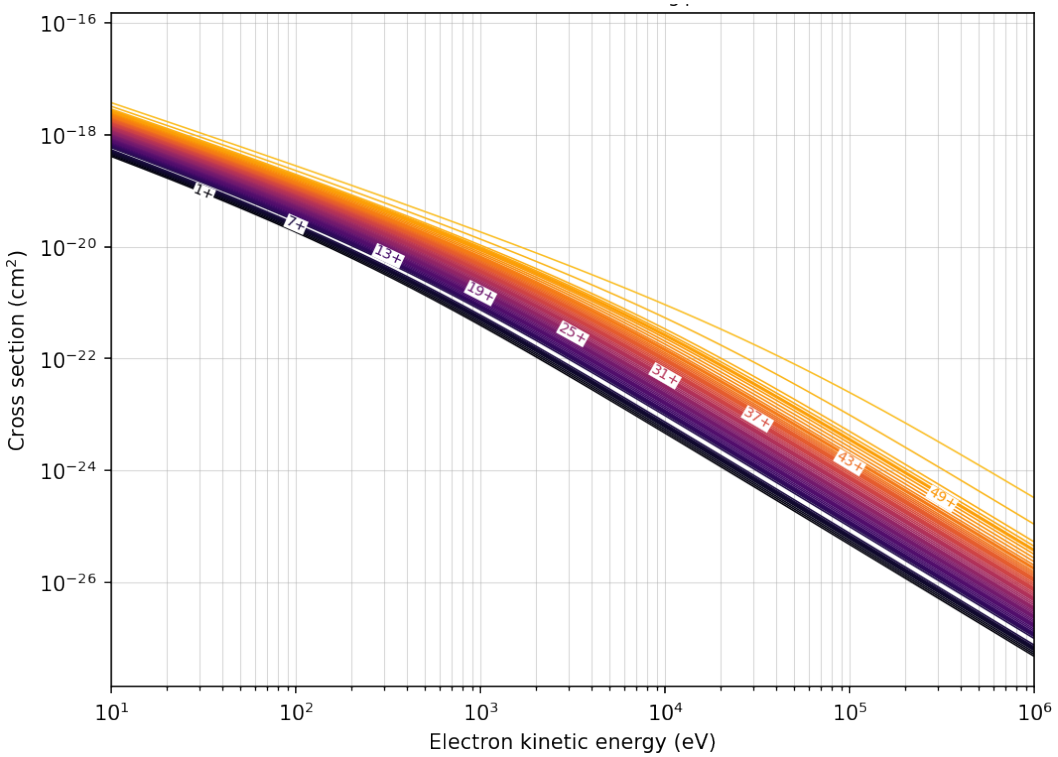

Figure A.2. Radiative recombination cross sections for 54-xenon. Calculated from Kim and Pratt formula and plotted using EBISIM.

A.3 Dielectronic Recombination

Dielectronic recomination is a resonant process, which similarly to the radiative recombination process involves the initial capture of an electron. However, when the electron beam energy is close from the energy required for a bound electron to be promoted to another shell, the ion enters a doubly excited intermediate state. The ion decays from this excited stated state through the emission of a photon or Auger emission.

$$A^{q+} + e^{-}\left(E_e\right) \rightarrow \left[A^{(q-1)+}\right]^{**} \rightarrow + A^{(q-1)+} + \hbar\omega \tag{A.6}$$

We do not apply a general model used for calculating all possible branching ratios as it is computationally heavy. Only KLL-dielectronic recombination processes are considered, so the promotion of a K shell-electron in the L shell following the capture of an electron in that same shell. The effective dielectronic capture cross section are derived from the branching ratios between radiative and auto-ionizing decay computed with Flexible Atomic Code [Gu, 2008].

A.4 Charge Exchange

During collisions with neutral atoms, ions can gain an electron from the atom. The electron capture may result in the excitation of the ion which decays with the emission of a photon.

$$A^{q+} + B \rightarrow \left[A^{(q-1)+}\right]^{*} + B^{+} \rightarrow A^{(q-1)} + B^{+} + \hbar\omega \tag{A.7}$$

The charge exchange cross section depends on the ion charge and the ionization potential of the neutral gas, and is independent of the energy of the projectiles [Müller and Salzborn, 1976]. The empirical charge exchange cross sections for collision energies below 25 keV/u, can be estimated using Mulller-Salzborn formula [Müller and Salzborn, 1977],

$$\sigma_q^{\mathrm{CX}}[\mathrm{cm}^2] \simeq (1.43 \pm 0.76 \cdot 10^{-12}) q^{1.17} \left(I_q[\mathrm{eV}]\right)^{-2.76} \tag{A.8}$$

where I_q is the ionisation potential of the neutral atom, which is computed using Flexible Atomic Code.

APPENDIX B

Longitudinal Loss Frequency

An expression of the longitudinal escape rate of ions inside an EBIS is shown in [Marrs, 1999]. It uses the escape rate calculated from the Fokker-Planck equation in the context of an arbitrary magnetic-mirror confinement [Khudik, 1997]. In this later reference, the escape rate is expressed for an ion of charge Q_i and temperature T_i and uses a Taylor development for high values of ω_i,

$$\omega_i = \frac{Q_i U_{\text{well}}}{k_B T_i} \tag{B.1}$$

with U_{well} the longitudinal trapping potential which corresponds to the difference between the minimum outer barrier potential and the maximum drift tube potential.

$$\nu_K = \frac{4\bar{v}_i e^{-\omega_i}}{\sqrt{\pi}\omega_i C_R}\left(\frac{1}{2}\right)\left(1 + \frac{\widetilde{A_1}}{\omega_i} + \frac{\widetilde{A_2}}{\omega_i^2} + o(\frac{1}{\omega_i^2})\right) \tag{B.2}$$

with $\bar{v}_i$ the average ion-ion collision rate. For a unitary magnetic mirror ($B_{\text{min}} = B_{\text{max}}$), the constant coefficients are

$$\mathrm{C_R} = 0.924 \quad \widetilde{\mathrm{A}_1} = -1.45 \quad \widetilde{\mathrm{A}_2} = 3.46 \tag{B.3}$$

The longitudinal losses per unit time and volume is finally $n_i \cdot \nu_K$, with n_i the ion density.

Bibliography

[Ames et al., 2001] Ames, F., Schmidt, P., Forstner, O., Bollen, G., Engels, O., Habs, D., and Huber, G. (2001). Space-Charge Effects with REXTRAP. *Hyperfine Interactions*, 132(1-4):465–468.

[Beebe et al., 1993] Beebe, E. et al. (1993). *Physica Scripta*, 47:470–474.

[Bongers et al., 1999] Bongers, H., Emhofer, S., Habs, D., Kester, O., Rudolph, K., Sieber, T., Schempp, A., Welsch, C., and Kühnel, J. W. (1999). Test of the REX-RFQ and Status of the Front Part of the REX-ISOLDE linac. In *Proceedings of PAC'99*, pages 3516–3518, New-York, USA.

[Braginskii, 1965] Braginskii, S. I. (1965). Transport Processes in a Plasma. *Reviews of Plasma Physics*, 1:205.

[Butler et al., 2007] Butler, P., Huyse, M., and Krücken, R. (2007). HIE-ISOLDE: the scientific opportunities. Technical Report October 2005.

[Chandrasekhar, 1943] Chandrasekhar, S. (1943). Stochastic problems in physics and astronomy. *Rev. Mod. Phys.*, 15:1–89.

[Chew et al., 1956] Chew, G. F., Goldberger, M. L., Low, F. E., and Chandrasekhar, S. (1956). The boltzmann equation an d the one-fluid hydromagnetic equations in the absence of particle collisions. *Proceedings of the Royal Society of London. Series A. Mathematical and Physical Sciences*, 236(1204):112–118.

[Currell, 2003] Currell, E. J. (2003). *Electron Beam Ion Traps and Their Use in the Study of Highly Charged Ions*, pages 39–75. Springer Netherlands, Dordrecht.

[Danared, 1998] Danared, H. (1998). Simulation of relaxation processes in electron beams at high magnetic fields. *Hyperfine Interactions*, 115(1-4):61–65.

[D'Arcy and Shemyakin, 2015] D'Arcy, R. and Shemyakin, A. (2015). Calculation of the effect of slit size on emittance measurements made by a two-slit scanner. pages 1–6.

[Delahaye, 2013] Delahaye, P. (2013). Ecris and ebis charge state breeders: Present performances, future potentials. *Nuclear Instruments and Methods in Physics Research Section B: Beam Interactions with Materials and Atoms*, 317:389–394. XVIth International Conference on ElectroMagnetic Isotope Separators and Techniques Related to their Applications, December 2–7, 2012 at Matsue, Japan.

[E. Matli, 2019] E. Matli, N. Bidault, E. P. . J. A. R. (2019). Phasing of superconductive cavities of the rex/hie-isolde linac. *Proc. 10th Int. Particle Accelerator Conf. (IPAC 19)*, pages 3786–3788.

[Fraser, 2012] Fraser, M. A. (2012). *Beam Dynamics Studies of the ISOLDE Post-accelerator for the High Intensity and Energy Upgrade*. PhD thesis, University of Manchester.

[Fraser et al., 2014] Fraser, M. A., Voulot, D., and Wenander, F. (2014). Beam Dynamics Simulations of the REX-ISOLDE A/q -separator. Technical Report HIE-ISOLDE-PROJECT-Note-0027, CERN.

[Fraser and Wenander, 2012] Fraser, M. A. and Wenander, F. (2012). Study of Effect of Ion Source Energy Spread on RFQ Beam Dynamics at REX-ISOLDE. Technical Report HIE-ISOLDE-PROJECT-Note-0018, CERN, Geneva, Switzerland.

[Gaffney et al., 2013] Gaffney, L. P., Butler, P. A., Scheck, M., Hayes, A. B., Wenander, F., Albers, M., Bastin, B., Bauer, C., Blazhev, A., Bo, S., Chupp, T., Cline, D., Cocolios, T. E., Davinson, T., Witte, H. D., Diriken, J., Grahn, T., Herzan, A., Bree, N., Cederka, J., Kwan, E., Lutter, R., Moschner, K., Huyse, M., Jenkins, D. G., Joss, D. T., Kesteloot, N., Konki, J., Kowalczyk, M., Napiorkowski, P., Pakarinen, J., Pfeiffer, M., Radeck, D., Reiter, P., Reynders, K., Rigby, S. V.,

Robledo, L. M., Rudigier, M., Sambi, S., Seidlitz, M., Siebeck, B., Stora, T., Thoele, P., Duppen, P. V., Vermeulen, M. J., Voulot, D., Warr, N., Wimmer, K., Wu, C. Y., and Zielinska, M. (2013). Studies of pear-shaped nuclei using accelerated radioactive beams. *Nature*, 497:199–204.

[Gu, 2008] Gu, M. F. (2008). The flexible atomic code. *Canadian Journal of Physics*, 86(5):675–689.

[Gustafsson et al., 2011] Gustafsson, A., Herlert, A., and Wenander, F. (2011). Mass-selective operation with REXTRAP. *Nuclear Instruments and Methods in Physics Research, Section A: Accelerators, Spectrometers, Detectors and Associated Equipment*, 626-627(1):8–15.

[Herrmann, 1958] Herrmann, G. (1958). Optical theory of thermal velocity effects in cylindrical electron beams. *Journal of Applied Physics*, 29(2):127–136.

[Hock et al., 2014] Hock, K. M., Ibison, M. G., Holder, D. J., Muratori, B. D., Wolski, A., Kourkafas, G., and Shepherd, B. J. (2014). Beam tomography research at Daresbury Laboratory. *Nuclear Instruments and Methods in Physics Research, Section A: Accelerators, Spectrometers, Detectors and Associated Equipment*, 753:38–55.

[Huba, 2004] Huba, J. (2004). Nrl: Plasma formulary. page 73.

[Kadi et al., 2017] Kadi, Y., Blumenfeld, Y., Delsolaro, W. V., Fraser, M. A., Huyse, M., Koufidou, A. P., Rodriguez, J. A., and Wenander, F. (2017). Post-accelerated beams at ISOLDE. *Journal of Physics G: Nuclear and Particle Physics*, 44(8).

[Khudik, 1997] Khudik, V. (1997). Longitudinal losses of electrostatically confined particles from a mirror device with arbitrary mirror ratio. *Nuclear Fusion*, 37(2):189–198.

[Kim and Pratt, 1983] Kim, Y. S. and Pratt, R. H. (1983). Direct radiative recombination of electrons with atomic ions: Cross sections and rate coefficients. *Phys. Rev. A*, 27:2913–2924.

[Kühnel, 1999] Kühnel, K.-U. (1999). Aufbau eines Splitringresonators als Rebuncher für das REX-ISOLDE Projekt. Master's thesis, Institute for Applied Physics, Goethe University.

[Lapierre, 2017] Lapierre, A. (2017). *Canadian Journal of Physics*, 95:361–369.

[Lotz, 1967] Lotz, W. (1967). An Empirical Formula for the Electron-Impact Ionization Cross-Section. *Zeitschrift für Physik*, 206:205–211.

[Marrs, 1999] Marrs, R. E. (1999). Self-cooling of highly charged ions during extraction from electron beam ion sources and traps. *Nuclear Instruments and Methods in Physics Research, Section B: Beam Interactions with Materials and Atoms*, 149(1-2):182–194.

[Minerbo, 1979] Minerbo, G. (1979). MENT: A maximum entropy algorithm for reconstructing a source from projection data. *Computer Graphics and Image Processing*, 10(1):48–68.

[Müller and Salzborn, 1976] Müller, A. and Salzborn, E. (1976). Single and double electron transfer in ari+-he collisions. *Physics Letters A*, 59(1):19–20.

[Müller and Salzborn, 1977] Müller, A. and Salzborn, E. (1977). Scaling of cross sections for multiple electron transfer to highly charged ions colliding with atoms and molecules. *Physics Letters A*, 62(6):391–394.

[Nilsson et al., 2006] Nilsson, T., Lindroos, M., Nilsson, T., and Lindroos, M. (2006). HIE-ISOLDE: the Technical Options. Technical Report November.

[Nolte et al., 1979] Nolte, E., Geschonke, G., Berdermann, K., Oberschmid, R., Zierl, R., Feil, M., Jahnke, A., Kress, M., and Morinaga, H. (1979). The munich heavy ion postaccelerator. *Nuclear Instruments and Methods*, 158:311–324.

[Pahl, 2021] Pahl, H. (2021). Ebisim. `https://github.com/HPLegion/ebisim`.

[Pikin et al., 2016] Pikin, A., Alessi, J. G., Beebe, E. N., Raparia, D., and Ritter, J. (2016). Analysis of magnetically immersed electron guns with non-adiabatic fields. *Review of Scientific Instruments*, 87(11).

[Pitters et al., 2019] Pitters, J., Breitenfeldt, M., Pinto, S. D., Pahl, H., Pikin, A., Shornikov, A., and Wenander, F. (2019). Pepperpot emittance measurements of ion beams from an electron beam ion source. *Nuclear Instruments and Methods in Physics Research, Section A: Accelerators, Spectrometers, Detectors and Associated Equipment*, 922(May 2018):28–35.

[Podlech et al., 1999] Podlech, H., Grieser, M., Hahn, R., Repnow, R., and Schwalm, D. (1999). The 7-gap-resonator-accelerator for the rex-isolde-linac. 5.

[Rodriguez et al., 2016] Rodriguez, J. A., Delsolaro, W. V., Andreazza, W., Bibby, J. M., Bidault, N., Bravin, E., Broere, J. C., Cantero, E. D., Catherall, R., Cobham, V., Elias, M., Fadakis, E., Fernier, P., Fraser, M. A., Gerigk, F., Hanke, K., Kadi, Y., Benito, M. L., Matli, E., Sadovich, S., Siesling, E., Valuch, D., Wenander, F., and Zhang, P. (2016). Beam commissioning of the HIE-ISOLDE post-accelerator. In *IPAC 2016 - Proceedings of the 7th International Particle Accelerator Conference*, pages 2045–2047.

[Sander, 1990] Sander, O. R. (1990). Transverse emittance: Its definition, applications, and measurement. *AIP Conference Proceedings*, 212(1):127–155.

[Sieber et al., 2004] Sieber, T., Habs, D., and Kester, O. (2004). Test and first experiment with the new REX-ISOLDE 200 MHz IH structure. In *LINAC 2004*, pages 318–320.

[Spitzer and Cook, 1957] Spitzer, L. and Cook, C. J. (1957). Physics of fully ionized gases: No. 3 of interscience tracts on physics and astronomy. *Physics Today*, 10(1):40–42.

[Stockli, 2006] Stockli, M. P. (2006). Measuring and Analyzing the Transverse Emittance of Charged Particle Beams. In *AIP Conference Proceedings*, volume 868, pages 25–62. AIP.

[Venturini Delsolaro and Miyazaki, 2020] Venturini Delsolaro, W. and Miyazaki, A. (2020). Seamless quarter wave resonators for Hie isolde. In *Proceedings of the 29th Linear Accelerator Conference, LINAC 2018*, pages 292–296.

[Villani, 2002] Villani, C. (2002). Chapter 2 - a review of mathematical topics in collisional kinetic theory. volume 1 of *Handbook of Mathematical Fluid Dynamics*, pages 71–74. North-Holland.

[Vondrasek, 2016] Vondrasek, R. (2016). On-line charge breeding using ECRIS and EBIS. *Nuclear Instruments and Methods in Physics Research, Section B: Beam Interactions with Materials and Atoms*, 376:16–23.

[Wangler, 1998] Wangler, T. P. (1998). Physics Textbook. Wiley-VCH, 2 edition.

[Warr et al., 2013] Warr, N. et al. (2013). *The European Physical Journal A*, 49:40.

[Wenander et al., 1999] Wenander, F., Jonson, B., Liljeby, L., and Nyman, G. (1999). The Electron Beam Ion Source for the REX-ISOLDE Project.

[Wiedemann, 2015] Wiedemann, H. (2015). *Particle Accelerator Physics*, volume 7 of *Graduate Texts in Physics*. Springer International Publishing.

[Zocca et al., 2012] Zocca, F., Fraser, M. A., Bravin, E., Pasini, M., Voulot, D., and Wenander, F. (2012). Development of a silicon detector monitor for the HIE-ISOLDE superconducting upgrade of the REX-ISOLDE heavy-ion linac. *Nuclear Instruments and Methods in Physics Research, Section A: Accelerators, Spectrometers, Detectors and Associated Equipment*, 672:21–28.